

Theoretical Methods for Spintronics in Semiconductors with Applications

Thesis by

Xavier Cartoixà Soler

In Partial Fulfillment of the Requirements

for the Degree of

Doctor of Philosophy

California Institute of Technology

Pasadena, California

2003

(Submitted September 18, 2002)

© 2003

Xavier Cartoixa Soler

All Rights Reserved

Als meus pares

List of Publications

Work related to this thesis has been or will be presented in the following publications:

- [1] **Theoretical investigations of spin splittings in asymmetric AlSb/InAs/GaSb heterostructures and the possibility of electric field induced magnetization,**
X. Cartoixà, D. Z.-Y. Ting, E. S. Daniel, and T. C. McGill, *Superlatt. Microstruct.*, **30** (6), pp. 309–319, 2001.
- [2] **Spin injection from ferromagnetic metals into gallium nitride,**
C. J. Hill, X. Cartoixà, R. A. Beach, D. L. Smith, and T. C. McGill, *cond-mat/0010058*, 2001.
- [3] **Theoretical investigations of spin splittings and optimization of the Rashba coefficient in asymmetric AlSb/InAs/GaSb heterostructures,**
X. Cartoixà, D. Z.-Y. Ting, and T. C. McGill, *J. Comp. Elec.*, 2002, in press.
- [4] **Modeling spin-dependent transport in InAs/GaSb/AlSb resonant tunneling structures,**
D. Z.-Y. Ting, X. Cartoixà, T. C. McGill, D. L. Smith, and J. N. Schulman, *J. Comp. Elec.*, 2002, in press.
- [5] **Rashba effect resonant tunneling spin filters,**
David Z.-Y. Ting, Xavier Cartoixà, David H. Chow, Jeong S. Moon, Darryl L. Smith, Thomas C. McGill, and Joel N. Schulman, *IEEE Trans. Magn.*, 2002, to be published.
- [6] **Spin filtering in asymmetric resonant interband tunneling diodes,**
D. Z.-Y. Ting, X. Cartoixà, D. H. Chow, D. L. Smith, T. C. McGill, and J. N. Schulman, in *Proceedings of the 26th International Conference on Physics of Semiconductors (ICPS-26)*, 2002, to be published.

- [7] **Resonant interband tunneling spin filter,**
David Z.-Y. Ting and Xavier Cartoixà, *Appl. Phys. Lett.*, 2002, to be published.
- [8] **Refraction effects in the emitted light of a spin LED,**
S. R. Ichiriu, X. Cartoixà, and T. C. McGill, in preparation.
- [9] **Bulk inversion asymmetry effects in zincblende heterostructures,**
X. Cartoixà, D. Z.-Y. Ting, and T. C. McGill, 2002, to be submitted.
- [10] **Description of bulk inversion asymmetry in the effective bond orbital model,**
X. Cartoixà, D. Z.-Y. Ting, and T. C. McGill, 2002, in preparation.
- [11] **Elimination of spurious solutions in finite difference method implementations of band structure calculation methods,**
X. Cartoixà and T. C. McGill, 2002, in preparation.

Work in which the author has been involved, but not related to this thesis, has been presented in the following publications:

- [1] **Coupled drift-diffusion/quantum transmitting boundary method simulations of thin oxide devices with specific application to a silicon based tunnel switch diode,**
E. S. Daniel, X. Cartoixà, W. R. Frensley, D. Z.-Y. Ting, and T. C. McGill, *IEEE Trans. Elec. Dev.*, **47** (5), pp. 1052–1060, 2000.
- [2] **Tunnel switch diode based an AlSb/GaSb heterojunctions,**
X. C. Cheng, X. Cartoixà, M. A. Barton, C. J. Hill, and T. C. McGill, *J. Appl. Phys.*, **88** (11), pp. 6948–6950, 2000.

Acknowledgements

During my years pursuing the Ph.D. degree at Caltech, I have had the pleasure of meeting many wonderful people. Without them, my stay here would have been far less enjoyable. So, I want to write a few lines to thank the people who helped me each in their own way all this time.

In Professor Thomas Conley McGill can be found a rare combination of scientific insight, political skills and wit. This combination of talents has helped Tom attract a group of extraordinary people around him and obtain enough capital resources to satisfy their expensive tastes—in lab equipment, of course. Working with Tom not only opened new avenues of thought in my scientific endeavors, but also provided me—and the members of the group—with valuable lessons about the intricacies of running a research operation as well as about life at large. He always protected his students from the occasional storm, and understood that science should not be our only passion. For this and more, I am thankful to him.

Also, I could not let the opportunity to thank David Z.-Y. Ting slip. It is largely because of his guidance that I am able to write these lines today instead of a year from now. Through regular collaboration and thought sharing with him, I have come to appreciate his creativity and insight. He has always been there to listen to the questions I posed him and, when he could not provide answers, I could count on him for some sympathy. The development of some of his ideas constitute a good part of this thesis.

I enjoyed lengthy lunch talks with Gerry Picus and his good humor. His wish to keep up to date with my work was a motivation to express my ideas in a clear fashion, and I sure appreciate his patience while trying to teach me some of his methodology in my adventures as an experimentalist. I also enjoyed speaking with Ogden Marsh and the late Jim McCaldin, who showed me that one can stay curious a whole life. Joel Schulman and Darryl Smith stopped me from trying to revolutionize semiconduc-

tor physics based on some considerations to which I had not given enough thought. I am also grateful to Andy Hunter for letting me show unpublished Shubnikov-de Haas measurements. This work would not have been possible without the support from Larry Cooper, of the Office of Naval Research, and Stuart Wolf, of the Defense Advanced Research Projects Agency.

The students in Tom's group have been wonderful to work with. I will hardly find anywhere else such companions, with whom I can discuss at length not only science, but almost every imaginable topic. The older students: Erik Daniel, Xiao-Chang Cheng, Eric Piquette, Alicia Alonzo, Paul Bridger, Zvonimir Bandic and Joel Jones always found time to guide me. Bob Beach, with his carefree, but not careless, approach to life infused us all with high spirits. Cory Hill was a loyal friend and his relentless pursuit of knowledge was a good counterpart to my excessive inclination to handwaving. Matt Barton and Rob Goettler shared the beginnings with me. Ed Preisler is one of the better hearted people I know. His knowledge of sports probably can only be matched by Neal Oldham's, who seems to know almost everything there is to know about materials science. The outgoing personality of Robert Strittmatter served as a catalyst for a number of social events within the group. The generosity of Stephan Ichiriu has showed up in many occasions, and we spent many hours together—my role being mainly watch-and-learn—doing the system administration tasks. Although in the more rewarding universe of postdoctoral research, Justin Brooke has become one more of us. The group's administrative assistant, Tim Harris, has been most helpful in shielding us from the bureaucracy that one must inevitably face. To all of them I wish the best in their future endeavors.

Of course, there is life outside of the lab; and over my years at Caltech many have been the friends with whom I shared experiences: Federico Spedalieri, Diego Dugatkin, Γιώργος Panatopoulos (don't quote me on the spelling), Bjarne Bergheim, Fok-Yan Leung, José Mumbru, Mariu Hernández, Alfredo Martínez, Javier González, Mario Múnich, Pili Gainza, Seong-Min Kim, Gabriela Surpi, Álvaro González, Pedro González, Martín Basch, Michela Muñoz, Enric Claverol, Maria Teresa Monserrat, Rodrigo Quian, Guifré Vidal, Anna Fontcuberta, my friends at home... Thank you

for all the good times!

Apart from their major role in my existing, none of this would be possible without my parents, Albert and Mercè. They have always stood behind me, and supported me in all my undertakings. Throughout the changing times I know their love stays the same.

Finally, I must thank my girlfriend, Virginia. Her good spirits always lift me up when I need it. I am really fortunate to be able to enjoy her love and companionship. I will always be grateful for the many things she has sacrificed during my stay here. I hope I will be able to make it up to her.

Gràcies.

Abstract

Theoretical studies of the role of structural inversion symmetry (SIA) and bulk inversion symmetry (BIA) in the band structure and tunneling properties of zincblende heterostructures have been carried out.

The effective bond orbital model (EBOM) method is used to examine the spin splitting due to SIA in AlSb/InAs/GaSb asymmetric heterostructures. It is found for the resulting two-dimensional electron gas (2DEG) that large theoretical values of the Rashba coefficient in the range of 50×10^{-10} eV·cm can be achieved for optimized structures. Structures presenting anticrossing of the conduction and valence bands show an appreciable reduction in the value of the Rashba coefficient. The possibility of extracting the Rashba coefficient from magnetization measurements is explored. An expression is derived, valid in the diffusive limit, for the spin polarization of the current resulting from a bias parallel to the plane of the quantum well.

The EBOM method is expanded to include BIA effects. The resulting formalism is then used to compute the band structure of an AlSb/GaSb superlattice, where the BIA-induced splitting is observed. The results agree with $\mathbf{k} \cdot \mathbf{p}$ calculations.

The first implementation of an 8-band Envelope Function Approximation method faithful to the T_d symmetry of bulk zincblendes has been made. It has been used to compute the bands for quantum wells with and without BIA effects included, and demonstrates that the BIA effects can be of the same order of magnitude as SIA (*i.e.*, Rashba) effects. A 2-band Hamiltonian describing BIA effects is proposed. The origin of spurious solutions for certain values of the input parameters is determined and a condition for its absence is derived. Modest modifications to the superlattice method allow the computation of spin-dependent transmission coefficients with the multiband quantum transmitting boundary method (MQTBM). The effect of BIA on the transmitted states and the spin filtering action of an asymmetric resonant interband tunneling diode are investigated.

Finally, a Monte Carlo single photon generation algorithm is devised. The photons generated are satisfactory for simulation of light emitted from band-to-band spontaneous transitions in crystals. The polarization is determined taking into account the electron spin, making the algorithm suitable for the analysis of optical detection of spin injection experiments.

Contents

List of Publications	iv
Acknowledgements	vi
Abstract	ix
1 Introduction	1
1.1 Thesis overview	1
1.2 Motivation	2
1.2.1 Theoretical methods	4
1.2.2 Spin injectors/filters	5
1.2.3 Detection of spin injection	6
1.3 Summary of results	7
1.3.1 Theoretical methods	7
1.3.2 Applications	8
1.3.3 Collaborative work	10
1.4 Chapter overview	10
Bibliography	11
2 Spin splittings in asymmetric AlSb/InAs/GaSb heterostructures and electric field induced magnetization	13
2.1 Introduction	13
2.2 Theoretical methods	14
2.3 Results	15
2.3.1 Band structure and spatial part of the wavefunction	15
2.3.2 Spin part of the wavefunction	17

2.3.3	Rashba coefficient for an asymmetric heterostructure made of AlSb/InAs/GaSb/AlSb	19
2.3.4	Spatial variation of the wavefunction	20
2.4	Physical explanation for the results	20
2.5	Electric field induced magnetic moment	22
2.6	Summary	26
Bibliography		27
3 Optimization of the Rashba coefficient in asymmetric AlSb/InAs/GaSb heterostructures		30
3.1	Introduction	30
3.2	Rashba coefficient as a function of the layer thicknesses	30
3.3	Rashba coefficient for wide wells	33
3.4	Summary	35
Bibliography		36
4 Description of bulk inversion asymmetry in the effective bond or- bital model		37
4.1	Introduction	37
4.2	Review of the EBOM method	38
4.3	Inclusion of bulk inversion asymmetry effects in EBOM	41
4.4	Bulk GaSb	43
4.5	Bulk inversion asymmetry effects in symmetric superlattices	47
4.6	Summary	48
Bibliography		49
5 Bulk inversion asymmetry effects on the bands of zincblende het- erostructures		51
5.1	Introduction	51

5.2	Background	52
5.3	$\mathbf{k} \cdot \mathbf{p}$ method applied to bulk III-Vs	54
5.3.1	Invariant expansion of the Hamiltonian	54
5.3.2	Parameters of the model	57
5.3.3	Analytic expressions of the energy values near the zone center	61
5.3.4	Numerical calculation of the energy bands	68
5.4	Eight-band effective mass theory for superlattices and quantum wells	72
5.4.1	EMA Hamiltonian	73
5.4.2	The finite difference method	74
5.4.3	Interface conditions and hermiticity in the FDM	77
5.5	Bulk inversion asymmetry effects on symmetric quantum wells	79
5.5.1	Symmetry group of the discretized Hamiltonian	79
5.5.2	SQWs without BIA terms	83
5.5.3	SQWs with BIA terms	84
5.6	Bulk inversion asymmetry effects on asymmetric quantum wells	88
5.6.1	AQWs without BIA terms	88
5.6.2	AQWs with BIA terms	90
5.7	Summary	94
	Bibliography	96
6	Spurious numerical solutions in the effective mass approximation	100
6.1	Introduction	100
6.2	Spurious solutions in an InP/In _{0.53} Ga _{0.47} As superlattice	101
6.3	Method for the study of the spurious solutions	105
6.4	Spurious solutions in the $\mathbf{k} \cdot \mathbf{p}$ method	106
6.4.1	The InP/In _{0.53} Ga _{0.47} As SL revisited	111
6.5	Potential for spurious solutions in sets of Luttinger parameters	113
6.6	Summary	115
	Bibliography	117

7	Spin filters based on resonant tunneling	120
7.1	Introduction	120
7.2	Theoretical method	121
7.2.1	The MQTBM	121
7.2.2	Computation of the velocity of the states	126
7.2.3	Preparation of the incoming states	126
7.2.4	Transmission coefficients and transmitted spin for an ensemble of electrons	131
7.3	Resonant tunneling in asymmetric double barriers	134
7.4	Asymmetric resonant tunneling diode (aRTD)	135
7.5	Asymmetric resonant interband tunneling diode (aRITD)	139
7.6	Summary	143
	Bibliography	145
8	Photon generation for a Monte Carlo ray tracing LED simulator	147
8.1	Introduction	147
8.2	The interaction Hamiltonian and Fermi's golden rule	149
8.2.1	The Wigner-Eckart theorem for point groups applied to momentum matrix elements	151
8.2.2	Application to III-V zincblendes	152
8.2.3	Complications following the path of Fermi's golden rule	153
8.3	Polarization of the emitted photon	154
8.4	Application to semiconductor structures	160
8.4.1	Bulk zincblende luminescence	160
8.4.2	Quantum well luminescence	163
8.4.3	Bulk wurtzite luminescence	169
8.5	Monte Carlo photon generation	171
8.5.1	Single event generation scheme	172
8.5.2	Equivalence of the Monte Carlo and the time-dependent perturbation pictures	175

8.6	Application to a bulk zincblende	176
8.7	Summary	179
	Bibliography	180
	A Explicit form of the 8-band $k \cdot p$ Hamiltonian	183
	Bibliography	185
	B Group theory for band structures	186
B.1	Definitions	186
B.2	Degeneracies, splittings and eigenstates	187
B.3	Matrix elements	189
	Bibliography	191
	C Derivation of the formula for the transmission coefficients	192
C.1	Expansion to the Hellmann-Feynman theorem	192
C.2	Transmission coefficient	193
	Bibliography	200
	D Velocity operator in the $k \cdot p$ formalism	201
	Bibliography	204

List of Figures

1.1	Intel's CPUs and Moore's law	3
1.2	Shubnikov-de Haas oscillations for a structure showing spin splitting	9
2.1	Structure under consideration and wavefunction.	16
2.2	Band structure for an AlSb/InAs/GaSb/AlSb quantum well	17
2.3	Spin directions for a 2DEG in an AlSb/InAs/GaSb/AlSb quantum well	18
2.4	Spin splitting for a 10/6/10 AlSb/InAs/GaSb superlattice	19
2.5	Schematic of the origin of the Rashba splitting	21
2.6	Integration region for the 2DEG magnetization	23
2.7	Origin of the electric field-induced magnetization	25
3.1	Rashba coefficient for an AlSb/InAs/GaSb/AlSb QW and fixed InAs thickness	31
3.2	Rashba coefficient for an AlSb/InAs/GaSb/AlSb QW and fixed AlSb thickness	32
3.3	Band structure of a broken gap QW with thick layers	34
4.1	Band structure of GaSb calculated with EBOM	44
4.2	Bands close to the zone center showing the spin splitting	45
4.3	Comparison of EBOM and $\mathbf{k} \cdot \mathbf{p}$ superlattice bands	47
5.1	Effect of BIA on HH and LH bands along [100] near the zone center	63
5.2	Effect of BIA on HH and LH bands along [110] near the zone center	66
5.3	Band structure for GaSb near Γ along [100].	68
5.4	Band structure for GaSb near Γ along [110].	69
5.5	Spin directions for a conduction subband of GaSb.	70
5.6	Polar plot of the spin splitting for the conduction band of GaSb. . .	72

5.7	Mesh used in the solution of the EMA.	75
5.8	Mesh used in the study of interface boundary conditions.	78
5.9	Effect of an extra atomic layer in a non-common atom QW.	80
5.10	Layer arrangement for a no-common-atom quantum well.	82
5.11	Bands for a symmetric quantum well w/o BIA terms.	84
5.12	Bands for a symmetric quantum well with BIA terms.	85
5.13	Linear and angular spin splitting dependence for a SQW.	86
5.14	Spin directions for the lower CB of an AlSb/GaSb/AlSb QW.	87
5.15	Bands for an asymmetric quantum well w/o BIA terms.	89
5.16	Bands for an asymmetric quantum well with BIA terms.	90
5.17	Angular dependence of the spin splitting for an AQW.	91
5.18	Spin splitting <i>vs.</i> k for an AQW.	93
5.19	Spin directions corresponding to the lower CB of an AlSb/InAs/GaSb/AlSb QW.	94
6.1	Bands of an InP/In _{0.53} Ga _{0.47} As SL showing spurious solutions	102
6.2	Comparison of spurious and physical envelope functions	103
6.3	Energy of the spurious states <i>vs.</i> number of mesh points	105
6.4	Energy <i>vs.</i> wavenumber of a hypothetical spurious solution	108
6.5	Predicted and actual spurious solution energy	109
6.6	Bands of an InP/In _{0.53} Ga _{0.47} As SL showing no spurious solutions	112
6.7	Same as Fig. 6.4 but for GaAs and GaSb	115
7.1	Band diagram of an RTD	122
7.2	Bands of a bulk zincblende for finite \mathbf{k}_{\parallel}	130
7.3	aRTD structure	135
7.4	Spin directions for a 2DEG in an AlSb/InAs/GaSb/AlSb quantum well	136
7.5	Resonant spin of an electron incident into an aRTD structure	137
7.6	Transmission coefficient for an aRTD structure	137
7.7	Transmission coefficient for an aRTD structure with BIA inclusion	138

7.8	\mathbf{k}_{\parallel} dependence of the spin of the transmitted states in an aRTD . . .	139
7.9	aRITD structure	140
7.10	Transmission coefficient for an aRITD structure	141
7.11	Bands of the aRITD structure and operation with a lateral electric field	142
7.12	Spin polarization as a function of lateral field for several emitter dopings	143
7.13	Transmission coefficient for an aRITD structure w/BIA effects . . .	144
8.1	Photon emission process in a crystal	149
8.2	Band structure for a zincblende near the zone center	163
8.3	Band structure near the zone center for a QW with D_{2d} symmetry .	165
8.4	Linear and circular polarization for CB-HH1 emission from a D_{2d} QW	167
8.5	Linear and circular polarization for CB-LH1 emission from a D_{2d} QW	168
8.6	Band structure near the zone center for a QW with C_{2v} symmetry .	169
8.7	Band structure near the zone center for GaN	171
8.8	Flowchart for the Monte Carlo photon generation process	173
8.9	Monte Carlo calculation of photon polarization for a zincblende . .	178
C.1	Illustration of the independence of $\int J_z dx dy$ with respect to the plane of integration.	194
C.2	Integration region for J_z	196

List of Tables

4.1	Relationship between the EBOM parameters and the $\mathbf{k} \cdot \mathbf{p}$ parameters	40
5.1	Band gap and γ_c for selected III-Vs	54
5.2	Matrix basis set for the H^{66} block of the Hamiltonian	56
5.3	Irreducible components $\mathcal{K}_m^{\Gamma_l}$ of \mathcal{K}	56
5.4	Material parameters used in the $\mathbf{k} \cdot \mathbf{p}$ model	58
5.5	Parameter values for some materials	60
5.6	Quantization axis for the basis functions of the Hamiltonian	62
5.7	Symmetry requirements on degeneracy and spin splitting for a D_{2d} structure.	81
5.8	Symmetry requirements on degeneracy and spin splitting for a C_{2v} structure.	81
6.1	Band structure parameters for InP and $\text{In}_{0.53}\text{Ga}_{0.47}\text{As}$	101
6.2	Luttinger parameters for $\text{In}_{0.53}\text{Ga}_{0.47}\text{As}$	112
6.3	Check for possibility of spurious solutions in the Luttinger parameters from Lawaetz	113
6.4	Check for possibility of spurious solutions in the Luttinger parameters from Vurgaftman <i>et al.</i>	114
8.1	Equivalence table of the irreducible representations of T_d and $SO(3)$	152
8.2	Character and basis functions table for T_d	161
8.3	Equivalence of basis functions for O and T_d	161
8.4	Clebsch-Gordan coefficients for T_d	162
8.5	Character and basis functions table for D_{2d}	164
8.6	Clebsch-Gordan coefficients for D_{2d}	165
8.7	Character and basis functions table for C_{2v}	169

8.8	Character and basis functions table for C_{6v}	170
8.9	Transition probability from the CB to the VB for a bulk zincblende	177
A.1	Matrix elements of the 8-band $\mathbf{k} \cdot \mathbf{p}$ Hamiltonian	184

Chapter 1 Introduction

1.1 Thesis overview

The bulk of this thesis describes a theoretical study of the spin splitting that takes place in the electronic band structure of semiconductor heterostructures when a source of inversion asymmetry is present due to the breakdown of the conditions for Kramers degeneracy [1]. In particular, this work focuses on the effect in the bands of heterostructures of two different sources of asymmetry; namely, structural inversion asymmetry (SIA) and bulk inversion asymmetry (BIA). In particular, these effects are studied in structures built from materials belonging to the so-called 6.1 Å system: AlSb, GaSb and InAs.

The splitting of the conduction subbands when the sequence of the layers making a heterostructure is not symmetric (SIA) is called the Rashba effect. This is the subject of the first two chapters. The subsequent chapters describe methods developed to include the effect of a different source of asymmetry: bulk inversion asymmetry (BIA), which arises from the different character of cations and anions in the unit cell of zincblende materials [2]. Then, these methods are applied to see how our understanding of the situation when SIA is present is affected by the inclusion of BIA for both bands and tunneling properties of heterostructures.

Finally, the last chapter, while having in common with the rest the study of spin-dependent electronic properties, dwells on how these affect the optical processes in semiconductors, and provides the backbone for Monte Carlo simulations where the effect of the electron spin on light production in band-to-band recombination is fully taken into account.

The major results obtained in this thesis are

- Obtention of the largest reported theoretical value of the Rashba coefficient.

- Development of efficient methods for the computation of spin-resolved band structures and transmission coefficients in heterostructures. BIA effects need to be included in a complete description of the behavior of the spins.
- Characterization of a new class of spurious solutions for the finite difference method in the context of the effective mass approximation and obtention of a test to predict their presence.
- Development of a Monte Carlo algorithm to generate photons with polarizations in accordance to quantum mechanical selection rules.

Chronologically, Chapters 2 and 3 were developed first. The analysis of results from spin injection using scanning tunneling microscopy [3] and the interpretation [4] of experiments with spin polarized LEDs led to Chapter 8. The need for the understanding and quantification of BIA effects resulted in Chapter 5. The adaptation of that $\mathbf{k} \cdot \mathbf{p}$ formalism to tunneling processes described in Chapter 7 was then implemented. Efforts to reproduce experimental data obtained at HRL gave birth to Chapter 6. Finally, the extension of code to calculate spin polarization in spin filter devices motivated Chapter 4.

1.2 Motivation

Since the invention of the transistor in December 1947, its uses have grown into a multibillion dollar market. Today's way of life relies heavily on the ability of a few million transistors to process data and a few million more to store it, whether temporarily or permanently. As the capabilities of modern computers grow larger, so do the demands they must satisfy. Applications such as weather forecasting, drug design, crash simulations, gene sequencing, nuclear test simulations...are sure to exhaust all the computing power available in today's and a near future's machines.

The increase in performance of computers depends critically on the ability to reduce the feature size of transistors. So far, scientists and engineers have managed to make Moore's "law" good. This "law," enunciated in 1965 [5], originally stated

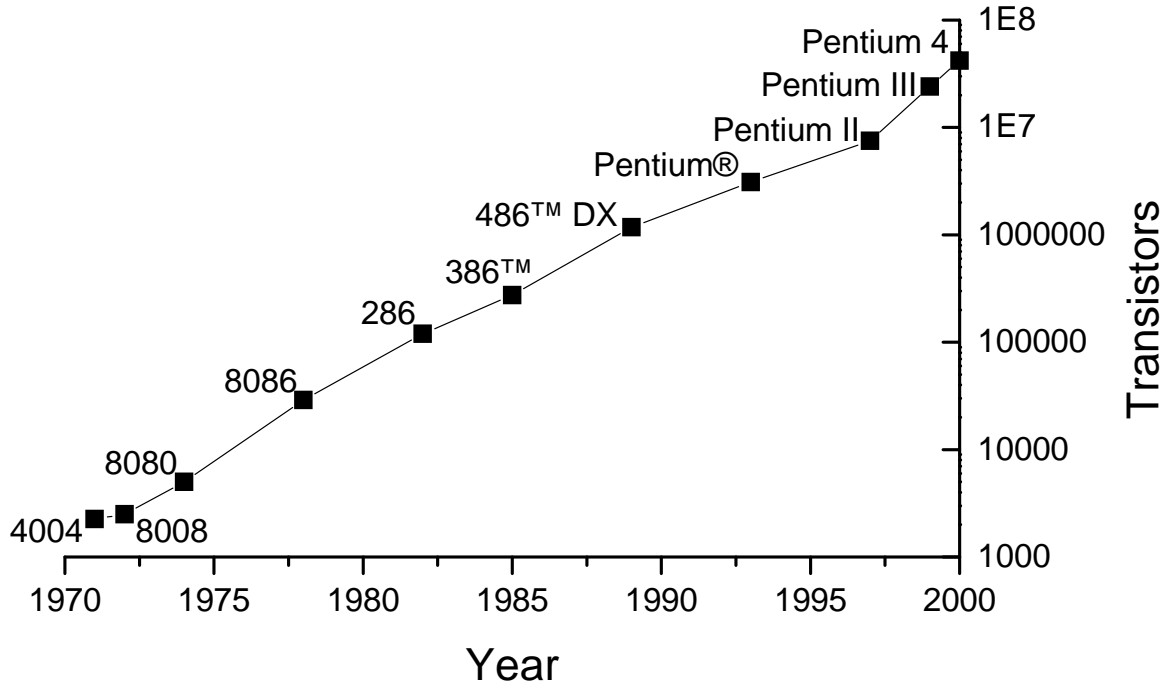


Figure 1.1: Intel's CPUs and Moore's law. Data taken from Intel's web site.

that the number of components in an integrated circuit would double every year, and in its present form that time constant is usually quoted as 18 months although, at least for Intel's CPUs, the number of transistors in a CPU doubles roughly every two years (see Fig. 1.1).

Eventually, sizes will be reached where quantum effects will affect the normal operation of the transistors. For example, tunneling leakage current in metal/oxide/semiconductor (MOS) structures was believed in 2001 [6] to limit the gate oxide thickness to 12 \AA^1 . A new approach to keep up with this continuing miniaturization is to come up with devices based precisely on the quantum properties of the electron. The resonant tunneling diode (RTD) [7] and the single electron transistor (SET) [8] are good examples of these devices.

¹This is a typical figure, which is really application dependent and is given by how much power density one can afford to consume.

1.2.1 Theoretical methods

Another quantum property of the electron that only recently has received attention for its potential for information storage and processing is its spin. The starting point for the field of SPIN elecTRONIC (spintronic) devices was the discovery of giant magnetoresistance (GMR) in 1988 by Baibich *et al.* [9]. So far, the only commercially available spintronic devices—the GMR read heads present in hard drives—or in the development phase—magnetic RAMs (MRAMs)—are based on the behavior of spin in metals. Nevertheless, the marriage of spin and semiconductors is a hot research topic. In 1990 Datta and Das [10] proposed a spin transistor where a gate voltage controlled the amount of precession of a collection of spins while traveling in a semiconductor between two ferromagnetic contacts, thus modulating the resistance seen by the electrons in transit. Typical precession frequencies of spins in semiconductor structures are of the order of a few THz. The prospect of logic at such frequencies has caused great interest among the funding agencies.

For applications such as Datta and Das’ spin transistor or even quantum computation with spins in semiconductors to become a reality, a hurdle that must be overcome is the achievement of reliable injection of spins into semiconductors. The control over the direction of the spins forced into a material is what is understood as spin injection. Once a nonequilibrium spin population has been established by means of spin injection, it is necessary that the time it takes for it to come back to equilibrium is long enough so that useful manipulations can be made.

On one hand, the proper description of transport, time evolution and interface phenomena of spin ensembles will require having at disposal electron band structures where all spin effects are included; in much the same way as thorough knowledge of the “regular” band structure is required to fully understand electronic devices. On the other hand, semiconductor heterostructures have been extensively used to create new classes of materials with engineered electronic properties, and they show promise to serve the same purpose for the spin properties. The methods developed in Chapters 4 and 5 provide an efficient and easy to implement way to obtain spin

resolved band structures in heterostructures. In particular, the extension of the effective bond orbital model (EBOM) method in Chapter 4 allows for the inclusion of BIA effects in existing code with negligible extra computational cost. Since EBOM is a full zone method, results from EBOM calculations will be valid further away from the zone center than $\mathbf{k} \cdot \mathbf{p}$ results. However, the EBOM method does poorly when strain and magnetic field effects need to be accounted for. These two external fields are straightforwardly included into the $\mathbf{k} \cdot \mathbf{p}$ formalism. This is the driving force behind Chapter 5, where an 8-band effective mass approximation (EMA) code that reproduces the zincblende T_d symmetry is implemented.

1.2.2 Spin injectors/filters

The Rashba effect is the building block on which several proposed spintronic devices are built. When referring to the spin splitting of the conduction band (CB) levels of a two-dimensional electron gas (2DEG) in an asymmetric potential, it constitutes the basis for Datta and Das' spin transistor [10]. Clearly, a greater value of the splitting, given by a larger value of the Rashba coefficient, would increase the frequency at which these spins are switched. A large Rashba coefficient will also improve the performance of the asymmetric resonant tunneling diode (aRTD) spin filter proposed by Voskoboynikov *et al.* [11] in 2000. In that device, electrons transmitted through an asymmetric double barrier heterostructure emerge with their spin aligned with the spin of the quasi-bound state through which they have tunneled. Note that spin filtering would be achieved without the presence of any external magnetic field or any ferromagnetic material.

Clearly, a method for experimental determination of the Rashba coefficient in heterostructures and theoretical understanding of its origin are required for the achievement of a spintronic device based on the Rashba effect. Since the Rashba effect is closely related to structural asymmetry, the 6.1 Å materials system, with its variety of band alignments, will be a candidate for the construction of structures with large Rashba splitting. This motivates the studies in Chapters 2 and 3.

Ting *et al.* [12] have proposed a modification of the aRTD idea that would have a higher performance as a spin filter by letting the electrons tunnel through the strongly spin split valence band states of an AlSb/InAs/GaSb/AlSb well region. Their original calculation of the current polarization did not include the effects of bulk inversion asymmetry. The formalism and structures studied in Chapter 7 address how the tunneling properties of an asymmetric barrier change when BIA is accounted for.

1.2.3 Detection of spin injection

Once a structure is chosen as a candidate for spin injection, the question of the measurement of the spin polarization of the injected electron population must be faced. For this, there are mainly two kinds of measurements: electrical and optical. In the electrical measurements, one looks for small changes in the voltage drop when a current is forced through a semiconductor between two aligned or antialigned ferromagnets. However, these kind of measurements are not free from controversy as the presence of ferromagnets is thought to produce spurious voltages due to local Hall effect.

The optical measurement method is preferred because of its direct relationship to the electron spin density. It basically consists in the analysis of the polarization of light coming from radiative recombination between an electron and a hole. The polarization of an emitted photon will be correlated with the spin of the electron that originated it, and this relationship is well understood. However, the polarization of photons emitted from a device will be affected by refractive effects at boundaries and interfaces, and these effects have not received sufficient attention. Monte Carlo ray tracing techniques are ideal for that purpose because they can easily be adapted to different characters of the emitting medium—bulk with varying crystal structure, quantum well, quantum dot—or a variation in the geometrical shape of the extracting medium. They might find an application too in the study of the optical transmission by polarized light of information stored in spins. These techniques will require a method of generating single photons in agreement with the quantum mechanical

selection rules. This and the understanding of the light emission process for arbitrary situations led to the study in Chapter 8.

1.3 Summary of results

1.3.1 Theoretical methods

The methods developed in this thesis can be divided into four parts:

1. An extension to the EBOM method capable of accounting for bulk inversion asymmetry (BIA) effects in zincblendes has been derived and implemented. This extension correctly reproduces the space group symmetry of the zincblende structure. By construction, it accurately describes the band structure near the zone center, including the spin splitting in the conduction band of bulk zincblendes. Calculations for superlattices using this new method agree with $\mathbf{k} \cdot \mathbf{p}$ results.
2. Starting with a bulk $\mathbf{k} \cdot \mathbf{p}$ Hamiltonian having the right T_d symmetry for zincblendes, an 8-band effective mass approximation (EMA) code has been implemented for [001] heterostructures. Contrary to most of the existing EMA implementations, the one presented here correctly describes the microscopic symmetry of most superlattices, making it an appropriate tool for phenomena such as the optical anisotropy [13], and the mixing of heavy hole and light hole states at the top of the valence band [14], whose existence is a consequence of the reduced symmetry due to the BIA.

Also, a source of spurious solutions for the finite difference method has been characterized. The application to the $\mathbf{k} \cdot \mathbf{p}$ method allows the derivation of a condition that the Luttinger parameters must meet for the spurious solutions not to appear.

3. A previous implementation of the multiband quantum transmitting boundary method (MQTBM) in the $\mathbf{k} \cdot \mathbf{p}$ framework [15] for the determination of tunneling

transmission coefficients has been cast in a form consistent with the finite difference method, eliminating some small spurious contributions. An algorithm for generating an incoming state with a predetermined spin has also been created.

4. A Monte Carlo algorithm for single polarized-photon generation in radiative recombination processes has been developed. This algorithm makes extensive use of the host crystal symmetry properties to reduce to a minimum the number of external inputs needed to determine the photon polarization. It allows the determination of the Stokes parameters for light emitted in arbitrary directions by a given electron spin population.

1.3.2 Applications

The 6.1 Å material system comprised of AlSb, GaSb and InAs is shown to offer great promise for spintronic devices based on the Rashba effect. The Rashba coefficient for AlSb/InAs/GaSb/AlSb 2DEGs is calculated theoretically to be able to achieve values of the order of 50×10^{-10} eV·cm. This is the highest value reported in the literature. The dependence of the Rashba coefficient on the thicknesses of the different layers is studied, finding that the structures with InAs thickness between 5 and 15 monolayers (MLs) and GaSb thickness of 8 or more MLs present optimal values of the Rashba coefficient. It is also observed that the presence of anticrossing between the conduction band of InAs and the valence band of GaSb in the 2DEG reduces the value of the coefficient substantially. The application of an in-plane bias in the 2DEG is shown to produce an amount of spin polarized current and some magnetization accompanying it. The degree of polarization of the current is of the order of 5×10^{-5} for typical values of the in-plane bias. Therefore, much larger Rashba coefficients would be needed to use this configuration as a source of spin polarized current.

The presence of spin splitting even in structurally symmetric quantum wells (QWs) is investigated. A 2-band Hamiltonian analogous to the Rashba Hamiltonian, but describing the splitting for these symmetric QWs due to the BIA and its interaction with the Rashba splitting is proposed, and its validity tested with numerical 8-band calcu-

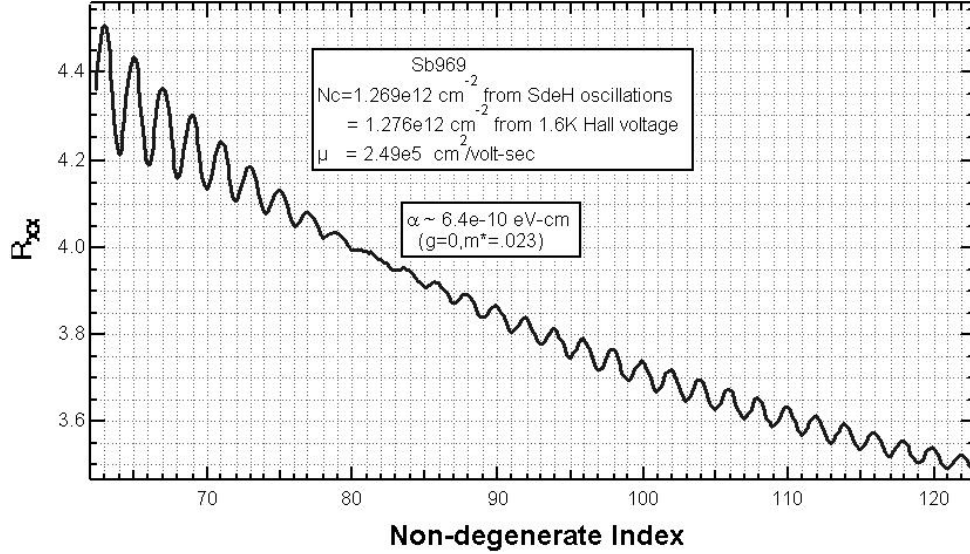


Figure 1.2: Shubnikov-de Haas oscillations for a (InAs/AlSb SL)/InAs/(InAs/AlSb SL) structure showing spin splitting. Data taken by Andy Hunter *et al.* [16]

lations. BIA effects are shown to be of the same order of magnitude as Rashba effects for the conduction band of the studied 6.1 Å heterostructures, hence its inclusion is necessary in the description of the bands in QWs.

Experiments support the theoretical predictions made in this thesis regarding the magnitudes of the Rashba coefficients. Figure 1.2 shows a node in Shubnikov-de Haas oscillations of a quantum Hall measurement, taken by Andy Hunter *et al.* [16] at HRL Laboratories. The node and the change of phase of the oscillations are signatures of the presence of the Rashba effect. The measured value ($6.4 \times 10^{-10} \text{ eV} \cdot \text{cm}$) and a calculation using the methods described in Chapter 5 ($7.6 \times 10^{-10} \text{ eV} \cdot \text{cm}$) show reasonable agreement.

The implementation of the MQTBM is used to study the spin-dependent tunneling properties of an asymmetric interband resonant tunneling diode (aRITD). It is shown that the predicted [12] spin filtering properties of the aRITD should not be largely affected when BIA is included into the calculation.

1.3.3 Collaborative work

Unless noted otherwise, all the material presented in this thesis is the work of the author. On the other hand, I must acknowledge David Ting for putting to my disposal his EBOM code, used to do the calculations in Chapters 2 and 3 and modified to obtain the numerical results in Chapter 4. Also, the code used to generate Fig. 8.9 was written by Steve Ichiriu.

1.4 Chapter overview

Chapter 2 presents the use of a previously established method for the calculation of band structures [the effective bond orbital model (EBOM) method] to calculate the magnitude of the Rashba effect in AlSb/InAs/GaSb/AlSb quantum wells. Then, the consequences of the Rashba splitting on the magnetization and spin polarization current of a two-dimensional electron gas (2DEG) are explored. Chapter 3 presents the search for a structure that will yield an optimized Rashba effect. Chapter 4 presents an extension to the EBOM method that reproduces the reduction in the symmetry due to the bulk inversion asymmetry (BIA) present in zincblendes, and describes the spin splitting resulting from that. In Chapter 5, the description of BIA in the $\mathbf{k} \cdot \mathbf{p}$ framework is discussed, and results for band structure calculations in symmetric and asymmetric quantum wells, with and without BIA effects are presented; and the role of BIA is delineated. Chapter 6 describes a new class of spurious solutions that can appear when using the finite difference method to solve the Envelope Function Approximation (EFA) equations and how to make sure they don't show up. Chapter 7 calculates the spin-dependent transmission coefficients in AlSb/InAs/GaSb/AlSb aR-ITDs with and without the BIA contribution and discusses the influence of BIA in existing current polarization calculations. Finally, Chapter 8 presents an algorithm for Monte Carlo single polarized-photon generation from electron-hole radiative recombination.

Bibliography

- [1] J. J. Sakurai, *Modern Quantum Mechanics*, 1st ed. (Addison-Wesley, Redwood City, CA, USA, 1985).
- [2] G. Dresselhaus, *Phys. Rev.* **100**, 580 (1955).
- [3] C. J. Hill, Ph.D. thesis, California Institute of Technology, Pasadena, Ca, 2001.
- [4] S. R. Ichiriu, X. Cartoixà, and T. C. McGill, , in preparation.
- [5] G. E. Moore, *Electronics* **38**, (1965).
- [6] D. Frank, R. Dennard, E. Nowak, P. Solomon, Y. Taur, and H. Wong, *Proc. IEEE* **89**, 259 (2001).
- [7] L. Esaki and R. Tsu, *IBM J. Res. Develop.* **14**, 61 (1970).
- [8] K. K. Likharev, *Proc. IEEE* **87**, 606 (1999).
- [9] M. N. Baibich, J. M. Broto, A. Fert, F. N. Vandau, F. Petroff, P. Eitenne, G. Creuzet, A. Friederich, and J. Chazelas, *Phys. Rev. Lett.* **61**, 2472 (1988).
- [10] S. Datta and B. Das, *Appl. Phys. Lett.* **56**, 665 (1990).
- [11] A. Voskoboynikov, S. S. Lin, C. P. Lee, and O. Tretyak, *J. Appl. Phys.* **87**, 387 (2000).
- [12] D. Z.-Y. Ting, X. Cartoixà, D. H. Chow, J. S. Moon, D. L. Smith, T. C. McGill, and J. N. Schulman, *IEEE Trans. Magn.* (2002), to be published.
- [13] O. Krebs and P. Voisin, *Phys. Rev. Lett.* **77**, 1829 (1996).
- [14] E. L. Ivchenko, A. Y. Kaminski, and U. Rossler, *Phys. Rev. B* **54**, 5852 (1996).
- [15] Y. X. Liu, D. Z.-Y. Ting, and T. C. McGill, *Phys. Rev. B* **54**, 5675 (1996).

- [16] A. Hunter, P. Deelman, D. Chow, L. Warren, J. N. Schulman, J. Zinck, and S. Skeith, , unpublished.

Chapter 2 Spin splittings in asymmetric AlSb/InAs/GaSb heterostructures and electric field induced magnetization

2.1 Introduction

In recent years, interest in developing spin-sensitive devices (spintronics) [1–4] has fueled renewed investigations into spin phenomena in semiconductors. The aim is to control not only the spatial degrees of freedom of the electron, but also the spin degree of freedom. Useful spintronic devices can be devised if such control is achieved. A number of such devices have already been proposed [5–8], and the search for phenomena which can lead to spin based devices is widespread [9–11]. Studies of asymmetric quantum wells have been carried out both theoretically and experimentally in other material systems [12–15]. One of the systems showing promise is the nearly lattice matched system comprised of InAs, GaSb and AlSb [16, 17].

In particular, one of the phenomena that might be of importance in the InAs/GaSb/AlSb heterojunction system is the Rashba effect [12]. The precise contributions to the magnitude of the effect are a subject of some recent studies [18, 19]. Previously, a number of studies have examined InAs quantum wells confined by InGaAs layers [20–23] or $\text{Al}_x\text{Ga}_{1-x}\text{As}/\text{GaAs}$ heterostructures [24, 25]. In this study, the focus is on the effects of the InAs/GaSb unique band offsets.

In Sec. 2.2 of this chapter, the results of a study of the band structure for an AlSb/InAs/GaSb/AlSb asymmetric well using the effective bond orbital model are presented. These results can also be described in terms of a Bychkov-Rashba Hamiltonian [12]. In Sec. 2.3 the dependence of the spin splitting on the electron momentum for the conduction band for several structures is shown and the orientation of the

electron spins is described. In Sec. 2.4 an intuitive picture of the physics behind the Rashba effect is presented. In Sec. 2.5, a derivation of an expression for the surface magnetization and the degree of spin polarization of the current when the nonmagnetic two-dimensional electron gas (2DEG) is under an in-plane electric field is shown.

2.2 Theoretical methods

Spin splitting can result from the lifting of Kramers degeneracy through the removal of inversion symmetry. Mechanisms for inversion symmetry removal include

- I. The specific spatial arrangement of the composing layers with their interfaces. [18]
- II. Bulk inversion symmetry as in the zincblende structure. [19]
- III. Asymmetry created by external fields and dopant-induced band bending. [18]

In this chapter, the primary interest is in examining effects in the band structure induced by an asymmetric spatial arrangement of the heterostructure. Hence, a band structure calculation technique was selected that allows treatment of layer arrangement contributions with the highest accuracy. Bulk inversion asymmetry (BIA) contributions are considered in Chapter 5.

The calculations shown are based on the EBOM method developed by Y.-C. Chang [26, 27]. It consists of a tight-binding [28] model taking bond orbitals [29] in an fcc lattice as a basis set, expanding the resulting matrix elements to second order in k and identifying the EBOM parameters with the $\mathbf{k} \cdot \mathbf{p}$ [30, 31] parameters. It accurately describes the lowest conduction band and the heavy hole, light hole and splitoff bands near the zone center, making it appropriate for the calculation of the band structure of the 2DEG, taking into account the strong coupling between the InAs conduction band and the GaSb valence band states due to the broken gap band alignment, as illustrated in Fig. 2.1.

The calculations are performed on [001] structures using superlattice boundary conditions, and it is found that the superlattice cells are effectively decoupled when the AlSb thickness is 8 monolayers (ML) or more, with a monolayer having a thickness of 3.048 Å.

The EBOM method accounts for the very different nature of the various interfaces, although it cannot describe properly the lack of inversion symmetry inherent intrinsic to the zincblende structure. An extension to the method to deal with BIA effects is presented in Chapter 4. In the bulk single crystal, that lack of inversion symmetry leads to the k^3 splitting [32]. This effect could lead to some corrections. In Chapter 5 they are found to be on the order of a 20% at most. There has been some work on BIA effects beginning with the work of Lommer *et al.* [33] and Cardona *et al.* [34]. A discussion of the relative tradeoff is included in the papers by Silva *et al.* [18, 19]. Space charge and gate generated electric fields are not included in the calculation either. These fields do make some contribution to the Rashba splitting [see Eq. (2.1)] [18, 35], and they are determined by the details of the doping and applied bias.

2.3 Results

2.3.1 Band structure and spatial part of the wavefunction

The structure under consideration and a typical result for the probability distribution of the electron wavefunction are illustrated in Fig. 2.1. The values of the band gaps and lattice constants are taken to be the widely accepted values [16, 17] for the plots in Fig. 2.1. The band offsets are taken from the review by Yu *et al.* [36] and reflect the Type II staggered alignment of the bands for the AlSb/InAs interface and the Type II broken gap alignment for the InAs/GaSb interface [37]. This configuration provides a strong asymmetry of the confining potential. As a result, the Rashba constant [see Eq. (2.1)] will have an enhanced value compared to previously studied systems [14, 15, 35].

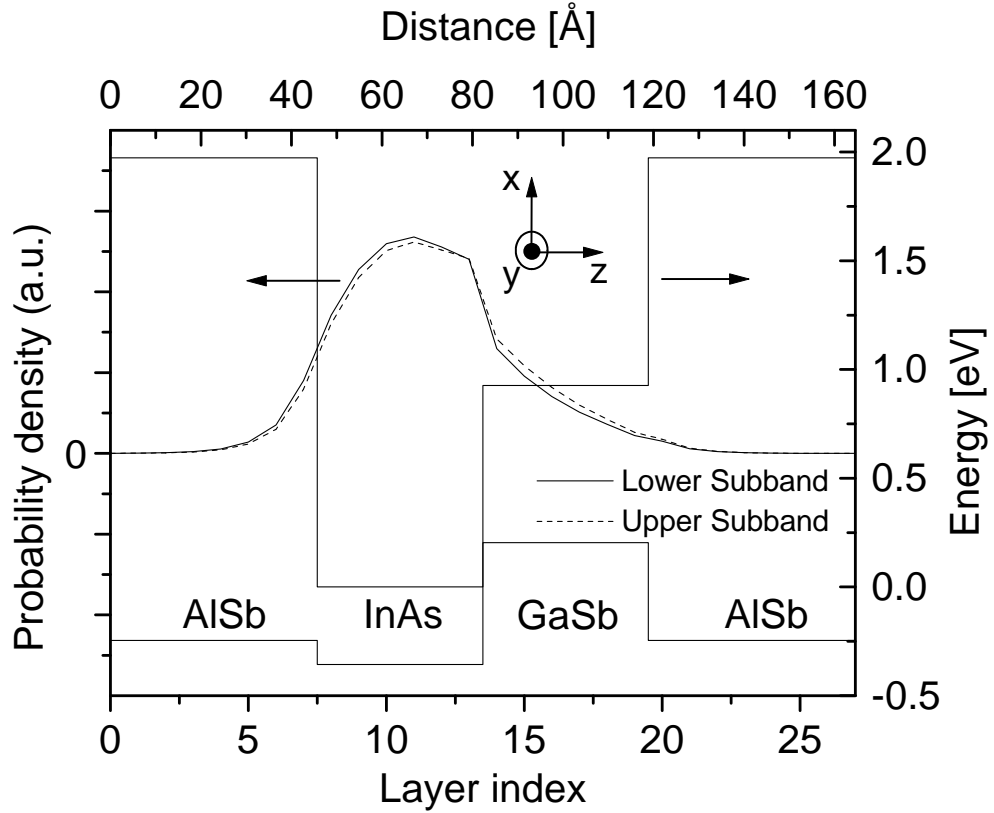


Figure 2.1: Flat band diagram (right scale) of the heterostructure under consideration. The structure consists of a superlattice constructed by repeating 16 layers of AlSb followed by 6 layers of InAs followed by 6 layers of GaSb. The energies reflect the accepted values of the band gaps and band offsets. Further, the calculated probability density (left scale) for conduction band states in the well for $\mathbf{k} = (0.02, 0, 0) 2\pi/a$, where a is the unit cell size. The solid line shows the lower energy spin split state. The dashed line shows the higher energy spin split state. The axes show the choice of coordinates.

Figure 2.2 shows the band structure near the Γ point for a superlattice composed of 16 layers of AlSb, 6 layers of InAs and 6 layers of GaSb. The bands become spin split due to the lack of inversion symmetry in the growth direction. Note that the energy minimum of the lower conduction subband is no longer at the point $k = 0$. Control calculations with symmetrical AlSb/InAs/AlSb and GaSb/InAs/GaSb structures and these showed no splitting.

The probability density of the spin split states is shown in Fig. 2.1. We see that the electron is mainly localized in the InAs layer, but it displays significant leakage into the AlSb and GaSb layers. Careful examination of this figure shows that the state

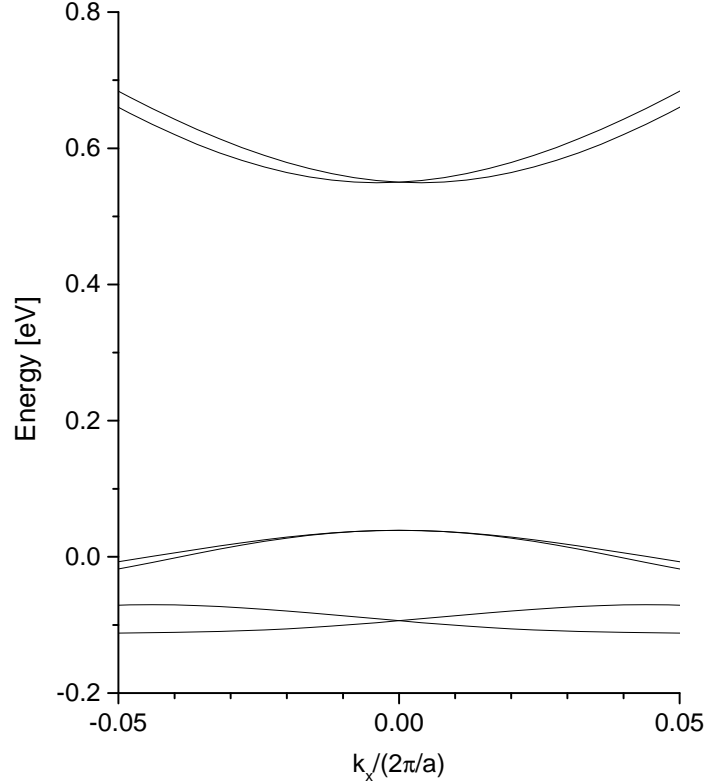


Figure 2.2: The calculated band structure of an 16ML (monolayers) AlSb/6ML InAs/6ML GaSb superlattice near the Γ point for light holes, heavy holes and conduction electrons. Note the splitting in the states of the 2DEG, corresponding to the conduction band.

corresponding to the lower (upper) energy band is displaced towards the AlSb/InAs (InAs/GaSb) interface. This point is further discussed in Sec. 2.3.4.

2.3.2 Spin part of the wavefunction

One of the most important features of the results is the spin character of the eigenstates. The result is shown in Fig. 2.3. The spin expectation value for the different states always lies on a circle in the $k_x - k_y$ plane. The $x - y$ plane is the quantum well plane (see Fig. 2.1). It is seen that for the lower (upper) conduction subband the spins point tangentially to the circle in a counterclockwise (clockwise) fashion. The z component of the expectation value of the spin is found to be zero within numerical

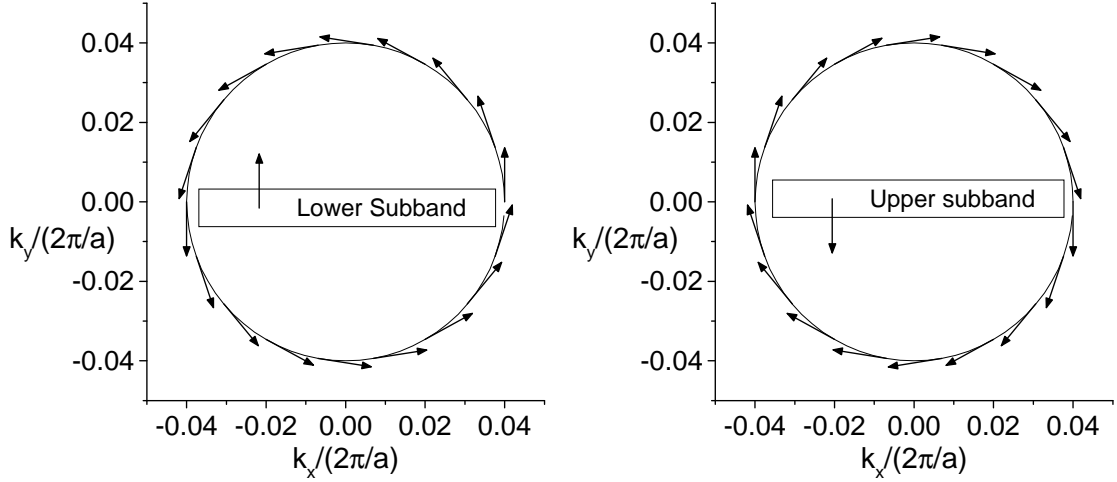


Figure 2.3: Calculated expectation value of the spin for states of a 2DEG lying on circles of constant k for the two conduction spin split subbands.

fluctuations. This is indeed the behavior predicted by the Rashba Hamiltonian [12]

$$H_{SO} = \alpha_R (\boldsymbol{\sigma} \times \mathbf{k}) \cdot \boldsymbol{\nu} \quad (2.1)$$

and found analytically by Schäpers *et al.* [35]. α_R is the Rashba constant (dependent on the details of the heterostructure), $\boldsymbol{\sigma}$ are the Pauli spin matrices, \mathbf{k} is the crystal momentum of the electron in the 2DEG and $\boldsymbol{\nu}$ is a unit vector parallel to the growth direction. The specific handedness of the rotation of each subband depends on the details of the well, and it would have been reversed had the order of the InAs and GaSb layers been reversed.

Note that, although there is spin splitting without the presence of an external magnetic field or magnetic constituents, Kramers time reversal degeneracy is preserved, for

$$\mathcal{E}(\mathbf{k}, |\uparrow\rangle_{\hat{n}}) = \mathcal{E}(-\mathbf{k}, |\downarrow\rangle_{\hat{n}}), \quad (2.2)$$

where the left- (right-) hand side term is the energy of a state with wavevector \mathbf{k} ($-\mathbf{k}$) and spin up (down) in the direction of a unit vector \hat{n} .

Another important consequence of this unique spin configuration is that, though there is a preferred spin direction for a single \mathbf{k} state, when averaging over the whole

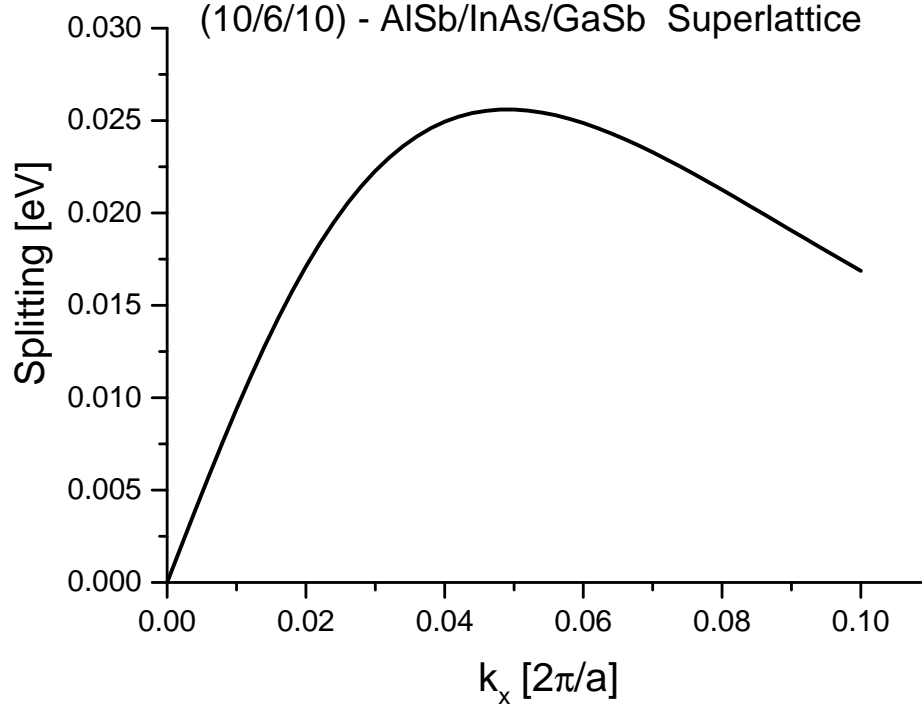


Figure 2.4: Spin splitting for a 10/6/10 AlSb/InAs/GaSb superlattice in the conduction band.

subband the net spin vanishes, so there is no electronic magnetism for this system in equilibrium.

2.3.3 Rashba coefficient for an asymmetric heterostructure made of AlSb/InAs/GaSb/AlSb

From Eq. (2.1) it can be seen that, close to the zone center, the splitting Δ_R due to the Rashba Hamiltonian is linear with the electron wavevector k , and is given by

$$\Delta_R = 2\alpha_R k. \quad (2.3)$$

Figure 2.4 shows the spin splitting for a 10/6/10 AlSb/InAs/GaSb superlattice in the conduction band along the [100] direction. As indicated by Eq. (2.3), the calculated splitting is linear close to Γ . Further away from the zone center, the terms of higher order in k coming from the numerical diagonalization of the 8×8 EBOM Hamiltonian start taking over.

A coefficient $\alpha_R = 38 \times 10^{-10}$ eV·cm is found for the (AlSb=16 ML, InAs=6 ML, GaSb=6 ML) heterostructure. In Chapter 3 optimization procedures are carried out and coefficients as large as 50×10^{-10} eV·cm have been found. This is one of the largest reported values for the Rashba coefficient.

As a validation of the method of calculation, the Rashba coefficient for an $\text{In}_{0.53}\text{Ga}_{0.47}\text{As}/\text{In}_{0.77}\text{Ga}_{0.23}\text{As}/\text{InP}$ heterostructure studied by Schäpers *et al.* [35] was calculated. They reported an experimental value $\alpha_R = (5.0 \pm 0.1) \times 10^{-10}$ eV·cm for that structure. They also compute a Type I interface contribution to α_R of 6.7×10^{-10} eV·cm. Making the calculation with the EBOM method one finds an interface contribution of 7.8×10^{-10} eV·cm. The reasonable agreement in the computed values for the interface contribution to the Rashba coefficient validates the procedure followed here and lends support to the claim for a large interface contribution to α_{BR} in the AlSb/InAs/GaSb/AlSb heterojunction studied here.

2.3.4 Spatial variation of the wavefunction

Figure 2.1 shows that the two eigenstates of the conduction subband have slightly different spatial behavior. This coupling of the spatial part with the spin part of the wavefunction is not modeled by the Bychkov-Rashba Hamiltonian in Eq. (2.1). The attraction towards one or the other interface comes from the preference of the electron to be located in regions with lower potential energy. The interface electric fields transform in the rest frame of the electron into magnetic fields to which the electron spin couples. Since the two interfaces have electric fields with opposite signs, hence, magnetic fields with opposite signs, the sign of the spin will dictate the preference for one of the interfaces. The lowest subband state tends towards the interface with larger band offsets, where the electric fields are larger.

2.4 Physical explanation for the results

The unusual configuration of the spins in the conduction band shown in Fig. 2.3 can be intuitively understood using the following argument. Classically, if the electrons in

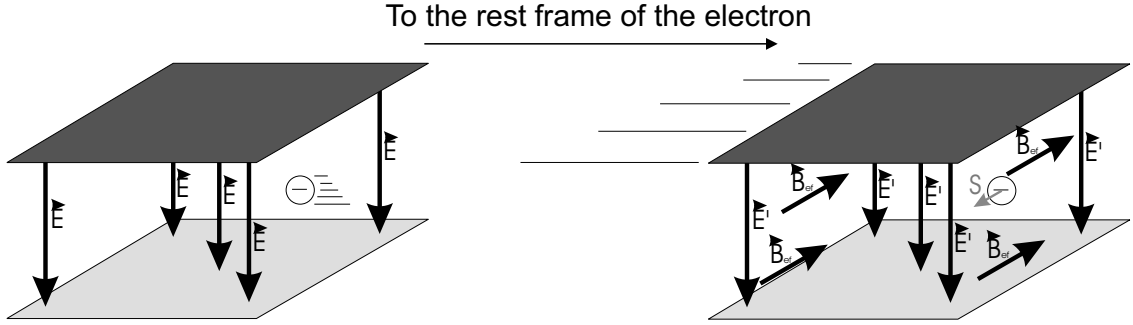


Figure 2.5: Schematic of the process by which the Rashba spin splitting arises. A moving electron in an electric field sees a magnetic field in its rest frame and its spin couples to it in a Zeeman-like manner.

the 2DEG are moving with a velocity \mathbf{v} under the presence of an electric field \mathbf{E} , this transforms relativistically in the rest frame of the electron into an effective magnetic field \mathbf{B}_{eff} given (in SI units) by (see, for example, Ref. [38])

$$\mathbf{B}_{eff} = -\frac{1}{c^2} \mathbf{v} \times \mathbf{E}, \quad (2.4)$$

where c is the speed of light.

The magnetic moment of the electron will then couple to \mathbf{B}_{eff} producing the splitting. The quantum version of this reasoning is nothing but the spin-orbit interaction, which includes a factor of $1/2$ to account for Thomas precession. Since $\mathbf{v} \propto \mathbf{k}$ and the only electric field that is not averaged to zero by the spatial extent of the wavefunction is $\mathbf{E} = E\boldsymbol{\nu}$ where $\boldsymbol{\nu}$ is a unit vector in the direction of the growth, one has for the spin-orbit Hamiltonian

$$H = -\boldsymbol{\mu} \cdot \mathbf{B}_{eff} \propto -\boldsymbol{\sigma} \cdot (\mathbf{k} \times \mathbf{E}), \quad (2.5)$$

where $\boldsymbol{\mu} \propto -\boldsymbol{\sigma}$ is the magnetic moment of the electron.

As shown in Fig. 2.5, this readily explains why the spins are pointing in-plane and perpendicular to the direction of propagation of the electron. Finally, if one makes the substitution $\mathbf{E} = \langle E \rangle \boldsymbol{\nu}$ into Eq. (2.5) with $\langle E \rangle$ being the expectation value of the electrical field for the conduction band states, the Hamiltonian (2.1) is recovered with

α_R just being the proportionality constant. In this description, the Bychkov-Rashba constant is proportional to the expectation value of the electrical field, agreeing with published experimental results [35, 39]. More sophisticated calculations [35] also find interface contributions.

It can be argued [40] that the expectation value of the electric field should vanish because the expectation value of the force that the electrons are subject to must definitely vanish. Hence, it would seem that the value of the Rashba coefficient must not depend on the expectation value of the electric field, in contradiction to the argument shown in this section. However, Malcher *et al.* [14] show that one can have a nonzero expectation value of the electrical field perpendicular to the plane of the quantum well and still have a vanishing expectation value for the force.

2.5 Electric field induced magnetic moment

A novel observation is that the presence of a DC electric field parallel to the plane of the 2DEG \mathbf{E}_{\parallel} can produce a net magnetic moment. Consider the application of an in-plane bias. It is a well-known result that, in the linear approximation and in the diffusive limit where the electrons are thermalized before reaching the collector, the equilibrium distribution function is displaced by a constant amount $\Delta\mathbf{k} = e\tau\mathbf{E}_{\parallel}/\hbar$, [41] where e is the electron charge, τ is the relaxation time and \mathbf{E}_{\parallel} is the electric field applied in-plane. Consider, for example, the displacement of the distribution function for the electrons in the lower conduction subband of Fig. 2.3. Figure 2.7 (a) shows a schematic of the effect of the applied electric field on a 2DEG at zero temperature. The gray region corresponds to states \mathbf{k} whose spins are compensated by opposite spins at $-\mathbf{k}$, thus making a zero contribution to any magnetization or spin polarization of the current. The white regions correspond to states that contribute to the total spin. This can be accomplished by states newly occupied (unoccupied), represented by the black (light gray) arrows. In the figure the displacement has been

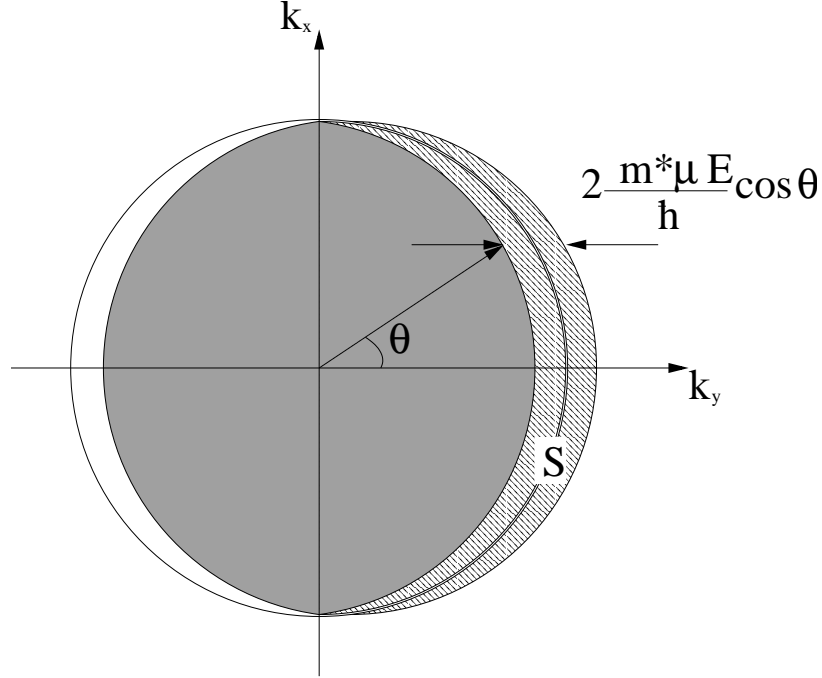


Figure 2.6: The hatched portion of \mathbf{k} space S denotes the integration region of uncompensated states where the magnetic moment of each electron will be added.

magnified for clarity and, using the relationship $e\tau = \mu m^*$, it is found to be

$$\frac{\Delta k}{k_F} = \frac{m^* \mu E_{\parallel}}{\hbar \sqrt{2\pi n}} \sim 10^{-4}, \quad (2.6)$$

where μ is the mobility of the electrons in the 2DEG and n is the surface density of electrons. The numerical estimate has been obtained using typical values for a 2DEG; $m^* \sim 0.02m_e$, $\mu \sim 80000 \text{ cm}^2/\text{V}\cdot\text{s}$, $E_{\parallel} \sim 1 \text{ V/cm}$ and $n \sim 10^{12} \text{ cm}^{-2}$. The sum of the spins coming from the white regions will have a non zero component perpendicular to the applied electric field. This yields a net magnetic moment and spin polarization of the current due to electrons in that subband.

The net magnetic moment \mathbf{M} coming from one subband can be obtained by integrating the spins over the uncompensated states in the spherical band approximation (see Fig. 2.6 for a schematic of the integration region):

$$\mathbf{M} = \int_S \lambda(\mathbf{k}) \frac{g}{2} \mu_B \langle \boldsymbol{\sigma} \rangle dS_k, \quad (2.7)$$

where $\lambda(\mathbf{k}) = \left(\frac{A}{2\pi}\right)^2$ is the surface density of states in \mathbf{k} space for a single subband; *i.e.*, no spin degeneracy factor of 2, A is the area of the sample, g is the free electron g -factor, μ_B is the Bohr magneton and $\langle\sigma\rangle$ is the unitless spin expectation value. For small displacements of the Fermi sphere, as it is the case here, the differential of surface in \mathbf{k} space dS_k can be written as

$$dS_k = 2\frac{m^*\mu}{\hbar}E_{\parallel}\cos\theta k_F d\theta, \quad (2.8)$$

where k_F is the Fermi wavevector for the subband under consideration.

Then, performing the integral for θ between $-\pi/2$ and $\pi/2$, one gets

$$M_{\uparrow} = -A\frac{g\mu m^*E_{\parallel}}{8\pi\hbar}\mu_B k_{F\uparrow}, \quad (2.9)$$

where M_{\uparrow} is the resulting net magnetic moment coming from that subband and $k_{F\uparrow}$ is the Fermi radius for the subband with spins pointing counterclockwise. Figure 2.7 (a) shows that the magnetization will be perpendicular to the direction of the electric field.

The combined effect of the two conduction subbands is shown in Fig. 2.7 (b). Each subband contributes with a surface magnetization pointing in a direction opposite to the other subband, but they do not cancel out due to the different size of the circles. Adding the contribution from both subbands, using

$$(k_{F\uparrow} - k_{F\downarrow}) = \frac{2m^*}{\hbar^2}\alpha_R \quad (2.10)$$

and assuming \mathbf{E}_{\parallel} pointing in a general direction in the plane, the resulting magnetic moment per unit area will be

$$\frac{\mathbf{M}}{A} = \frac{g\mu m^{*2}}{4\pi\hbar^3}\mu_B\alpha_R (\mathbf{E}_{\parallel} \times \boldsymbol{\nu}), \quad (2.11)$$

where $\boldsymbol{\nu}$ is a unit vector pointing perpendicular to the 2DEG plane.

If one substitutes into this expression the values representative of the structure

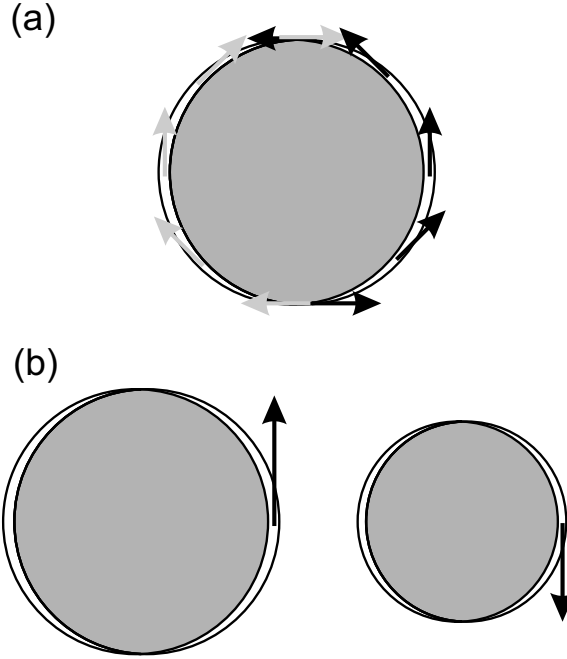


Figure 2.7: Illustration of the influence of a DC electric field on Fermi surfaces in k-space. Part (a) shows a schematic of the displacement of the Fermi circle for one of the conduction subbands of a 2DEG under the application of an in-plane external electric field. The amount of displacement is greatly exaggerated for clarity. The black arrows represent the spins of the newly occupied states, while the light gray arrows represent the contribution from the states that have become unoccupied, thus yielding the net current polarization and magnetization in the direction perpendicular to the displacement of the circle. In part (b), the net effect for the two conduction subbands is shown. The difference in size of the circles has been exaggerated for clarity. Since the size of the regions contributing to the magnetization is different, the “up” and “down” magnetizations will not compensate and there will be a net surface magnetization in a direction perpendicular to the applied electric field.

$\mu \sim 8 \text{ m}^2/\text{V}\cdot\text{s}$, $m^* \sim 0.02m_e$, $\alpha_R \sim 38 \times 10^{-10} \text{ eV}\cdot\text{cm}$ and $E_{\parallel} \sim 1 \text{ V/cm}$ one gets a surface magnetization of the order of $10^{-12} \text{ J/T}\cdot\text{m}^2$. This magnetization corresponds to $\sim 10^5$ Bohr magnetons for a 1 mm^2 sample. Measurement of this small effect might be possible, for example, using Wernsdorfer’s μ -SQUID technique [42]. This magnetic field would be distinguishable from a field produced by the current *à la* Ampère because of the different directions that the Ampère field and the one proposed here would have.

Also, the spin polarization of the current can be estimated by assuming all the

magnetization is supplied by a difference

$$n_{\uparrow} - n_{\downarrow} = \frac{2\mathbf{M}}{Ag\mu_B} \quad (2.12)$$

to obtain the spin polarization of the 2DEG under an applied bias

$$P = \frac{j_{\uparrow} - j_{\downarrow}}{j_{\uparrow} + j_{\downarrow}} = \frac{n_{\uparrow} - n_{\downarrow}}{n_{\uparrow} + n_{\downarrow}} \sim 5 \times 10^{-5}. \quad (2.13)$$

This small value shows that this scheme is not a good candidate as a source of spin polarized current, unless structures with a much higher Bychkov-Rashba coefficient can be found.

2.6 Summary

In conclusion, it has been shown that there is a large spin splitting in the conduction band of the two-dimensional electron gas (2DEG) formed in an asymmetric AlSb/InAs/GaSb/AlSb quantum well. This theoretical value is the largest such splitting reported for nonmagnetic 2DEGs confined by asymmetric walls. This splitting and the behavior of the spins are well described, at low \mathbf{k} 's, by a Rashba Hamiltonian. The Rashba coefficients obtained with the effective bond orbital model (EBOM) have been shown to be in agreement with those obtained with other methods. However, EBOM has the added benefits that it takes into account the coupling of the space and spin parts of the wavefunction and the interaction between the conduction and valence bands in situations where it cannot be treated perturbatively. Also, it is predicted that when an electric field is applied in the plane of the 2DEG, it should display a surface magnetization estimated to be of the order of 10^{-12} J/T·m² for values typical of the structures in this chapter. The degree of spin polarization of the resulting current is found to be $\sim 0.01\%$. These results are not encouraging for practical applications, but other approaches using the Rashba effect [43, 44] show more promise towards the realization of a spin injector.

Bibliography

- [1] S. A. Wolf, *J. Supercond.* **13**, 195 (2000).
- [2] R. Gawel, *Electron. Des.* **48**, 30 (2000).
- [3] S. Das Sarma, J. Fabian, X. D. Hu, and I. Zutic, *Superlattice. Microstruct.* **27**, 289 (2000).
- [4] B. Heinrich, *Can. J. Phys.* **78**, 161 (2000).
- [5] S. Datta and B. Das, *Appl. Phys. Lett.* **56**, 665 (1990).
- [6] R. Fiederling, M. Keim, G. Reuscher, W. Ossau, G. Schmidt, A. Waag, and L. W. Molenkamp, *Nature* **402**, 787 (1999).
- [7] S. S. P. Parkin, K. P. Roche, M. G. Samant, P. M. Rice, R. B. Beyers, R. E. Scheuerlein, E. J. O'Sullivan, S. L. Brown, J. Bucchigano, D. W. Abraham, Y. Lu, M. Rooks, P. L. Trouilloud, R. A. Wanner, and W. J. Gallagher, *J. Appl. Phys.* **85**, 5828 (1999).
- [8] A. Morinaga and K. Shiiki, *Jpn. J. Appl. Phys.* **38**, 4741 (1999).
- [9] G. Schmidt, R. Fiederling, M. Keim, G. Reuscher, T. Gruber, W. Ossau, A. Waag, and L. W. Molenkamp, *Superlattice. Microst.* **27**, 297 (2000).
- [10] I. Malajovich, J. M. Kikkawa, D. D. Awschalom, J. J. Berry, and N. Samarth, *J. Appl. Phys.* **87**, 5073 (2000).
- [11] D. D. Awschalom and J. M. Kikkawa, *Phys. Today* **52**, 33 (1999).
- [12] Y. A. Bychkov and E. I. Rashba, *J. Phys. C* **17**, 6039 (1984).
- [13] D. Stein, K. Von Klitzing, and G. Weimann, *Phys. Rev. Lett.* **51**, 130 (1983).

- [14] F. Malcher, G. Lommer, and U. Rossler, *Superlatt. Microstruct.* **2**, 267 (1986).
- [15] J. Luo, H. Munekata, F. F. Fang, and P. J. Stiles, *Phys. Rev. B* **38**, 10142 (1988).
- [16] T. C. McGill and D. A. Collins, *Semicond. Sci. Tech.* **8**, S1 (1993).
- [17] R. H. Miles, J. N. Schulman, D. H. Chow, and T. C. McGill, *Semicond. Sci. Tech.* **8**, S102 (1993).
- [18] E. A. D. E. Silva, G. C. LaRocca, and F. Bassani, *Phys. Rev. B* **55**, 16293 (1997).
- [19] E. A. D. E. Silva, G. C. LaRocca, and F. Bassani, *Phys. Rev. B* **50**, 8523 (1994).
- [20] S. Brosig, K. Ensslin, R. J. Warburton, C. Nguyen, B. Brar, M. Thomas, and H. Kroemer, *Phys. Rev. B* **60**, R13989 (1999).
- [21] T. Matsuyama, R. Kursten, C. Meissner, and U. Merkt, *Phys. Rev. B* **61**, 15588 (2000).
- [22] D. Grundler, *Phys. Rev. Lett.* **84**, 6074 (2000).
- [23] R. Winkler, *Phys. Rev. B* **62**, 4245 (2000).
- [24] P. Ramvall, B. Kowalski, and P. Omling, *Phys. Rev. B* **55**, 7160 (1997).
- [25] L. Wissinger, U. Rossler, R. Winkler, B. Jusserand, and D. Richards, *Phys. Rev. B* **58**, 15375 (1998).
- [26] Y. C. Chang, *Phys. Rev. B* **37**, 8215 (1988).
- [27] G. T. Einevoll and Y. C. Chang, *Phys. Rev. B* **40**, 9683 (1989).
- [28] J. C. Slater and G. F. Koster, *Phys. Rev.* **94**, 1498 (1954).
- [29] W. A. Harrison, *Phys. Rev. B* **8**, 4487 (1973).
- [30] G. Bastard, *Heterojunctions and Semiconductor Superlattices*, 2nd ed. (Springer-Verlag New York, New York, Ny, 1986).

- [31] E. O. Kane, *J. Phys. Chem. Solids* **1**, 82 (1956).
- [32] G. Dresselhaus, *Phys. Rev.* **100**, 580 (1955).
- [33] G. Lommer, F. Malcher, and U. Rossler, *Phys. Rev. Lett.* **60**, 728 (1988).
- [34] M. Cardona, N. E. Christensen, and G. Fasol, *Phys. Rev. B* **38**, 1806 (1988).
- [35] T. Schäpers, G. Engels, J. Lange, T. Klocke, M. Hollfelder, and H. Lüth, *J. Appl. Phys.* **83**, 4324 (1998).
- [36] E. T. Yu, J. O. McCaldin, and T. C. McGill, *Solid State Phys.* **46**, 1 (1992).
- [37] M. P. Mikhailova and A. N. Titkov, *Semicond. Sci. Technol.* **9**, 1279 (1994).
- [38] C. Cohen-Tannoudji, B. Diu, and F. Laloë, *Quantum Mechanics*, 2nd ed. (Wiley, New York, 1977).
- [39] J. Nitta, T. Akazaki, H. Takayanagi, and T. Enoki, *Phys. Rev. Lett.* **78**, 1335 (1997).
- [40] A. Därr, J. P. Kotthaus, and T. Ando, in *Proc. of the 13th Int. Conf. Physics Semiconductors (ICPS-13)* (Rome, 1976), pp. 774–777.
- [41] J. M. Ziman, *Principles of the Theory of Solids*, 2nd ed. (Cambridge University Press, Cambridge, Uk, 1972), pp. 216–217.
- [42] W. Wernsdorfer, K. Hasselbach, A. Benoit, W. Wernsdorfer, B. Barbara, D. Mailly, J. Tuailon, J. P. Perez, V. Dupuis, J. P. Dupin, G. Guiraud, and A. Perex, *J. Appl. Phys.* **78**, 7192 (1995).
- [43] A. Voskoboynikov, S. S. Lin, C. P. Lee, and O. Tretyak, *J. Appl. Phys.* **87**, 387 (2000).
- [44] D. Z.-Y. Ting, X. Cartoixà, D. H. Chow, J. S. Moon, D. L. Smith, T. C. McGill, and J. N. Schulman, *IEEE Trans. Magn.* (2002), to be published.

Chapter 3 Optimization of the Rashba coefficient in asymmetric AlSb/InAs/GaSb heterostructures

3.1 Introduction

In Chapter 2, it has been shown that, in order for any device exploiting the Rashba splitting to be useful, large Rashba coefficients are required. In particular, large Rashba splittings would help achieve a bigger spin polarization of the current in the proposed [1] asymmetric Resonant Tunneling Device (a-RTD) realization of a spin injector.

It has also been shown in Chapter 2 that predictions of the magnitude of the Rashba coefficient in the 6.1 Å system composed by the nearly lattice matched compounds AlSb, GaSb and InAs, with its unique band offsets [2], are among the largest in the literature.

In this chapter, a systematic exploration of different AlSb/InAs/GaSb heterostructures is undertaken leading to a set of design rules for a structure having an optimized Rashba coefficient. In Sec. 3.2 the Rashba coefficient is found for structures having a varying number of monolayers. In Sec. 3.3 it is shown how the Rashba coefficient is significantly reduced in wide wells and finally a summary is presented.

3.2 Rashba coefficient as a function of the layer thicknesses

In this chapter, following the line of Chapter 2, the band structures are computed using the effective bond orbital model (EBOM) method [3, 4]. For computational

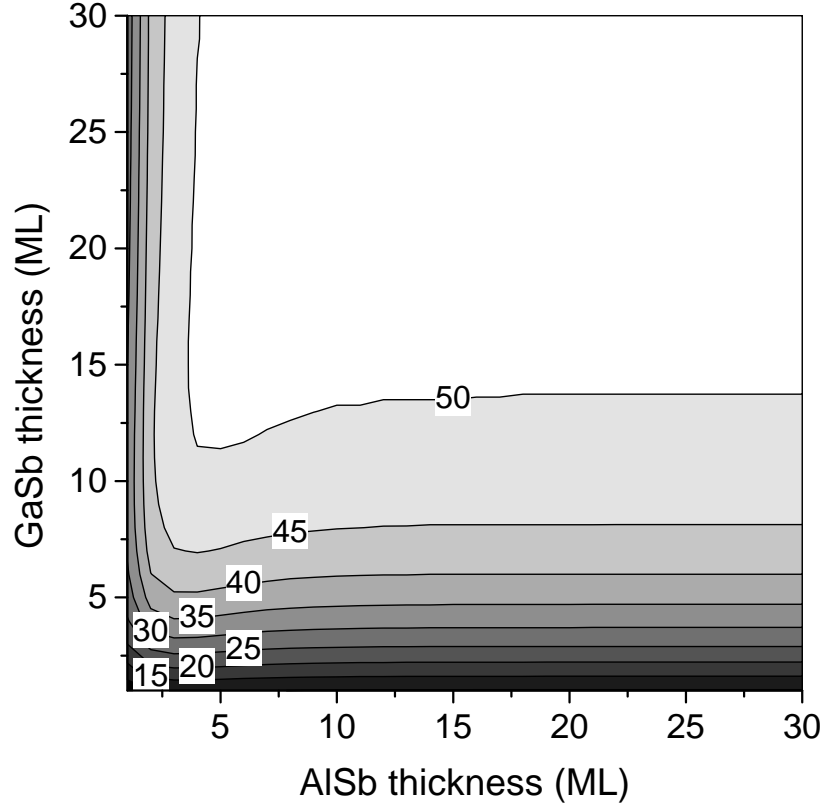


Figure 3.1: The Rashba coefficient as a function of AlSb and GaSb thicknesses for InAs thickness fixed to 9 ML. The numbers in the plot are contour lines of the Rashba coefficient in units of 10^{-10} eV·cm.

convenience purposes, the calculations will be made using superlattice boundary conditions. The superlattice results will be valid for the quantum well case as long as the AlSb layers are thick enough that all the instances of the superlattice are in effect isolated from one another. One finds that the superlattice cells are effectively decoupled when the AlSb thickness is 8 monolayers (ML) or more, with a monolayer having a thickness of 3.048 \AA . A flat band plot of the structure with its corresponding band alignments can be found in Fig. 2.1.

The computations of the Rashba coefficient (see Chapter 2) are made in the same conditions as in Chapter 2. Therefore, structural symmetry breaking mechanisms for the well other than the layer sequencing [5, 6] will not be dealt with. The bulk inversion asymmetry inherent to bulk zincblendes and the spin splitting originating from it [7] will not be taken into account, either.

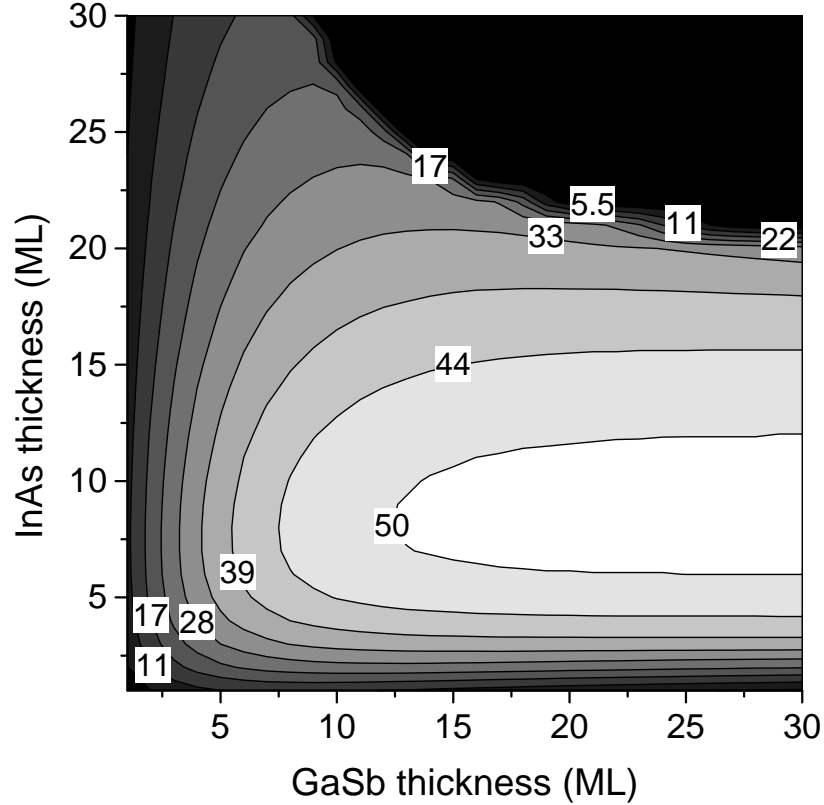


Figure 3.2: The Rashba coefficient as a function of InAs and GaSb thicknesses for AlSb thickness fixed to 16 ML.

A systematic exploration of structures with different layer thicknesses has been undertaken with the purpose of looking for the configuration optimizing the Rashba coefficient and delineating the role of each of the composing layers. The thickness of each of the layers has been swept from 1 to 30 ML. The Rashba coefficient α_R is calculated from the splitting at 0.2% of the zone edge along the [100] direction and then applying

$$\Delta_R = 2\alpha_R k. \quad (2.3)$$

Figure 3.1 shows the Rashba coefficient as a function of the AlSb and GaSb thicknesses while keeping the InAs thickness fixed to 9 ML. It is seen that the Rashba coefficient is independent of the AlSb and GaSb thicknesses in a wide range. It only changes its value when the AlSb layer is very thin—the quantum well approximation ceases to be valid—and when the GaSb layer is less than 8 ML. In this case, a thinner GaSb layer reduces the amount of asymmetry in the quantum well and,

therefore, reduces the Rashba coefficient. This behavior can be understood looking at the wavefunction in Fig. 2.1. The tail of the wavefunction vanishes into the AlSb on one side and into the GaSb on the other. Once the point has been reached where the tail of the wavefunction vanishes inside one layer, it is of little consequence that more monolayers of material are added, since that would affect a region where the electron is barely present. This explains the independence of the AlSb and GaSb thicknesses for most of the range.

Figure 3.2 shows the Rashba coefficient as a function of the InAs and GaSb thicknesses while keeping the AlSb thickness fixed to 16 ML. It is seen that, in order to achieve a high Rashba coefficient, the GaSb thickness must be bigger than approximately 8 ML and the InAs layer must be between 5 and 15 ML. But in the previous paragraph it has been shown that the AlSb thickness is of little importance as long as it is thick enough; therefore, these design rules apply for quantum wells with AlSb barriers thicker than 15 Å.

3.3 Rashba coefficient for wide wells

Another interesting feature in Fig. 3.2 that requires attention is the region of thick GaSb and InAs where the Rashba coefficient is appreciably diminished, *i.e.*, the dark region. This sudden reduction is due to the anticrossing of the InAs electron states with the GaSb hole states.

Figure 3.3 shows an example of such anticrossing. It displays the band structure of a 24 ML GaSb / 24 ML InAs quantum well. In bulk, the InAs conduction band electron states lie below the GaSb valence band hole states [2]. For a thin quantum well, the InAs electron states are pushed up in energy, while the GaSb hole states are pushed down; thus making the well behave as if it were made of a direct band gap material. However, for the case shown in Fig. 3.3, the GaSb and InAs layers are not thin enough for the valence and the conduction bands to be separated, and the anticrossing takes place.

The inset in Fig. 3.3 shows that the amount of splitting only recovers its linear

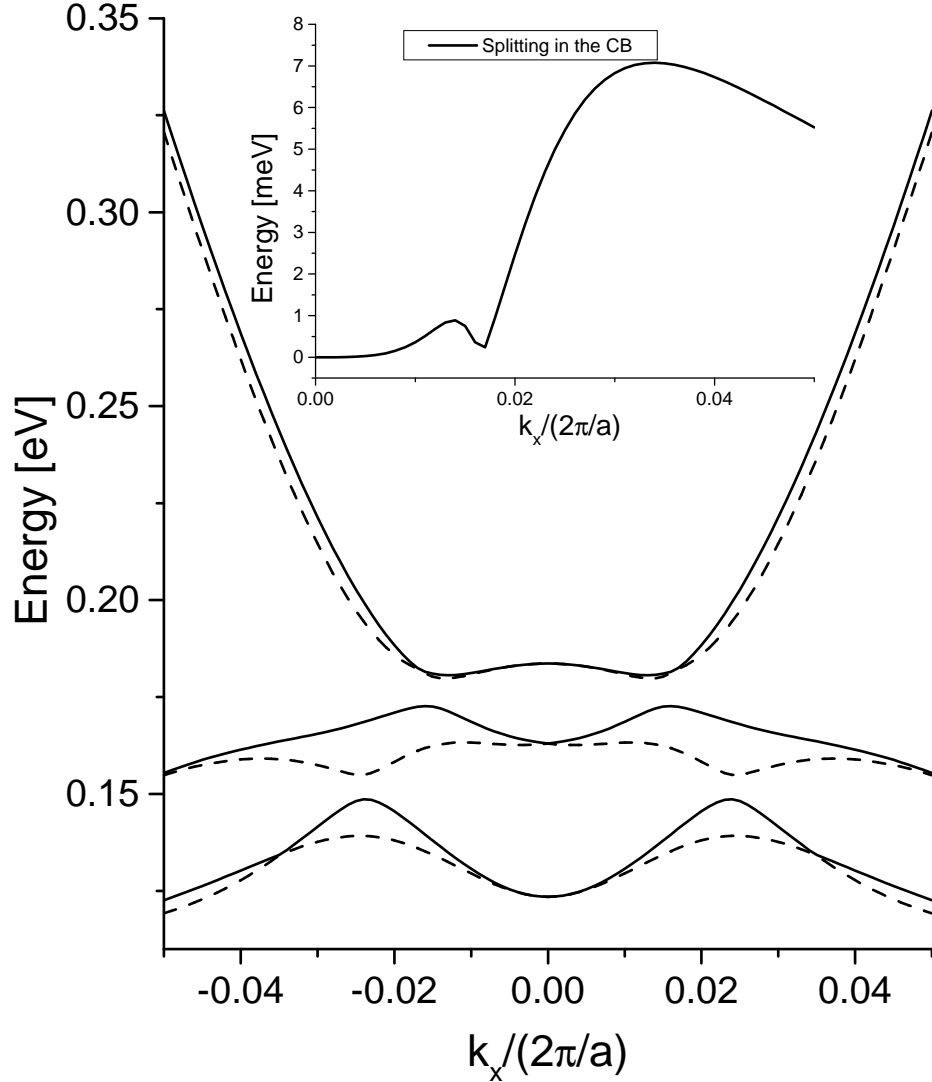


Figure 3.3: Band structure of a 12ML AlSb/24ML InAs/24ML GaSb/12ML AlSb quantum well, showing the anticrossing of the conduction and valence bands. The inset shows the splitting in the conduction band.

k dependence once the electron states don't couple with the hole states. In this situation, the Rashba coefficient defined as one half of the slope of the splitting at the Γ point loses much of its meaning, and it is more appropriate instead to look at the total amount of splitting. For example, the splitting at $\mathbf{k} = (0.03, 0, 0) \text{ \AA}^{-1}$ is reduced to about one third of the value for thin wells [cf. plot (c) in Fig. 2.2]. This illustrates the reduction in the magnitude of splitting that takes place whenever anticrossing of the states occurs.

It is important to note that an eight-band method is needed to fully consider the

interplay of the conduction and valence bands leading to the reduction of the Rashba coefficient. This would have been impossible if, instead, a two-band method had been employed.

3.4 Summary

In summary, it has been shown that the AlSb/GaSb/InAs system shows promise to be the material system of choice to obtain large Rashba effect splittings. The Rashba coefficient has been seen to be critically dependent on the InAs thickness, while showing almost no dependence on the AlSb and GaSb thicknesses once these are above some threshold value. The optimal thickness of the InAs layer has been determined. Finally, the importance of designing the sample in such a way that there is no anticrossing between the InAs electron states and the GaSb hole states in order to achieve large values of the Rashba coefficient has been highlighted.

Bibliography

- [1] A. Voskoboynikov, S. S. Lin, C. P. Lee, and O. Tretyak, *J. Appl. Phys.* **87**, 387 (2000).
- [2] E. T. Yu, J. O. McCaldin, and T. C. McGill, *Solid State Phys.* **46**, 1 (1992).
- [3] Y. C. Chang, *Phys. Rev. B* **37**, 8215 (1988).
- [4] G. T. Einevoll and Y. C. Chang, *Phys. Rev. B* **40**, 9683 (1989).
- [5] J. Luo, H. Munekata, F. F. Fang, and P. J. Stiles, *Phys. Rev. B* **38**, 10142 (1988).
- [6] J. Nitta, T. Akazaki, H. Takayanagi, and T. Enoki, *Phys. Rev. Lett.* **78**, 1335 (1997).
- [7] G. Dresselhaus, *Phys. Rev.* **100**, 580 (1955).

Chapter 4 Description of bulk inversion asymmetry in the effective bond orbital model

4.1 Introduction

Since its inception in 1954 [1], the empirical tight binding method (TB) has been extensively used to compute band structures of bulk metals [1–3], semiconductors [1, 4], and heterostructures [5, 6], yielding a good compromise between accuracy and ease of implementation. Tight binding is a full zone method and, as such, it has been used to describe situations where states corresponding to more than one extremum are needed, such as short period superlattices [7] or X -point tunneling influence on the escape time of electrons inside leaky quantum wells [8].

One of the difficulties tight binding users encounter is the choice of parameters. Usually, tight binding parameters bear only an indirect relation with measurable quantities, and their determination usually requires a tedious fitting procedure. The effective bond orbital model (EBOM) method by Chang [9, 10] reviewed in Sec. 4.2 provides a way of matching the TB parameters using a reduced bond orbital basis set [11] with the measurable $\mathbf{k} \cdot \mathbf{p}$ parameters. As originally developed, the EBOM method does not account for the bulk inversion asymmetry (BIA) present in zincblendes, predicting no spin splitting in structures where BIA does cause a nonzero splitting (cf. Sec. 5.5). In Sec. 4.3, an extension to EBOM capable of describing BIA effects in the conduction band is presented. In Sec. 4.4 the method is applied to bulk GaSb. Sec. 4.5 shows the application of the method to a symmetric AlSb/GaSb superlattice, predicting the appearance of spin splitting in the conduction band. This is a distinct feature of this method, while standard $\mathbf{k} \cdot \mathbf{p}$ implementations or the original

EBOM formulation would predict the absence of splitting. These results are shown to agree with $\mathbf{k} \cdot \mathbf{p}$ calculations that do account for BIA (cf. Chapter 5). Finally, a summary of the results is presented.

4.2 Review of the EBOM method

The basic idea of the EBOM method is to take the TB Hamiltonian expressed in a bond orbital model basis set, series expand it for small k 's and then compare the matrix elements with the $\mathbf{k} \cdot \mathbf{p}$ matrix elements [12] to obtain the TB parameters in terms of the $\mathbf{k} \cdot \mathbf{p}$ parameters.

Following Chang [9], the orbitals are located at points of an *fcc* lattice. A state at a site \mathbf{R} with character $\alpha = s, x, y$ or z is labeled $|\mathbf{R}, \alpha\rangle$. The bond orbitals are taken to be the Löwdin symmetrized orbitals [13] that most closely resemble the top of the valence and bottom of the conduction band states. The requirement that they originate from linear combination of atomic orbitals in a unit cell does not really need to be made. The success of the method (and of the $\mathbf{k} \cdot \mathbf{p}$ method as well) comes precisely from the fact that detailed knowledge of the wavefunctions isn't needed because the matrix elements are only determined on symmetry grounds plus a few parameters fitted empirically [1, 14].

The interaction between the p -type orbitals $|\mathbf{R}, \beta\rangle$ and $|\mathbf{R}', \beta'\rangle$ ($\beta = x, y, z$) is, for the *fcc* lattice, given by [10]:

$$\begin{aligned} \langle \mathbf{R}, \beta | H | \mathbf{R}', \beta' \rangle = \\ E_p \delta_{R, R'} \delta_{\beta, \beta'} + \sum_{\tau} \delta_{R' - R, \tau} \left\{ E_{xy} \tau_{\beta} \tau_{\beta'} (1 - \delta_{\beta, \beta'}) + [E_{xx} \tau_{\beta}^2 + E_{zz} (1 - \tau_{\beta}^2)] \delta_{\beta, \beta'} \right\}, \end{aligned} \quad (4.1)$$

where E_p is the on-site energy and E_{xy} , E_{xx} and E_{zz} are different nearest-neighbors interaction parameters. The vectors τ join the twelve nearest neighbors, and they can have values

$$\tau = \frac{a}{2} ([\pm 1, \pm 1, 0], [\pm 1, 0, \pm 1], [0, \pm 1, \pm 1]), \quad (4.2)$$

with a being the lattice constant.

The interaction of s orbitals is quite simple

$$\langle \mathbf{R}, s | H | \mathbf{R}', s \rangle = E_s \delta_{R,R'} + \sum_{\tau} E_{ss} \delta_{R'-R,\tau}, \quad (4.3)$$

with E_s and E_{ss} having analogous meanings as E_p and E_{xx} . The remaining interaction is between the s - and p -like orbitals at nearest neighbor sites:

$$\langle \mathbf{R}, s | H | \mathbf{R}', \beta \rangle = E_{sx} \delta_{R'-R,\tau} \tau \beta. \quad (4.4)$$

At this point, a clarification must be made. The inadequacy of the ordinary EBOM method to describe the reduced T_d symmetry of zincblendes does not originate from the basis set being located on an fcc lattice, but rather on the fact that a basis with a definite parity has been used to obtain Eqs. (4.1)-(4.4). In the next section this assumption is relaxed, yielding the correction necessary to describe spin splitting in the conduction band.

From the Löwdin functions $|\mathbf{R}, \alpha\rangle$, Bloch sums can be written in the form

$$|\mathbf{k}, \alpha\rangle = \frac{1}{\sqrt{N}} \sum_{\mathbf{R}} e^{i\mathbf{k}\cdot\mathbf{R}} |\mathbf{R}, \alpha\rangle, \quad (4.5)$$

where N is the number of unit cells in the sample. Each eigenstate with a wavevector \mathbf{k} is written as a linear combination of Bloch sums [15]:

$$|\Psi_{\mathbf{k}}\rangle = \sum_{\alpha} u_{\alpha} |\mathbf{k}, \alpha\rangle. \quad (4.6)$$

The coefficients u_{α} are found by seeking stationary values of $\langle \Psi_{\mathbf{k}} | H | \Psi_{\mathbf{k}} \rangle / \langle \Psi_{\mathbf{k}} | \Psi_{\mathbf{k}} \rangle$, which leads to the diagonalization of a Hamiltonian with matrix elements

$$\langle \mathbf{k}, \alpha | H | \mathbf{k}, \alpha' \rangle = \frac{1}{N} \sum_{\mathbf{R}, \mathbf{R}'} e^{i\mathbf{k}\cdot(\mathbf{R}'-\mathbf{R})} \langle \mathbf{R}, \alpha | H | \mathbf{R}', \alpha' \rangle = \sum_{\mathbf{R}'} e^{i\mathbf{k}\cdot\mathbf{R}'} \langle \mathbf{R} = 0, \alpha | H | \mathbf{R}', \alpha' \rangle. \quad (4.7)$$

Parameters
$E_s = E_c + 12 \frac{A' + \hbar^2/2m_0}{a^2}$
$E_{ss} = -\frac{A' + \hbar^2/2m_0}{a^2}$
$E_p = E_v + 2 \frac{3\hbar^2/2m_0 + 2L' + 4M}{a^2}$
$E_{xx} = -\frac{\hbar^2/2m_0 + 2L'}{2a^2}$
$E_{zz} = -\frac{\hbar^2/2m_0 - 2L' + 4M}{2a^2}$
$E_{xy} = E_{xy}(110) = -\frac{N'}{a^2}$
a) $E_{sx} = \frac{P}{4a}$ or b) $(E_{zz} - E_{xx}) = X_{hl}/8 = 0.5 \text{ eV}$

Table 4.1: Relationship between the EBOM parameters and the $\mathbf{k} \cdot \mathbf{p}$ parameters.

For the p subblock, plugging Eq. (4.1) into Eq. (4.7) yields

$$H_{\beta,\beta'}(\mathbf{k}) = E_p \delta_{\beta,\beta'} + \sum_{\tau} e^{i\mathbf{k}\cdot\boldsymbol{\tau}} \{ E_{xy} \tau_{\beta} \tau_{\beta'} (1 - \delta_{\beta,\beta'}) + [E_{xx} \tau_{\beta}^2 + E_{zz} (1 - \tau_{\beta}^2)] \delta_{\beta,\beta'} \}. \quad (4.8)$$

Similarly, it is easy to see that

$$H_{s,s}(\mathbf{k}) = E_s + \sum_{\tau} e^{i\mathbf{k}\cdot\boldsymbol{\tau}} E_{ss} \quad (4.9)$$

and

$$H_{s,\beta}(\mathbf{k}) = \sum_{\tau} e^{i\mathbf{k}\cdot\boldsymbol{\tau}} E_{sx} \tau_{\beta}. \quad (4.10)$$

In order to find values for the EBOM parameters, the sums over first neighbors in Eqs. (4.8)-(4.10) are evaluated. For example, it is easy to see that

$$H_{s,x} = 4i E_{sx} \sin \xi (\cos \eta + \cos \zeta), \quad (4.11)$$

where $\xi = k_x a/2$, $\eta = k_y a/2$ and $\zeta = k_z a/2$. This agrees with the value in Table II of Ref. [1], provided that terms occupied in the sc but not in the fcc lattices are disregarded.

Then, the matrix elements are series expanded up to second order in \mathbf{k} and compared to $\mathbf{k} \cdot \mathbf{p}$ matrix elements [14] to obtain the relations listed in Table 4.1. The values of the $\mathbf{k} \cdot \mathbf{p}$ parameters L' , N' in terms of the more common L , N are available,

for example, Eq. (13) in Ref. [16]. Note that the last entry in that table is not totally determined. Taking $E_{sx} = P/4a$ might seem the sensible thing to do, but it produces spurious solutions [9]. Instead, the auxiliary constraint $(E_{zz} - E_{xx}) = X_{hl}/8$, where X_{hl} is the heavy hole–light hole separation at the X point, is used.

Spin-orbit effects are simply introduced by adding spin to the basis states, performing a change of basis on the Hamiltonian into a $|j, m\rangle$ basis and then modifying the diagonal components of the energies to include the spin-orbit splitting.

4.3 Inclusion of bulk inversion asymmetry effects in EBOM

As previously indicated, the EBOM Hamiltonian in zincblendes reproduces an O_h point group symmetry rather than the reduced T_d because the basis states (specifically, the p states) are implicitly assumed to be parity eigenstates. The simplest way to introduce an inversion symmetry breaking component consistent with the Γ_5^1 symmetry of the valence states is to add some d character to the p states. Thus, the substitutions

$$\begin{aligned} |\mathbf{R}, x\rangle &\rightarrow c_p |\mathbf{R}, x\rangle + c_d |\mathbf{R}, yz\rangle \\ |\mathbf{R}, y\rangle &\rightarrow c_p |\mathbf{R}, y\rangle + c_d |\mathbf{R}, zx\rangle \\ |\mathbf{R}, z\rangle &\rightarrow c_p |\mathbf{R}, z\rangle + c_d |\mathbf{R}, xy\rangle \end{aligned} \quad (4.12)$$

are made, where c_p and c_d are taken to be real and weight the importance of the odd and even (under inversion) components, respectively, in the new state.

Keeping with the matrix element $H_{s,x}$ as an example, the change in the states will transform it to

$$H_{s,x} = c_p \langle \mathbf{k}, s | H | \mathbf{k}, x \rangle + c_d \langle \mathbf{k}, s | H | \mathbf{k}, yz \rangle. \quad (4.13)$$

¹The KDWS notation is being used (see Ref. [17]).

Looking up again in Table II of Ref. [1], one can see that

$$H_{s,x} = 4iE_{sx} \sin \xi (\cos \eta + \cos \zeta) - 4E_{s,xy} \sin \eta \sin \zeta, \quad (4.14)$$

where the coefficients c_i have been absorbed into the adjustable parameters E_i . Now, comparing Eq. (4.14) with the corresponding element in the $\mathbf{k} \cdot \mathbf{p}$ Hamiltonian in Ref. [14], one sees that the parameter B describing the BIA in the $\mathbf{k} \cdot \mathbf{p}$ formalism (see Sec. 5.3) can be introduced in EBOM by taking

$$E_{s,xy} = -B/a^2. \quad (4.15)$$

Therefore, the inclusion of BIA is made at a negligible computational cost and its implementation is straightforward because only a supplemental matrix element is being added instead of extending the basis set to include, say, anion and cation orbitals. Another computational advantage is that the number of neighbors included in the calculation is not increased.

It remains to be seen how the remaining matrix elements are affected by the substitutions (4.12). $H_{s,s}$ is left unchanged, while the other diagonal elements become

$$\begin{aligned} H_{x,x} &= |c_p|^2 [4E_{xx}(\cos \xi \cos \eta + \cos \xi \cos \zeta) + 4E_{zz} \cos \eta \cos \zeta] + \\ &|c_d|^2 [4E_{xy,xy}(110) \cos \eta \cos \zeta + 4E_{xy,xy}(011)(\cos \xi \cos \eta + \cos \xi \cos \zeta)] = \\ &[|c_p|^2 4E_{xx} + |c_d|^2 4E_{xy,xy}(011)](\cos \xi \cos \eta + \cos \xi \cos \zeta) + \\ &[|c_p|^2 4E_{zz} + |c_d|^2 4E_{xy,xy}(110)] \cos \eta \cos \zeta = \\ &4E_{xx}(\cos \xi \cos \eta + \cos \xi \cos \zeta) + 4E_{zz} \cos \eta \cos \zeta, \quad (4.16) \end{aligned}$$

where in the last step E_{xx} and E_{zz} have been redefined so that Table 4.1 still holds. The other diagonal elements can be obtained by the appropriate cyclic permutations.

The nondiagonal elements between Γ_5 states also change:

$$\begin{aligned}
H_{x,y} = & |c_p|^2[-4E_{xy} \sin \xi \sin \eta] + |c_d|^2[-4E_{xy,xz}(011) \sin \xi \sin \eta] + \\
& c_p c_d [4iE_{x,xy}(110) \cos \xi \sin \zeta + 4iE_{x,xy}(011) \cos \eta \sin \zeta] + \\
& c_d c_p [-4iE_{x,xy}(110) \cos \eta \sin \zeta - 4iE_{x,xy}(011) \cos \xi \sin \zeta] = \\
& -4E_{xy}(110) \sin \xi \sin \eta - 4iE_{xy}(011) \sin \zeta [\cos \xi - \cos \eta], \quad (4.17)
\end{aligned}$$

with the usual redefinition of parameters in the last step. $H_{y,z}$ and $H_{z,x}$ are obtained by cyclic permutations. The results here obtained for the tight binding zincblende matrix elements agree with those of Hass *et al.* [18], which correct the misprints in Table V of Ref. [1].

Comparison with the $\mathbf{k} \cdot \mathbf{p}$ Hamiltonian doesn't provide the value of the $E_{xy}(011)$ parameter because it only introduces terms of order k^3 or higher when the corresponding matrix element is expanded. This should not be a concern when properties are sought involving only states near Γ . A look at the matrix elements reveals that the contribution of $E_{xy}(011)$ reaches its peak near the K point. Since only properties near the zone center are of interest here, its value will be set to zero for the following calculations.

4.4 Bulk GaSb

The considerations above are illustrated with an example calculation of bulk GaSb. Figure 4.1 shows the bands of bulk GaSb for a few special directions. The dashed and dotted lines in plot (a) correspond to the EBOM model without the zincblende symmetry corrections. The dotted line is obtained under the original requirement [9] that the separation $X_{hl} = 4.0$ eV is used to obtain E_{sx} . This will be called X model. The dashed line is obtained taking $E_{sx} = \frac{P}{4a}$, with P obtained from the value of the effective mass given by Eq. (5.17). This will be called P model. With the parameters used, looking at the X and L points, in the P model the conduction (CB) and split off (SO) bands are pushed further apart than in the X model. In the P model, the

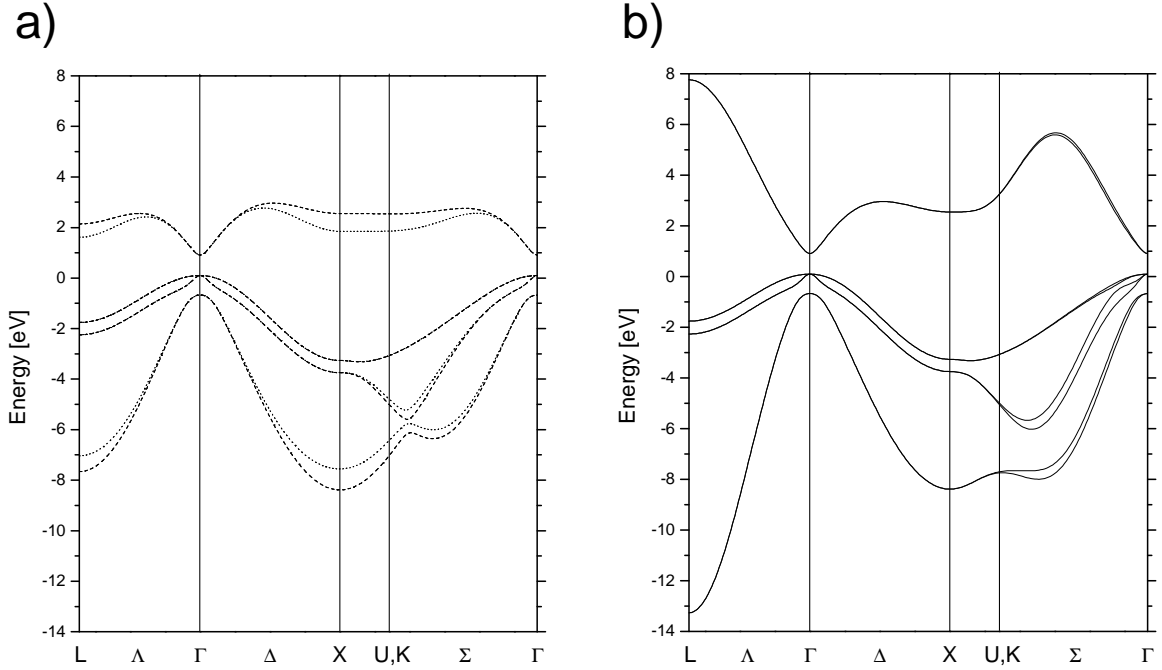


Figure 4.1: Band structure of GaSb calculated with EBOM under different assumptions for the parameters. The dotted line in plot (a) is obtained under the original requirement [9] that the separation $X_{hl} = 4.0$ eV is used to obtain E_{sx} . The dashed line is obtained taking $E_{sx} = \frac{P}{4a}$. A term describing BIA has been included in plot (b), which otherwise uses the same set of parameters as in the calculations represented by the dashed line.

positions of the CB and SO bands are very sensitive to the value of the CB effective mass. For example, changing m_c^* in InAs from 0.025 to 0.024 changes the position of the SO band at the X point from about -10 eV to about -6.5 eV. Going one step further and setting $m_c^* = 0.023$ makes the SO band anticross with the heavy and light holes, and the spurious heavy hole (HH) - light hole (LH) crossing described in Ref. [9] appears. Therefore, it is reasonable to assume that very small changes in the value of the m_c^* parameter can not only get rid of spurious solutions present in the P model but also tune the position of the CB at the X point.

Plot (b) in Fig. 4.1 is generated under the same conditions as model P , but with BIA effects turned on by letting $E_{s,xy} = -B/a^2$. This will be called PB model. In agreement with predictions from the character tables for the T_d group [17], the bands become spin split in the Σ direction because of the breakdown of Kramers degeneracy. However, the correct description of the zincblende symmetry is made at the cost of

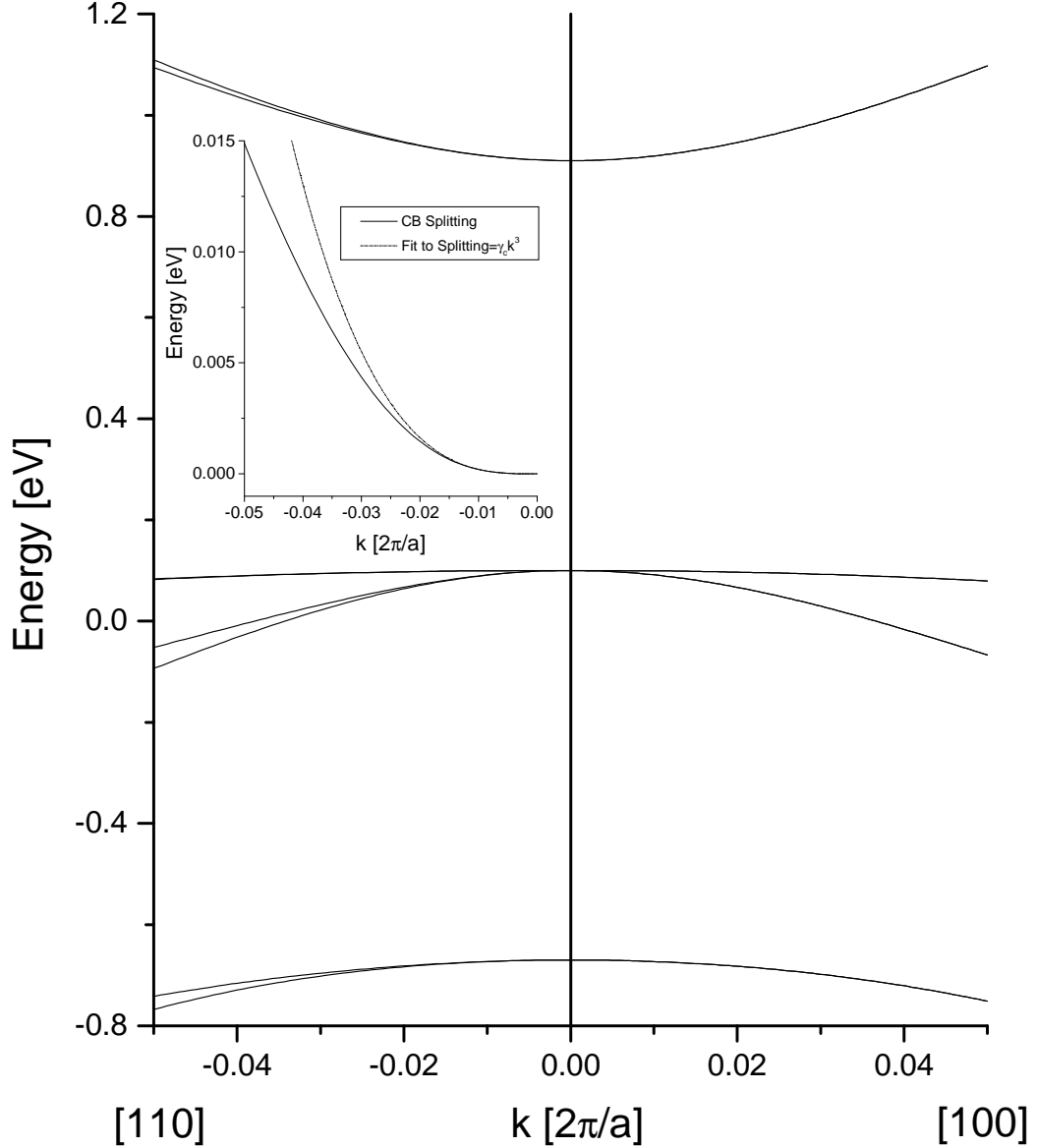


Figure 4.2: Bands close to the zone center showing the spin splitting, calculated with EBOM. The inset shows the amount of CB splitting and its k^3 dependence at low values of k .

the loss of accuracy for the CB and SO bands, specially along the Λ line, where they take values quite far from pseudopotential calculations [19]. The preference of having a correct description of the bands near the Γ point or the Δ line including spin—with its ability to describe short period 100 superlattices—or a more accurate full zone description will determine the model to be used. The inclusion of second nearest neighbors matrix elements [20] might reconcile the energy values at the L point in

the PB model with the pseudopotential calculations and experimental findings [21].

Figure 4.2 shows the bands in more detail close to the zone center, with the spin splitting in the bands along the $[110]$ direction. The inset shows the splitting in the conduction band along the Σ line for the CB, and a fit using

$$\text{Splitting} = \gamma_c k^3, \quad (4.18)$$

where γ_c is the k^3 splitting proportionality constant. The value used for γ_c is $186 \text{ eV}\cdot\text{\AA}^3$, in good agreement with the measured value of $187 \text{ eV}\cdot\text{\AA}^3$ [22]. This shows that the parameter B determines the CB splitting near the zone center in the PB model in the same way as it does in the $\mathbf{k}\cdot\mathbf{p}$ method, as expected from the derivation in Sec. 4.3. A look at the inset reveals that, for GaSb, expression (4.18) is good until about 2% of the zone edge. The only qualitative aspect of the bulk bands that the extension in Sec. 4.3 cannot incorporate is the linear spin splitting in the valence bands close to the zone center [23] (cf. Fig. 5.2). In $\mathbf{k}\cdot\mathbf{p}$, this is described by a parameter C coming from second-order mixed $\mathbf{k}\cdot\mathbf{p}$ and spin-orbit terms in the perturbation expansion [14, 24]. It is this relation of C to the spin orbit interaction that makes it impossible to include its effects in the EBOM method. This is because the starting tight binding formulation includes spin orbit effects only in a limited and *ad hoc* fashion. Boykin [25] has extended the tight binding method to include the linear k splittings in the valence band, but the fact that four extra parameters are needed in his treatment while a single one does the job in $\mathbf{k}\cdot\mathbf{p}$ suggests that a tight binding formulation with spin orbit effects included from the beginning should yield the linear splitting naturally and reveal constraints due to symmetry between Boykin's parameters. In any case, its effects are normally small, and its importance for heterostructures is studied, for a particular case, in the following section.

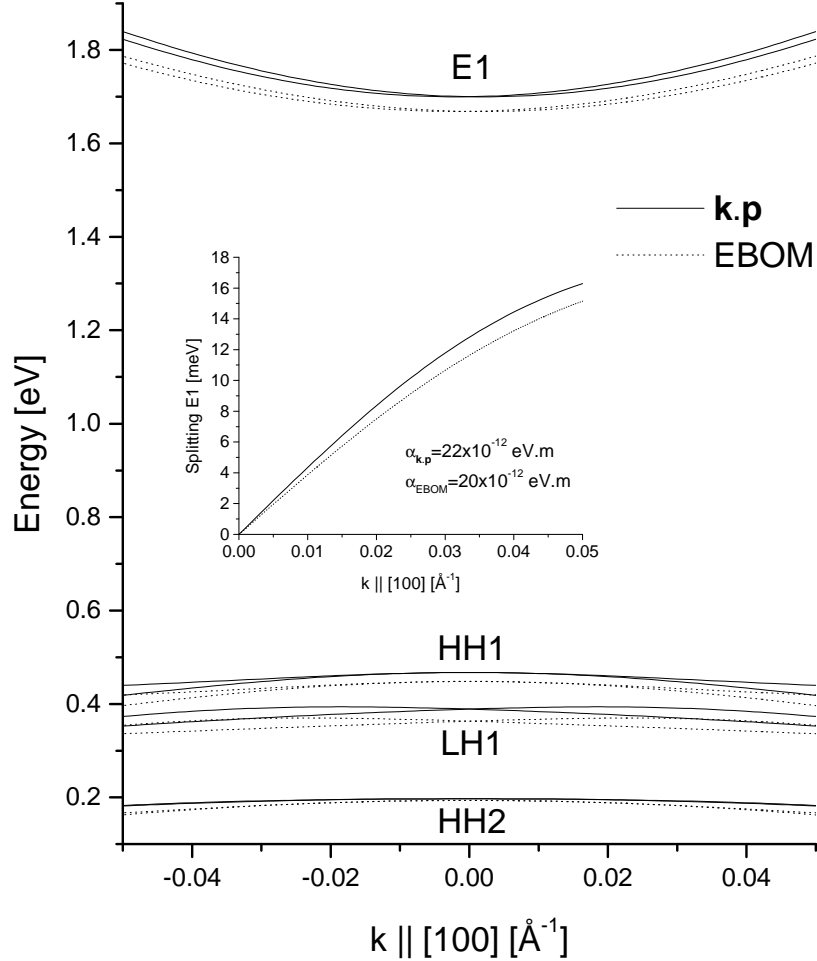


Figure 4.3: Comparison of EBOM and $\mathbf{k} \cdot \mathbf{p}$ superlattice bands. The structure is an 8/8/8 AlSb/GaSb/AlSb SL. The solid (dotted) lines are the $\mathbf{k} \cdot \mathbf{p}$ (EBOM) results. The bands are spin split away from Γ due to the bulk inversion asymmetry. The inset shows, for both methods, the amount of splitting in the E1 band and the values for the splitting coefficients as defined in Eq. (5.69).

4.5 Bulk inversion asymmetry effects in symmetric superlattices

The extension of the EBOM method in Sec. 4.3 is tested with the calculation of the band structure of an AlSb/GaSb/AlSb symmetric superlattice (SL). The reduction of the symmetry due to the confinement causes the states in the CB to become spin split even along the [100] direction [26], contrary to the predictions of most of the “oversymmetrized” $\mathbf{k} \cdot \mathbf{p}$ implementations.

Figure 4.3 shows the comparison of the bands of an 16/8 AlSb/GaSb SL calculated by both the $\mathbf{k} \cdot \mathbf{p}$ and the EBOM methods. In the $\mathbf{k} \cdot \mathbf{p}$ calculation, the parameters B and C describing BIA are both set to finite values for GaSb. In the EBOM calculation, as stated previously, only B can be set. Control calculations have been performed with $C = 0$ and $C \neq 0$ for this structure and for a 16/8/8 AlSb/GaSb/InAs SL, always finding that the inclusion of C modified the splittings only by a few tenths of meV. Thus, at least for this system, the inability of the PB model to describe the linear splitting in the valence bands of bulk zincblendes does not constitute a serious drawback when studying splittings in heterostructures. The solid (dotted) lines correspond to the $\mathbf{k} \cdot \mathbf{p}$ (EBOM) results. It can be seen that the value of the gap is similar, although the absolute position of the levels is slightly different. In the inset, the amount of splitting between the E1 subbands is shown, with both methods yielding similar results.

4.6 Summary

Summarizing, an extension to Chang's EBOM method [9] for calculating full zone band structures has been presented. This extension can describe the most important effects of bulk inversion asymmetry in zincblendes [23]. Also, the problem of spurious solutions in the original formulation has been shown to be solvable with small changes in the parameters. Finally, the new method has been applied to the calculation of bulk GaSb and an AlSb/GaSb/AlSb superlattice, and shown to have good agreement with $\mathbf{k} \cdot \mathbf{p}$ results close to the zone center.

Bibliography

- [1] J. C. Slater and G. F. Koster, Phys. Rev. **94**, 1498 (1954).
- [2] M. Asdente and J. Friedel, Phys. Rev. **124**, 384 (1961).
- [3] M. J. Mehl and D. A. Papaconstantopoulos, Phys. Rev. B **54**, 4519 (1996).
- [4] J. M. Jancu, R. Scholz, F. Beltram, and F. Bassani, Phys. Rev. B **57**, 6493 (1998).
- [5] J. N. Schulman and Y. C. Chang, Phys. Rev. B **24**, 4445 (1981).
- [6] J. N. Schulman and Y. C. Chang, Phys. Rev. B **27**, 2346 (1983).
- [7] T. Matsuoka, T. Nakazawa, T. Ohya, K. Taniguchi, C. Hamaguchi, H. Kato, and Y. Watanabe, Phys. Rev. B **43**, 11798 (1991).
- [8] M. K. Jackson, D. Ting, D. H. Chow, D. A. Collins, J. R. Soderstrom, and T. C. McGill, Phys. Rev. B **43**, 4856 (1991).
- [9] Y. C. Chang, Phys. Rev. B **37**, 8215 (1988).
- [10] G. T. Einevoll and Y. C. Chang, Phys. Rev. B **40**, 9683 (1989).
- [11] W. A. Harrison, Phys. Rev. B **8**, 4487 (1973).
- [12] E. O. Kane, J. Phys. Chem. Solids **1**, 82 (1956).
- [13] P.-O. Löwdin, J. Chem. Phys. **18**, 365 (1950).
- [14] E. O. Kane, in *Semiconductors and Semimetals*, edited by R. K. Willardson and A. C. Beer (Academic, New York, 1966), Vol. 1, pp. 75–100.
- [15] W. A. Harrison, *Electronic Structure and the Properties of Solids*, 1st ed. (Dover, Mineola, USA, 1989).

- [16] R. Enderlein, G. M. Sipahi, L. M. R. Scolfaro, and J. R. Leite, *Phys. Stat. Sol. (B)* **206**, 623 (1998).
- [17] G. F. Koster, J. O. Dimmock, R. G. Wheeler, and H. Statz, *Properties of the Thirty-Two Point Groups*, 1st ed. (M.I.T. Press, Cambridge, MA, USA, 1963).
- [18] K. C. Hass, H. Ehrenreich, and B. Velicky, *Phys. Rev. B* **27**, 1088 (1983).
- [19] J. R. Chelikowski and M. L. Cohen, *Phys. Rev. B* **14**, 556 (1976).
- [20] J. P. Loehr, *Phys. Rev. B* **50**, 5429 (1994).
- [21] T. C. Chiang and D. E. Eastman, *Phys. Rev. B* **22**, 2940 (1980).
- [22] G. E. Pikus, V. A. Marushchak, and A. N. Titkov, *Soviet Physics Semiconductors-USSR* **22**, 115 (1988).
- [23] G. Dresselhaus, *Phys. Rev.* **100**, 580 (1955).
- [24] M. Cardona, N. E. Christensen, and G. Fasol, *Phys. Rev. B* **38**, 1806 (1988).
- [25] T. B. Boykin, *Phys. Rev. B* **57**, 1620 (1998).
- [26] R. Eppenga and M. F. H. Schuurmans, *Phys. Rev. B* **37**, 10923 (1988).

Chapter 5 Bulk inversion asymmetry effects on the bands of zincblende heterostructures

5.1 Introduction

In recent years, interest in developing spin-sensitive devices (spintronics) [1–4] has fueled renewed investigations into spin phenomena in semiconductors. The aim is to control not only the spatial degrees of freedom of the electron, but also the spin degree of freedom. Useful spintronic devices can be devised if such control is achieved. A number of such devices have already been proposed [5–7]. If a full understanding of the operation of spintronic devices is wanted, a thorough knowledge of the band structure including all spin details will be needed; in much the same way as thorough knowledge of the “regular” band structure is required to fully understand electronic devices.

In this chapter, the band structure of AlSb/GaSb/AlSb and AlSb/InAs/GaSb/AlSb quantum wells is calculated using the $\mathbf{k} \cdot \mathbf{p}$ method taking into account spin-orbit effects. Among others, the coupling through the spin-orbit interaction between electron and hole states is taken into account, leading to the appearance of a spin splitting in the conduction states. This splitting can be viewed as a consequence of the removal of inversion symmetry in these heterostructures. The contribution to the splitting of the different sources of asymmetry will be explored quantitatively. Thus, the apparently contradictory statements of Lommer *et al.* [8] and Cardona *et al.* [9] regarding this matter can be clarified.

Following the literature, throughout this chapter the term spin splitting will be used to refer to the splitting of levels otherwise degenerate due to Kramers degeneracy,

even though in the valence band the total angular momentum is the correct quantum number to use.

Section 5.2 provides introductory remarks about how the breakdown of Kramers' degeneracy translates into spin splitting, and also quotes the apparently contradictory positions on the magnitude of the contributions to the splitting. In Sec. 5.3 the method of the invariants for the construction of a Hamiltonian with the correct point group symmetry is described. The validity of the constructed Hamiltonian is tested by obtaining analytical expressions for the dispersion relation and then comparing them to known expressions. Section 5.4 describes how the bulk Hamiltonian yields the effective mass approximation equations and how they are solved. In Secs. 5.5 and 5.6 the effects of bulk inversion asymmetry on symmetric and asymmetric quantum wells are explored and the results are finally summarized in Sec. 5.7.

5.2 Background

The appearance of spin splitting in the electronic band structure can be viewed as a consequence of the removal of inversion symmetry. In systems possessing inversion symmetry, the argument for the existence of spin degeneracy, most widely known as Kramers' degeneracy, goes as follows:

- I. Time reversal is always a property of the system¹. Since the Hamiltonian is invariant under time reversal, the following pair of eigenstates linked by the time reversal operator will be degenerate:

$$|\mathbf{k}, \uparrow\rangle \xrightarrow{\Theta} |-\mathbf{k}, \downarrow\rangle, \quad (5.1)$$

where Θ is the time reversal operator.

- II. If the system possesses inversion symmetry, the following pair of states will also

¹In ferromagnetic materials, time reversal must be applied to the whole system, including the ions responsible for the magnetic moment. This makes the following analysis invalid for that case.

be degenerate:

$$|\mathbf{k}, \uparrow\rangle \xrightarrow{I} |-\mathbf{k}, \uparrow\rangle, \quad (5.2)$$

with I being the inversion operator.

III. And finally, the sequential action of these two operators would yield a pair of degenerate eigenstates at the same \mathbf{k} point in the Brillouin zone:

$$|\mathbf{k}, \uparrow\rangle \xrightarrow{I\Theta} |\mathbf{k}, \downarrow\rangle. \quad (5.3)$$

In the case of bulk zincblendes, the splitting arising from the lack of inversion symmetry is commonly called the k^3 splitting due to its dependence near the zone center [10]. Along the [110] direction, this splitting can be written for the conduction band as [11]

$$\Delta_{BIA [110]} = \gamma_c k^3, \quad (5.4)$$

where $\Delta_{BIA [110]}$ is the splitting due to the bulk induced asymmetry (BIA), k is the modulus of the wavevector and γ_c is the proportionality constant. Traditionally, the term in the Hamiltonian leading to this splitting has been omitted in $\mathbf{k} \cdot \mathbf{p}$ calculations [12, 13].

However, in the case of quantum wells, other sources of inversion asymmetry can be present. These sources include the different composition of the confining layers, an asymmetric doping profile, an applied external electric field. All these mechanisms are grouped into the so-called structure induced asymmetry (SIA) [14].

There have been some contradictory statements in the literature regarding the relative contribution of SIA versus that of BIA in asymmetric heterostructures. In Ref. [8] Lommer, Malcher and Rössler say, “*Spin splitting of subband states ... is ascribed to the inversion-asymmetry-induced bulk k^3 term, which dominates in large gap materials, and to the interface spin-orbit or Rashba term, which becomes important in narrow-gap systems.*” On the other hand, Cardona, Christensen and Fasql [9] compile the measured coefficients γ_c shown in Table 5.1. From there it can be seen that, for the compounds shown, the k^3 splitting is bigger in narrow gap than in wide

Material	Band Gap (eV)	γ_c (eV·Å ³)
GaAs	1.52	25.5
InP	1.42	8.5
GaSb	0.81	186.3
InAs	0.418	130
InSb	0.235	226.8

Table 5.1: Band gap and γ_c for selected III-Vs, adapted from [9]. The value for InAs has been taken from [11].

gap materials. The numerical calculations performed in the following sections will clarify these statements.

5.3 $\mathbf{k} \cdot \mathbf{p}$ method applied to bulk III-Vs

In order to calculate the band structure of the heterostructures under study, the effective mass approximation (EMA) [13] based on an 8-band $\mathbf{k} \cdot \mathbf{p}$ formalism is used. There are several published 8-band $\mathbf{k} \cdot \mathbf{p}$ Hamiltonians [13], each including a more or less detailed set of effects.

For the calculations shown, the Hamiltonian constructed by Trebin *et al.* [15] has been implemented. This 8-band $\mathbf{k} \cdot \mathbf{p}$ Hamiltonian is constructed solely on group theory arguments and, when applied correctly, guarantees the inclusion of all matrix elements compatible with the T_d symmetry group of the zincblendes up to the desired order in the electron wavevector \mathbf{k} .

5.3.1 Invariant expansion of the Hamiltonian

This method to construct $\mathbf{k} \cdot \mathbf{p}$ Hamiltonians was first outlined by Luttinger [16], and developed generally by Bir and Pikus [17–19]. It is based solely on symmetry arguments. For the case of zincblendes, it basically goes as follows. The bulk Hamiltonian can be written in the following way:

$$H = \sum_{i,j \in T_d \text{ irreps}} H^{ij}, \quad (5.5)$$

where the H^{ij} operator corresponds to the block in the Hamiltonian matrix coupling the states of the Γ_j irreducible representation (irrep) to the states of Γ_i . Taking $|\Gamma_i, k\rangle$ defined as the k -th basis state of the Γ_i irrep of the T_d point group, these operators can be written explicitly as:

$$H^{ij} = \sum_{k \in \Gamma_i} \sum_{m \in \Gamma_j} H_{km}(\mathbf{k}) |\Gamma_i, k\rangle \langle \Gamma_j, m|, \quad (5.6)$$

where $H_{km}(\mathbf{k})$ are the matrix elements, and they are a function of the electron wavevector \mathbf{k} only.

Now, each of the matrices $|\Gamma_i, k\rangle \langle \Gamma_j, m|$ in H^{ij} can be thought of as a vector that will transform according to the product group representation $\Gamma_i \otimes \Gamma_j^*$ of T_d . It is more convenient to work with linear combinations of the $|\Gamma_i, k\rangle \langle \Gamma_j, m|$'s that transform according to the irreps contained in $\Gamma_i \otimes \Gamma_j^*$.

Since it is being required that H is invariant under the point group operations, each of the H^{ij} must transform according to the trivial irreducible representation, where all the group elements are represented by the unity. To achieve this, the Hamiltonian blocks must have the following form [19]:

$$H^{ij}(\mathcal{K}) = \sum_{\Gamma_l \in \Gamma_i \otimes \Gamma_j^*} a_l \sum_{m \in \Gamma_l} X_m^{\Gamma_l} (\mathcal{K}_m^{\Gamma_l})^*, \quad (5.7)$$

where the first sum is carried over the irreps contained in $\Gamma_i \otimes \Gamma_j^*$, the second one over the elements of Γ_l , \mathcal{K} is a general tensor from the components of \mathbf{k} , the strain $\bar{\epsilon}$ and the magnetic field \mathbf{H} ; $(\mathcal{K}_m^{\Gamma_l})^*$ is the complex conjugate of the m -th irreducible component of \mathcal{K} , $X_m^{\Gamma_l}$ is the m -th basis matrix coming transforming as $\Gamma_i \otimes \Gamma_j^*$, and the a_l 's are parameters that later can be mapped into standard $\mathbf{k} \cdot \mathbf{p}$ parameters.

In the case of interest here, the irreps building the Hamiltonian blocks are the Γ_6 , Γ_8 and Γ_7 of T_d , corresponding to the conduction, valence and split off bands respectively.

To exemplify the method, consider the H^{66} block of the Hamiltonian, containing all the possible coupling of the conduction bands states among themselves. The first

Block	Representations	Matrices
H^{66}	$\Gamma_6 \otimes \Gamma_6^* = \Gamma_1 + \Gamma_4$	$\Gamma_1 : 1_\sigma$ $\Gamma_4 : \sigma_x, \sigma_y, \sigma_z$

Table 5.2: Matrix basis set for the block of the Hamiltonian coupling the conduction band states to themselves (adapted from [15]). 1_σ is the 2×2 identity matrix, and the σ_i 's are the Pauli matrices.

Terms involving \mathbf{k} and \mathbf{H}
$\Gamma_1 : 1, k^2$
$\Gamma_3 : \sqrt{3} (k_z^2 - \frac{1}{3}k^2), k_x^2 - k_y^2$
$\Gamma_4 : [k_y, k_z] = eH_x/i\hbar c, [k_z, k_x] = eH_y/i\hbar c, [k_x, k_y] = eH_z/i\hbar c$
$\Gamma_5 : k_x, k_y, k_z; \{k_y k_z\}, \{k_z k_x\}, \{k_x k_y\}$
$\{k_y k_z\} \equiv \frac{1}{2} (k_y k_z + k_z k_y)$

Table 5.3: Irreducible components $\mathcal{K}_m^{\Gamma_i}$ of \mathcal{K} (adapted from [15]).

entry of Table II in Ref. [15] shows that the basis matrices of that block can only transform as Γ_1 and Γ_4 , and lists the explicit matrices (see Table 5.2). Therefore, only the combinations of the components of \mathbf{k} up to the desired (second) order transforming as Γ_1 and Γ_4 will play a role. These are shown in Table 5.3.

Now, by application of Eq. (5.7), the most general H^{66} compatible with the symmetry requirements can be constructed:

$$H^{66} = a_1 1_\sigma + a'_1 k^2 1_\sigma + a_4 \frac{e}{i\hbar c} (\sigma_x H_x + \sigma_y H_y + \sigma_z H_z), \quad (5.8)$$

where 1_σ is the 2×2 identity matrix, and the σ_i 's are the Pauli matrices. For clarity, the strain and mixed \mathbf{k} -strain terms are not shown. In order to find the value of the a_i parameters, one just needs to compare with the $\mathbf{k} \cdot \mathbf{p}$ perturbation results, and it can be seen that a_1 corresponds to the energy of the conduction band edge, a'_1 must be $\frac{\hbar^2}{2m}$ and a_4 must be $-g_s \frac{i\hbar^2}{4m}$, with g_s being the effective g factor.

For completeness, Appendix A reproduces the full 8-band $\mathbf{k} \cdot \mathbf{p}$ Hamiltonian from Ref. [15], which has been implemented to perform the bulk and heterostructure calculations. Note that, due to the way that it has been constructed, this Hamiltonian takes into account all the effects of the spin-orbit interaction in the matrix elements up to k^2 , and in particular the $s - p$ coupling responsible for the existence of spin

splitting in the conduction band. Strain and coupled strain/spin-orbit effects are also properly described by this method.

To minimize the probability of introducing hard-to-detect typos in the coded definition of the matrix elements, the Hamiltonian was first entered in Mathematica [20]. From there, the appropriate C code for each matrix element was generated automatically with the instruction `CForm`. This method also has the advantage that it allows the algebraic operation of the Hamiltonian to find analytical forms for the dispersion relation very near the zone center (cf. Sec. 5.3.3).

When implementing the Hamiltonian described in [15], one must be careful to note the following typos in appearing in that article. The matrix T_{xx} in Table I there must read

$$T_{xx} = \frac{1}{3\sqrt{2}} \begin{pmatrix} 0 & -1 & 0 & \sqrt{3} \\ -\sqrt{3} & 0 & 1 & 0 \end{pmatrix} \quad (5.9)$$

and the last equation in the group (A3) must also be corrected:

$$X_{12} = -i \left(X_2^{(2)} - X_{-2}^{(2)} \right) / 2. \quad (5.10)$$

There is another remark about a point that can lead to confusion. Koster *et al.* [21] have developed a set of tables for the Clebsch-Gordan coefficients for point groups that are very helpful when constructing explicit subspace-invariant matrices or when checking the symmetry properties of the Hamiltonian. However, in their Table 83 the values they show can be used as displayed for the O point group, but for T_d the values should be taken according to the lookup table shown in Table 8.3.

5.3.2 Parameters of the model

When implementing a $\mathbf{k} \cdot \mathbf{p}$ Hamiltonian, one of the most crucial tasks is obtaining a good set of parameters for the model. Unfortunately, this task is made harder because there are in the literature a number of models that vary in the number of bands considered and, even within the same number of basis states, with a different set of effects included [22, 23].

Parameter	Description
a	Lattice constant.
E_g	Energy gap.
E_v	Position of the valence band edge.
Δ_{SO}	Spin orbit splitting.
A'	Correction to the conduction effective mass due to the interaction with farther bands.
γ_1	First Kane parameter. Related to the effective mass of heavy and light holes.
γ_2	Second Kane parameter. Related to the effective mass of heavy and light holes.
γ_3	Third Kane parameter. Measures the warping—directional dependence of the effective mass—of the heavy and light hole bands.
κ	Related to the hole g -factor.
q	Related to the anisotropy of the hole g -factor respect to the direction of an applied uniaxial stress [24].
C	Linear splitting coefficient of the HH-LH bands due to the bulk inversion asymmetry. Measures the intra-valence band coupling due to the atomic electric field.
P	Momentum irreducible matrix element.
B	Measures momentum coupling of conduction and valence band via farther Γ_5 bands. Contributes to most of the k^3 splitting in the conduction band. Vanishes when the crystal possesses inversion symmetry.
C_1	Change in the conduction band edge due to hydrostatic strain.
D_d	Change in the valence band edge due to hydrostatic strain.
D_u	Related to the Bir-Pikus b deformation potential [19].
D'_u	Related to the Bir-Pikus d deformation potential [19].
C_2	Measures coupling of the conduction band to the valence band under shear stress.
C_4	Related to uniaxial strain- \mathbf{k} coupling.
C'_5	Related to shear strain- \mathbf{k} coupling.
C_{11}, C_{12}, C_{44}	Elastic moduli.

Table 5.4: Material parameters used in the $\mathbf{k} \cdot \mathbf{p}$ model and their description.

When taking a parameter set from the literature, one must make sure that parameters with the same name have the same meaning. The Luttinger parameters γ_L [16] are one example of this. The values of the 8-band Luttinger parameters, also known as Kane parameters, differ greatly from the more widely used 6-band Luttinger parameters. The γ_L shown in Table II in Lawaetz [22] are related to the γ 's in the current implementation (cf. Appendix A) by

$$\begin{aligned}\gamma_1 &= \gamma_{1L} - \frac{1}{3} \frac{E_P}{E_g} \\ \gamma_2 &= \gamma_{2L} - \frac{1}{6} \frac{E_P}{E_g} \\ \gamma_3 &= \gamma_{3L} - \frac{1}{6} \frac{E_P}{E_g} \\ \kappa &= \kappa_L - \frac{1}{3} \frac{E_P}{E_g},\end{aligned}\tag{5.11}$$

where E_g is the energy gap of the compound, and E_P has been defined as

$$E_P \equiv \frac{2m_e P^2}{\hbar^2},\tag{5.12}$$

where m_e is the free electron mass and P is the irreducible momentum matrix element.

A list of the parameters employed in the implementation of the Hamiltonian in Appendix A [15] and their meaning are shown in Table 5.4. Table 5.5 shows the numerical values used in the calculations for the parameters of a number of materials.

The effects of an applied magnetic field will not be considered in the calculations in this chapter. Therefore, the parameters κ and q will not be needed. Similarly, C_2 , C_4 and C'_5 will not be needed because they only appear when the material is under some sort of shear stress. When finding energy values for heterostructures in Secs. 5.5 and 5.6, they will be supposed to be grown along the [001] direction, hence introducing no shear stress. Finally, the effect of remote bands on the conduction effective mass will be neglected. This amounts to setting the A' parameter to zero.

Table 5.5: Parameter values for some materials.

Parameter	InSb	GaSb	AlSb	InAs	GaAs	AlAs	Al _{0.08} Ga _{0.92} As	Al _{0.12} Ga _{0.88} As
a (Å) ^a	6.4794	6.096	6.136	6.058	5.653	5.66	5.6539	5.6541
E_g (eV) ^b	0.235	0.813	2.219	0.356	1.52	3.002	1.639	1.633
E_v (eV) ^c	0	0.56	0.11	0	0	-0.55	-0.044	-0.055
Δ_{SO} (eV) ^b	0.803	0.8	0.75	0.41	0.341	0.279	0.336	0.335
γ_1^b	2.59	2.58	1.44	2.05	2.01	1.74	2	1.99
γ_2^b	-0.6	-0.58	-0.35	-0.44	-0.41	-0.37	-0.5	-0.53
γ_3^b	0.67	0.65	0.39	0.48	0.46	0.42	0.45	0.44
C (eV·Å) ^d	-9.32×10^{-3}	7.00×10^{-4}	0	-1.12×10^{-2}	-3.40×10^{-3}	2.00×10^{-3}	-2.97×10^{-3}	-2.86×10^{-3}
P (eV·Å) ^b	9.35	9.21	8.41	9.17	9.86	8.94	9.79	9.77
B (eV·Å ²) ^e	10.3	49.9	0	13.7 ^f	30.4	21.3 ^g	29.7	29.5
C_1 (eV) ^h	-6.17	-6.85	-6.97	-5.08	-7.17	-5.64	-7.05	-7.02
D_d (eV) ^h	0.36	0.79	1.38	1	1.16	2.47	1.26	1.29
D_u (eV) ^h	-3.1	-3	-2.1	-2.7	-2.6	-2.6	-2.6	-2.6
D'_u (eV) ^h	-4.3	-4.2	-3.7	-3.1	-3.9	-3.9	-3.9	-3.9
C_{11} (GPa) ^a	69.18	88.34	87.69	83.29	112.6	120.2	113.2	113.4
C_{12} (GPa) ^a	37.88	40.23	43.41	45.26	57.1	57	57.02	57.09
C_{44} (GPa) ^a	31.32	43.22	40.76	39.59	60	58.9	59.91	59.89

^aRef. [25].

^bRef. [22].

^cThe valence band offsets are consistent within the systems comprised of (InSb), (GaSb, AlSb, InAs) and (Al_xGa_{1-x}As).

^dRef. [9].

^eFrom γ_c obtained in Ref. [26].

^fFrom γ_c obtained in Ref. [11].

^gFrom γ_c obtained in Ref. [27].

^hAdapted from the Bir-Pikus deformation potentials a, b, d in Ref. [28].

5.3.3 Analytic expressions of the energy values near the zone center

Starting from the full Hamiltonian shown in Appendix A, analytical expressions for the bands near the zone center can be found. These are useful to find measurable quantities such as effective masses and intraband splittings as a function of the model parameters. These expressions can also be useful when relating the parameters of the model to the parameters used in other families of $\mathbf{k} \cdot \mathbf{p}$ Hamiltonians. Unstrained bulk material will be assumed in this section.

In order to obtain an analytic approximation to the energy dispersion relation, the 8-band Hamiltonian is first divided into two 4×4 blocks for the direction required. To achieve this decoupling, the Hamiltonian in Appendix A is expressed in a basis whose quantization axis has been selected according to Table 5.6. The matrix that transforms the Hamiltonian from a z quantization axis into an arbitrary θ, φ axis is

$$R(\theta, \varphi) = \begin{pmatrix} D^{1/2}(\theta, \varphi) & \mathbf{0} & \mathbf{0} \\ \mathbf{0} & D^{3/2}(\theta, \varphi) & \mathbf{0} \\ \mathbf{0} & \mathbf{0} & D^{1/2}(\theta, \varphi) \end{pmatrix} \quad (5.13)$$

where

$$D^{1/2}(\theta, \varphi) = \begin{pmatrix} e^{-\frac{i}{2}\varphi} \cos(\frac{\theta}{2}) & -e^{-\frac{i}{2}\varphi} \sin(\frac{\theta}{2}) \\ e^{\frac{i}{2}\varphi} \sin(\frac{\theta}{2}) & e^{\frac{i}{2}\varphi} \cos(\frac{\theta}{2}) \end{pmatrix} \quad (5.14)$$

and

$$D^{3/2}(\theta, \varphi) = \begin{pmatrix} \frac{\cos(\frac{\theta}{2})^3}{e^{\frac{3i}{2}\varphi}} & -\frac{\sqrt{3} \cos(\frac{\theta}{2})^2 \sin(\frac{\theta}{2})}{e^{\frac{3i}{2}\varphi}} & \frac{\sqrt{3} \cos(\frac{\theta}{2}) \sin(\frac{\theta}{2})^2}{e^{\frac{3i}{2}\varphi}} & -\frac{\sin(\frac{\theta}{2})^3}{e^{\frac{3i}{2}\varphi}} \\ \frac{\sqrt{3} \cos(\frac{\theta}{2})^2 \sin(\frac{\theta}{2})}{e^{\frac{i}{2}\varphi}} & \frac{\cos(\frac{\theta}{2}) + 3 \cos(\frac{3\theta}{2})}{4 e^{\frac{i}{2}\varphi}} & \frac{\sin(\frac{\theta}{2}) - 3 \sin(\frac{3\theta}{2})}{4 e^{\frac{i}{2}\varphi}} & \frac{\sqrt{3} \cos(\frac{\theta}{2}) \sin(\frac{\theta}{2})^2}{e^{\frac{i}{2}\varphi}} \\ \frac{\sqrt{3} \cos(\frac{\theta}{2}) \sin^2(\frac{\theta}{2})}{e^{-\frac{i}{2}\varphi}} & \frac{-e^{\frac{i}{2}\varphi} (\sin(\frac{\theta}{2}) - 3 \sin(\frac{3\theta}{2}))}{4} & \frac{e^{\frac{i}{2}\varphi} (\cos(\frac{\theta}{2}) + 3 \cos(\frac{3\theta}{2}))}{4} & -\frac{\sqrt{3} \cos(\frac{\theta}{2})^2 \sin(\frac{\theta}{2})}{e^{-\frac{i}{2}\varphi}} \\ e^{\frac{3i}{2}\varphi} \sin(\frac{\theta}{2})^3 & \sqrt{3} e^{\frac{3i}{2}\varphi} \cos(\frac{\theta}{2}) \sin(\frac{\theta}{2})^2 & \sqrt{3} e^{\frac{3i}{2}\varphi} \cos(\frac{\theta}{2})^2 \sin(\frac{\theta}{2}) & e^{\frac{3i}{2}\varphi} \cos(\frac{\theta}{2})^3 \end{pmatrix} \quad (5.15)$$

Direction in \mathbf{k} space	Notation for the line	Quantization axis
[001]	Δ	\hat{z}
[010]	Δ	\hat{y}
[100]	Δ	\hat{x}
[110]	Σ	$\hat{y} - \hat{x}$
[111]	Λ	$\hat{y} - \hat{x}$

Table 5.6: Quantization axis for the basis functions of the Hamiltonian.

After the Hamiltonian has been expressed in the basis with the new quantization axis, another change of basis consisting of a rearranging of the vectors is applied in order to leave it in its final block diagonal form. The basis states are reordered from the set $\{|\Gamma_6, +\frac{1}{2}\rangle, |\Gamma_6, -\frac{1}{2}\rangle, |\Gamma_8, +\frac{3}{2}\rangle, |\Gamma_8, +\frac{1}{2}\rangle, |\Gamma_8, -\frac{1}{2}\rangle, |\Gamma_8, -\frac{3}{2}\rangle, |\Gamma_7, +\frac{1}{2}\rangle, |\Gamma_7, -\frac{1}{2}\rangle\}$ into $\{|\Gamma_6, +\frac{1}{2}\rangle, |\Gamma_8, -\frac{3}{2}\rangle, |\Gamma_8, +\frac{1}{2}\rangle, |\Gamma_7, +\frac{1}{2}\rangle, |\Gamma_6, -\frac{1}{2}\rangle, |\Gamma_8, +\frac{3}{2}\rangle, |\Gamma_8, -\frac{1}{2}\rangle, |\Gamma_7, -\frac{1}{2}\rangle\}$ for the Δ directions, or $\{|\Gamma_6, +\frac{1}{2}\rangle, |\Gamma_8, +\frac{3}{2}\rangle, |\Gamma_8, -\frac{1}{2}\rangle, |\Gamma_7, -\frac{1}{2}\rangle, |\Gamma_6, -\frac{1}{2}\rangle, |\Gamma_8, -\frac{3}{2}\rangle, |\Gamma_8, +\frac{1}{2}\rangle, |\Gamma_7, +\frac{1}{2}\rangle\}$ for the Σ and Λ directions.

Taking one of the 4×4 blocks, the secular equation to obtain the eigenvalues would be a fourth degree polynomial. Instead, the standard procedure of taking the unperturbed energy for the bands that are not under consideration will require the solving of two first-degree equations—for the conduction and the split off bands—and one second-degree polynomial for the heavy and light hole bands to yield the approximate energies near the zone center.

Bands along the [100] direction

The energy dispersion relation for the conduction band (CB) along the [100] direction up to second order in \mathbf{k} is given by

$$E_{CB}(\mathbf{k}) = E_g + \frac{\hbar^2 k_x^2}{2m_e m_{CB}^*}, \quad (5.16)$$

where m_e is the free electron mass, m_{CB}^* is the conduction band effective mass, with a value of

$$\frac{1}{m_{CB}^*} = 1 + \frac{1}{3} \frac{E_P}{E_g} \frac{3E_g + 2\Delta_{SO}}{(E_g + \Delta_{SO})}, \quad (5.17)$$

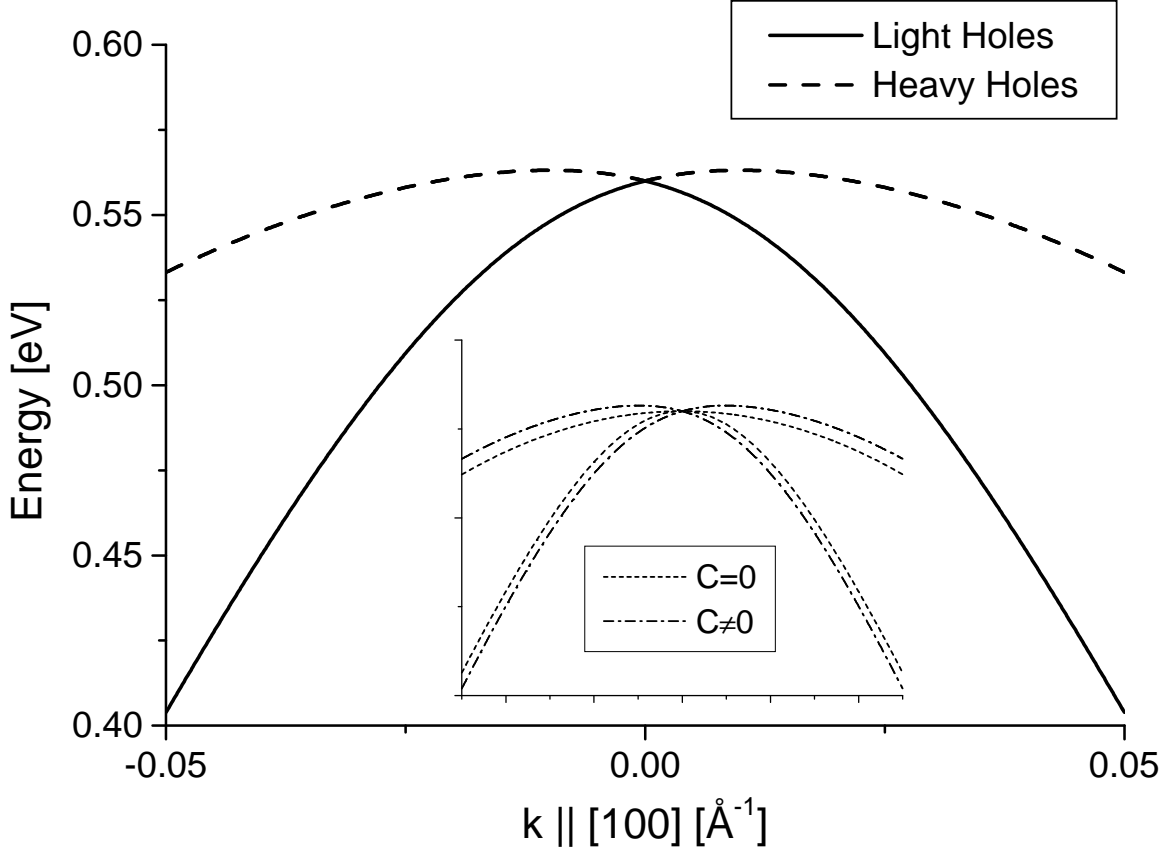


Figure 5.1: Linear splitting of the HH and LH bands along [100] near the zone center due to bulk induced asymmetry (BIA) effects. The inset compares the bands with BIA included $C \neq 0$ to the bands with BIA not included $C = 0$. The value of C has been artificially augmented 1,000-fold for $C \neq 0$.

where the symbols have the meaning listed in Table 5.4. This effective mass is isotropic—the same along any direction on \mathbf{k} space.

For the heavy hole (HH) band, the dispersion relation is

$$E_{HH}(\mathbf{k}) = Ck_x - \frac{(3E_g\gamma_1\hbar^2/m_e + 2P^2)k_x^2}{6E_g}, \quad (5.18)$$

while for the light hole (LH) band

$$E_{LH}(\mathbf{k}) = -Ck_x - \frac{(3E_g\gamma_1\hbar^2/m_e + 2P^2)k_x^2}{6E_g}. \quad (5.19)$$

These results indicate that, very close to the Γ point, the valence bands have a linear behavior. Also, the effective mass seems to be quite different from the usual

expressions [29, 30]. This can be reconciled with the conventional wisdom. The plot in Fig. 5.1 shows the numerical diagonalization of the HH and LH bands close to the Γ point for GaSb, except that the valence band splitting parameter C has been increased by a factor of 1,000 to show more clearly its effects. It is seen that very close to the zone center the HH and LH bands split linearly instead of quadratically, following the behavior described in Eqs. (5.18)-(5.19); and it is not until farther into the Brillouin zone that the bands recover the usual quadratic behavior. The inset in Fig. 5.1 compares these bands to the case where the splitting has been set to zero. It is seen that even with the inclusion of the bulk inversion asymmetry effects, the bands recover soon the shape of the $C = 0$ case. The only difference then is that the HH-LH separation is slightly bigger than predicted in the models not taking C into account.

Setting $C = 0$ in the analytical Hamiltonian and expanding it to second order yields the more usual expressions for the HH and LH effective masses

$$\begin{aligned}\frac{1}{m_{HH}^*} &= \gamma_1 - 2\gamma_2 \\ \frac{1}{m_{LH}^*} &= \gamma_1 + 2\gamma_2 + \frac{4}{3} \frac{E_P}{E_g},\end{aligned}\tag{5.20}$$

which have been expressed in terms of the Kane parameters. In terms of the Luttinger parameters (see Eq. (5.11)), they adopt the form

$$\begin{aligned}\frac{1}{m_{HH}^*} &= \gamma_{1L} - 2\gamma_{2L} \\ \frac{1}{m_{LH}^*} &= \gamma_{1L} + 2\gamma_{2L}.\end{aligned}\tag{5.21}$$

Finally, the spin-orbit split off (SO) band has the following dispersion relation

$$E_{SO}(\mathbf{k}) = -\Delta_{SO} - \frac{\hbar^2 k_x^2}{2m_e m_{SO}^*},\tag{5.22}$$

where m_{SO}^* is the split off band effective mass, with a value of

$$\frac{1}{m_{SO}^*} = \gamma_1 + \frac{2}{3} \frac{E_P}{(E_g + \Delta_{SO})}. \quad (5.23)$$

The effective mass for the SO band is also isotropic.

Note that the expressions of the effective masses of the CB and SO bands are not affected by the inclusion of BIA effects.

Bands along the [110] direction

Along the [110] direction, the energy of the electrons in the CB as a function of the wavevector \mathbf{k} is, up to third order,

$$E_{CB}(\mathbf{k}) = E_g + \frac{\hbar^2 k^2}{2m_e m_{CB}^*} \pm \frac{1}{2} \gamma_c k^3, \quad (5.24)$$

with m_{CB}^* given by Eq. (5.17), and the k^3 splitting coefficient (see Eq. (5.4)) in terms of the model parameters given by

$$\gamma_c = \frac{P}{3} \frac{2BE_g \Delta_{SO} - \sqrt{3}CP(E_g + \Delta_{SO})}{E_g^2 (E_g + \Delta_{SO})}. \quad (5.25)$$

It is easy to show that the contribution to γ_c of the part containing C is only about 4% for InSb and InAs. That contribution goes down to about 0.3% for GaAs and AlAs, and it drops to a mere 0.03% for GaSb. Therefore, it is a good approximation to consider that all the splitting in the conduction band is due to the nonvanishing bulk inversion parameter B , which has its source in the momentum coupling of the conduction and valence bands via remote Γ_5 states [15].

Note that, in order to turn off BIA effects, both parameters B and C need to be set to zero.

As in the [100] case, the inclusion of $C \neq 0$ changes the characteristics of the bands very close to the Γ point respect to the more common assumption of $C = 0$. In particular, it provides them with a small linear component. But, in opposition to the [100] case, here the HH and LH bands are not doubly degenerate. The LH1–

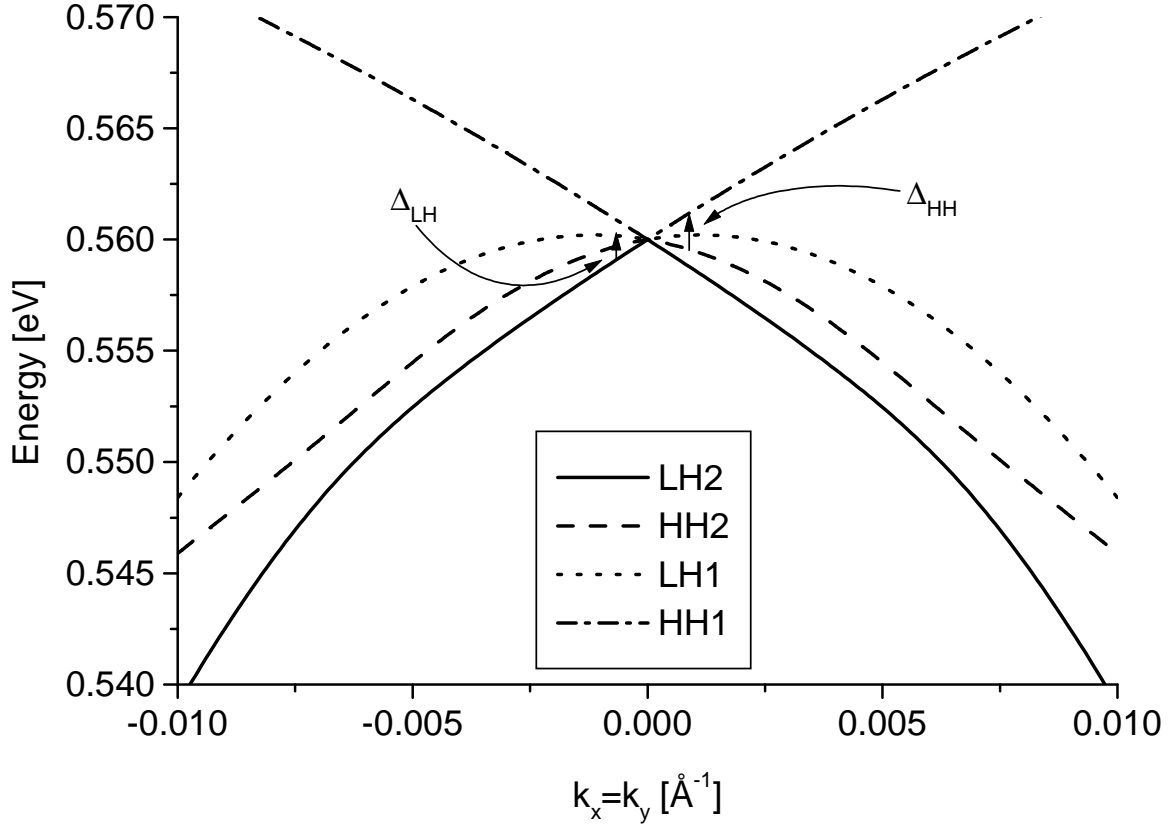


Figure 5.2: Linear splitting of the HH and LH bands along [110] near the zone center. The value of the parameter C has been artificially augmented 1,000-fold.

LH2 and HH1–HH2—the number indicating subbands—linear splittings (Δ_{LH} [110] and Δ_{HH} [110] respectively) turn out to be the same for both HH and LH bands (see Fig. 5.2), and are given by

$$\Delta_{HH} [110] = \Delta_{LH} [110] = \sqrt{3}Ck. \quad (5.26)$$

This result is slightly different from the one indicated in Ref. [9] in their Eq. (7.5). A numerical diagonalization of the Hamiltonian has been performed to check the validity of Eq. (5.26). The discrepancy arises because the splittings in Ref. [9] are valid in the region where the quadratic (effective mass) splitting predominates, while the result obtained here is valid in the region where the linear splitting dominates.

In the materials studied, one needs not go far from Γ to enter a regime where the bands basically behave according to the standard behavior, described by the effective

masses

$$\frac{1}{m_{HH}^*} = \gamma_{1L} - \sqrt{\gamma_{2L}^2 + 3\gamma_{3L}^2} \quad (5.27)$$

$$\frac{1}{m_{LH}^*} = \gamma_{1L} + \sqrt{\gamma_{2L}^2 + 3\gamma_{3L}^2}, \quad (5.28)$$

which agree with the expressions in Ref. [30]. In this regime, there is some LH and HH splitting proportional to k^3 due to the effect of B :

$$\delta_{HH [110]} = \frac{BP}{3E_g} \frac{\gamma_{2L} - 3\gamma_{3L} + \sqrt{\gamma_{2L}^2 + 3\gamma_{3L}^2}}{\sqrt{\gamma_{2L}^2 + 3\gamma_{3L}^2}} k^3 \quad (5.29)$$

$$\delta_{LH [110]} = \frac{BP}{3E_g} \frac{3\gamma_{3L} - \gamma_{2L} + \sqrt{\gamma_{2L}^2 + 3\gamma_{3L}^2}}{\sqrt{\gamma_{2L}^2 + 3\gamma_{3L}^2}} k^3. \quad (5.30)$$

Note that the k^3 splitting in the heavy hole band is a good indicator of the anisotropy of the hole effective masses, because it should vanish for a material with isotropic hole effective masses ($\gamma_{2L} = \gamma_{3L}$).

The SO band also presents k^3 splitting $\Delta_{SO [110]}$, proportional to the B parameter only:

$$\Delta_{SO [110]} = \frac{2BP}{3(E_g + \Delta_{SO})} k^3. \quad (5.31)$$

Bands along the [111] direction

Along this direction, in the region where the linear splitting dominates, the heavy hole (HH) band has the dispersion relation

$$E_{HH}(\mathbf{k}) = \pm\sqrt{2}Ck_x - \frac{\hbar^2 k^2}{2m_e} (\gamma_{1L} - 2\gamma_{3L}) + O(k^4), \quad (5.32)$$

while for the light holes

$$E_{LH}(\mathbf{k}) = -\frac{\hbar^2 k^2}{2m_e} (\gamma_{1L} + 2\gamma_{3L}) + O(k^4), \quad (5.33)$$

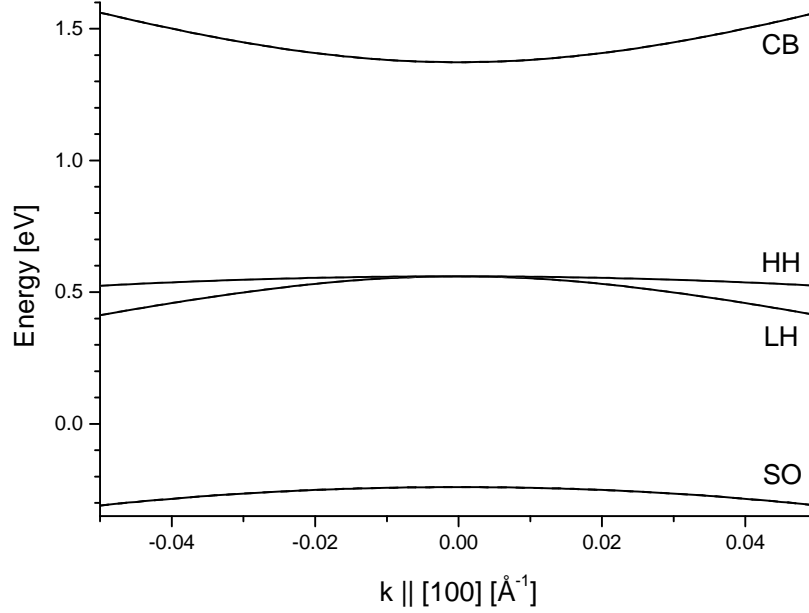


Figure 5.3: Band structure for GaSb near Γ along $[100]$.

from which

$$\frac{1}{m_{HH}^*} = \gamma_{1L} - 2\gamma_{3L} \quad (5.34)$$

$$\frac{1}{m_{LH}^*} = \gamma_{1L} + 2\gamma_{3L}. \quad (5.35)$$

The light hole, conduction and split-off bands are degenerate along the $[111]$ direction, as can also be deduced by group theory arguments [10]. The heavy hole band shows a linear splitting near the zone center.

5.3.4 Numerical calculation of the energy bands

In the preceding section, it was assumed that the \mathbf{k} point under consideration was close enough to the zone center that the analytic expressions derived were valid. In this section, \mathbf{k} will still be supposed to be within the range of validity of the $\mathbf{k} \cdot \mathbf{p}$ theory, but farther out into the Brillouin zone, so that the analytical expressions lose their validity. In this section the $\mathbf{k} \cdot \mathbf{p}$ Hamiltonian will be diagonalized numerically, giving special attention to the spin behavior of the conduction band states.

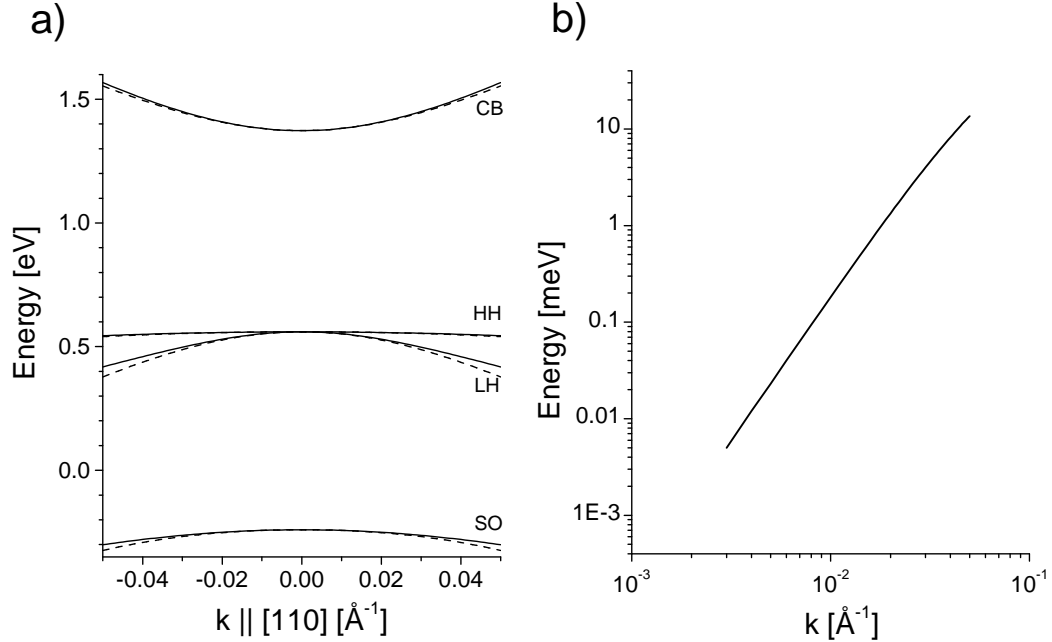


Figure 5.4: Band structure for GaSb near Γ along [110] and spin splitting of the conduction band.

Bands along the [100] direction

Figure 5.3 shows the band structure of bulk GaSb along the [100] direction. In accordance with the group symmetry requirements, the bands are spin degenerate for finite \mathbf{k} 's.

Bands along the [110] direction and k^3 splitting

Figure 5.4.a) shows the band structure of bulk GaSb along the [110] direction. For this direction, all bands are spin split except at the Γ point due to the bulk inversion asymmetry (BIA) effects. Plot (b) shows the energy splitting of the CB states as a function of k in a loglog graph. Close to the zone center, the splitting in the conduction band follows a power law, with exponent 3. This is in agreement with the results derived in Eq. (5.24).

This so-called k^3 splitting [10] can also be predicted by the methods described in Sec. 5.3.1. Going up to order 3 in the combinations of components of \mathbf{k} and constructing an invariant 2-band Hamiltonian for the conduction band, it is found

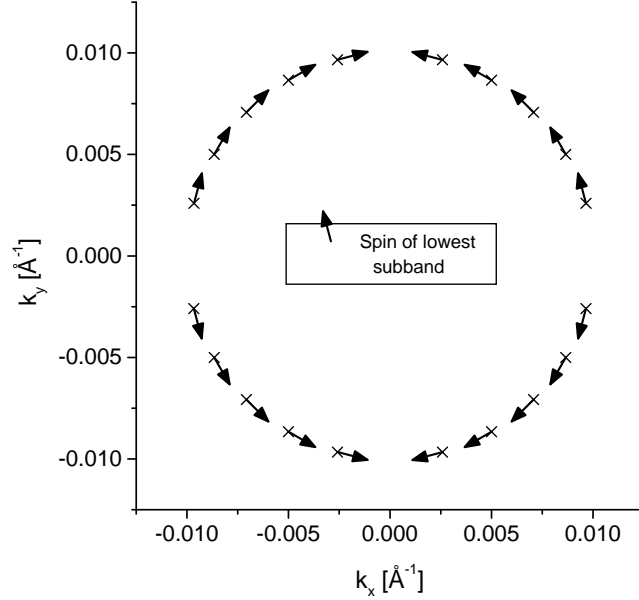


Figure 5.5: Direction for the spin of the spin-split states of the lowest conduction subband of GaSb. This plot sweeps a circular path in \mathbf{k} space with $k_z = 0$. No spin direction is specified for the $\langle 100 \rangle$ family because the states are spin degenerate.

that the Hamiltonian will include the following term breaking the spin degeneracy [11]:

$$H_{k^3} = \gamma_c [\sigma_x k_x (k_y^2 - k_z^2) + \text{cyclic permutations}]. \quad (5.36)$$

The fact that effects of order k^3 are being studied with a Hamiltonian with terms of order up to k^2 might lead to some inaccuracies. A future study might deal with the effect of these higher-order terms in the CB spin splitting. Since the main contribution to γ_c comes from the parameter B , describing the coupling of the CB and the LH band via remote states, one might expect that the third order terms in the 8-band Hamiltonian block H_{cc} would have a contribution of about $\frac{E_{\Gamma_{8c}-\Gamma_{6c}}}{E_g}$ smaller than B , where $E_{\Gamma_{8c}-\Gamma_{6c}}$ is the distance in energy from the CB to the closest, non valence band, Γ_8 band, which normally lies above the conduction band. For GaAs, $\frac{E_{\Gamma_{8c}-\Gamma_{6c}}}{E_g}$ is about 2. Basically, this would not have a big effect on the band structure calculations, but it would affect substantially the values of the calculated matrix elements.

The two-band Hamiltonian in Eq. (5.36) also predicts the direction where the split spins will be pointing. For example, it is easily seen from the previous equation that if

$\mathbf{k} = (1, \delta, 0)$, with δ a positive infinitesimal, the spin will point along the $\pm y$ direction. Similarly, symmetry requires the spin to point along $(-1, 1, 0)$ or $(1, -1, 0)$ for \mathbf{k} along the $[110]$ direction. This is indeed obtained in the numerical diagonalization of the Hamiltonian including the BIA effects, as seen in Fig. 5.5. That figure shows a circular sweep in \mathbf{k} space with $k_z = 0$. The arrows represent the direction towards which the spin of the lowest conduction subband states is pointing. The horizontal axis represents k_x , while the vertical axis indicates the k_y component of the state. The states belonging to the $\langle 100 \rangle$ directions are spin degenerate; therefore, no spin direction is given for them in Fig. 5.5.

The expectation value of the spin is calculated using the following spin operator, given in the $\{|\Gamma_6, +\frac{1}{2}\rangle, |\Gamma_6, -\frac{1}{2}\rangle, |\Gamma_8, +\frac{3}{2}\rangle, |\Gamma_8, +\frac{1}{2}\rangle, |\Gamma_8, -\frac{1}{2}\rangle, |\Gamma_8, -\frac{3}{2}\rangle, |\Gamma_7, +\frac{1}{2}\rangle, |\Gamma_7, -\frac{1}{2}\rangle\}$ basis:

$$S_x = \frac{\hbar}{2} \begin{pmatrix} 0 & 1 & 0 & 0 & 0 & 0 & 0 & 0 \\ 1 & 0 & 0 & 0 & 0 & 0 & 0 & 0 \\ 0 & 0 & 0 & \frac{1}{\sqrt{3}} & 0 & 0 & \sqrt{\frac{2}{3}} & 0 \\ 0 & 0 & \frac{1}{\sqrt{3}} & 0 & \frac{2}{3} & 0 & 0 & \frac{\sqrt{2}}{3} \\ 0 & 0 & 0 & \frac{2}{3} & 0 & \frac{1}{\sqrt{3}} & -\frac{\sqrt{2}}{3} & 0 \\ 0 & 0 & 0 & 0 & \frac{1}{\sqrt{3}} & 0 & 0 & -\sqrt{\frac{2}{3}} \\ 0 & 0 & \sqrt{\frac{2}{3}} & 0 & -\frac{\sqrt{2}}{3} & 0 & 0 & -(\frac{1}{3}) \\ 0 & 0 & 0 & \frac{\sqrt{2}}{3} & 0 & -\sqrt{\frac{2}{3}} & -(\frac{1}{3}) & 0 \end{pmatrix} \quad (5.37)$$

$$S_y = \frac{\hbar}{2} \begin{pmatrix} 0 & -1 & 0 & 0 & 0 & 0 & 0 & 0 \\ 1 & 0 & 0 & 0 & 0 & 0 & 0 & 0 \\ 0 & 0 & 0 & -(\frac{1}{\sqrt{3}}) & 0 & 0 & -\sqrt{\frac{2}{3}} & 0 \\ 0 & 0 & \frac{1}{\sqrt{3}} & 0 & -(\frac{2}{3}) & 0 & 0 & -\frac{\sqrt{2}}{3} \\ 0 & 0 & 0 & \frac{2}{3} & 0 & -(\frac{1}{\sqrt{3}}) & -\frac{\sqrt{2}}{3} & 0 \\ 0 & 0 & 0 & 0 & \frac{1}{\sqrt{3}} & 0 & 0 & -\sqrt{\frac{2}{3}} \\ 0 & 0 & \sqrt{\frac{2}{3}} & 0 & \frac{\sqrt{2}}{3} & 0 & 0 & \frac{1}{3} \\ 0 & 0 & 0 & \frac{\sqrt{2}}{3} & 0 & \sqrt{\frac{2}{3}} & -(\frac{1}{3}) & 0 \end{pmatrix} \quad (5.38)$$

$$S_z = \frac{\hbar}{2} \begin{pmatrix} 1 & 0 & 0 & 0 & 0 & 0 & 0 & 0 \\ 0 & -1 & 0 & 0 & 0 & 0 & 0 & 0 \\ 0 & 0 & 1 & 0 & 0 & 0 & 0 & 0 \\ 0 & 0 & 0 & \frac{1}{3} & 0 & 0 & -\frac{2\sqrt{2}}{3} & 0 \\ 0 & 0 & 0 & 0 & -(\frac{1}{3}) & 0 & 0 & -\frac{2\sqrt{2}}{3} \\ 0 & 0 & 0 & 0 & 0 & -1 & 0 & 0 \\ 0 & 0 & 0 & -\frac{2\sqrt{2}}{3} & 0 & 0 & -(\frac{1}{3}) & 0 \\ 0 & 0 & 0 & 0 & -\frac{2\sqrt{2}}{3} & 0 & 0 & \frac{1}{3} \end{pmatrix}. \quad (5.39)$$

The amount of spin splitting in bulk materials is highly anisotropic. The polar plot in Fig. 5.6 shows the splitting as a function of angle for a circular sweep in \mathbf{k} space with $k_z = 0$ and $k_{\parallel} = 0.01 \text{ \AA}^{-1}$. In that plot, an angle of 0° corresponds to an

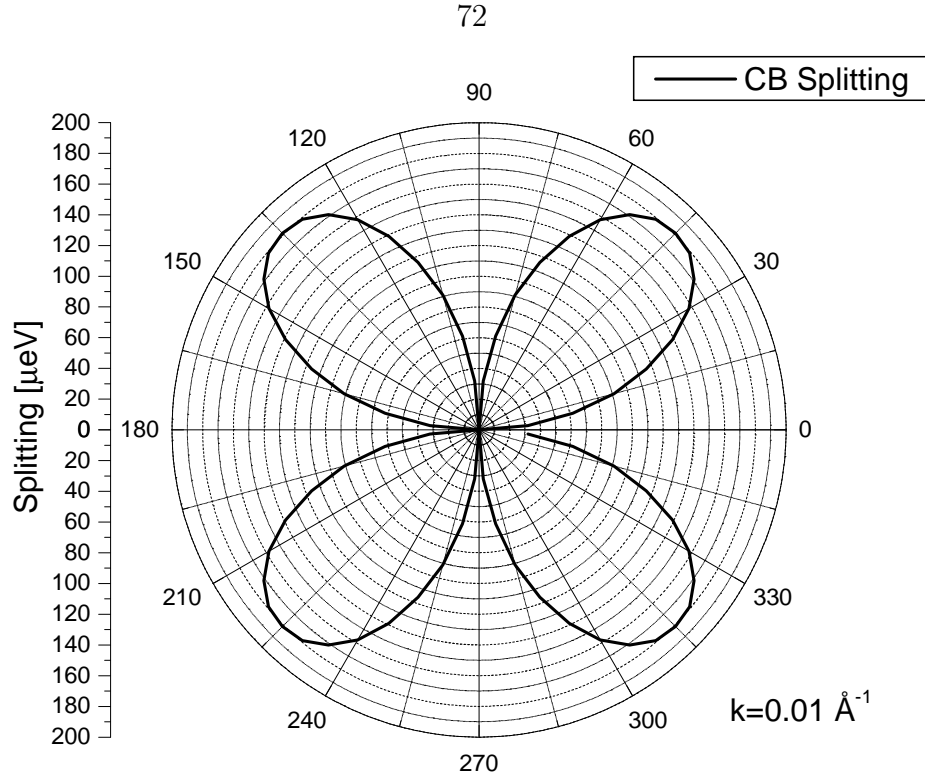


Figure 5.6: Spin splitting in the CB for an electron with $k_{\parallel} = 0.01 \text{ \AA}^{-1}$ and traveling in the plane $k_x - k_y$.

electron traveling with positive k_x only, an angle of 90° corresponds to an electron traveling with positive k_y only, and the rest taking the usual meaning. The amount of splitting is given by the axis on the left or, equivalently, by the distance of the plot line to the center.

5.4 Eight-band effective mass theory for superlattices and quantum wells

In this section the method used to find the band structure and eigenstates for superlattices and quantum wells is shown. Following the effective mass approximation (EMA) theory [13], the 8 band $\mathbf{k} \cdot \mathbf{p}$ Hamiltonian of Eq. (A.1) is transformed into a set of eight linear, second-order, ordinary differential equations. The appropriate boundary conditions are enforced and the equations are solved by means of a finite difference scheme.

5.4.1 EMA Hamiltonian

In the effective mass approximation (EMA) [12], the bulk Hamiltonian H_0 is modified by some gentle—changing little in a lattice constant—potential $U(\mathbf{r})$. Then, the wavefunction of the structure under study is written as

$$\Psi_{\mathbf{k}_{\parallel}}(\mathbf{r}) = \sum_n e^{i\mathbf{k}_{\parallel} \cdot \mathbf{r}} F_n(z) u_{n0}(\mathbf{r}), \quad (5.40)$$

where $\mathbf{k}_{\parallel} = k_x \hat{x} + k_y \hat{y}$ is the electron wavevector in the $k_x - k_y$ plane, u_{n0} is the Bloch wavefunction at the zone center, the $F_n(z)$'s are the envelope function components, a set of supposedly slow varying functions that take all the effect of $U(z)$; and it has been assumed that the translational bulk symmetry is broken along the z axis only (*i.e.*, the superlattice or quantum well has been grown along the [001] direction). Burt has developed a rigorous effective mass theory [31], which has the Luttinger theory as a limiting case and explains the success of the latter in treating structures with abrupt interfaces. The simpler Luttinger approximation will be used throughout this study.

It has been shown [12, 13] that the equation

$$[H_0(\mathbf{k}_{\parallel}, k_z; z) + U(z)] \Psi_{\mathbf{k}_{\parallel}}(\mathbf{r}) = E \Psi_{\mathbf{k}_{\parallel}}(\mathbf{r}), \quad (5.41)$$

with $H_0(\mathbf{k}_{\parallel}, k_z; z)$ being the bulk Hamiltonian with an allowance for a change of material as a function of z , can be written in what is the key equation of the effective mass approximation:

$$[H_0(\mathbf{k}_{\parallel}, -i\partial_z; z) + U(z)] \mathbf{F}(z) = E \mathbf{F}(z), \quad (5.42)$$

where $\mathbf{F}(z)$ is a multicomponent vector constructed from the different $F_n(z)$'s. In an 8-band theory, \mathbf{F} would have 8 components, each one multiplying the conduction band (CB), heavy hole (HH), light hole (LH) and split off (SO) basis states.

On the other hand, the bulk $\mathbf{k} \cdot \mathbf{p}$ Hamiltonian can be expanded into its polynomial

form for k_z in the following manner:

$$\mathbf{H}_0(\mathbf{k}) = \mathbf{H}^{(2)} k_z^2 + \mathbf{H}^{(1)}(\mathbf{k}_{\parallel}) k_z + \mathbf{H}^{(0)}(\mathbf{k}_{\parallel}). \quad (5.43)$$

Putting together Eq. (5.42) and Eq. (5.43), a system of eight coupled differential equations results:

$$[-\mathbf{H}^{(2)} \partial_z^2 - i\mathbf{H}^{(1)}(\mathbf{k}_{\parallel}) \partial_z + \mathbf{H}^{(0)}(\mathbf{k}_{\parallel}) + U(z)] \mathbf{F}(z) = E \mathbf{F}(z). \quad (5.44)$$

This is the system of equations that must be solved to obtain the energies and eigenstates of the system.

5.4.2 The finite difference method

There are several methods to solve numerically the system of coupled ordinary differential equations given by Eq. (5.44), such as the transfer-matrix method [32, 33], the finite element method [34], the basis expansion method [35]. In this study, the finite difference method (FDM) has been employed because of its conceptual simplicity, its ability to describe tunneling phenomena with only a few changes (see Sec. 7) and its numerical stability respect to the transfer-matrix method, which requires the truncation of growing exponential states [36].

In the finite difference method, the differential operators are first written in a Hermitian form and then substituted by their finite difference approximations over a discrete mesh (see Fig. 5.7) with N points. Following Chuang and Chang [37], the following discretization scheme is used:

$$\begin{aligned} \mathbf{H}^{(2)}(z) \partial_z^2 f|_{z_i} \rightarrow \partial_z (\mathbf{H}^{(2)}(z) \partial_z f)|_{z_i} \approx & \frac{\mathbf{H}^{(2)}(z_{i+1}) + \mathbf{H}^{(2)}(z_i)}{2(\Delta z)^2} f(z_{i+1}) - \\ & \frac{\mathbf{H}^{(2)}(z_{i+1}) + 2\mathbf{H}^{(2)}(z_i) + \mathbf{H}^{(2)}(z_{i-1})}{2(\Delta z)^2} f(z_i) + \frac{\mathbf{H}^{(2)}(z_{i-1}) + \mathbf{H}^{(2)}(z_i)}{2(\Delta z)^2} f(z_{i-1}) \end{aligned} \quad (5.45)$$

$N_1/N_2/N_3$ Quantum Well or Superlattice

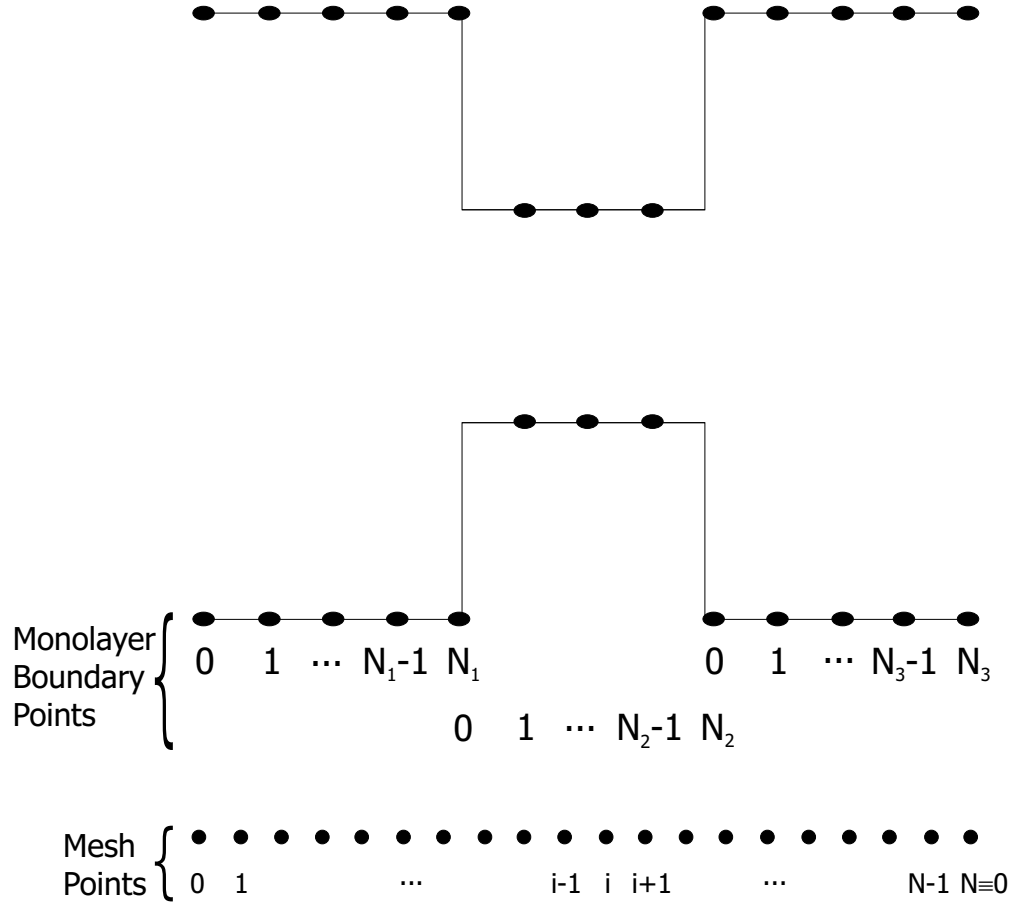


Figure 5.7: Schematic of the structure under study, with points separating the monolayers, and mesh used when solving the effective mass approximation equations. The mesh points need not coincide with the monolayer boundaries.

$$\begin{aligned}
 -i\mathbf{H}^{(1)}(z) \partial_z f \Big|_{z_i} &\rightarrow \frac{-i}{2} [\mathbf{H}^{(1)}(z) \partial_z f + \partial_z \mathbf{H}^{(1)}(z) f] \Big|_{z_i} \approx \\
 &-i \frac{\mathbf{H}^{(1)}(z_{i+1}) + \mathbf{H}^{(1)}(z_i)}{4\Delta z} f(z_{i+1}) + i \frac{\mathbf{H}^{(1)}(z_{i-1}) + \mathbf{H}^{(1)}(z_i)}{4\Delta z} f(z_{i-1}), \quad (5.46)
 \end{aligned}$$

where Δz is the separation between the mesh points, and z_i is the position of the i -th mesh point.

Now, the application of the above equations to Eq. (5.44) yields the following system of N algebraic equations:

$$\mathbf{H}_{i,i-1} \mathbf{F}_{i-1} + \mathbf{H}_{i,i} \mathbf{F}_i + \mathbf{H}_{i,i+1} \mathbf{F}_{i+1} = E \mathbf{F}_i \quad (5.47)$$

where \mathbf{F}_i is the eight-vector containing the envelope function components corresponding to the i -th mesh point. This eigenproblem can be written in matrix form to better appreciate its sparse structure:

$$\begin{pmatrix} \mathbf{H}_{0,0} & \mathbf{H}_{0,1} & \mathbf{0} & \dots & \dots & \dots & \mathbf{H}_{0,-1} \\ \mathbf{H}_{1,0} & \mathbf{H}_{1,1} & \mathbf{H}_{1,2} & \mathbf{0} & \dots & \dots & \mathbf{0} \\ \mathbf{0} & \mathbf{H}_{2,1} & \mathbf{H}_{2,2} & \mathbf{H}_{2,3} & \mathbf{0} & \dots & \mathbf{0} \\ \vdots & \dots & \ddots & \ddots & \ddots & \vdots & \vdots \\ \mathbf{0} & \dots & \dots & \mathbf{0} & \mathbf{H}_{N-2,N-3} & \mathbf{H}_{N-2,N-2} & \mathbf{H}_{N-2,N-1} \\ \mathbf{H}_{N-1,N} & \mathbf{0} & \dots & \dots & \mathbf{0} & \mathbf{H}_{N-1,N-2} & \mathbf{H}_{N-1,N-1} \end{pmatrix} \mathbf{F} = E \mathbf{F}, \quad (5.48)$$

where \mathbf{F} is a column vector composed of the different \mathbf{F}_i 's.

The discretized Hamiltonian matrices when inside only one material are given by:

$$\mathbf{H}_{i,i} = \frac{2\mathbf{H}^{(2)}}{(\Delta z)^2} + \mathbf{H}^{(0)} + U_i \quad (5.49)$$

$$\mathbf{H}_{i,i+1} = -\frac{\mathbf{H}^{(2)}}{(\Delta z)^2} - i\frac{\mathbf{H}^{(1)}}{2\Delta z} \quad (5.50)$$

$$\mathbf{H}_{i,i-1} = -\frac{\mathbf{H}^{(2)}}{(\Delta z)^2} + i\frac{\mathbf{H}^{(1)}}{2\Delta z} = \mathbf{H}_{i,i+1}^\dagger. \quad (5.51)$$

Note that the above discretization scheme treats with equal footing the inner and interface mesh points. Therefore, the general expression for the discretized 8×8 Hamiltonian matrices can be used without modification when dealing with interface mesh points:

$$\mathbf{H}_{i,i} = \frac{\mathbf{H}_{i+1}^{(2)} + 2\mathbf{H}_i^{(2)} + \mathbf{H}_{i-1}^{(2)}}{2(\Delta z)^2} + \mathbf{H}_i^{(0)} + U_i \quad (5.52)$$

$$\mathbf{H}_{i,i+1} = -\frac{\mathbf{H}_{i+1}^{(2)} + \mathbf{H}_i^{(2)}}{2(\Delta z)^2} - i\frac{\mathbf{H}_{i+1}^{(1)} + \mathbf{H}_i^{(1)}}{4\Delta z} \quad (5.53)$$

$$\mathbf{H}_{i,i-1} = -\frac{\mathbf{H}_{i-1}^{(2)} + \mathbf{H}_i^{(2)}}{2(\Delta z)^2} + i\frac{\mathbf{H}_{i-1}^{(1)} + \mathbf{H}_i^{(1)}}{4\Delta z}. \quad (5.54)$$

$\mathbf{H}_{0,-1}$ and $\mathbf{H}_{N-1,N}$ in Eq. (5.48) express the boundary conditions (BCs) of the problem. When studying a quantum well, the BCs are that the wavefunction must

vanish far from the well region. This is accomplished by setting the barrier region wide enough, and requesting

$$\mathbf{F}_{-1} = \mathbf{F}_N = 0, \quad (5.55)$$

which translates into

$$\mathbf{H}_{0,-1} = \mathbf{H}_{N-1,N} = \mathbf{0}. \quad (5.56)$$

When finding the energies and states of a superlattice, the Bloch BCs apply, and the envelope function is requested to have the supercell periodicity d , modulated by a phase:

$$\mathbf{F}_N = e^{iqd}\mathbf{F}_0 \quad \Rightarrow \quad \mathbf{H}_{N-1,N} = e^{iqd}\mathbf{H}_{N-2,N-1} \quad (5.57)$$

$$\mathbf{F}_{-1} = e^{-iqd}\mathbf{F}_{N-1} \quad \Rightarrow \quad \mathbf{H}_{0,-1} = e^{-iqd}\mathbf{H}_{1,0}, \quad (5.58)$$

where q is the electron wavevector along the z direction, and it has been assumed that the same material is at mesh points 0 and $N - 1$.

5.4.3 Interface conditions and hermiticity in the FDM

The hermiticity of the discretized Hamiltonian operator in Eq. (5.48) is ensured if $\mathbf{H}_{i,i+1}^\dagger = \mathbf{H}_{i+1,i}$. Since the $\mathbf{H}^{(j)}$'s are themselves Hermitian, an inspection of Eqs. (5.52)-(5.54) shows that this is indeed the case. It is also clearly seen that the introduction of the BCs as defined in the previous section doesn't affect the hermiticity of the Hamiltonian.

There exist in the literature several proposals on what are the correct quantities to match at the interface between two materials [29, 37–39]. Most of them require the continuity of the envelope function and a quantity that has the general form:

$$[\mathbf{A}\partial_z + \mathbf{B}]\mathbf{F}, \quad (5.59)$$

where \mathbf{A} and \mathbf{B} take different values depending on the author. Using the finite difference formulae Eqs. (5.45)-(5.46), the continuity of Eq. (5.59) can be written in

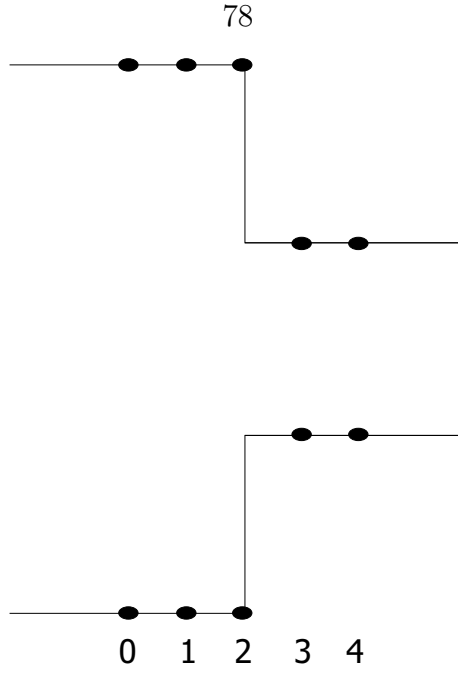


Figure 5.8: Mesh used in the study of interface boundary conditions.

a form similar to Eq. (5.47):

$$\mathbf{H}_{2,1}\mathbf{F}_1 + \mathbf{H}_{2,2}\mathbf{F}_2 + \mathbf{H}_{2,3}\mathbf{F}_3 = 0, \quad (5.60)$$

where the $\mathbf{H}_{i,j}$ take the appropriate values and the subindexes i, j are referred to the mesh points in Fig. 5.8. Isolating \mathbf{F}_2 from Eq. (5.60) and plugging it into the corresponding equations for the \mathbf{F}_i 's, one obtains

$$\mathbf{H}_{1,0}\mathbf{F}_0 + (\mathbf{H}_{1,1} - \mathbf{H}_{1,2}\mathbf{H}_{2,2}^{-1}\mathbf{H}_{2,1})\mathbf{F}_1 - \mathbf{H}_{1,2}\mathbf{H}_{2,2}^{-1}\mathbf{H}_{2,3}\mathbf{F}_3 = E\mathbf{F}_1 \quad (5.61)$$

$$-\mathbf{H}_{3,2}\mathbf{H}_{2,2}^{-1}\mathbf{H}_{2,1}\mathbf{F}_1 + (\mathbf{H}_{3,3} - \mathbf{H}_{3,2}\mathbf{H}_{2,2}^{-1}\mathbf{H}_{2,3})\mathbf{F}_3 + \mathbf{H}_{3,4}\mathbf{F}_4 = E\mathbf{F}_4. \quad (5.62)$$

Now, in order to preserve the hermiticity of the discretized Hamiltonian, one should have

$$(\mathbf{H}_{1,2}\mathbf{H}_{2,2}^{-1}\mathbf{H}_{2,3})^\dagger = \mathbf{H}_{3,2}\mathbf{H}_{2,2}^{-1}\mathbf{H}_{2,1} \quad (5.63)$$

or, equivalently

$$\mathbf{H}_{2,3}^\dagger = \mathbf{H}_{3,2} \quad \mathbf{H}_{2,1}^\dagger = \mathbf{H}_{1,2}. \quad (5.64)$$

However, the requirements in Eq. (5.64) are not satisfied by the discretized version

of the interface conditions. From this it must be concluded that the enforcement of interface boundary conditions of the form (5.59) is not possible if the hermiticity of the Hamiltonian is to be preserved.

5.5 Bulk inversion asymmetry effects on symmetric quantum wells

In this section, the methods outlined in Sec. 5.4 will be used to calculate the electronic properties of a symmetric quantum well. In particular, focus will fall on AlSb/GaSb/AlSb quantum wells. However, some of the results derived are a consequence of the underlying symmetry of the structure rather than the constituents themselves. Therefore, these particular results will illustrate general considerations about symmetric quantum wells.

In Sec. 5.5.1, the underlying symmetry of the discretized Hamiltonian is identified, and its requirements on the energies and states of the well are listed. In Sec. 5.5.2, the band structure and eigenstates of symmetric quantum wells (SQWs) *without* bulk inversion asymmetry (BIA) terms will be studied, taking an AlSb/GaSb/AlSb QW as a paradigm. Finally, in Sec. 5.5.3, the assumption of negligible BIA effects is relaxed, the resulting energies and states are computed and the differences respect to the case with higher symmetry are highlighted.

5.5.1 Symmetry group of the discretized Hamiltonian

This section deals with symmetric quantum wells, but the word “symmetric” needs a more precise definition. Here, “symmetric” will be taken to mean that the sequence of materials and their respective thicknesses are left unchanged under the inversion operation (*i.e.*, they are macroscopically symmetric). Thus, an AlSb/InAs/AlSb quantum well (QW) is called symmetric, while an AlSb/InAs/GaSb/AlSb QW is called asymmetric. This definition is made in order to avoid confusion with the microscopic symmetry, that is, the symmetry group, of the QW. All asymmetric

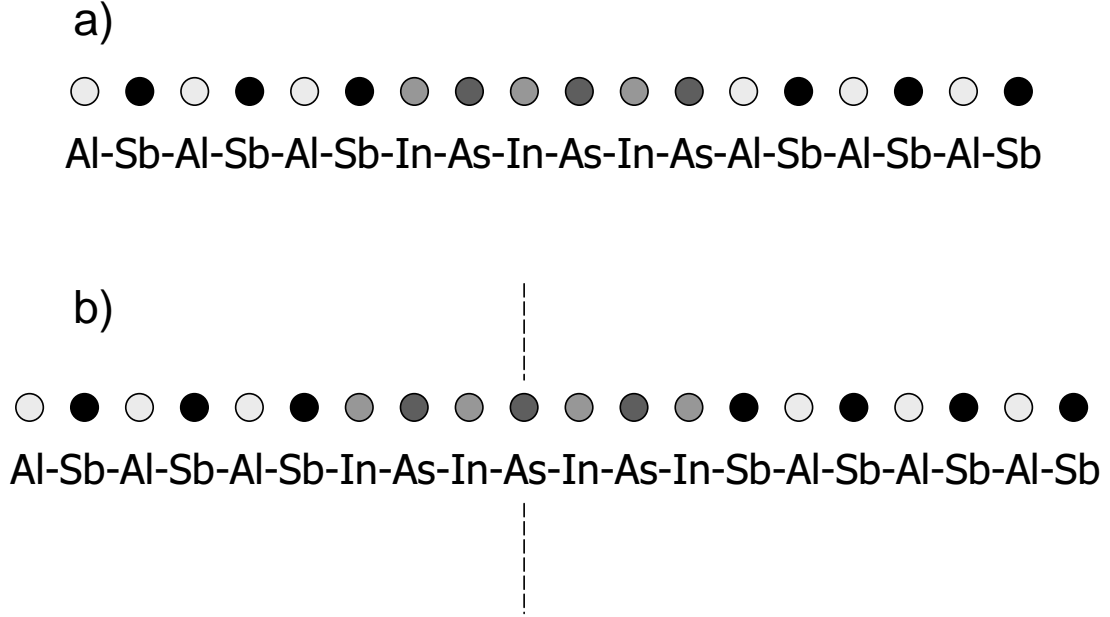


Figure 5.9: Effect of an extra atomic layer in a non-common atom AlSb/InAs/AlSb QW. (a) shows the QW having complete monolayers, belonging to the C_{2v} point group. (b) shows the effect of adding one extra In atomic layer in the InAs. New symmetry operations appear and among them, the C_2 symmetry axis shown. The point group is now D_{2v} although it is a non-common-atom QW [41].

[001] heterostructures made from zincblendes are described by the C_{2v} point group. On the other hand, symmetric [001] QWs can belong to either the C_{2v} or the D_{2d} symmetry groups depending on an interplay of characteristics such as the parity of the number of monolayers, the existence of a common atom in the constituents [40], or the existence of an extra atomic layer [41] (see Fig. 5.9).

The symmetry group of the discretized Hamiltonian in Eq. (5.48) can be found by the brute force method consisting on verifying for all the operations g of the T_d point group whether the relationship

$$D^{-1}(g)\mathbf{H}(\mathbf{k}_{\parallel})D(g) = \mathbf{H}(g^{-1}\mathbf{k}_{\parallel}) \quad (5.65)$$

is sustained [19], where $D(g)$ is the representation of the g operator in the basis of the discretized Hamiltonian $\mathbf{H}(\mathbf{k}_{\parallel})$, and $\mathbf{k}_{\parallel} = (k_x, k_y)$. This tedious procedure can be done with the help of computer software, such as *Mathematica* [20], which auto-

Point/Line	Point Group Symmetry	Spin Splitting	Spin directions
Γ	D_{2d}	No	
Δ [100]	C_2	Yes	[100],[$\bar{1}00$]
Σ [110]	C_s	Yes	[$\bar{1}10$],[1 $\bar{1}0$]
Other points	C_1	Yes	Undetermined

Table 5.7: Symmetry requirements on spin splitting and directions for points in the $k_x - k_y$ plane in a D_{2d} structure.

mates algebraic manipulations. It is seen that the EMA Hamiltonian corresponding to structures possessing macroscopic symmetry under inversion transforms according to D_{2d} , while for macroscopically asymmetric structures it transforms according to C_{2v} . This is in opposition to the majority of EMA implementations, which lack the inclusion of bulk inversion asymmetry effects and reproduce an approximate D_{4h} symmetry [42] for symmetric structures. There have been reports in the literature of other 2-band [27], 14-band [43], and 16-band [9] EMA models describing the spin splitting effects due to the reduced symmetry. Zhu and Chang [44] have started from an 8-band model to generate perturbatively a 2-band Hamiltonian for electrons and a 4-band Hamiltonian for holes, and they performed their calculations of inversion asymmetry effects in that reduced basis set. No 8-band model, combining the more accurate description of interband couplings respect to 2-band models and the simplicity and numerical performance advantages over the 14- and 16-band models, had been previously used in numerical studies of the BIA effects.

Tables 5.7 and 5.8 show the requirements that the underlying symmetry of the atom arrangement imposes on the spin degeneracy of the energy levels and the direction where the spins are pointing in case the levels are not degenerate.

Although the $\mathbf{k}\cdot\mathbf{p}$ method is not designed taking into account the interface charac-

Point/Line	Point Group Symmetry	Spin Splitting	Spin directions
Γ	C_{2v}	No	
Δ [100]	C_1	Yes	Undetermined
Σ [110]	C_s	Yes	[$\bar{1}10$],[1 $\bar{1}0$]
Other points	C_1	Yes	Undetermined

Table 5.8: Symmetry requirements on spin splitting and directions for points in the $k_x - k_y$ plane in a C_{2v} structure.



Figure 5.10: Layer arrangements for a no-common-atom quantum well. An arrangement as in (a) in the EMA would yield D_{2d} symmetry. The alternative arrangement (b) yields the correct C_{2v} symmetry of the heterostructure.

Characteristics of no-common-atom (NCA) heterostructures, it is possible in some situations to modify the simulated structure to obtain at least the right symmetry effects. Figure 5.10 a) shows a NCA quantum well. The way that the boundaries of the layers are set up, the well would be symmetric and, therefore, the Hamiltonian would have D_{2d} symmetry instead of the C_{2v} corresponding to the asymmetric interface bonds. However, the material boundaries in the $\mathbf{k} \cdot \mathbf{p}$ method are arbitrary to half a monolayer. As seen in Fig. 5.10 b), a simple rearrangement of the material boundaries reproduces the asymmetry in the bonds and allows to take into account, at least qualitatively, the effects of the lower symmetry. The case where a NCA QW is added an extra atomic layer to make it symmetric, as seen in Fig. 5.9 b), does not require any rearrangement of the layers in order to make the calculated structure have the correct D_{2d} symmetry.

The only case that cannot be modeled through these rearrangements is when a common atom structure, such as an AlAs/GaAs/AlAs QW, has C_{2v} symmetry due to the well having an odd number of monolayers. In that case, even though the species participating at the bond at the interface are the same, there is an asymmetry in the bond orientation, which the EMA method cannot take into account.

With the control that the proposed model allows over the symmetry of the calculated heterostructures, it is possible to use the EMA in studies of the spin splitting appearing in heterostructures aiming at delineating the role of bulk inversion asymmetry *vs.* structure inversion asymmetry, layer asymmetry *vs.* interface asymmetry. . . This model also provides a straightforward and easy to implement tool to study effects in QWs and superlattices derived from the possession of the reduced symmetry, such as the presence of optical anisotropy [45, 46], and the mixing of heavy hole and light hole states on top of the valence band [47, 48].

There is room for future improvement if the interface equations Eqs. (5.52)-(5.54) are considered. One possible way to expand the model would be to treat the weighted average of bulk parameters appearing in those equations as adjustable parameters. This would improve the accuracy at the expense of simplicity. The addition of interface parameters to the EMA theory had been previously proposed in the optical anisotropy [45, 48] and the hole spin splitting and relaxation [49] contexts.

5.5.2 SQWs without BIA terms

Figure 5.11 shows the band structures along the [100] and the [110] directions of a common atom AlSb/GaSb/AlSb symmetric quantum well (SQW) grown along the [001] direction and with a well thickness of 8 monolayers (24.4 Å). Since no inversion asymmetry affects are included, the bands show Kramers degeneracy throughout the Brillouin zone and the quantization axes of the spins are not univocally defined.

The labels E1, HH1, LH1 and HH2 shown in the plots correspond to the first electron, first heavy hole, first light hole and second heavy hole states in the QW respectively. They refer to the main bulk state contribution at $\mathbf{k} = 0$. For a well

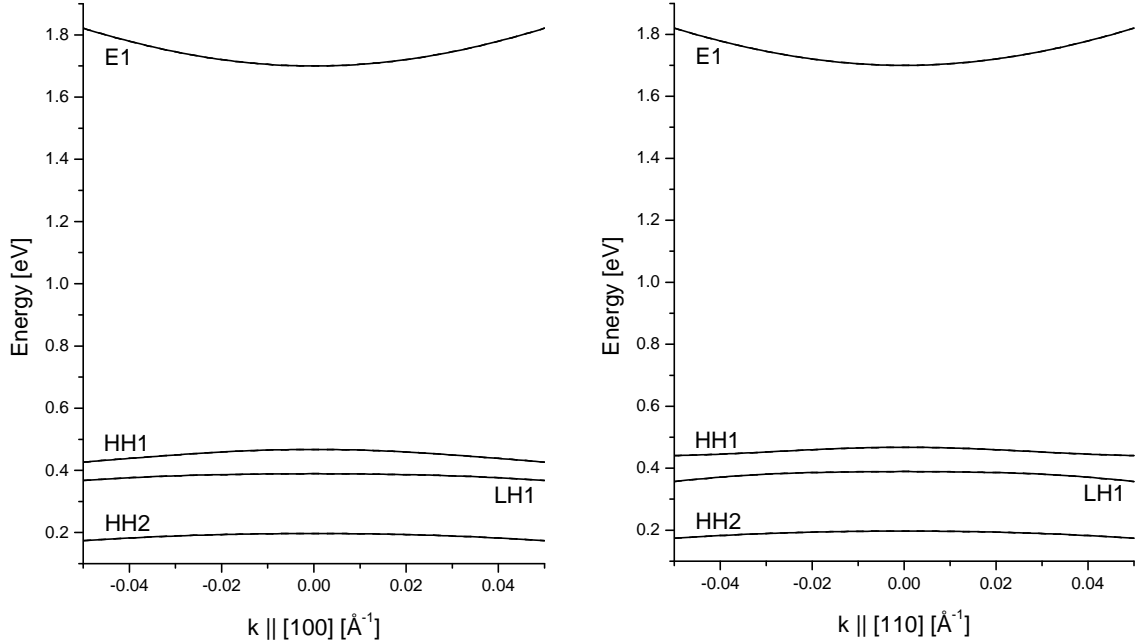


Figure 5.11: Bands along [100] and [110] for an AlSb/GaSb/AlSb SQW 8 monolayers thick without BIA terms.

without BIA terms and in the zone center, the heavy holes decouple from the rest of the bands, and the HHn states have only bulk heavy hole components. This is in opposition to the En (LHn) bands, which have small bulk light hole (electron) and split off contributions even at the zone center due to the loss of translational symmetry along [001] caused by the well potential.

5.5.3 SQWs with BIA terms

Figure 5.12 shows the same band structures as in Fig. 5.11, but with the BIA terms included. As predicted by the group theory (cf. Table 5.7), the bands are split along both directions except at the zone center. This is the major difference with most of the EMA models in the literature. Another point that must be noticed is that, even though there is no spin splitting in bulk bands along [100], in the SQW a finite splitting appears along that direction [27].

With the inclusion of BIA terms, the heavy hole states couple with the light holes by means of remote states through a perturbative mixed spin orbit and $\mathbf{k}\cdot\mathbf{p}$ interaction parametrized by C [9]. Thus, the HHn states lose their pure bulk heavy hole character

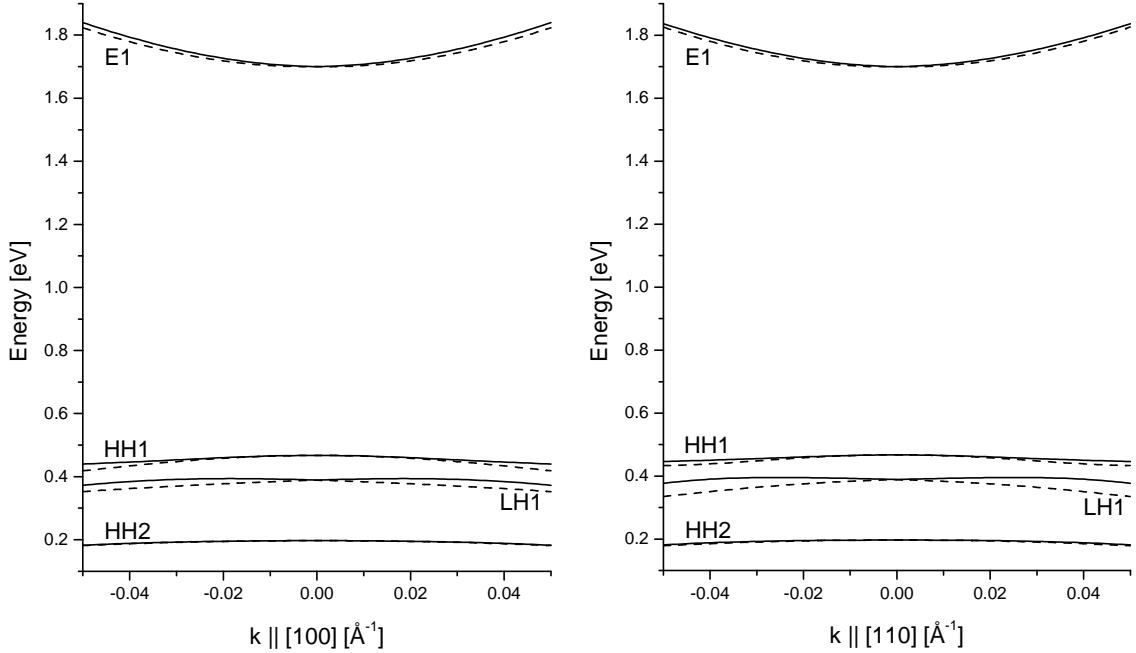


Figure 5.12: Bands along [100] and [110] for an AlSb/GaSb/AlSb SQW 8 monolayers thick with BIA terms.

and, in particular, the *HH_{even}* (*HH_{odd}*) mix with the *LH_{odd}* (*LH_{even}*). However, looking at the wavefunction for the HH1 state, it can be seen that the contribution from bulk components other than the HH to the probability density is about 8 orders of magnitude less than the heavy hole contribution.

The linear behavior and the isotropicity close to the zone center of the spin splitting between the conduction subbands is manifest in Fig. 5.13. Plot (a) shows the dependence of the spin splitting along the [100] line. It is seen that the splitting is linear close to the Γ point, with a “Rashba” coefficient of $\alpha_R = 22 \times 10^{-10}$ eV·cm. Bychkov and Rashba introduced that coefficient in the context of asymmetric quantum wells [50]. In their article, the splitting in the conduction subbands is given by

$$\Delta_R = 2\alpha_R k. \quad (5.66)$$

However, this splitting is derived from a model Hamiltonian that describes only structural inversion asymmetry (SIA) effects, but not bulk inversion asymmetry. As a consequence, the spin directions that they predict don’t apply to the SQW situation

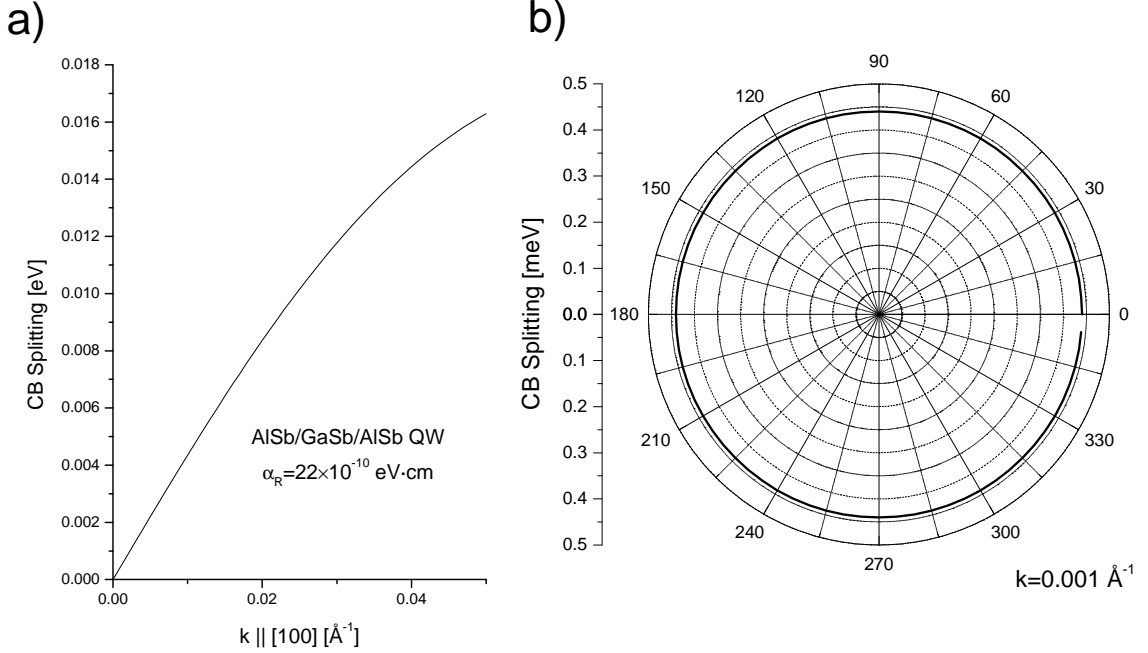


Figure 5.13: a) Spin splitting dependence for an AlSb/GaSb/AlSb QW along the [100] line. The calculated “Rashba” coefficient is $\alpha_R = 22 \times 10^{-10} \text{ eV}\cdot\text{cm}$. (b) Splitting dependence along a circle in the $k_x - k_y$ plane, with $k = 0.001 \text{ \AA}^{-1}$.

(cf. Sec. 5.6).

A model Hamiltonian for spins in the conduction subbands of SQWs in the same spirit as the Rashba Hamiltonian can be derived in the following fashion. From Eq. (5.36) the operator nature of k_z in the effective mass approximation can be made explicit [27], and keeping only up to second-order terms in k_x and k_y the following perturbation to the 2-band EMA Hamiltonian can be written:

$$H_{\text{Split Sym}} = \gamma_c \left[-\sigma_x k_x \partial_z^2 + \sigma_y k_y \partial_z^2 + \sigma_z \partial_z (k_x^2 - k_y^2) \right]. \quad (5.67)$$

If $|F_s; k_x, k_y\rangle$ is the spatial part and $|\chi\rangle$ is the spin part of the envelope function corresponding to the electron traveling in the plane with wavevector k_x, k_y , the energy change caused by the perturbation $H_{\text{Split Sym}}$ will be given by

$$\Delta = \langle \chi | \langle F_s; k_x, k_y | H_{\text{Split Sym}} | F_s; k_x, k_y \rangle | \chi \rangle = \alpha_R [\langle \chi | \sigma_x | \chi \rangle k_x - \langle \chi | \sigma_y | \chi \rangle k_y], \quad (5.68)$$

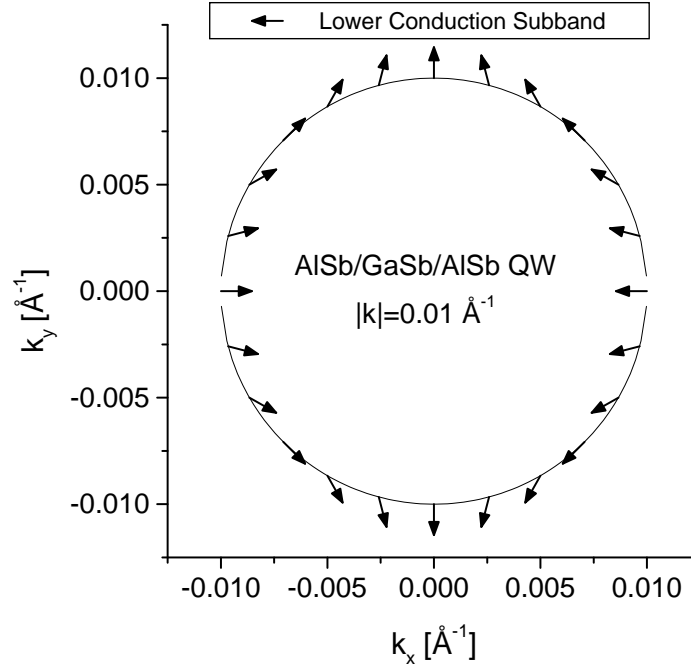


Figure 5.14: Spin directions for the lower conduction subband of an AlSb/GaSb/AlSb SQW. The thickness of the well is 8 ML (24.4 Å). The spins are plot at 15° intervals, and correspond to states lying on a circle in the $k_x - k_y$ plane with $k = 0.01 \text{ \AA}^{-1}$.

with the “Rashba” coefficient for symmetric heterostructures α_R given by $\alpha_R = -\langle F_s; k_x, k_y | \gamma_c \partial_z^2 | F_s; k_x, k_y \rangle$. The term depending on ∂_z vanishes because the envelope function has a definite parity. So, it is readily seen that a phenomenological Hamiltonian

$$H = \alpha_R (\sigma_x k_x - \sigma_y k_y) \quad (5.69)$$

will have the desired effect. From the definition of α_R it is easy to see that in the conduction band BIA effects will be bigger in narrow quantum wells because states there are made from larger perpendicular wavevectors.

The behavior of the spins when BIA terms are included is very interesting. Figure 5.14 shows the direction towards where the spins of the eigenstates of the lowest conduction subband point. The spin directions are shown for a circular sweep in the $k_x - k_y$ plane keeping $k = 0.01 \text{ \AA}^{-1}$. The directions of the spins agree with what would be predicted from Eq. (5.69). The spins at a given point in the plane point opposite for the two subbands. Note that in a given subband, although the x and y axes are

equivalent, in one of the axes the spin points outward while in the other it points inward. The explanation lies in the way that the x and y axes are connected and in the fact that spinors don't change sign under inversion. For a QW with D_{2d} symmetry, the x and y axes are equivalent through a reflection by the plane containing the $[110]$ and $[001]$ directions. The reflection by this plane can be thought of as a rotation of 180° along the $[\bar{1}10]$ direction followed by an inversion. Starting with a state $|k_y, \uparrow_{\hat{x}}\rangle$ (spin pointing outward), the rotation will send it to $|-k_x, \uparrow_{-\hat{x}}\rangle$ (still outward). Then, the inversion will flip \mathbf{k} , but not the spin, sending the state to $|k_x, \downarrow_{-\hat{x}}\rangle$ (spin pointing inward).

5.6 Bulk inversion asymmetry effects on asymmetric quantum wells

In this section the structure under study will be an AlSb/InAs/GaSb/AlSb asymmetric quantum well (AQW) grown along the $[001]$ direction compliant with a GaSb substrate. The thickness of the InAs and GaSb layers is 8 monolayers (ML) each one, with a monolayer having 3.048 \AA .

5.6.1 AQWs without BIA terms

Figure 5.15 shows the band structure along the $[100]$ and the $[110]$ directions of the AQW *without* the inclusion of BIA terms. The structural inversion asymmetry (SIA) reduces the symmetry group from D_{4h} to C_{2v} , and a spin splitting appears between the conduction subbands. The splitting due to SIA effects is usually modeled using a Hamiltonian first introduced by Bychkov and Rashba [50]:

$$H_R = \alpha_R (\boldsymbol{\sigma} \times \mathbf{k}) \cdot \boldsymbol{\nu}, \quad (5.70)$$

where α_R is the so-called Rashba constant, $\boldsymbol{\sigma}$ is a vector composed of the Pauli matrices, \mathbf{k} is the electron wavevector and $\boldsymbol{\nu}$ is the axis of symmetry of the structure.

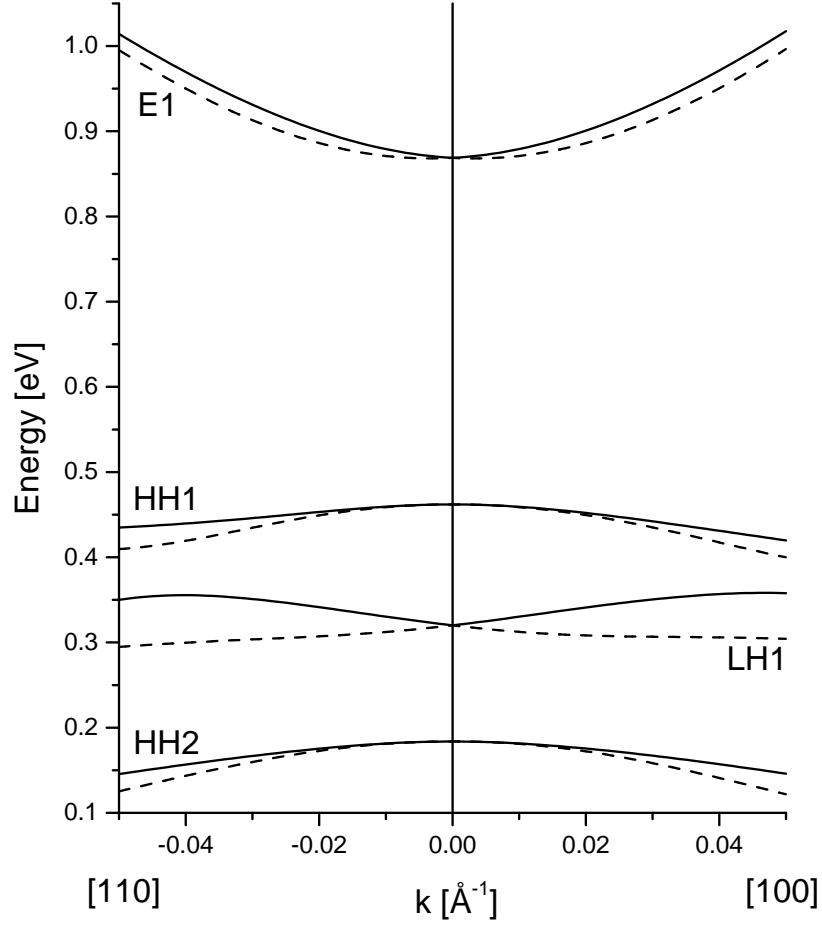


Figure 5.15: Bands without BIA effects for an AlSb/InAs/GaSb/AlSb AQW grown along the [001] direction compliant with a GaSb substrate. The bands are along [100] and [110]. The thickness of the InAs and GaSb layers is 8 ML each.

This Hamiltonian is valid to describe the SIA contributions close to the zone center. It predicts a linear and isotropic splitting

$$\Delta_R = 2\alpha_R k, \quad (5.71)$$

where k is the magnitude of the electron wavevector. It also predicts that the spins will point tangentially to the circles of constant k in the $k_x - k_y$ plane, which is verified in the numerical calculations (see Fig. 2.3). The Rashba effect in asymmetric heterostructures is studied in detail in Chapter 2.

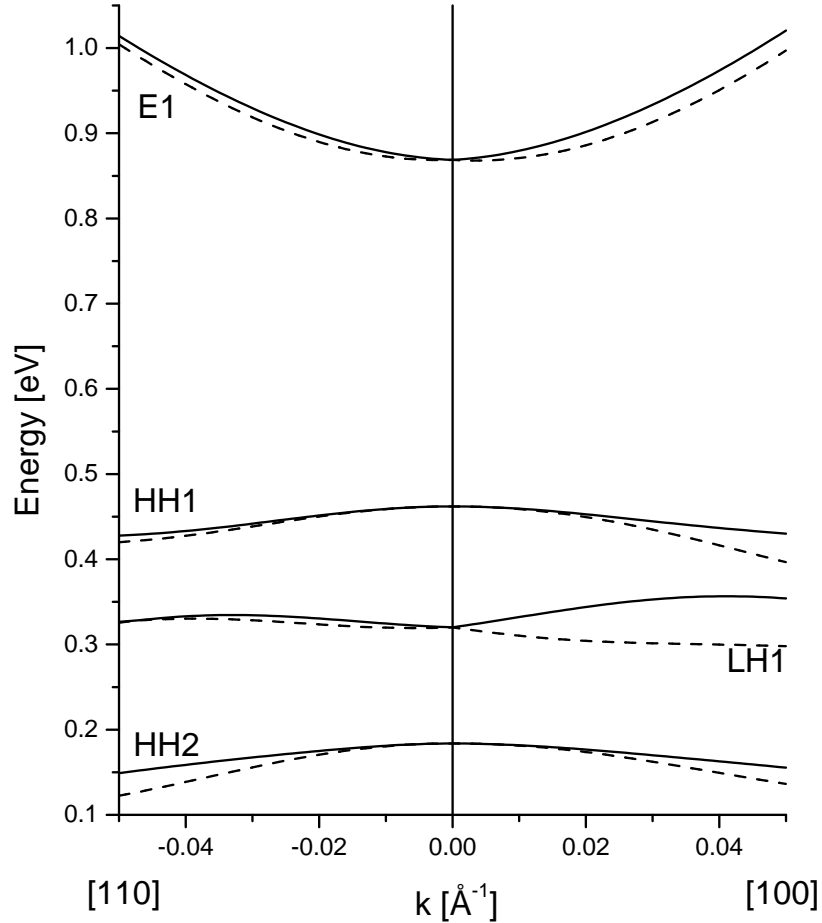


Figure 5.16: Bands along [100] and [110] for an AlSb/InAs/GaSb/AlSb AQW with BIA effects.

5.6.2 AQWs with BIA terms

The band structure for the AQW under study *with* BIA effects is shown in Fig. 5.16. The effects of inversion asymmetry are highly anisotropic in bulk [10], and this reflects on the directional dependence of the bands. Comparing with Fig. 5.15, it is seen that the BIA effects are necessary to obtain accurate bands in the [110] direction.

The interplay of SIA and BIA effects in asymmetric quantum wells (AQWs) adds a level of variety to the analysis of the behavior of the spins in the conduction band. However, the inclusion of the Hamiltonian (5.69) keeps the analysis quite simple. For a [001] structure, the SIA and BIA contributions to the splitting can be described by

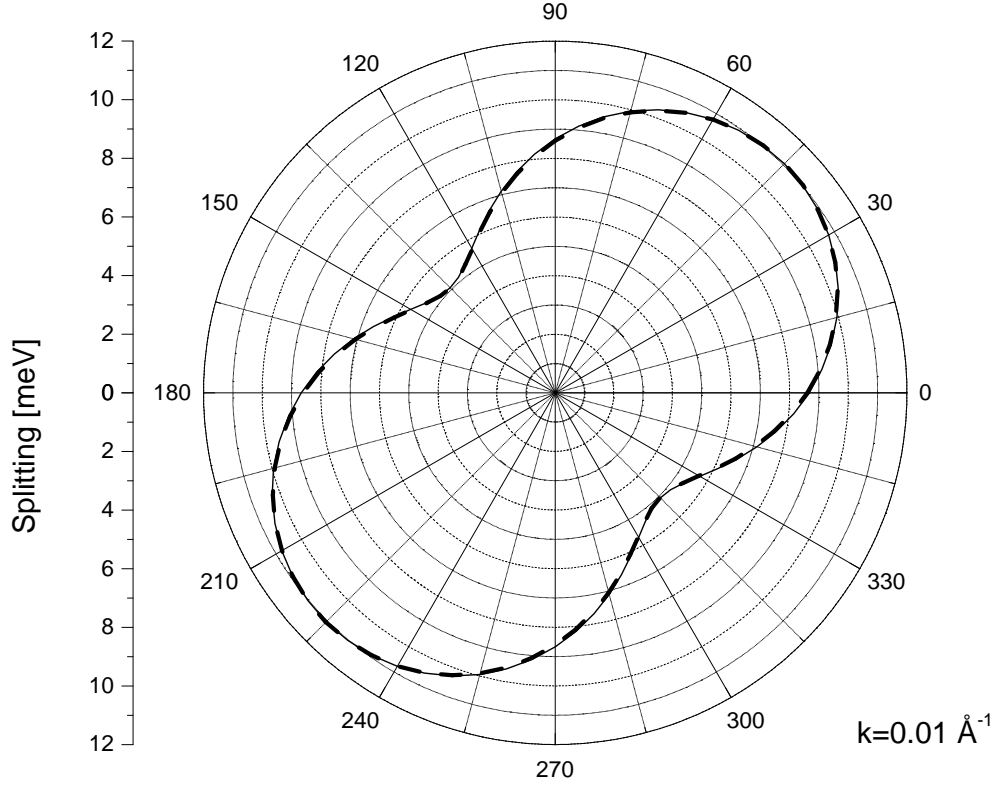


Figure 5.17: Angular dependence of the spin splitting for an AlSb/InAs/GaSb/AlSb AQW. The solid line is the 8-band model numerical result. The dashed line is a fit using Eq. (5.73) with $\alpha_{\text{SIA}} = 40.3 \times 10^{-10}$ eV·cm and $\alpha_{\text{BIA}} = 15.0 \times 10^{-10}$ eV·cm.

Hamiltonian H_{IA} made from the addition of Eq. (5.69) and Eq. (5.70):

$$H_{\text{IA}} = \alpha_{\text{BIA}} (\sigma_x k_x - \sigma_y k_y) + \alpha_{\text{SIA}} (\sigma_x k_y - \sigma_y k_x) = \sigma_x (\alpha_{\text{SIA}} k_y + \alpha_{\text{BIA}} k_x) - \sigma_y (\alpha_{\text{BIA}} k_y + \alpha_{\text{SIA}} k_x), \quad (5.72)$$

where α_{BIA} (α_{SIA}) is the coefficient describing BIA (SIA) effects. From here, making an analogy with the Zeeman splitting, it is easy to find that the splitting in the conduction band (CB) close to the zone center will be

$$\Delta_{\text{IA}} = 2k \sqrt{\alpha_{\text{SIA}}^2 + 2\alpha_{\text{SIA}}\alpha_{\text{BIA}} \sin 2\theta + \alpha_{\text{BIA}}^2}, \quad (5.73)$$

where θ is the in-plane polar angle.

A full 8-band numerical calculation of the splitting along a circle in the $k_x - k_y$

plane and the 2-band prediction from expression (5.73) are shown in Fig. 5.17. The values from the analytic expression show very good agreement with the numerical results. The numerical results are fitted with $\alpha_{\text{SIA}} = 40.3 \times 10^{-10}$ eV·cm and $\alpha_{\text{BIA}} = 15.0 \times 10^{-10}$ eV·cm. This way the BIA effects are quantified, and it must be concluded that they must be taken into account for an accurate description of the bands. This is clearly so in the [110] direction, where the contributions are added linearly, but it is also true in a lesser degree in the [100] direction, where the contributions are added quadratically.

For a quantum well where the 2-band model is valid, the BIA splitting coefficient for the CB can be estimated with

$$\alpha_{\text{BIA}} \approx \frac{\gamma_{cW}}{L_W^2}, \quad (5.74)$$

where γ_{cW} and L_W^2 are the k^3 splitting coefficient of the CB and the thickness respectively of the layer where the electrons are confined. This estimate will become more accurate as the well becomes thicker. From this expression and Eq. (5.25) it is readily seen that BIA effects will be considerable when the material in the well layer has a low band gap and high spin-orbit interaction, such as InAs, GaSb and InSb (cf. Table 5.1). So, it has been seen that, a priori, it is not possible to consider only SIA effects for an asymmetric structure even if the constituents are low band gap materials.

Figure 5.18 compares the splitting in the CB along the [100] and [110] directions for the same AQW with and without the BIA terms. The values of half the slope, *i.e.*, the ‘‘Rashba’’ coefficient including bulk and inversion asymmetry, are listed for each curve under the symbol α . With no BIA terms, the slope near the origin is the same for both directions, and the values only depart when higher order $O(k^3)$ contributions start to take over. For the curves with BIA effects, the linear splitting behavior predicted by Eq. (5.72) holds only until about 1.5% of the zone boundary. So, that equation can be applied to wells with electron concentrations up to 10^{11} cm $^{-2}$. It would be interesting to study the effects that higher order contributions to

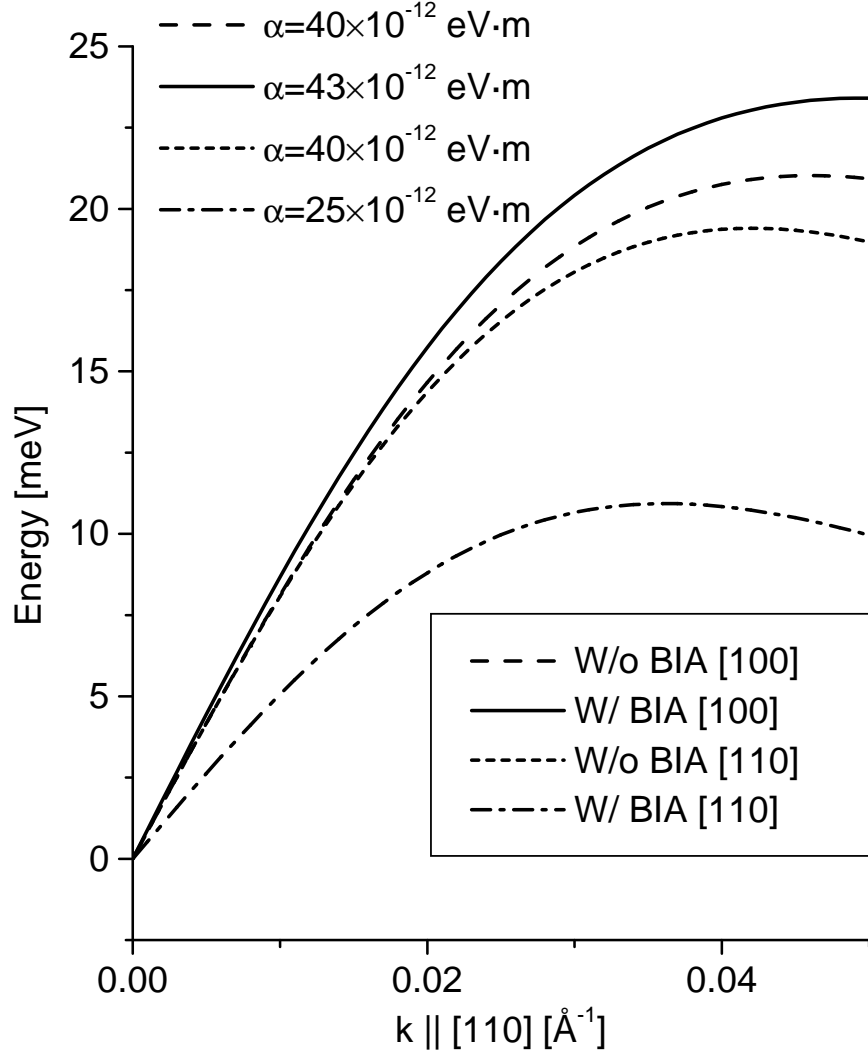


Figure 5.18: Spin splitting *vs.* k for an AlSb/InAs/GaSb/AlSb quantum well along the [100] and the [110] direction with and without BIA terms. The α 's are half the slope at $k = 0$.

the splitting and BIA-induced anisotropy can have on the interpretation of the wide body of Shubnikov-de Haas measurements of α_R (see, for example, Refs. [51–53]) that have so far assumed Eq. (5.70) to describe the splitting for all electrons in the well.

Finally, the electron spins are also affected by the inclusion of BIA terms. In Fig. 5.19 the spins of the lowest conduction subband are shown for states lying on a circle in the $k_x - k_y$ plane of radius $k = 0.01 \text{ \AA}$. The direction of the spins has changed respect to the case without BIA terms (see Fig. 2.3). As it can be deduced from Eq. (5.72), it corresponds to the vector sum of the spins in Fig. 2.3 and the spins

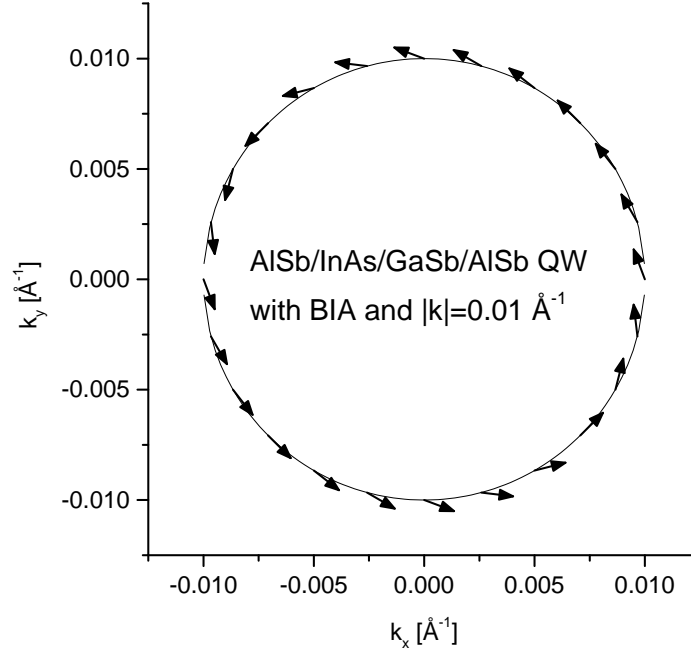


Figure 5.19: Spin directions for the lower conduction subband of an AISb/InAs/GaSb/AISb AQCW. The spins are plot at 15° intervals, and correspond to the lowest conduction subband states lying on a circle in the $k_x - k_y$ plane with $k = 0.01 \text{ \AA}^{-1}$.

in Fig. 5.19, each one weighted by their corresponding splitting coefficients α 's.

5.7 Summary

In summary, an implementation of an 8-band effective mass approximation (EMA) method for calculating band structures has been obtained. This implementation is faithful to the T_d microscopic symmetry of bulk zincblendes. As a consequence, all symmetry effects close to the zone center, including the spin splitting of the bands, are correctly described. When the method is applied to symmetric heterostructures, linear splittings in k are predicted as a consequence of the reduced symmetry. This is not found for standard EMA implementations. A 2-band Hamiltonian describing this splitting due to the bulk inversion asymmetry (BIA) is derived. The bands of asymmetric heterostructures are also studied and described in the context of the BIA Hamiltonian obtained for heterostructures. It is seen that, in the case studied, the SIA and BIA contributions to the spin splitting are of the same order of magnitude

even though the well is composed by narrow gap materials. Therefore, an accurate description of the bands will require the inclusion of both effects.

Bibliography

- [1] S. A. Wolf, J. Supercond. **13**, 195 (2000).
- [2] R. Gawel, Electron. Des. **48**, 30 (2000).
- [3] S. Das Sarma, J. Fabian, X. D. Hu, and I. Zutic, Superlattice. Microstruct. **27**, 289 (2000).
- [4] B. Heinrich, Can. J. Phys. **78**, 161 (2000).
- [5] S. Datta and B. Das, Appl. Phys. Lett. **56**, 665 (1990).
- [6] R. Fiederling, M. Keim, G. Reuscher, W. Ossau, G. Schmidt, A. Waag, and L. W. Molenkamp, Nature **402**, 787 (1999).
- [7] A. Morinaga and K. Shiiki, Jpn. J. Appl. Phys. **38**, 4741 (1999).
- [8] G. Lommer, F. Malcher, and U. Rossler, Phys. Rev. Lett. **60**, 728 (1988).
- [9] M. Cardona, N. E. Christensen, and G. Fasol, Phys. Rev. B **38**, 1806 (1988).
- [10] G. Dresselhaus, Phys. Rev. **100**, 580 (1955).
- [11] E. A. D. E. Silva, G. C. LaRocca, and F. Bassani, Phys. Rev. B **50**, 8523 (1994).
- [12] J. M. Luttinger and W. Kohn, Phys. Rev. **97**, 869 (1955).
- [13] G. Bastard, *Heterojunctions and Semiconductor Superlattices*, 2nd ed. (Springer-Verlag New York, New York, Ny, 1986).
- [14] P. Pfeffer, Phys. Rev. B **59**, 15902 (1999).
- [15] H.-R. Trebin, U. Rössler, and R. Ranvaud, Phys. Rev. B **20**, 686 (1979).
- [16] J. M. Luttinger, Phys. Rev. **102**, 1030 (1956).

- [17] G. E. Pikus, Zh. Eksp. Teor. Fiz. **41**, (10) (1961).
- [18] G. E. Pikus, Zh. Eksp. Teor. Fiz. **41**, (11) (1961).
- [19] G. L. Bir and G. E. Pikus, *Symmetry and Strain-Induced Effects in Semiconductors*, 1st ed. (Wiley, New York, USA, 1974).
- [20] I. Wolfram Research, *Mathematica*, version 4 ed. (Wolfram Research, Inc., Champaign, Illinois, 1999).
- [21] G. F. Koster, J. O. Dimmock, R. G. Wheeler, and H. Statz, *Properties of the Thirty-Two Point Groups*, 1st ed. (M.I.T. Press, Cambridge, MA, USA, 1963).
- [22] P. Lawaetz, Phys. Rev. B **4**, 3460 (1971).
- [23] T. B. Bahder, Phys. Rev. B **41**, 11992 (1990).
- [24] J. C. Hensel and K. Suzuki, Phys. Rev. Lett. **22**, 838 (1969).
- [25] O. E. Madelung, *Semiconductors – Basic Data*, 2nd ed. (Springer-Verlag, Berlin, Germany, 1996).
- [26] G. E. Pikus, V. A. Marushchak, and A. N. Titkov, Soviet Physics Semiconductors-USSR **22**, 115 (1988).
- [27] R. Eppenga and M. F. H. Schuurmans, Phys. Rev. B **37**, 10923 (1988).
- [28] C. G. Van de Walle, Phys. Rev. B **39**, 1871 (1989).
- [29] R. Eppenga, M. F. H. Schuurmans, and S. Colak, Phys. Rev. B **36**, 1554 (1987).
- [30] R. Enderlein, G. M. Sipahi, L. M. R. Scolfaro, and J. R. Leite, Phys. Stat. Sol. (B) **206**, 623 (1998).
- [31] M. G. Burt, Semicond. Sci. Tech. **3**, 739 (1988).
- [32] E. O. Kane, in *Tunneling Phenomena in Solids*, edited by E. Burstein and S. Lundqvist (Plenum Press, New York, 1969), p. 1.

- [33] S. L. Chuang, Phys. Rev. B **43**, 9649 (1991).
- [34] K. Nakamura, A. Shimizu, M. Koshihara, and K. Hayata, IEEE J. Quantum Elect. **27**, 2035 (1991).
- [35] G. E. W. Bauer and T. Ando, Phys. Rev. B **38**, 6015 (1988).
- [36] D. Y. K. Ko and J. C. Inkson, Phys. Rev. B **38**, 9945 (1988).
- [37] S. L. Chuang and C. S. Chang, Semicond. Sci. Technol. **12**, 252 (1997).
- [38] T. Yamanaka, H. Kamada, Y. Yoshikuni, W. W. Lui, S. Seki, and K. Yokoyama, J. Appl. Phys. **76**, 2347 (1994).
- [39] B. A. Foreman, Phys. Rev. B **56**, 12748 (1997).
- [40] L. W. Wang, S. H. Wei, T. Mattila, A. Zunger, I. Vurgaftman, and J. R. Meyer, Phys. Rev. B **60**, 5590 (1999).
- [41] P. Vogl, private communication.
- [42] P. Tronc and Y. E. Kitaev, Phys. Rev. B **63**, art. no. (2001).
- [43] U. Rössler, Solid State Commun. **49**, 943 (1984).
- [44] B.-F. Zhu and Y.-C. Chang, Phys. Rev. B **50**, 11932 (1994).
- [45] O. Krebs and P. Voisin, Phys. Rev. Lett. **77**, 1829 (1996).
- [46] R. Magri and S. Ossicini, Phys. Rev. B **63**, art. no. (2001).
- [47] R. Magri and A. Zunger, Phys. Rev. B **62**, 10364 (2000).
- [48] E. L. Ivchenko, A. Y. Kaminski, and U. Rossler, Phys. Rev. B **54**, 5852 (1996).
- [49] L. Vervoort, R. Ferreira, and P. Voisin, Phys. Rev. B **56**, 12744 (1997).
- [50] Y. A. Bychkov and E. I. Rashba, J. Phys. C **17**, 6039 (1984).
- [51] J. Luo, H. Munekata, F. F. Fang, and P. J. Stiles, Phys. Rev. B **38**, 10142 (1988).

- [52] J. Luo, H. Munekata, F. F. Fang, and P. J. Stiles, *Phys. Rev. B* **41**, 7685 (1990).
- [53] T. Schäpers, G. Engels, J. Lange, T. Klocke, M. Hollfelder, and H. Lüth, *J. Appl. Phys.* **83**, 4324 (1998).

Chapter 6 Spurious numerical solutions in the effective mass approximation

6.1 Introduction

The effective mass approximation (EMA) [1, 2] has long been a favorite among researchers as a method that is fast and easy to implement for calculating the energy levels in quantum wells and superlattices [3–7], quantum wires [8–10], quantum dots [8, 11, 12]. . . It is also the tool of choice for engineers to model devices such as lasers and photodetectors [13–18]. Also, its use is widespread in the calculation of tunneling coefficients [19–21] and times [22, 23], with application to the modeling of resonant tunneling devices (RTDs).

Some of the implementations have the undesirable characteristic that they produce spurious solutions [3, 24–26]. Their origin is traced to the statement of a secular equation having too high a polynomial degree in the electron wavevector k . In some cases, the presence of the spurious solutions is required for consistent boundary conditions at the interface to be satisfied [3], thus raising doubts about the validity of the results [24]. In some other cases, interface or surface states are predicted to lie in the gap [27], but the physical meaning of these solutions is a point still in discussion [28]. There exist several proposals to solve the $\mathbf{k} \cdot \mathbf{p}$ spurious solution problem ranging from methods to eliminate them [29, 30] to pointing out the necessity of keeping them for a complete description [31].

In this chapter a new class of spurious solutions (SSs) particular to the finite difference method (FDM) [32, 33] is studied. In Sec. 6.2 these SSs are presented, they are characterized and different failed attempts to suppress them are presented. Then, in Sec. 6.3, a general method for the study of this class of SSs is presented. In Sec. 6.4 a condition that the Luttinger parameters must satisfy for the SSs not to

Quantity	InP ^a	In _{0.53} Ga _{0.47} As ^b
a (Å)	5.8693	5.8693
E_g (eV)	1.35	0.839
E_v (eV)	-0.351	0
Δ_{SO} (eV)	0.108	0.362
γ_1	1.49	1.84 ^c
γ_2	-0.31	-0.87 ^c
γ_3	0.37	0.25 ^c
C (eV·Å)	-1.44×10^{-2}	7.53×10^{-3}
P (eV·Å)	8.79	9.49
B (eV·Å ²)	-27.5	21.5
C_1 (eV)	-5.04	-6.06
D_d (eV)	1.27	1.08
D_u (eV)	-2.4	-2.7
D'_u (eV)	-3.6	-3.5
C_{11} (GPa)	101.1	97.07
C_{12} (GPa)	56.1	50.82
C_{44} (GPa)	45.6	49.18

^aSame source as in Table 5.5.

^bObtained by linear interpolation unless otherwise noted.

^cObtained by harmonic averaging [34].

Table 6.1: Band structure parameters for InP and In_{0.53}Ga_{0.47}As.

exist is derived. Finally, in Sec. 6.5 this condition is applied to popular compilations of Luttinger parameters to identify sets of parameters leading to SSs, and then the results are summarized.

6.2 Spurious solutions in an InP/In_{0.53}Ga_{0.47}As superlattice

The structure that will be used to illustrate the spurious solutions (SSs) is an InP/In_{0.53}Ga_{0.47}As symmetric superlattice (SL) grown along the [001] direction with an In_{0.53}Ga_{0.47}As width of 65 Å and an InP width of 88 Å. The method of calculation is described in Sec. 5.4. Table 6.1 lists the numerical parameters employed in the calculations¹. When there is no explicit source for the parameters of In_{0.53}Ga_{0.47}As, they

¹The meaning of the parameters is shown in Table 5.4.

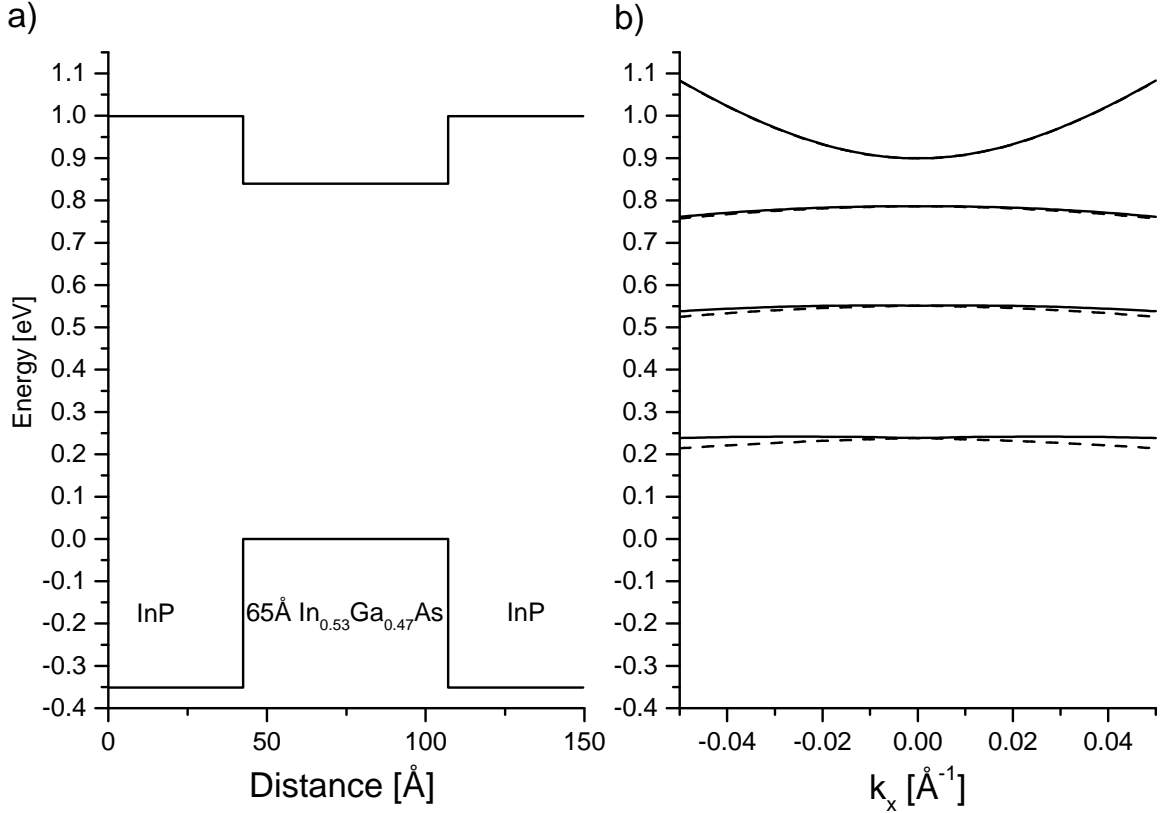


Figure 6.1: Bands of an 88 Å/65 Å InP/In_{0.53}Ga_{0.47}As SL showing spurious solutions. (a) shows the spatial profile of the bands. (b) shows the bands in \mathbf{k} space in the same energy scale as in (a). It is seen that the first three hole bands lie in the forbidden gap.

have been obtained as a linear interpolation between InAs and GaAs, except for the 8-band Luttinger parameters γ_i , where a harmonic average has been performed [34].

Figure 6.1.a) shows the band edge spatial profile for that structure. Figure 6.1.b) shows a calculation of the first electron band and first three hole bands near the Γ point for the SL. The energy scales in plots (a) and (b) are matched. Note that the energy of the hole states lies inside the forbidden gap of the superlattice, showing that there is something wrong with the computational procedure employed.

In order to obtain more insight into the nature of these spurious solutions, the norm and the relevant envelope function components of the wavefunction corresponding to the first SS (counting from the conduction band edge) were plotted and compared to a nonspurious wavefunction. This is shown in Fig. 6.2. Plot (a) depicts

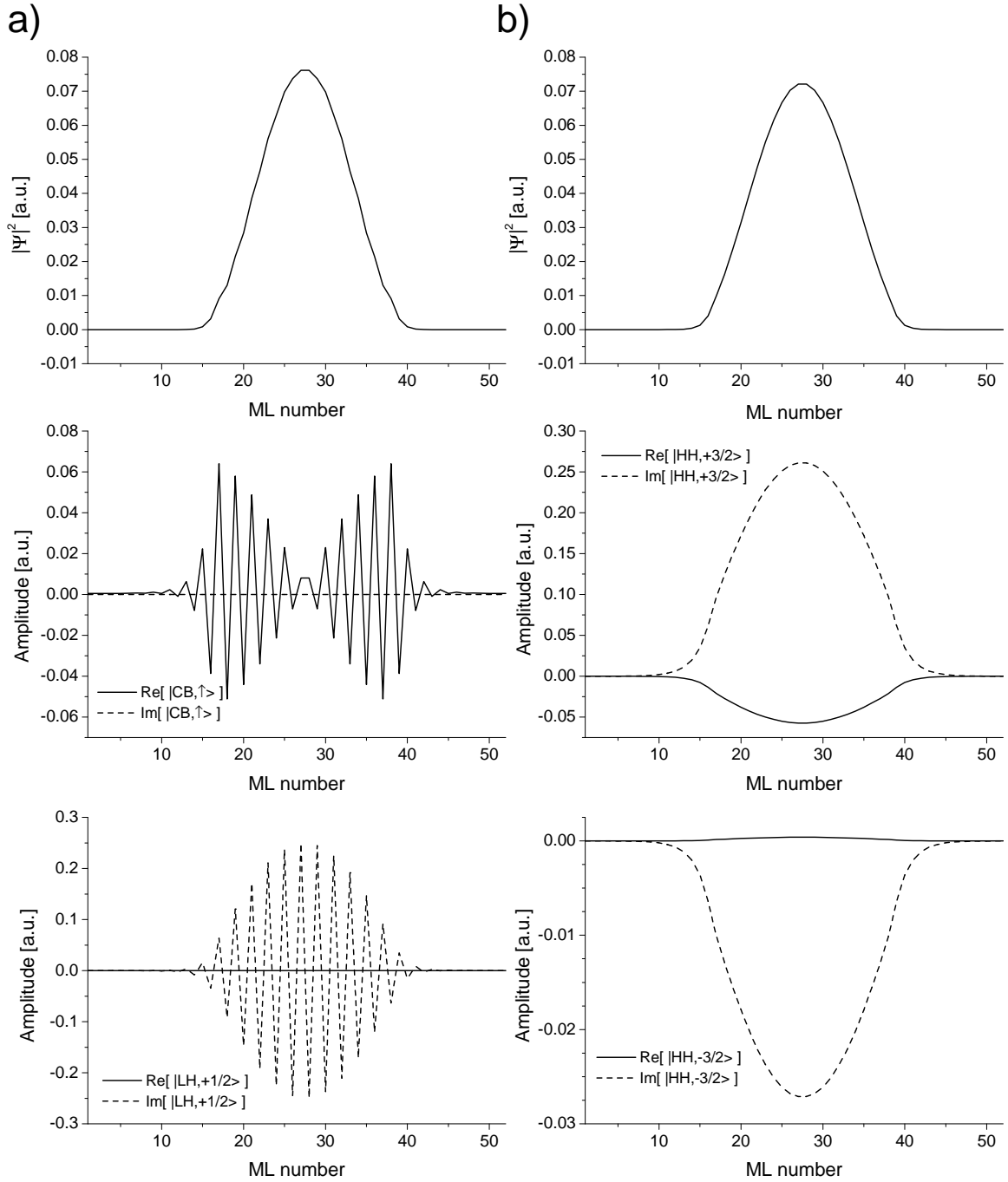


Figure 6.2: Comparison of spurious and physical envelope functions. (a) corresponds to a spurious state. (b) corresponds to the first heavy hole state. The top plots correspond to the probability density of finding the electron in a given monolayer, while the bottom two show the real and imaginary parts of selected envelope components.

the spurious wavefunction, while plot (b) refers to the non spurious one. It can be seen that the probability density $F(z) = \sum_{i=1}^8 |F_i(z)|^2$ of finding the electron in a given monolayer is similar in both cases and doesn't supply any information. However, a look at the individual components of the envelope function reveals that they are highly oscillatory in nature for the spurious case, while they are smooth for the physical state. The period for these spurious oscillations is twice the mesh spacing, thus indicating that they might be somewhat related to the chosen discretization mesh (see Sec. 5.4.2). The fact that the states are located mainly in the center of the $\text{In}_{0.53}\text{Ga}_{0.47}\text{As}$ layer discards the possibility that the SSs might originate from boundary condition induced interface states [28, 35], because the latter should decay exponentially away from the interface.

The relationship of the SSs and the discretization grid is further investigated in Fig. 6.3. There, the band edge energies are plotted *vs.* the number of mesh points to look for any dependencies. Four SSs appear in the range of mesh points and energies under study. It is seen that while, as expected, the energies of the physical states don't depend strongly on the number of mesh points², the energies of the SSs do depend on the number of mesh points. After this, it must be concluded that the SSs presented here are not only nonphysical, but also that they are not intrinsically attached to the system of coupled differential equations (5.44) that must be solved in the EMA model. Instead, they appear only due to the procedure followed to solve these equations.

A heuristic approach was first tried to remove the spurious solutions. First, a number of different boundary conditions for the interfaces was tried, without affecting the SSs. The highly oscillatory behavior of the SSs might induce to think that there was something wrong with the discretized version of the kinetic energy operator [36], but they also remained there when different discretization schemes were tried, 2nd neighbor difference formulae used or unevenly spaced grids employed.

Finally, it was realized that, since the role of the boundary conditions is merely to

²Except for a very coarse grid, where, as per the Nyquist theorem, there are not enough mesh points to properly describe the oscillation of the envelope function in the confinement region.

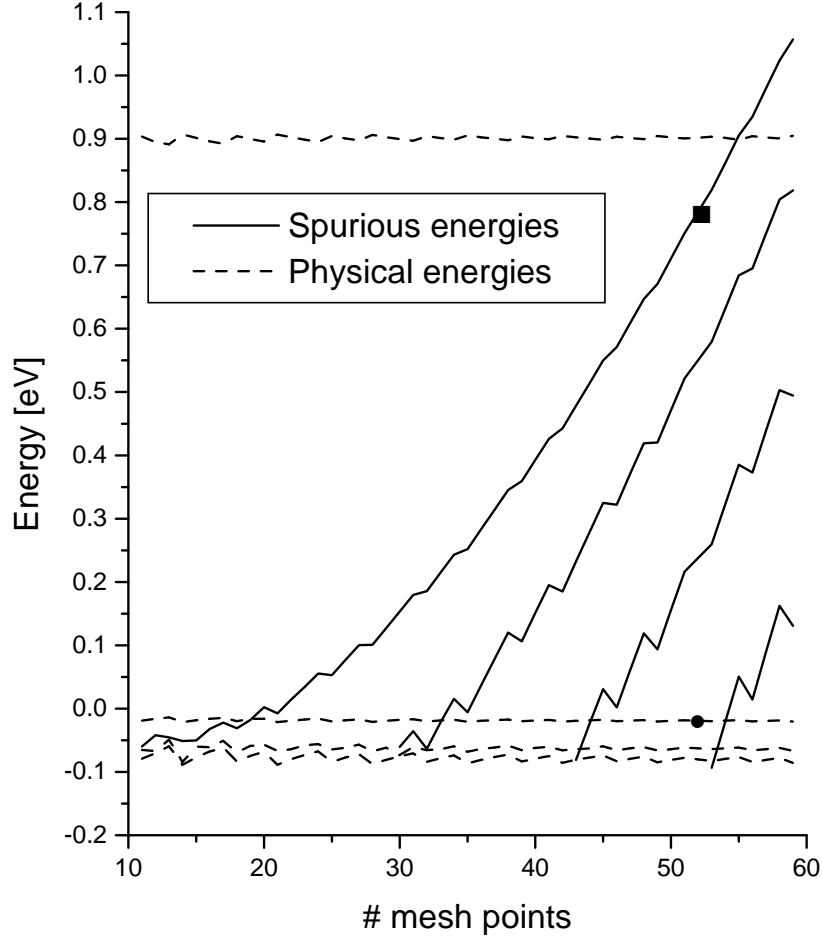


Figure 6.3: Energy of the spurious states *vs.* number of mesh points for a 88 Å/65 Å InP/In_{0.53}Ga_{0.47}As SL. The state labeled with the square (round) dot corresponds to plot (a) [(b)] in Fig. 6.2.

connect the bulk solutions, the SSs should be present also in bulk In_{0.53}Ga_{0.47}As, because that is where the envelope functions are oscillating. After this was understood, it was possible to study the origin of the SSs and predict when they would appear.

6.3 Method for the study of the spurious solutions

Several practical implementations of calculations of band structures of heterostructures, including the multiband $\mathbf{k} \cdot \mathbf{p}$ [32, 33] and EBOM [37] methods, require the

solution of a set of equations

$$\mathbf{H}_{\sigma,\sigma-1}\mathbf{F}_{\sigma-1} + \mathbf{H}_{\sigma,\sigma}\mathbf{F}_{\sigma} + \mathbf{H}_{\sigma,\sigma+1}\mathbf{F}_{\sigma+1} = E\mathbf{F}_{\sigma} \quad (6.1)$$

for each of the points $\{\sigma\}$ in the mesh (cf., for example, Sec. 5.4), where E is the sought energy, \mathbf{F}_{σ} are the envelope function coefficients at the mesh point σ and the $\mathbf{H}_{\sigma,\nu}$ are transfer Hamiltonians.

In bulk, the envelope functions of the physical solutions at the Γ point should be flat. On the other hand, it has been shown in the previous section that SSs oscillate with a period of double the mesh spacing. Both cases can be studied if it is assumed that the envelope must follow the Bloch behavior, relating the value of the envelope at a point $\sigma + 1$ to the value at σ ,

$$\mathbf{F}_{\sigma+1} = e^{i\Delta z k_z} \mathbf{F}_{\sigma}, \quad (6.2)$$

where Δz is the mesh spacing and k_z is the z component of the electron wavevector in bulk.

Now, plugging Eq. (6.2) into Eq. (6.1), a single eigenvalue equation

$$\left[e^{-i\Delta z k_z} \mathbf{H}_{\sigma,\sigma-1} + \mathbf{H}_{\sigma,\sigma} + e^{i\Delta z k_z} \mathbf{H}_{\sigma,\sigma+1} \right] \mathbf{F}_{\sigma} = E\mathbf{F}_{\sigma} \quad (6.3)$$

is obtained that must be solved in order to know the effect of an oscillating envelope function on the energies. Any further advance requires an explicit form for the Hamiltonian.

6.4 Spurious solutions in the $\mathbf{k} \cdot \mathbf{p}$ method

In the 8-band EMA method, the starting point is a model that treats the coupling between the conduction band (CB), heavy hole (HH), light hole (LH) and split-off (SO) bands exactly, and the interactions with the rest of the bands perturbatively. Bulk inversion asymmetry effects [38] will be ignored to keep the results simple and

obtain analytical expressions. This will cause the bands to be degenerate. The diagonalization of Eq. (6.3) can be carried out numerically if some of the assumptions need to be relaxed. Also, since only spurious solutions at the zone center are sought, the k_x and k_y components of the wavevector are set to zero. Then a simple change in the ordering of the basis states described in Sec. 5.3.3 diagonalizes the $\mathbf{k} \cdot \mathbf{p}$ Hamiltonian into two 4×4 blocks, and each one of them is block diagonalized again into a 1×1 block describing the HH band and a 3×3 block describing the CB, LH and SO bands:

$$H_{3 \times 3} = \begin{matrix} & |\Gamma_6, +\frac{1}{2}\rangle & |\Gamma_8, +\frac{1}{2}\rangle & |\Gamma_7, +\frac{1}{2}\rangle \\ \langle \Gamma_6, +\frac{1}{2}| & \left(E_g + \frac{\hbar^2 k_z^2}{2m} \right. & \sqrt{\frac{2}{3}} P k_z & -\frac{P k_z}{\sqrt{3}} \\ \langle \Gamma_8, +\frac{1}{2}| & \left. \sqrt{\frac{2}{3}} P k_z \right. & -(\gamma_1 + 2\gamma_2) \frac{\hbar^2 k_z^2}{2m} & \sqrt{2}\gamma_2 \frac{\hbar^2 k_z^2}{2m} \\ \langle \Gamma_7, +\frac{1}{2}| & \left. -\frac{P k_z}{\sqrt{3}} \right. & \sqrt{2}\gamma_2 \frac{\hbar^2 k_z^2}{2m} & -\Delta_{SO} - \gamma_1 \frac{\hbar^2 k_z^2}{2m} \end{matrix} \quad (6.4)$$

where m is the free electron mass and the rest of the parameters is defined in Table 5.4.

After the application of the discretization procedure described in Sec. 5.4.2 to Eq. (6.4) and plugging the result into Eq. (6.3) one obtains that the finite difference algorithm is effectively solving the Hamiltonian

$$H_{3 \times 3} \text{ FDM} = \begin{pmatrix} E_g + \frac{\hbar^2}{m} \frac{1 - \cos(\Delta z k_z)}{\Delta z^2} & \frac{\sqrt{\frac{2}{3}} P \sin(\Delta z k_z)}{\Delta z} & -\frac{P \sin(\Delta z k_z)}{\sqrt{3} \Delta z} \\ \frac{\sqrt{\frac{2}{3}} P \sin(\Delta z k_z)}{\Delta z} & -(\gamma_1 + 2\gamma_2) \frac{\hbar^2}{m} \frac{1 - \cos(\Delta z k_z)}{\Delta z^2} & \frac{\hbar^2}{m} \frac{2\sqrt{2}\gamma_2 \sin(\frac{\Delta z k_z}{2})^2}{\Delta z^2} \\ -\frac{P \sin(\Delta z k_z)}{\sqrt{3} \Delta z} & \frac{\hbar^2}{m} \frac{2\sqrt{2}\gamma_2 \sin(\frac{\Delta z k_z}{2})^2}{\Delta z^2} & -\Delta_{SO} - \gamma_1 \frac{\hbar^2}{m} \frac{1 - \cos(\Delta z k_z)}{\Delta z^2} \end{pmatrix}. \quad (6.5)$$

Expanding this Hamiltonian about $k_z = 0$ up to second order it is easily seen that Eq. (6.4) is recovered, which ensures the correct description of the bands when $\Delta z k_z \ll 1$.

Now, the eigenvalues of Eq. (6.5) can be plotted as a function of k_z for both the InP and the $\text{In}_{0.53}\text{Ga}_{0.47}\text{As}$ parameters in Table 6.1. This is shown in Fig. 6.4. Plot (a) shows the results for $\text{In}_{0.53}\text{Ga}_{0.47}\text{As}$. Consider, say, six mesh points in bulk $\text{In}_{0.53}\text{Ga}_{0.47}\text{As}$ with cyclic boundary conditions (see the insets in Fig. 6.4). The dif-

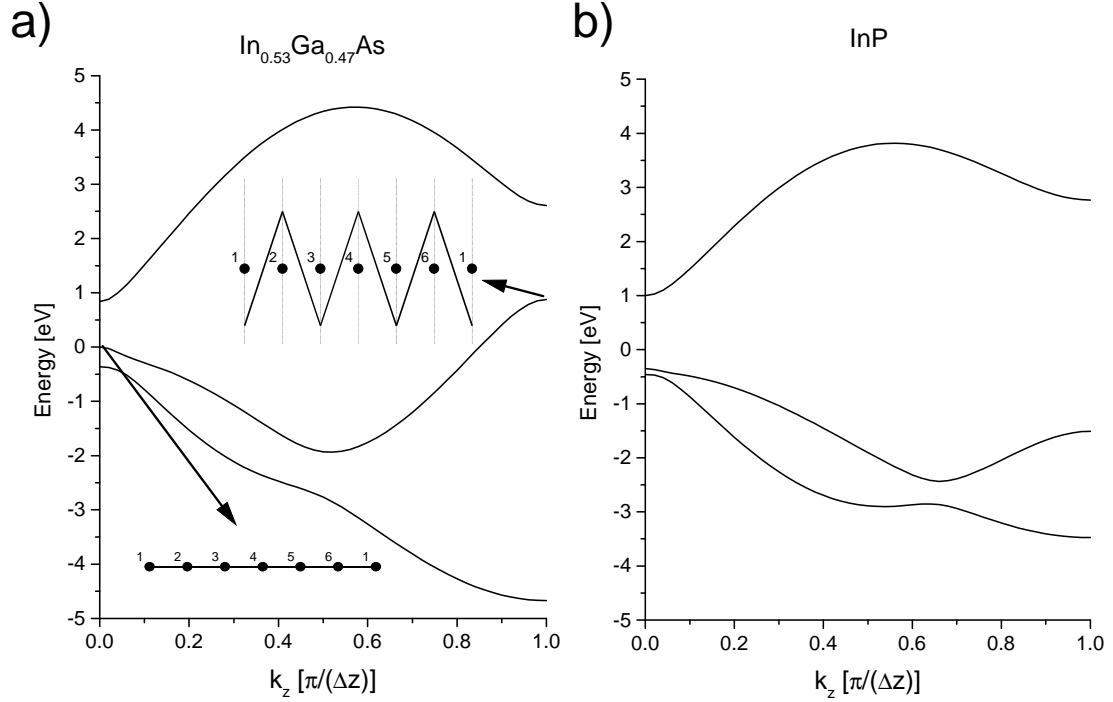


Figure 6.4: Energy *vs.* wavenumber of a hypothetical spurious solution. (a) [(b)] shows the dispersion relation for $\text{In}_{0.53}\text{Ga}_{0.47}\text{As}$ (InP). The insets show two kinds of light hole envelope functions ($k_z = 0$ and $k_z = \frac{\pi}{\Delta z}$) satisfying cyclic boundary conditions. Δz is taken to be half the unit cell constant.

ferential equations from the EMA Hamiltonian (6.4) can be solved analytically to obtain flat envelopes. The FDM should give the same results. From Fig. 6.4.a), it is seen that the point $k_z = 0$ reproduces the expected results. However, an envelope with $k_z = \frac{\pi}{\Delta z}$ will also satisfy the boundary conditions. The existence of this kind of solutions is unavoidable in the FDM but, at least, one can demand that they lie far from the energy range of interest. This is indeed the case with InP in Fig. 6.4.b) but, on the other hand, the LH band of $\text{In}_{0.53}\text{Ga}_{0.47}\text{As}$ enters the gap, thus giving opportunity to the presence of SSs in the midgap.

Also, one finds that, for $k_z = \frac{\pi}{\Delta z}$, the energy of the three branches (with E_v set

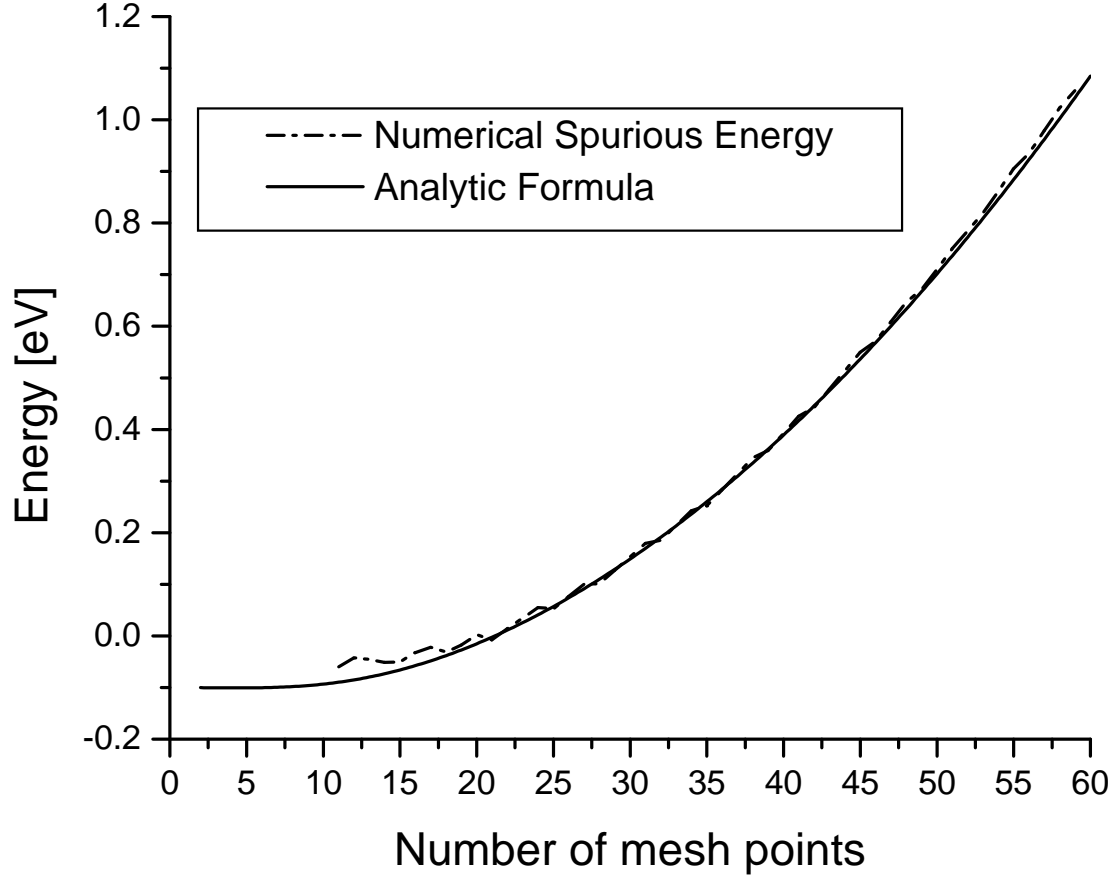


Figure 6.5: Prediction from Eq. (6.6) and actual spurious solution energy. The actual spurious energy corresponds to the highest spurious energy in Fig. 6.3.

to zero) is

$$\left\{ E_g + \frac{2\hbar^2}{m\Delta z}, -\frac{4(\gamma_1 + \gamma_2)\hbar^2/m + \Delta_{SO}(\Delta z)^2}{2(\Delta z)^2} \pm \frac{\sqrt{48\gamma_2^2\hbar^4/m^2 - 8(\Delta z)^2\gamma_2\Delta_{SO}\hbar^2/m + \Delta_{SO}^2(\Delta z)^4}}{2(\Delta z)^2} \right\}. \quad (6.6)$$

One can argue that, since the well region in the SL is quite wide, the first electron and hole levels will be close to the corresponding edges. Then, the analytic expression corresponding to the plus sign in front of the square root in Eq. (6.6), describing the energy of the $k_z = \frac{\pi}{\Delta z}$ light hole (LH) states in bulk $\text{In}_{0.53}\text{Ga}_{0.47}\text{As}$ can be used to make a rough approximation of the energy of the SS in the superlattice (SL) studied in Fig. 6.3. Figure 6.5 shows a comparison of the energy of the SS estimated this way

and the highest energy SS from the calculation in Fig. 6.3. The agreement is quite good, and it supports the claim that the mechanism presented in the previous and the present sections is responsible for the apparition of this class of mesh-dependent SSs. It is expected that a similar study to the one in Sec. 6.3, but extended this way

$$\mathbf{H}_{\sigma,\sigma-1}\mathbf{F}_{\sigma-1} + \mathbf{H}_{\sigma,\sigma}\mathbf{F}_{\sigma} + \mathbf{H}_{\sigma,\sigma+1}\mathbf{F}_{\sigma+1} = E\mathbf{F}_{\sigma} \quad (6.7)$$

$$\mathbf{H}_{\sigma+1,\sigma}\mathbf{F}_{\sigma} + \mathbf{H}_{\sigma+1,\sigma+1}\mathbf{F}_{\sigma+1} + \mathbf{H}_{\sigma+1,\sigma+2}\mathbf{F}_{\sigma+2} = E\mathbf{F}_{\sigma+2} \quad (6.8)$$

and keeping Eq. (6.2) could describe lower energy SSs. The condition that will be derived is expected at least to delay the apparition of these lower energy SSs.

The SSs will first originate from the eigenvalue in Eq. (6.6) with the plus sign in front of the square root (*i.e.*, the LH band). A reasonable requirement to avoid solutions in the gap is that the LH energy for $k_z = \frac{\pi}{\Delta z}$ be less than the valence band edge (which is set to zero). Therefore, it is wanted that

$$\sqrt{48\gamma_2^2\hbar^4/m^2 - 8(\Delta z)^2\gamma_2\Delta_{SO}\hbar^2/m + \Delta_{SO}^2(\Delta z)^4} < 4(\gamma_1 + \gamma_2)\hbar^2/m + \Delta_{SO}(\Delta z)^2 \quad (6.9)$$

or, equivalently, taking squares on both sides of the inequality,

$$0 < -2(2\gamma_2^2 - 2\gamma_1\gamma_2 - \gamma_1^2)\frac{\hbar^2}{m} + \Delta_{SO}(\gamma_1 + 2\gamma_2)(\Delta z)^2. \quad (6.10)$$

Assuming $\gamma_1 + 2\gamma_2 > 0$, the condition that the mesh spacing must satisfy in order to ensure that there are no solutions in the gap is obtained:

$$(\Delta z)^2 > \frac{2(2\gamma_2^2 - 2\gamma_1\gamma_2 - \gamma_1^2)\frac{\hbar^2}{m}}{\Delta_{SO}(\gamma_1 + 2\gamma_2)}. \quad (6.11)$$

This condition will always be satisfied if the right hand side of that inequality is less than zero. So this yields the condition that the modified Luttinger parameters must satisfy in order to avoid SSs in the FDM method for any mesh spacing:

$$\frac{1 - \sqrt{3}}{2}\gamma_1 < \gamma_2 < \frac{1 + \sqrt{3}}{2}\gamma_1 \Rightarrow -0.3666025\gamma_1 < \gamma_2 < 1.366025\gamma_1. \quad (6.12)$$

If the above condition is not satisfied for a material, Eq. (6.11) can be used to find a safe mesh spacing. Of course, for some choice of parameters the safe mesh spacing will be too big for the solutions to be accurate. In that case, a different set of parameters or a different solution method for the EMA equations should be employed.

On the other hand, if $\gamma_1 + 2\gamma_2 < 0$, it is easy to see from Eq. (6.10) that Δz must satisfy

$$(\Delta z)^2 < \frac{2(2\gamma_2^2 - 2\gamma_1\gamma_2 - \gamma_1^2) \frac{\hbar^2}{m}}{\Delta_{SO}(\gamma_1 + 2\gamma_2)}, \quad (6.13)$$

which can only be satisfied if the right hand side is positive, leading to the conditions (6.12) again.

Finally, imposing that the branch with the minus sign in front of the square root in Eq. (6.6) (the spin-orbit band) also has a negative energy at $k_z = \frac{\pi}{\Delta z}$ results in the requirement

$$-\sqrt{48\gamma_2^2\hbar^4/m^2 - 8(\Delta z)^2\gamma_2\Delta_{SO}\hbar^2/m + \Delta_{SO}^2(\Delta z)^4} < 4(\gamma_1 + \gamma_2)\hbar^2/m + \Delta_{SO}(\Delta z)^2. \quad (6.14)$$

In principle, this requirement can be satisfied in two ways. The first way is that the absolute value of the right hand side (RHS) is smaller than the absolute value of the left hand side (LHS). However, this leads to conditions that are not compatible with demanding that the light hole band has an energy below the band edge at $k_z = \frac{\pi}{\Delta z}$. The other way that the inequality can be satisfied is requiring that absolute value of the RHS is positive and larger than the absolute value of the LHS. It is not hard to see that this leads to Eq. (6.9) and, therefore, will result in the same set of conditions (6.12).

6.4.1 The InP/In_{0.53}Ga_{0.47}As SL revisited

Looking back at the parameters for In_{0.53}Ga_{0.47}As in Table 6.1, it is seen that $-0.3666025\gamma_1 = -0.67 > -0.87 = \gamma_2$. Therefore, the conditions for the absence of spurious solutions in the gap were not satisfied. For that case, any mesh spacing smaller than 22.4 Å would have triggered the appearance of a spurious solution close

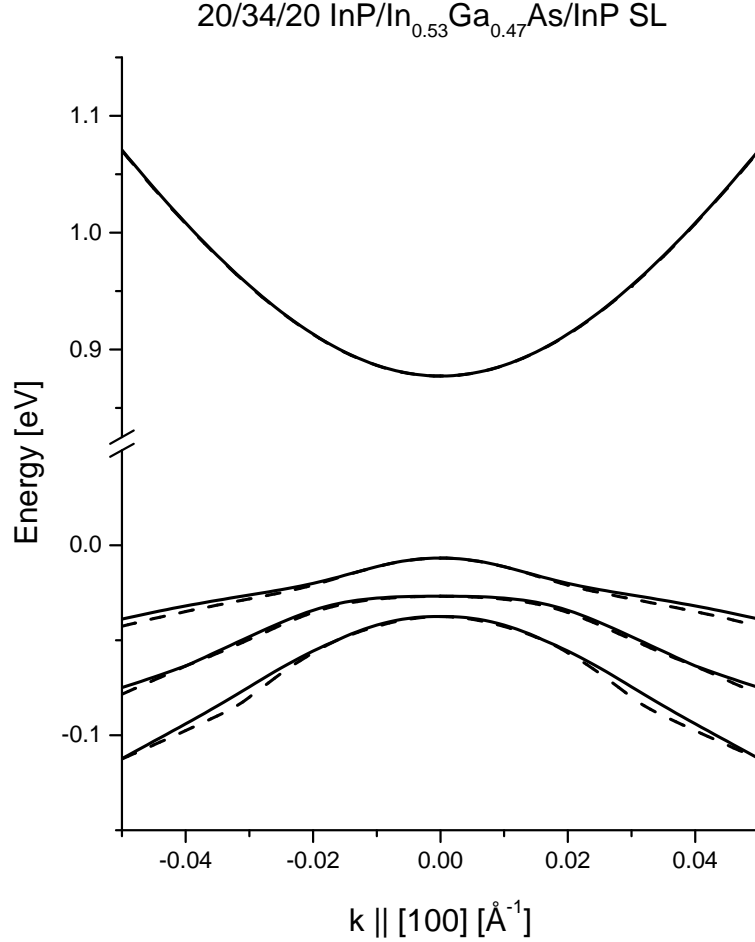


Figure 6.6: Bands of an 88 Å/65 Å InP/In_{0.53}Ga_{0.47}As SL showing no spurious solutions.

to or in the gap.

A different set of Luttinger parameters for In_{0.53}Ga_{0.47}As was found [39] and the band structure of the InP/In_{0.53}Ga_{0.47}As superlattice recalculated. These bands are plotted in Fig. 6.6, and they show no spurious solutions. The Luttinger parameters used are listed in Table 6.2. They are calculated from the ones shown in Ref. [39] using Eq. (5.11).

	γ_1	γ_2	γ_3
In _{0.53} Ga _{0.47} As	1.63	-0.27	-1.37

Table 6.2: Luttinger parameters for In_{0.53}Ga_{0.47}As satisfying the condition for the absence of SSs (adapted from Ref. [39]).

	γ_1	γ_2	γ_3	$\frac{1-\sqrt{3}}{2}\gamma_1$	$\frac{1+\sqrt{3}}{2}\gamma_1$
AlP	2.32	-0.52	0.57	-0.85	3.17
AlAs	1.74	-0.37	0.42	-0.64	2.38
AlSb	1.44	-0.35	0.39	-0.53	1.97
GaP	1.62	-0.31	0.37	-0.59	2.22
GaAs	2.01	-0.41	0.46	-0.74	2.75
GaSb	2.58	-0.58	0.65	-0.95	3.53
InP	1.49	-0.31	0.37	-0.55	2.04
InAs	2.05	-0.44	0.48	-0.75	2.80
InSb	2.59	-0.60	0.67	-0.95	3.54

Table 6.3: Check for possibility of spurious solutions in the Luttinger parameters from Lawaetz [41].

6.5 Potential for spurious solutions in sets of Luttinger parameters

A great amount of literature can be found about calculations and measurement of Luttinger parameters for compounds and alloys. A comprehensive review was published by Vurgaftman *et al.* [40]. Another commonly used list of parameters was tabulated by Lawaetz [41]. In this section the condition derived in Eq. (6.12) will be applied to the listed parameters in the above two references for selected materials to detect the potential presence of SSs when using those data.

Table 6.3 lists the 8-band Luttinger parameters adapted from Lawaetz [41] for a set of III-Vs and the limits of the interval where γ_2 must lie in order to avoid SSs. It is seen that none of those sets of parameters present a potential for SSs. An interesting feature of writing the modified Luttinger parameters is that they depend strongly on the anion but weakly on the cation (except when the cation is Al).

However, the situation for alloys requires a more careful consideration. A possible approach to obtain the modified Luttinger parameters for alloys such as $\text{In}_x\text{Ga}_{1-x}\text{As}$ or $\text{Al}_x\text{Ga}_{1-x}\text{As}$ is to take averages of the parameters of the base compounds. If this is the approach followed, the calculated parameters are not at risk of producing SSs. On the other hand, another plausible approach would be to take the direct [42] or reciprocal [34] averages of the true Luttinger parameters instead, and then use Eq. (5.11) to

	γ_1	γ_2	γ_3	$\frac{1-\sqrt{3}}{2}\gamma_1$	$\frac{1+\sqrt{3}}{2}\gamma_1$
AlP	1.72	-0.10	0.42	-0.63	2.36
AlAs	1.49	-0.31	0.29	-0.55	2.04
AlSb	2.57	-0.12	0.66	-0.94	3.51
GaP	0.42	-1.32	1.12	-0.15	0.58
GaAs	0.66	-1.10	-0.23	-0.24	0.90
GaSb	2.32	-0.84	0.46	-0.85	3.16
InP	0.23	-0.82	-0.32	-0.09	0.32
InAs	2.81	-0.09	0.61	-1.03	3.84
InSb	1.75	-1.02	-0.02	-0.64	2.39

Table 6.4: Check for possibility of spurious solutions in the Luttinger parameters from Vurgaftman *et al.* [40].

find the modified parameters. Since the $\mathbf{k}\cdot\mathbf{p}$ Hamiltonian is mostly expressed in terms of the true Luttinger parameters, the averages of these are mainly used in the literature. Nevertheless, a linear interpolation for an alloy of all the terms in Eq. (5.11) can introduce considerable bowing in the modified (aka. Kane [43]) parameters, so one should be careful when calculating Kane parameters using the latter approach and make sure to check that the condition (6.12) is satisfied. An experimental study of the hole effective masses as a function, say, of the Ga composition, and then finding from there the Kane parameters using Eqs. (5.20) should be able to discern which one of the two approaches is more accurate or whether a more complex interpolation formula should be used.

The bulk Luttinger parameters tabulated for III-Vs in Vurgaftman *et al.* [40] are more dangerous to use in a FDM implementation of the EMA. Table 6.4 shows the Kane parameters calculated from the Luttinger parameters in Ref. [40]. Any trace of independence of the parameters respect to the cation is lost. The independence seen in Table 6.3 might come from underlying assumptions in the way Lawaetz calculates the parameters, but a test of this conjecture is out of the scope of this Chapter. It is easy to check that GaP, GaAs, InP and InSb don't satisfy Eq. (6.12), and that GaSb is close to the lower limit. Figure 6.7 shows the energy of the states given by Eq. (6.2) for GaAs and GaSb computed with Eq. (6.5) using parameters from Ref. [40]. Again, the light hole and split off bands start bending downward reproducing the physical

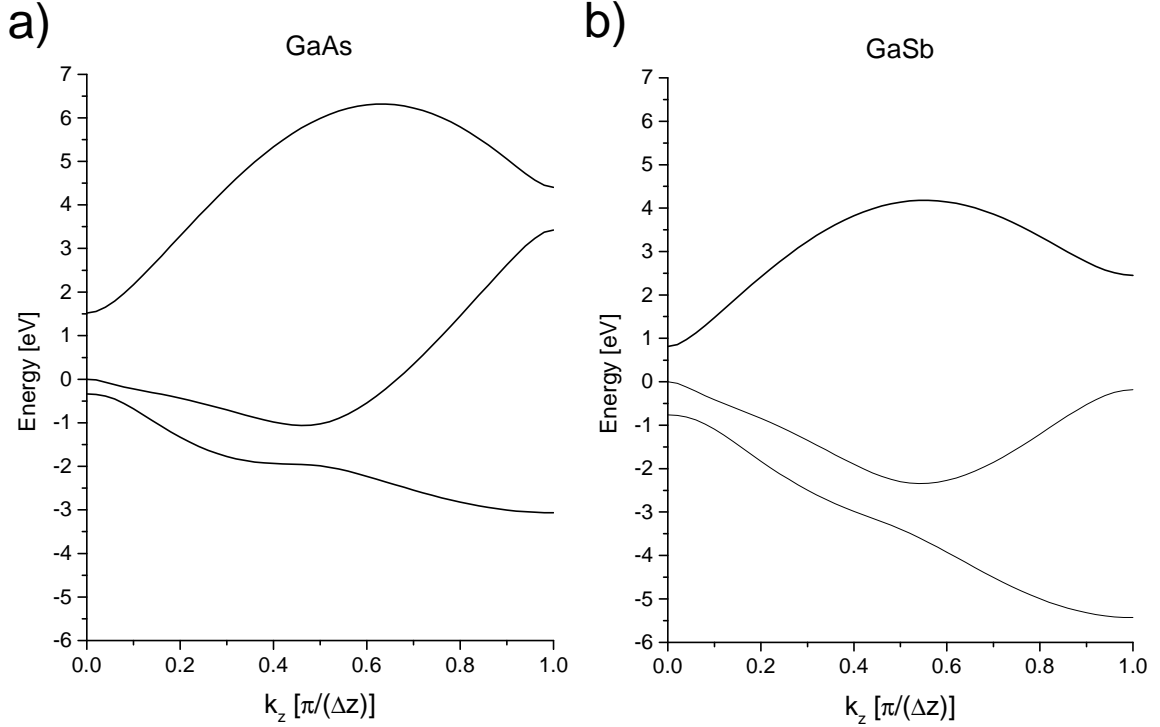


Figure 6.7: Plot (a) [(b)] is the same as Fig. 6.4 but for GaAs (GaSb) with Luttinger parameters from Ref. [40].

effective mass, but at about $k_z = \frac{\pi}{2\Delta z}$ the LH band bends up and enters the gap region for GaAs and finishes close to it for GaSb. In the case of GaAs the spurious solution would be out of the energy range of interest, but still there might be problems due to other lower light hole folded bands that could invade the gap region. The set of GaSb parameters isn't ideal for the FDM method, either, because the energy of the LH solution at $k_z = \frac{\pi}{2\Delta z}$ is too close to the valence band edge [see Fig. 6.7.b)]. This state might interfere with states mainly in the GaSb layer in a quantum well or superlattice.

6.6 Summary

In summary, a new class of spurious solutions for the effective mass approximation, which appears when trying to solve the EMA equations with the finite difference method, has been presented. A general approach to the study of this class of

SSs in systems requiring the solution of a set of equations $\mathbf{H}_{\sigma,\sigma-1}\mathbf{F}_{\sigma-1} + \mathbf{H}_{\sigma,\sigma}\mathbf{F}_{\sigma} + \mathbf{H}_{\sigma,\sigma+1}\mathbf{F}_{\sigma+1} = E\mathbf{F}_{\sigma}$ has been formulated, and has been applied to the 8-band EMA. A set of conditions has been derived to predict the appearance of SSs. The proposed theory shows excellent agreement with the numerical values of the spurious energies. Finally, popular tabulations of Luttinger parameters have been examined with the derived conditions to identify those that might be problematic when carrying out FDM 8-band EMA calculations. The table by Lawaetz [41] is free from danger, but the parameters in the review article by Vurgaftman *et al.* [40] can lead to SSs for some of the compounds listed.

Bibliography

- [1] J. M. Luttinger and W. Kohn, Phys. Rev. **97**, 869 (1955).
- [2] G. Bastard, *Heterojunctions and Semiconductor Superlattices*, 2nd ed. (Springer-Verlag New York, New York, Ny, 1986).
- [3] S. R. White and L. J. Sham, Phys. Rev. Lett. **47**, 879 (1981).
- [4] G. Bastard, Phys. Rev. B **24**, 5693 (1981).
- [5] G. Bastard, Phys. Rev. B **25**, 7584 (1982).
- [6] G. D. Sanders and Y. C. Chang, Phys. Rev. B **32**, 4282 (1985).
- [7] L. C. Andreani, A. Pasquarello, and F. Bassani, Phys. Rev. B **36**, 5887 (1987).
- [8] P. C. Sercel and K. J. Vahala, Phys. Rev. B **42**, 3690 (1990).
- [9] G. A. Baraff and D. Gershoni, Phys. Rev. B **43**, 4011 (1991).
- [10] H. Ando, S. Nojima, and H. Kanbe, J. Appl. Phys. **74**, 6383 (1993).
- [11] U. Merkt, J. Huser, and M. Wagner, Phys. Rev. B **43**, 7320 (1991).
- [12] G. T. Einevoll, Phys. Rev. B **45**, 3410 (1992).
- [13] I. Suemune, IEEE J. Quantum Elect. **27**, 1149 (1991).
- [14] M. Rosenzweig, M. Mohrle, H. Duser, and H. Venghaus, IEEE J. Quantum Elect. **27**, 1804 (1991).
- [15] S. L. Chuang, IEEE J. Quantum Elect. **32**, 1791 (1996).
- [16] H. Schneider, F. Fuchs, B. Dischler, J. D. Ralston, and P. Koidl, Appl. Phys. Lett. **58**, 2234 (1991).

- [17] P. Man and D. S. Pan, Appl. Phys. Lett. **61**, 2799 (1992).
- [18] J. J. Shi and E. M. Goldys, IEEE T. Electron Dev. **46**, 83 (1999).
- [19] R. Wessel and M. Altarelli, Phys. Rev. B **39**, 12802 (1989).
- [20] J. R. Soderstrom, E. R. Brown, C. D. Parker, L. J. Mahoney, J. Y. Yao, T. G. Andersson, and T. C. McGill, Appl. Phys. Lett. **58**, 275 (1991).
- [21] C. Chao and S. L. Chuang, Phys. Rev. B **43**, 7027 (1991).
- [22] B. Lee, Superlattices And Microstructures **14**, 295 (1993).
- [23] V. V. Paranjape, Phys. Rev. B **52**, 10740 (1995).
- [24] M. Schuurmans and G. W. 't Hooft, Phys. Rev. B **31**, 8041 (1985).
- [25] M. J. Godfrey and A. M. Malik, Phys. Rev. B **53**, 16504 (1996).
- [26] L. W. Wang, Phys. Rev. B **61**, 7241 (2000).
- [27] P. C. Sercel, A. L. Efros, and M. Rosen, Phys. Rev. Lett. **83**, 2394 (1999).
- [28] W. Jaskolski, R. Oszwaldowski, and G. W. Bryant, Vacuum **63**, 191 (2001).
- [29] R. Eppenga, M. F. H. Schuurmans, and S. Colak, Phys. Rev. B **36**, 1554 (1987).
- [30] B. A. Foreman, Phys. Rev. B **56**, 12748 (1997).
- [31] M. G. Burt, Superlattices And Microstructures **23**, 531 (1998).
- [32] Y. X. Liu, D. Z.-Y. Ting, and T. C. McGill, Phys. Rev. B **54**, 5675 (1996).
- [33] S. L. Chuang and C. S. Chang, Semicond. Sci. Technol. **12**, 252 (1997).
- [34] O. Stier, M. Grundmann, and D. Bimberg, Phys. Rev. B **59**, 5688 (1999).
- [35] Q. G. Zhu and H. Kroemer, Phys. Rev. B **27**, 3519 (1983).
- [36] D. L. Smith, private communication.

- [37] D. Z.-Y. Ting, E. T. Yu, and T. C. McGill, Phys. Rev. B **45**, 3583 (1992).
- [38] G. Dresselhaus, Phys. Rev. **100**, 580 (1955).
- [39] J. Taylor and V. Tolstikhin, J. Appl. Phys. **87**, 1054 (2000).
- [40] I. Vurgaftman, J. R. Meyer, and L. R. Ram-Mohan, J. Appl. Phys. **89**, 5815 (2001).
- [41] P. Lawaetz, Phys. Rev. B **4**, 3460 (1971).
- [42] S. L. Chuang, Phys. Rev. B **43**, 9649 (1991).
- [43] R. Enderlein, G. M. Sipahi, L. M. R. Scolfaro, and J. R. Leite, Phys. Stat. Sol. (B) **206**, 623 (1998).

Chapter 7 Spin filters based on resonant tunneling

7.1 Introduction

A major challenge for the development of spintronics [1–4] is the fabrication of a spin injector. In the context of this chapter, spin injection refers to injection into a semiconductor, as opposed to injection into a paramagnetic metal, which has been demonstrated [5]. Up to date, there have been demonstrations of spin injection from a ferromagnet [6] and dilute magnetic semiconductors (DMS) [7, 8] into a semiconductor. Recent studies show the possibility of filtering the spin of electrons traveling through an appropriately designed resonant tunneling structure [9] in order to obtain a spin injector [10] with a high degree of spin polarization using only nonmagnetic materials. The operating principle of this device would be the Rashba effect (see Ref. [11] and Chapter 2) appearing in asymmetric structures.

In this chapter, a variation on the resonant tunneling spin filter described in Ref. [10] proposed by Ting *et al.* [12] is considered. In this device, the electrons tunnel through the valence band of the active region rather than the conduction band. This allows the electron spins to interact with the strongly spin orbit split valence band states. The focus will fall on how the inclusion of bulk inversion asymmetry (BIA) affects the tunneling properties on which the device is based.

Section 7.2 describes the method used to find the transmission coefficients for the resonant tunneling structures. In Sec. 7.4, the principles of operation of the asymmetric resonant tunneling diode (aRTD) is reviewed and the effects of BIA on the aRTD are studied. Section 7.5 does the same for the asymmetric resonant interband tunneling diode (aRITD). Finally, a summary of the results is presented.

7.2 Theoretical method

The method used to find the transmission coefficients is the multiband quantum transmitting boundary method (MQTBM) described in Ref. [13] adapted to the $\mathbf{k} \cdot \mathbf{p}$ formalism. This adaptation differs from the one in Ref. [14] in that the method used here to obtain the bulk imaginary band structure is less accurate, but is consistent with the rest of the procedure and thus it avoids the introduction of small spurious solutions. The MQTBM is based on the single band formalism by Frensley [15]. It does not have the stability problems of the transfer matrix method [16, 17] while keeping the efficiency that the S -matrix method [18] loses when solving the stability issues. Also, the $\mathbf{k} \cdot \mathbf{p}$ implementation allows for the use of a wide body of parameters available in the literature and the easy inclusion of strain and magnetic field effects.

7.2.1 The MQTBM

The MQTBM is a method for specifying the boundary conditions appropriate for tunneling in heterostructures. The calculation of the transmission coefficients starts with the construction of the Hamiltonian of the system. For that purpose, the effective mass approximation (EMA) Hamiltonian is implemented as described in Sec. 5.4. In that section, it was shown that the solution of the EMA equations in the finite difference method (FDM) required the solution of a set of equations

$$\mathbf{H}_{\sigma,\sigma-1}\mathbf{F}_{\sigma-1} + \mathbf{H}_{\sigma,\sigma}\mathbf{F}_{\sigma} + \mathbf{H}_{\sigma,\sigma+1}\mathbf{F}_{\sigma+1} = E\mathbf{F}_{\sigma}, \quad (5.47)$$

where the symbols were defined in Sec. 5.4. For the case of tunneling, Eq. (5.47) is more conveniently written as

$$\mathbf{H}_{\sigma,\sigma-1}\mathbf{F}_{\sigma-1} + \bar{\mathbf{H}}_{\sigma,\sigma}\mathbf{F}_{\sigma} + \mathbf{H}_{\sigma,\sigma+1}\mathbf{F}_{\sigma+1} = 0, \quad (7.1)$$

where $\bar{\mathbf{H}}_{\sigma,\sigma}\mathbf{F}_{\sigma} = \mathbf{H}_{\sigma,\sigma}\mathbf{F}_{\sigma} - E\mathbf{F}_{\sigma}$.

Figure 7.1 shows a schematic of a general structure under an applied bias V for which the transmission coefficients are sought. The arrows represent the incoming (I),

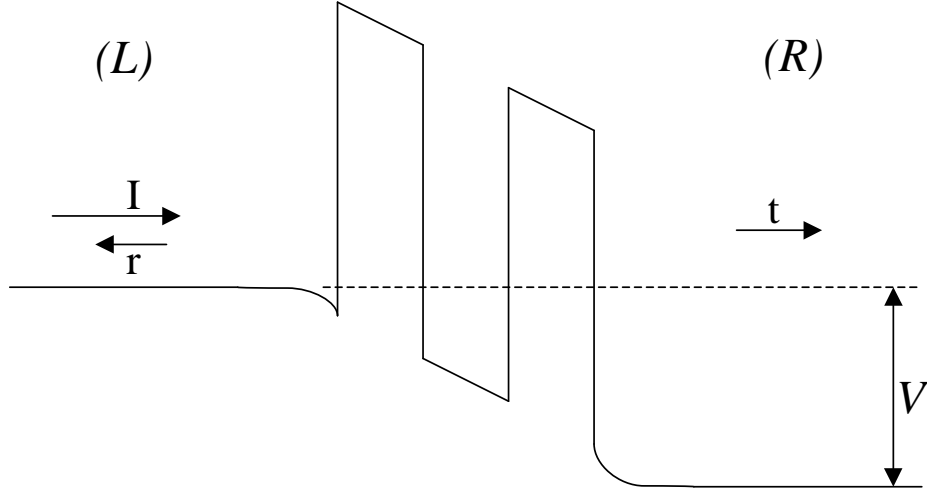


Figure 7.1: Band diagram of a conduction band RTD under an applied bias V . The arrows represent the incoming (I), reflected (r) and transmitted (t) components. The left (right) electrode is labeled by (L) [(R)].

reflected (r) and transmitted (t) components. As plotted, the figure would represent an intraband device—tunneling through the same band as in the incoming state (conduction band in this case), but the development in this section is general to any tunneling structure. The electrodes at the left (L) and right (R) are assumed to have bulk properties and to be in the flat band condition. Under these conditions, the envelope function components of a Bloch state will have the form

$$\mathbf{F}_{\mathbf{k}, \text{ flat band, Bloch}} = \mathbf{B}_{\mathbf{k}} = e^{i\mathbf{k}\cdot\mathbf{r}}\mathbf{C}_{\mathbf{k}}, \quad (7.2)$$

where the $\mathbf{C}_{\mathbf{k}}$ are 8-component vectors whose components weight the contribution of each of the bulk zone center states. In particular, the $\mathbf{B}_{\mathbf{k}}$ will satisfy

$$\mathbf{B}_{\sigma} = e^{ik_z d}\mathbf{B}_{\sigma-1}, \quad (7.3)$$

where σ is the mesh point index in the discretized structure, d is the mesh point separation and k_z is the electron wavevector in the z direction. The Bloch states $\mathbf{B}_{\mathbf{k}}$

of course satisfy Eq. (5.47), which can be rewritten in a transfer matrix form [13]

$$\begin{pmatrix} -\mathbf{H}_{\sigma,\sigma-1}^{-1}\bar{\mathbf{H}}_{\sigma,\sigma} & -\mathbf{H}_{\sigma,\sigma-1}^{-1}\mathbf{H}_{\sigma,\sigma+1} \\ \mathbf{1} & \mathbf{0} \end{pmatrix} \begin{pmatrix} \mathbf{B}_\sigma \\ \mathbf{B}_{\sigma+1} \end{pmatrix} = e^{-ik_z d} \begin{pmatrix} \mathbf{B}_\sigma \\ \mathbf{B}_{\sigma+1} \end{pmatrix}. \quad (7.4)$$

The above 16×16 eigensystem yields the Bloch states and their corresponding wavevectors—which can be complex, describing in that case evanescent states—for a given energy of the state E and an in-plane wavevector k_{\parallel} . On the other hand, a general state in the left electrode with a definite energy and k_{\parallel} will be a linear combination of the Bloch states found in the solution of Eq. (7.4)

$$|L\rangle = |I\rangle + |r\rangle = \sum_{j=1}^8 I_j |\mathbf{B}_{k_{\parallel}, k_{z,j}}, L\rangle + \sum_{j=9}^{16} r_j |\mathbf{B}_{k_{\parallel}, k_{z,j}}, L\rangle, \quad (7.5)$$

where the k_z 's and the Bloch states

$$|\mathbf{B}_{k_{\parallel}, k_{z,j}}, L\rangle = e^{ik_{\parallel} \cdot \mathbf{r}} e^{ik_{z,j} z} |u_{k_{\parallel}, k_{z,j}}\rangle = e^{ik_{\parallel} \cdot \mathbf{r}} e^{ik_{z,j} z} C_{k_{\parallel}, k_{z,j}}^l |u_{\Gamma}^l\rangle \quad (7.2')$$

have been ordered so that first 8 eight $k_{z,j}$ correspond to propagation towards the right (*i.e.*, $k_{z,j}$ is either positive real or has positive imaginary part for electron states and viceversa for holes) and the last eight to propagation towards the left. Similarly, for the transmitted state

$$|R\rangle = |t\rangle = \sum_{j=1}^8 t_j |\mathbf{B}_{k_{\parallel}, k_{z,j}}, R\rangle. \quad (7.6)$$

Following Ting *et al.* [13], equations for the envelopes at the left and right boundaries can be written by letting \mathbf{I} , \mathbf{r} and \mathbf{t} be the column 8-vectors obtained from putting together the coefficients $\{I_j\}$, $\{r_j\}$ and $\{t_j\}$, respectively:

$$\begin{pmatrix} \mathbf{F}_0 \\ \mathbf{F}_1 \end{pmatrix} = \mathbf{D}^L \begin{pmatrix} \mathbf{I} \\ \mathbf{r} \end{pmatrix} = \begin{pmatrix} \mathbf{D}_{11}^L & \mathbf{D}_{12}^L \\ \mathbf{D}_{21}^L & \mathbf{D}_{22}^L \end{pmatrix} \begin{pmatrix} \mathbf{I} \\ \mathbf{r} \end{pmatrix} \quad (7.7)$$

and

$$\begin{pmatrix} \mathbf{F}_{N-2} \\ \mathbf{F}_{N-1} \end{pmatrix} = \mathbf{D}^R \begin{pmatrix} \mathbf{t} \\ \mathbf{0} \end{pmatrix} = \begin{pmatrix} \mathbf{D}_{11}^R & \mathbf{D}_{12}^R \\ \mathbf{D}_{21}^R & \mathbf{D}_{22}^R \end{pmatrix} \begin{pmatrix} \mathbf{t} \\ \mathbf{0} \end{pmatrix}, \quad (7.8)$$

where \mathbf{D}^L and \mathbf{D}^R are 16×16 matrices whose column vectors are the normalized eigenvectors, arranged in the same order as the eigenvalues, from the solution of Eq. (7.4) in the left or right electrodes. For degenerate k_z 's, the eigenvectors from Eq. (7.4) are orthogonalized. Each \mathbf{D} matrix is divided into submatrices \mathbf{D}_{ij} for convenience.

The incident state \mathbf{I} is specified in the statement of the problem. Therefore, Eq. (7.7) can be viewed as a system of two equations for the three 8-vector unknowns \mathbf{r} , \mathbf{F}_0 and \mathbf{F}_1 . It can be transformed in a single equation with two unknowns

$$\mathbf{F}_0 - \mathbf{D}_{12}^L \mathbf{D}_{22}^{L-1} \mathbf{F}_1 = \left(\mathbf{D}_{11}^L - \mathbf{D}_{12}^L \mathbf{D}_{22}^{L-1} \mathbf{D}_{21}^L \right) \mathbf{I}. \quad (7.9)$$

Similarly, \mathbf{t} can be eliminated from Eq. (7.8) to yield the other boundary condition

$$-\mathbf{D}_{21}^R \mathbf{D}_{11}^{R-1} \mathbf{F}_{N-2} + \mathbf{F}_{N-1} = \mathbf{0}. \quad (7.10)$$

Including the boundary conditions into Eq. (5.48), the wavefunction is found by

solving the sparse linear system

$$\begin{pmatrix}
\mathbf{1} & -\mathbf{D}_{12}^L \mathbf{D}_{22}^{L-1} & \mathbf{0} & \dots & \dots & \dots & \mathbf{0} \\
\mathbf{H}_{1,0} & \bar{\mathbf{H}}_{1,1} & \mathbf{H}_{1,2} & \mathbf{0} & \dots & \dots & \mathbf{0} \\
\mathbf{0} & \mathbf{H}_{2,1} & \bar{\mathbf{H}}_{2,2} & \mathbf{H}_{2,3} & \mathbf{0} & \dots & \mathbf{0} \\
\vdots & \dots & \ddots & \ddots & \ddots & \vdots & \vdots \\
\mathbf{0} & \dots & \dots & \mathbf{0} & \mathbf{H}_{N-2,N-3} & \bar{\mathbf{H}}_{N-2,N-2} & \mathbf{H}_{N-2,N-1} \\
\mathbf{0} & \mathbf{0} & \dots & \dots & \mathbf{0} & -\mathbf{D}_{21}^R \mathbf{D}_{11}^{R-1} & \mathbf{1}
\end{pmatrix}
\begin{pmatrix}
\mathbf{F}_0 \\
\mathbf{F}_1 \\
\mathbf{F}_2 \\
\vdots \\
\mathbf{F}_{N-2} \\
\mathbf{F}_{N-1}
\end{pmatrix}
=
\begin{pmatrix}
\left(\mathbf{D}_{11}^L - \mathbf{D}_{12}^L \mathbf{D}_{22}^{L-1} \mathbf{D}_{21}^L \right) \mathbf{I} \\
\mathbf{0} \\
\mathbf{0} \\
\vdots \\
\mathbf{0} \\
\mathbf{0}
\end{pmatrix}. \quad (7.11)$$

Once the envelope function components for the entire wavefunction have been found, the coefficients of the transmitted part in terms of the Bloch states for the right electrode can be found from Eq. (7.8):

$$\mathbf{t} = \mathbf{D}_{21}^{R-1} \mathbf{F}_{N-1}. \quad (7.12)$$

And from there, the transmission coefficient can be expressed as the sum of transmission coefficients into each Bloch state channel¹:

$$T(E, k_{\parallel}) = \sum_{j=1}^8 |t_j(E, k_{\parallel})|^2 \frac{|v_j(E, k_{\parallel}; R)|}{|v_I(E, k_{\parallel}; L)|}, \quad (7.13)$$

where $v_I(E, k_{\parallel}; L)$ and $v_j(E, k_{\parallel}; R)$ are the velocities along the z direction of the incident and the transmitted bulk plane wave states respectively.

¹The sum should only include terms due to transmitting, as opposed to evanescent, components.

7.2.2 Computation of the velocity of the states

In appendices C and D it has been shown that

$$v_j(E, k_{\parallel}; R) = \frac{1}{\hbar} \left. \frac{\partial E(k_{\parallel}, k_z; R)}{\partial k_z} \right|_{k_z, j} = \frac{1}{\hbar} \left\langle \mathbf{B}_{k_{\parallel}, k_z, j}, R \left| \frac{\partial H(\mathbf{k})}{\partial k_z} \right|_{k_z, j} \right| \mathbf{B}_{k_{\parallel}, k_z, j}, R \rangle. \quad (7.14)$$

The expansion in Eq. (5.43) can be used to evaluate $\partial H(\mathbf{k})/\partial k_z$ and obtain

$$v_j(E, k_{\parallel}; L) = \frac{1}{\hbar} \left\langle \mathbf{B}_{k_{\parallel}, k_z, j}, R \left| 2\mathbf{H}_R^{(2)} k_{z, j} + \mathbf{H}_R^{(1)}(k_{\parallel}) \right| \mathbf{B}_{k_{\parallel}, k_z, j}, R \right\rangle, \quad (7.15)$$

which can be written in matrix notation because, apart from an overall phase factor, the components of $|\mathbf{B}_{k_{\parallel}, k_z, j}, R\rangle$ in the zone center basis are given by the j -th column of \mathbf{D}_{11}^R , $\mathbf{D}_{11, j}^R$:

$$v_j(E, k_{\parallel}; L) = \frac{1}{\hbar} \mathbf{D}_{11, j}^{R \dagger} \left(2\mathbf{H}_R^{(2)} k_{z, j} + \mathbf{H}_R^{(1)} \right) \mathbf{D}_{11, j}^R. \quad (7.16)$$

Incidentally, the operator

$$\hat{v} = \frac{1}{\hbar} (2\mathbf{H}^{(2)} k_z + \mathbf{H}^{(1)}) \quad (7.17)$$

coincides with the current density operator found by Wu *et al.* [19].

7.2.3 Preparation of the incoming states

Since the transmission properties of the spin filter structure are assumed to be spin-dependent, one has to carefully prepare the incoming state and have control over its spin (for electrons) or total angular momentum (for holes). The method used to achieve this is described below.

Electrons

When electrons are injected into the resonant structure, the incoming state can only be a linear combination of right propagating Bloch states in the conduction band (CB) for the left electrode. Since the electrons are assumed to have a given energy E

and parallel component of the wavevector \mathbf{k}_{\parallel} , the intervening Bloch states will have that E and \mathbf{k}_{\parallel} .

The incoming state is given by the first summand in Eq. (7.5):

$$|I\rangle = \sum_{j \in CB} I_j |\mathbf{B}_{k_{\parallel}, k_{z,j}}, L\rangle, \quad (7.18)$$

where the sum over Bloch states only includes the two in the CB satisfying the E and \mathbf{k}_{\parallel} requirements.

If the electron spin is required to point in the θ, φ direction, first one must construct the dimensionless spin operator in an arbitrary direction $\sigma_{\theta, \varphi}$:

$$\sigma_{\theta, \varphi} = \sigma_x \sin \theta \cos \varphi + \sigma_y \sin \theta \sin \varphi + \sigma_z \cos \theta, \quad (7.19)$$

where the σ_i 's are derived from Eqs. (5.37)-(5.39).

At first it would seem logical to look for eigenstates of $\sigma_{\theta, \varphi}$, but states away from the zone center will have a finite hole component. This will cause electron states to cease being spin eigenstates because holes don't have a definite spin. Therefore, one must satisfy oneself with requiring that the expectation value of $\sigma_{\theta, \varphi}$ is maximized. That is, one seeks a set of $\{I_j\}$'s such that

$$\langle \sigma_{\theta, \varphi} \rangle_I = \sum_{j, l \in CB} I_l^* I_j \langle \mathbf{B}_{k_{\parallel}, k_{z,l}}, L | \sigma_{\theta, \varphi} | \mathbf{B}_{k_{\parallel}, k_{z,j}}, L \rangle \quad (7.20)$$

is maximized. These matrix elements are taken with respect to the primitive cell in the left electrode right before entering the active region of the device. This is so to make sure the electron is coming into the structure with the desired spin. If the matrix elements were taken all over the crystal, the elements relating states with $k_{z,l} \neq k_{z,j}$ would vanish by the space group selection rules. Physically, this translates into the fact that, when the Kramers degeneracy is broken, it is impossible to construct a state that will maximize $\langle \sigma_{\theta, \varphi} \rangle_I$ at all points of the space at the same time because the difference in k_z 's will affect the relative phases of the Bloch states. This is seen

in the following example. Consider a free electron described by the wavefunction

$$\Psi(x, t) = e^{i[kx - \omega t]} \begin{pmatrix} 1/\sqrt{2} \\ 0 \end{pmatrix} + e^{i[(k+\Delta k)x - \omega t]} \begin{pmatrix} 0 \\ 1/\sqrt{2} \end{pmatrix}, \quad (7.21)$$

where the same ω indicates that even if the two components have different wavevector, there is some (spin-dependent) mechanism putting their energies together. It is easily seen that the expectation value of the, say, x component of the spin is space dependent:

$$\langle \sigma_x \rangle(x) = \Psi^\dagger \sigma_x \Psi = \cos \Delta k x, \quad (7.22)$$

and that is why $\langle \sigma_{\theta, \varphi} \rangle_I$ is maximized as close to the active region as possible.

In structures presenting Rashba splitting (cf. Chapter 2), the separation between the k_z 's with the same energy is of the order of $\Delta k \approx 10^{-3} \text{\AA}^{-1}$. At typical values of the Fermi radius k_F , it takes about 3000\AA for the relative phase of the two Bloch states to change by π . Of course, real electrons in a crystal will have some wavepacket size. As long as this wavepacket size is substantially smaller than these 3000\AA , one can say that the spin of the electron is the same throughout its spatial extent. Another way to think about it is that the spin of the electron will be independent of space if the spread in \mathbf{k} space corresponding to its localization is bigger than Δk . If this condition is not fulfilled, taking a snapshot in time and looking along the z direction one would see the spin precessing in a helix-like fashion.

Therefore, instead of maximizing the expression in Eq. (7.20), one should construct

$$|I\rangle = \sum_{j \in CB} I_j |u_{k_{\parallel}, k_{z,j}}\rangle \quad (7.23)$$

and maximize

$$\langle \sigma_{\theta, \varphi} \rangle_I = \langle I | \sigma_{\theta, \varphi} | I \rangle \quad (7.20')$$

subject to the constraint

$$\langle I | I \rangle = 1. \quad (7.24)$$

This is an optimization problem that can be solved with the standard Lagrange multiplier technique. Since the $|u_{k_{\parallel}, k_z, j}\rangle$'s in $|I\rangle$ need not be orthogonal with one another, it easily seen that the optimization procedure leads to the solution of a generalized eigenvalue problem

$$\hat{\sigma}\mathbf{I} = \lambda\hat{\mathbf{g}}\mathbf{I}, \quad (7.25)$$

where, for electrons, $\hat{\sigma}$ is a 2×2 matrix whose matrix elements are

$$\sigma_{jl} = \left\langle u_{k_{\parallel}, k_z, j} \left| \sigma_{\theta, \varphi} \right| u_{k_{\parallel}, k_z, l} \right\rangle, \quad (7.26)$$

and $\hat{\mathbf{g}}$ is a metric tensor with elements

$$g_{jl} = \langle u_{k_{\parallel}, k_z, j} | u_{k_{\parallel}, k_z, l} \rangle. \quad (7.27)$$

Holes

The determination of the coefficients \mathbf{I} for holes is quite similar to the electron case. The main difference is that one is presented with the dilemma of choosing the incoming state to have a given spin or making it have a given total angular momentum. Of course, the same discussion as for the electron case applies, and, for a fixed E and \mathbf{k}_{\parallel} , only states that maximize the expectation value of the chosen measurable quantity can be constructed. Physically, holes in the valence bands of bulk zincblendes are better characterized by their total angular momentum, so the incoming states will be constructed maximizing the expectation value of

$$\langle J_{\theta, \varphi} \rangle_I = \sum_{j, l \in CB} I_l^* I_j \left\langle \mathbf{B}_{k_{\parallel}, k_z, l}, L \left| J_{\theta, \varphi} \right| \mathbf{B}_{k_{\parallel}, k_z, j}, L \right\rangle, \quad (7.28)$$

where $J_{\theta, \varphi}$ is the (dimensionless) total angular momentum along an arbitrary axis, and is defined analogously to Eq. (7.19). The angular momentum components along

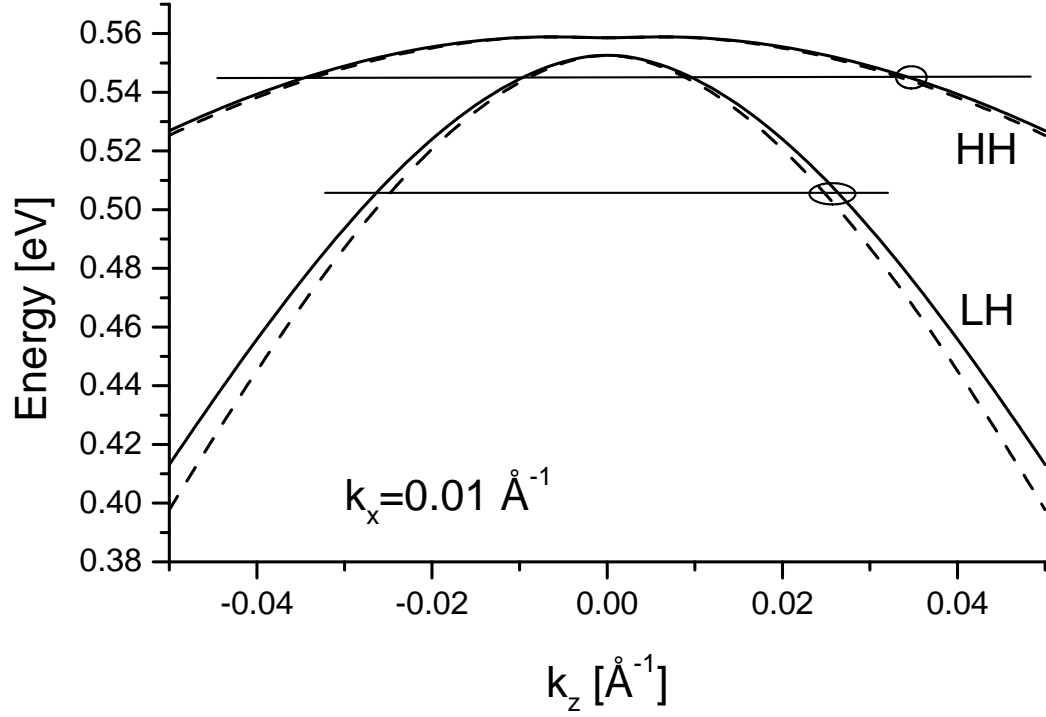


Figure 7.2: Bands of InAs for $\mathbf{k}_{\parallel} = (0.01, 0)\text{\AA}^{-1}$ as a function of k_z . The horizontal lines indicate possible energies of the incoming particle, and the circles signal the states whose linear combination creates an incoming state with heavy or light hole character.

the x, y and z axes are given by

$$J_i = \begin{pmatrix} J_i^{1/2} & 0 & 0 \\ 0 & J_i^{3/2} & 0 \\ 0 & 0 & J_i^{1/2} \end{pmatrix}, \quad (7.29)$$

with

$$J_x^{1/2} = \begin{pmatrix} 0 & 1 \\ 1 & 0 \end{pmatrix} \quad J_y^{1/2} = \begin{pmatrix} 0 & -i \\ i & 0 \end{pmatrix} \quad J_z^{1/2} = \begin{pmatrix} 1 & 0 \\ 0 & -1 \end{pmatrix} \quad (7.30)$$

and

$$\begin{aligned}
 J_x^{3/2} &= \begin{pmatrix} 0 & \sqrt{3} & 0 & 0 \\ \sqrt{3} & 0 & 2 & 0 \\ 0 & 2 & 0 & \sqrt{3} \\ 0 & 0 & \sqrt{3} & 0 \end{pmatrix} & J_y^{3/2} &= \begin{pmatrix} 0 & -\sqrt{3}i & 0 & 0 \\ \sqrt{3}i & 0 & -2i & 0 \\ 0 & 2i & 0 & -\sqrt{3}i \\ 0 & 0 & \sqrt{3}i & 0 \end{pmatrix} \\
 J_z^{3/2} &= \begin{pmatrix} 3 & 0 & 0 & 0 \\ 0 & 1 & 0 & 0 \\ 0 & 0 & -1 & 0 \\ 0 & 0 & 0 & -3 \end{pmatrix}, & & & & (7.31)
 \end{aligned}$$

and the rest of the procedure is analogous to the electron case.

7.2.4 Transmission coefficients and transmitted spin for an ensemble of electrons

In normal operation of the device, the incoming spins will be randomly oriented. If the approximations that *a*) they come from degenerate bands and *b*) that spin is a good quantum number are used to simplify the calculations, they can be described by the following density matrix

$$\hat{\rho}_I = \frac{1}{4\pi} \int_{\Omega} |\uparrow_{\Omega}\rangle \langle \uparrow_{\Omega}| d\Omega, \quad (7.32)$$

where the integral is over spins pointing in any direction with equal probability and $|\uparrow_{\Omega}\rangle$ is a spin pointing in the direction given by the solid angle Ω . This integral can be easily performed to obtain

$$\hat{\rho}_I = \frac{1}{2} (|\uparrow_{\theta,\varphi}\rangle \langle \uparrow_{\theta,\varphi}| + |\downarrow_{\theta,\varphi}\rangle \langle \downarrow_{\theta,\varphi}|), \quad (7.33)$$

where $|\uparrow_{\theta,\varphi}\rangle$ ($|\downarrow_{\theta,\varphi}\rangle$) labels a spin up (down) along the direction given by the polar angles θ and φ . Note that Eq. (7.33) will hold no matter what the choice for θ and

φ is, therefore the angle labels are dropped.

If t_{ij} denotes the component of the transmitted state for spin j when the incident state is a spin i , the density matrix for the transmitted ensemble will be

$$\hat{\rho}_t = \frac{1}{2} \sum_{i,j,k \in \uparrow, \downarrow} t_{ij} t_{ik}^* |j\rangle \langle k|. \quad (7.34)$$

The transmission coefficient will be given by the ratio of currents of the transmitted respect to the incident state. From Appendix C it is easily seen that ratio of probability currents can be given as

$$T(E, k_{\parallel}) = \frac{\text{tr}(\hat{\rho}_t \hat{v})}{\text{tr}(\hat{\rho}_I \hat{v})}, \quad (7.35)$$

where \hat{v} is the velocity operator as defined in Appendix D. Evaluating the traces in this equation using the $|\uparrow\rangle, |\downarrow\rangle$ basis yields

$$T(E, k_{\parallel}) = \frac{(|t_{\uparrow\uparrow}|^2 + |t_{\downarrow\uparrow}|^2)v_{\perp\uparrow,t} + (|t_{\downarrow\downarrow}|^2 + |t_{\uparrow\downarrow}|^2)v_{\perp\downarrow,t}}{v_{\perp\uparrow,I} + v_{\perp\downarrow,I}}, \quad (7.36)$$

where the dependencies of t_{ij} and v_i on E and k_{\parallel} are not explicitly shown. With the assumptions stated at the beginning of this section, one has $v_{\perp\uparrow} = v_{\perp\downarrow}$, and Eq. (7.36) can be rewritten as

$$\begin{aligned} T(E, k_{\parallel}) &= \frac{1}{2} \frac{(|t_{\uparrow\uparrow}|^2 + |t_{\downarrow\uparrow}|^2)v_{\perp,t} + (|t_{\downarrow\downarrow}|^2 + |t_{\uparrow\downarrow}|^2)v_{\perp,t}}{v_{\perp,I}} \\ &= \frac{1}{2} [(T_{\uparrow\uparrow} + T_{\uparrow\downarrow}) + (T_{\downarrow\downarrow} + T_{\downarrow\uparrow})], \end{aligned} \quad (7.37)$$

where

$$T_{ij} \equiv \frac{|t_{ij}|^2 v_{\perp,t}}{v_{\perp,I}} \quad (7.38)$$

Thus it has been shown that, in the approximation where the bands are degenerate, the transmission coefficient for a random population of spins will simply be the average of the coefficients for spin up and down in an arbitrary direction even when the properties of the barrier are spin-dependent and it might introduce ‘‘channel

mixing.”

A good measure of the filtering efficiency of a spin filter can be given by the ratio of transmitted spin polarized current to the incoming current

$$\eta(E, k_{\parallel}) = \frac{|\text{tr}(\hat{\rho}_t \boldsymbol{\sigma} \hat{v})|}{\text{tr}(\hat{\rho}_I \hat{v})}, \quad (7.39)$$

where $\eta(E, k_{\parallel})$ measures the filtering efficiency for a given energy and k_{\parallel} of the incoming particles. This measure gives the maximum possible efficiency, which is achieved when the transmitted spins are analyzed in the same direction as $\text{tr}(\hat{\rho}_t \boldsymbol{\sigma} \hat{v})$.

To evaluate the trace in the numerator of Eq. (7.39), it is convenient to define raising and lowering operators

$$\sigma_+ = \frac{1}{2}(\sigma_x + i\sigma_y) = \begin{pmatrix} 0 & 1 \\ 0 & 0 \end{pmatrix}, \quad (7.40)$$

$$\sigma_- = \frac{1}{2}(\sigma_x - i\sigma_y) = \begin{pmatrix} 0 & 0 \\ 1 & 0 \end{pmatrix}, \quad (7.41)$$

where the z axis is chosen along to be parallel with the $|\uparrow\rangle$ spin.

Then

$$\text{tr}(\hat{\rho}_t \sigma_+ \hat{v}) = \frac{1}{2}(t_{\uparrow\downarrow} t_{\uparrow\uparrow}^* + t_{\downarrow\downarrow} t_{\downarrow\uparrow}^*) v_{\perp,t} \quad (7.42)$$

$$\text{tr}(\hat{\rho}_t \sigma_- \hat{v}) = \frac{1}{2}(t_{\uparrow\downarrow}^* t_{\uparrow\uparrow} + t_{\downarrow\downarrow}^* t_{\downarrow\uparrow}) v_{\perp,t} \quad (7.43)$$

$$\text{tr}(\hat{\rho}_t \sigma_z \hat{v}) = \frac{1}{2}(|t_{\uparrow\uparrow}|^2 + |t_{\downarrow\uparrow}|^2) v_{\perp,t} - (|t_{\downarrow\downarrow}|^2 + |t_{\uparrow\downarrow}|^2) v_{\perp,t}, \quad (7.44)$$

or, in cartesian components

$$\text{tr}(\hat{\rho}_t \sigma_x \hat{v}) = \Re [(t_{\uparrow\downarrow} t_{\uparrow\uparrow}^* + t_{\downarrow\downarrow} t_{\downarrow\uparrow}^*) v_{\perp,t}] \quad (7.45)$$

$$\text{tr}(\hat{\rho}_t \sigma_y \hat{v}) = \Im [(t_{\uparrow\downarrow} t_{\uparrow\uparrow}^* + t_{\downarrow\downarrow} t_{\downarrow\uparrow}^*) v_{\perp,t}] \quad (7.46)$$

$$\text{tr}(\hat{\rho}_t \sigma_z \hat{v}) = \frac{1}{2}(|t_{\uparrow\uparrow}|^2 + |t_{\downarrow\uparrow}|^2) v_{\perp,t} - (|t_{\downarrow\downarrow}|^2 + |t_{\uparrow\downarrow}|^2) v_{\perp,t} \quad (7.47)$$

and, from here, the efficiency will be

$$\eta(E, k_{\parallel}) = \frac{\sqrt{[\text{tr}(\hat{\rho}_t \sigma_x \hat{v})]^2 + [\text{tr}(\hat{\rho}_t \sigma_y \hat{v})]^2 + [\text{tr}(\hat{\rho}_t \sigma_z \hat{v})]^2}}{v_{\perp, I}/2}. \quad (7.48)$$

The spin polarization p , defined as the magnitude of the spin polarized current divided by the transmitted current, is related to the filter efficiency by

$$\eta(E, k_{\parallel}) = p(E, k_{\parallel}) T(E, k_{\parallel}). \quad (7.49)$$

These expressions adopt simpler forms when the incoming spins are chosen to be resonant with the barrier (*i.e.*, there is no up-down channel mixing). This translates into $t_{\uparrow\downarrow} = t_{\downarrow\uparrow} = 0$, which simplifies the above expressions considerably to

$$\eta = T_{\uparrow\uparrow} - T_{\downarrow\downarrow} \quad (7.50)$$

and

$$p = \frac{T_{\uparrow\uparrow} - T_{\downarrow\downarrow}}{T_{\uparrow\uparrow} + T_{\downarrow\downarrow}}. \quad (7.51)$$

7.3 Resonant tunneling in asymmetric double barriers

In this section the basic operating principle of the Rashba spin filters is explained. To do that, a barrier structure comprised of AlSb/GaSb/InAs/AlSb clad by InAs electrodes is considered (see Fig. 7.3), with the GaSb and InAs layer thicknesses chosen to yield a large Rashba splitting (*cf.* Chapter. 3).

The quasi-bound states for the structure in Fig. 7.3 without the inclusion of bulk inversion asymmetry (BIA) effects [20] are described in Sec. 5.6.1. The spin of these quasi-bound states has a \mathbf{k}_{\parallel} dependence shown in Fig. 7.4.

Consider now an incoming electron whose spin is pointing according to the directions in Fig. 7.4, belonging to either the lower or the highest conduction subband.

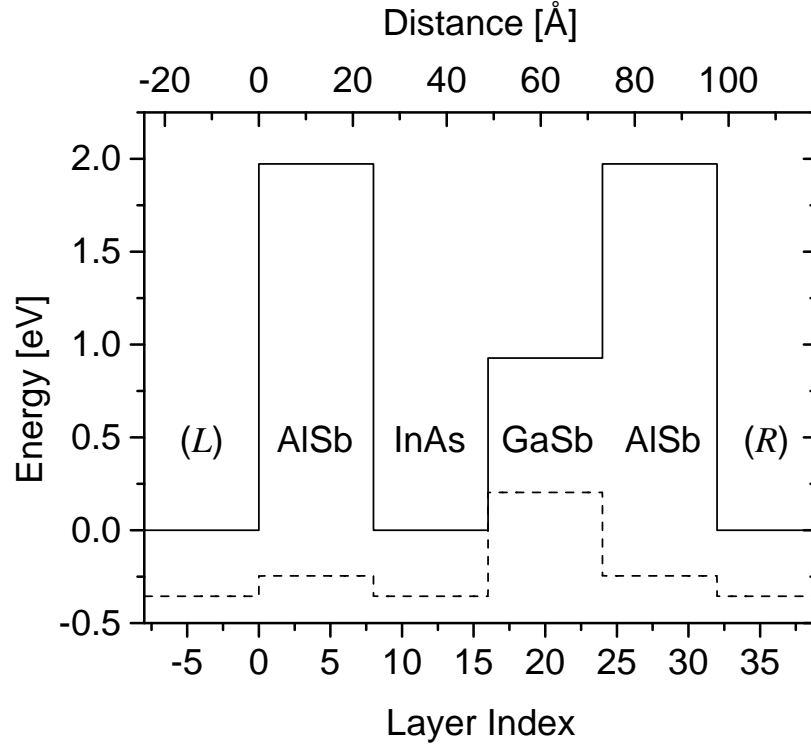


Figure 7.3: aRTD structure at zero bias. The AISb, GaSb and InAs layers are 8 monolayers (MLs) each ($3.048 \text{ \AA}/\text{ML}$), and the electrodes are InAs.

A schematic of this situation is shown in Fig. 7.5. The transmission coefficient of such an electron, with $\mathbf{k}_{\parallel} = (0.02, 0) \text{ \AA}^{-1}$ and the spin pointing in the $\pm y$ direction, is shown in Fig. 7.6. It is seen that the transmission curves appear decoupled due to the incident electron interacting with only one of the quasi-bound states. The transmission peaks are split by the Rashba effect. Looking at the spin of the transmitted electron it is seen that it does not change after going through the barrier. Therefore, Fig. 7.4 also indicates the spin of the transmitted electrons as a function of their \mathbf{k}_{\parallel} .

7.4 Asymmetric resonant tunneling diode (aRTD)

The aRTD spin filter is based in the intraband tunneling phenomena through an asymmetric structure as described in the previous section. The origin of that asymmetry can be different barrier thicknesses [10], different constituent materials of the barrier [10, 12] or the inclusion of spatially dependent doping profiles [21].

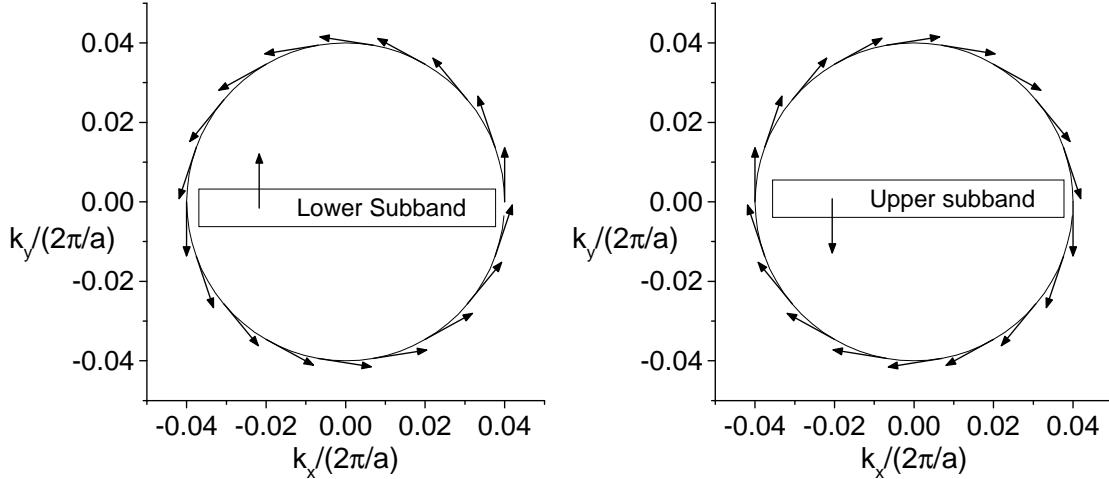


Figure 7.4: Spin directions for the quasi-bound states in the aRTD (same as Fig. 2.3).

Looking at Fig. 7.4 it must be noted that, for an electron gas with thermal distribution, the spin contribution for each incoming electron with some \mathbf{k}_{\parallel} will be compensated by an electron with $-\mathbf{k}_{\parallel}$. Therefore, in order to obtain spin injection an anisotropy in the distribution of \mathbf{k}_{\parallel} must be created. This can be done, for example, with the addition of a lateral electric field that gives the incoming electrons a nonvanishing average \mathbf{k}_{\parallel} component [10]. Then, if the lateral electric field points, say, in the x direction, the transmitted current should be analyzed along the y axis to obtain a maximum effect. Calculations for this family of devices show current polarizations p of the order of 20% [12].

The inclusion of BIA effects does not change the qualitative picture for the aRTD very much. The biggest change is due to the spins of the quasi-bound states being tilted respect to when no BIA was considered (see, for example, Fig. 5.19). As shown in Fig. 7.7, this introduces supplementary peaks in the transmission curves if the incoming spins are left unchanged. This is just due to the fact that spins pointing along $\pm y$ are no longer resonant when BIA is taken into account. However, the peak strength is very little affected by the inclusion of the BIA terms and one expects the current polarization prediction to be similar, with the caveat that the spin analysis must be made along the new resonant direction.

There are mainly two effects that limit the performance of the aRTD as a spin

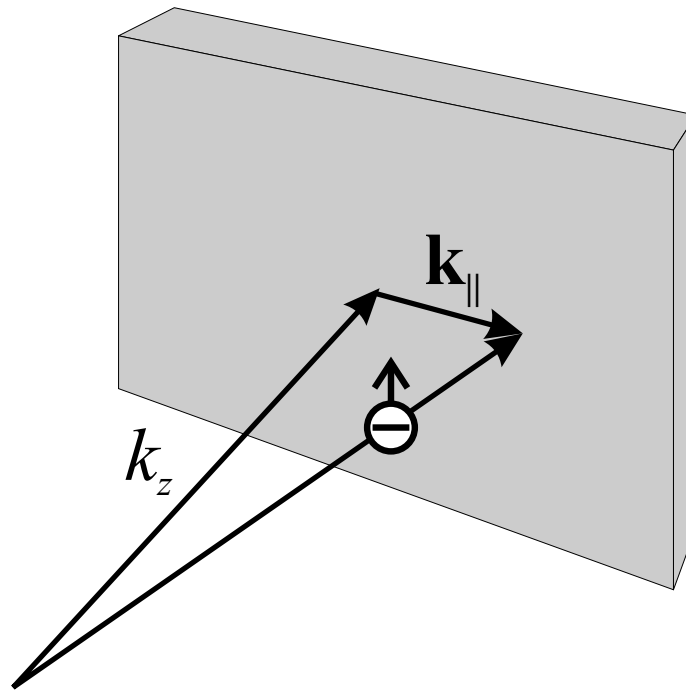


Figure 7.5: Resonant spin of an electron incident into an aRTD structure.

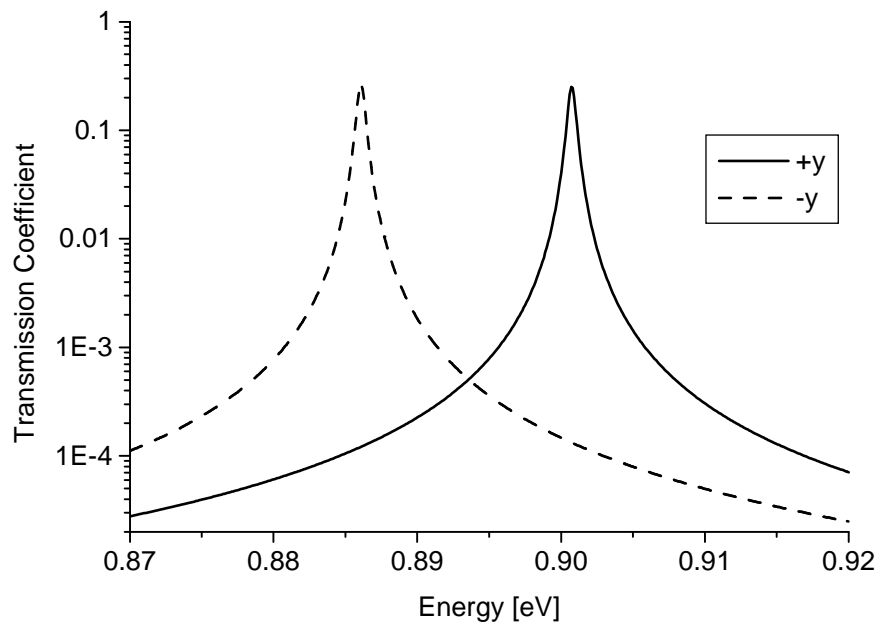


Figure 7.6: Transmission coefficient for the aRTD structure described in Fig. 7.3. The incoming electrons are assumed to have $\mathbf{k}_{\parallel} = (0.02, 0)\text{\AA}^{-1}$ and the spin pointing in the $\pm y$ direction. This direction is chosen for the electron to couple only to one of the two quasi-bound states.

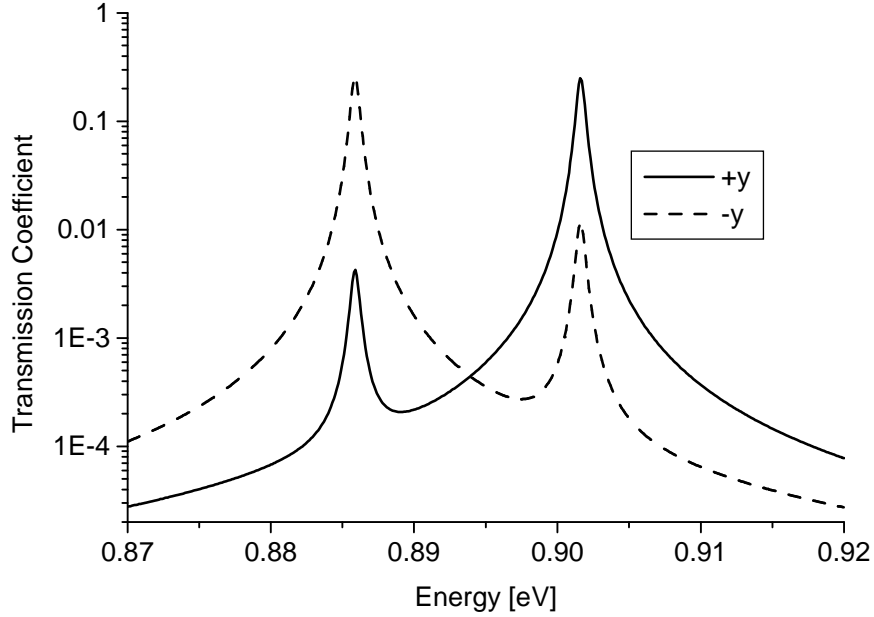


Figure 7.7: As in Fig. 7.6, but with BIA effects included.

filter (see Fig. 7.8):

I. Cancellation of net spin between spin split subbands:

The two conduction subbands have spins pointing in different directions. Since an electron has to tunnel through a barrier state, the amount of current polarization will go as the ratio in the number of quasi-bound states in the barrier below the emitter Fermi level (*i.e.*, the area enclosed by the Fermi circles for each subband). Therefore, the amount of polarization will only be appreciable when the Fermi level of the emitter lines close to the conduction band edge of the barrier.

II. Cancellation in the same band:

Even within a subband there is cancellation because of the spins in the barrier states pointing in a circular fashion (cf. Fig. 7.4). This will also decrease the filter efficiency.

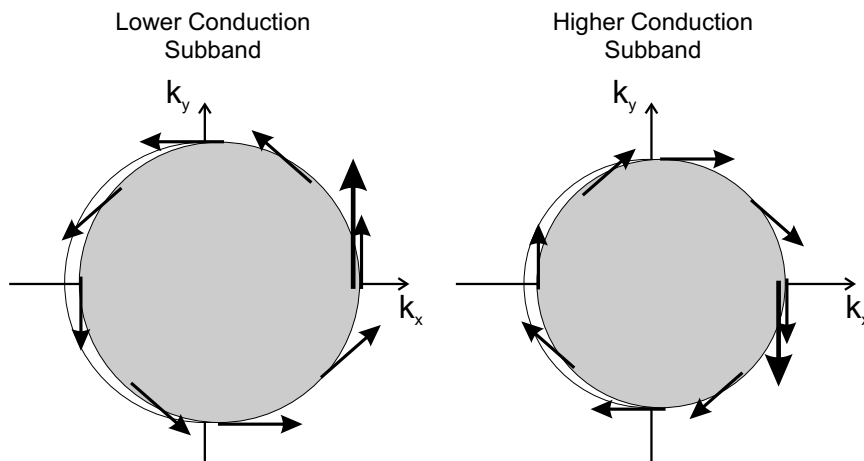


Figure 7.8: \mathbf{k}_{\parallel} dependence of the spin of the transmitted states in an aRTD and illustration of the difficulties in the aRTD. Not only do electrons tunneling through different subbands have opposite spin (the net contribution is represented by the big arrow), but also the spin contribution within a subband cancels out for states where both \mathbf{k}_{\parallel} and $-\mathbf{k}_{\parallel}$ participate in the tunneling process. The big arrows indicate the total spin contribution for each subband.

7.5 Asymmetric resonant interband tunneling diode (aRITD)

The aRITD [12] attempts to deal with some of the problems of the aRTD mentioned above by making the transmitted electrons tunnel through the barrier valence band states rather than the conduction band. A typical aRITD structure is shown in Fig. 7.9. The aRITD would be a low voltage device because of the little voltage (always less than ~ 200 mV) necessary to align the barrier quasi-bound valence band states with the Fermi level of the emitter.

A typical tunneling transmission curve through an aRITD structure is shown in Fig. 7.10. The resonant peaks where the energy and \mathbf{k}_{\parallel} of the incident electron match those of the quasi-bound barrier states are clearly shown. As for the aRTD, choosing the incoming spins to be $\pm y$ for \mathbf{k}_{\parallel} along [100] decouples the two peaks. It can be seen that having the spins point in-plane and perpendicular to \mathbf{k}_{\parallel} (*e.g.*, clock and counterclockwise) also decouples the peaks exactly when \mathbf{k}_{\parallel} is along the [110] direction and to a very good approximation for a general \mathbf{k}_{\parallel} 's intervening in

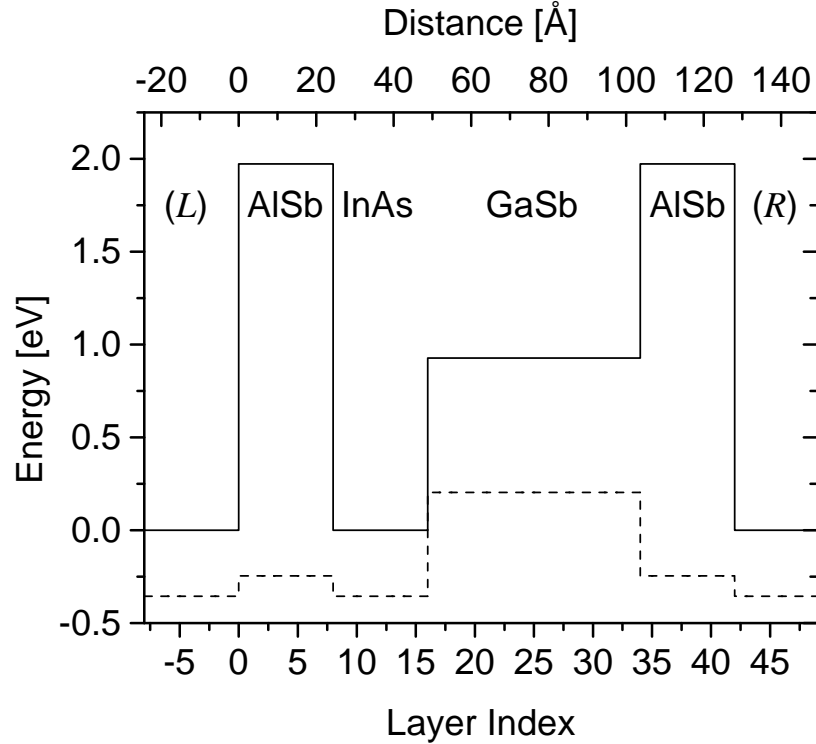


Figure 7.9: aRITD structure at zero bias. The AlSb and InAs layers are 8 monolayers (MLs) each ($3.048 \text{ \AA}/\text{ML}$), the GaSb is 18 MLs thick and the electrodes are InAs.

the tunneling process. A surprising feature of this curve is that the peak strength is heavily dependent on the incident spin orientation. This is also found in calculations using the effective bond orbital model method. This effect can be used to minimize the contribution of the upper subband to the transmitted current. Thus, the impact of one of the difficulties mentioned earlier for the aRTD can be lessened.

Figure 7.11 (a) shows how the emitter (strained to a GaSb substrate) conduction band and the barrier valence states match up for the aRITD. The structure can be designed in such a way that, for the operating bias, tunneling takes place through the HH1 bands only. The fact that the bands have opposite curvatures makes that only states with big \mathbf{k}_{\parallel} can tunnel. This allows the device to work far from the zone center, where the splitting vanishes. Plots (b) and (c) show the effect of the application of a lateral electric field on the states participating in the tunneling process. The Fermi sea tilts [22] and some of the channels used at zero lateral field no longer contribute due to the lack of incident states at that \mathbf{k}_{\parallel} . In the structure studied here, the transmitted

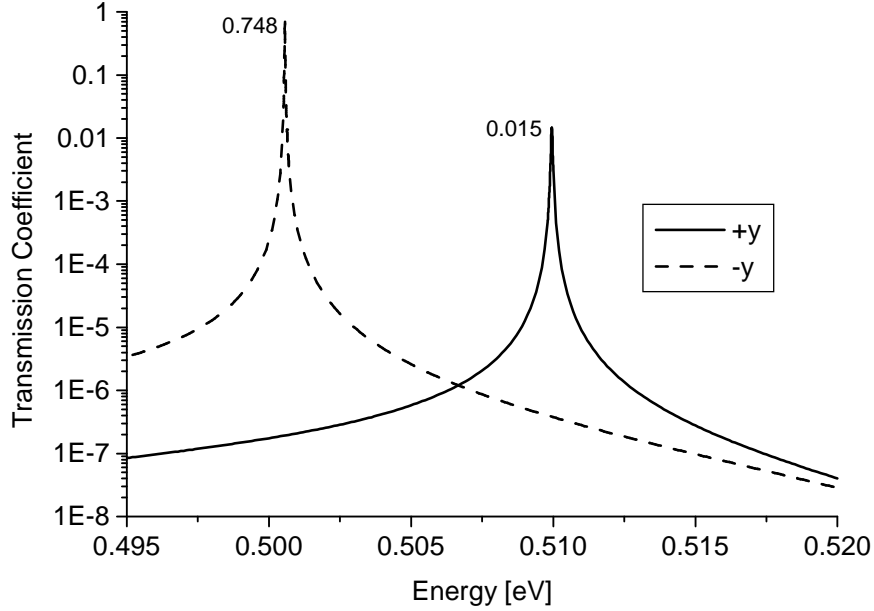


Figure 7.10: Transmission coefficient for the aRITD structure described in Fig. 7.9. The incoming electrons are assumed to have $\mathbf{k}_{\parallel} = (0.02, 0)\text{\AA}^{-1}$ and the spin pointing in the $\pm y$ direction. This direction is chosen for the electron to couple only to one of the two quasi-bound states. Note the asymmetry in the peak strengths.

current will mainly originate from tunneling through the lower HH1 subband (cf. Fig. 7.10). As the applied lateral electric field gets larger, the Fermi sea will tilt more and the number of unwanted \mathbf{k}_{\parallel} channels within a band reducing the average spin will decrease. Thus, the aRITD is less sensible to within band cancellation effects.

The reduction of the two aforementioned adverse effects allows the increase of the spin polarization levels up to $\sim 60\%$ [12]. The curves in that reference, reproduced in Fig. 7.12, show that the amount of filtering is strongly dependent on the electrode doping. Alternatively, the regime of high filtering can be achieved with the application of an appropriate bias across the barrier.

Figure 7.13 shows the effect in the transmission curves of the inclusion of BIA, with the incoming spin directions left unchanged. The spin preferred directions of the holes in the barrier are more sensitive to the BIA terms than its conduction band (CB) counterparts. This makes new peaks appear in the transmission curves. The asymmetry in peak strengths for the lowest and highest energy peaks (considering the sum of both spin contributions at a given energy) isn't affected very much by the

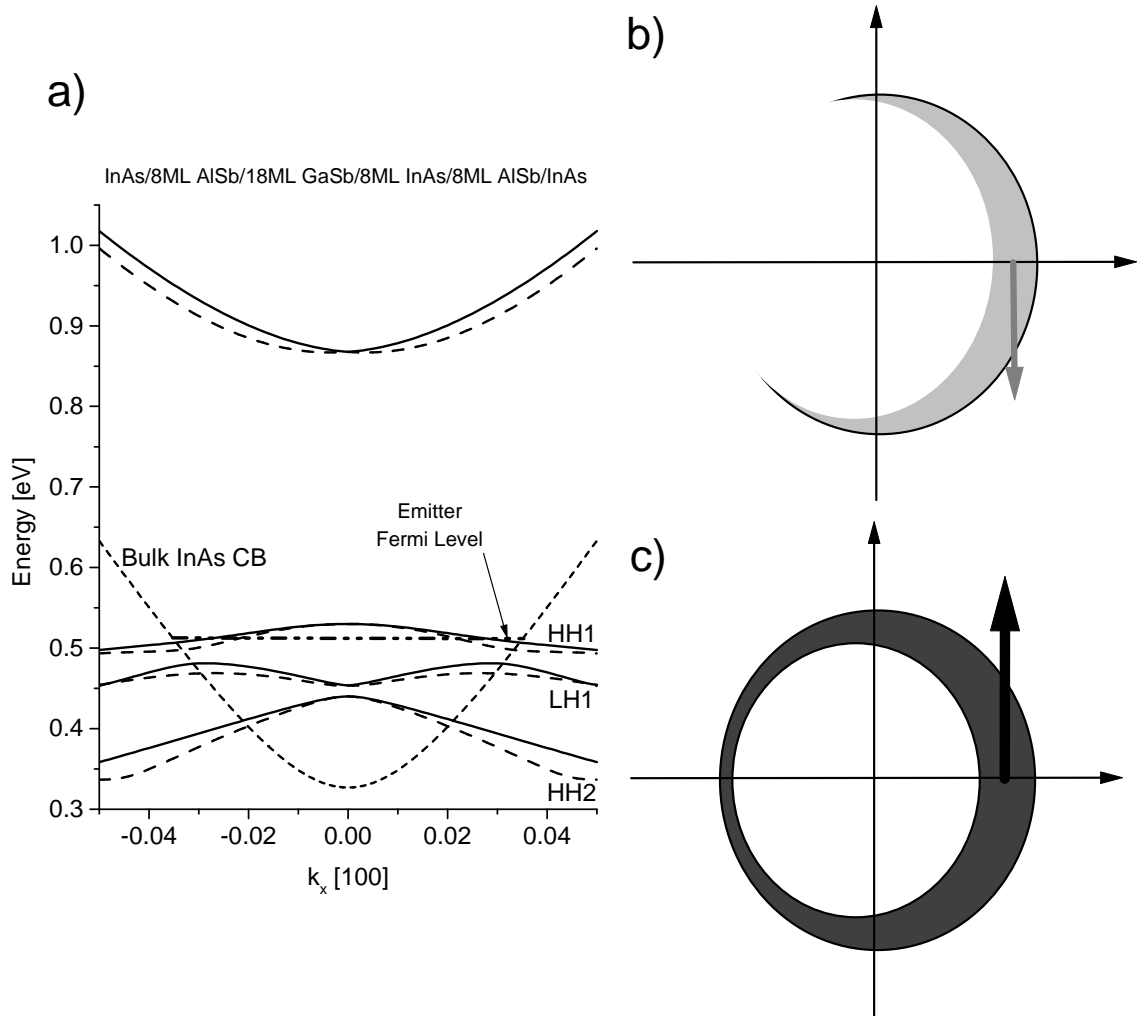


Figure 7.11: a) Bands of the aRITD structure and operation with a lateral electric field. The short dashed line shows the conduction band of bulk InAs strained to a GaSb substrate. The desired position of the Fermi level of the emitter respect to the barrier bands is indicated. (b) [c)] shows the participating channels and their spin contribution of the upper (lower) HH1 subband. The light grey arrow signifies the weaker peak strength for transmission through the upper HH1 subband (cf. Fig. 7.10).

inclusion of BIA. So, one of the key aspects of the operation of the device is still there with the BIA terms present. The origin of the asymmetry in the peak strength is a subject still under investigation. The direction where the spins should be analyzed for optimum performance will change, and depends on the interplay of BIA and SIA (structural inversion asymmetry) effects for a particular structure, but that is not expected to influence heavily on the magnitude of the polarization.

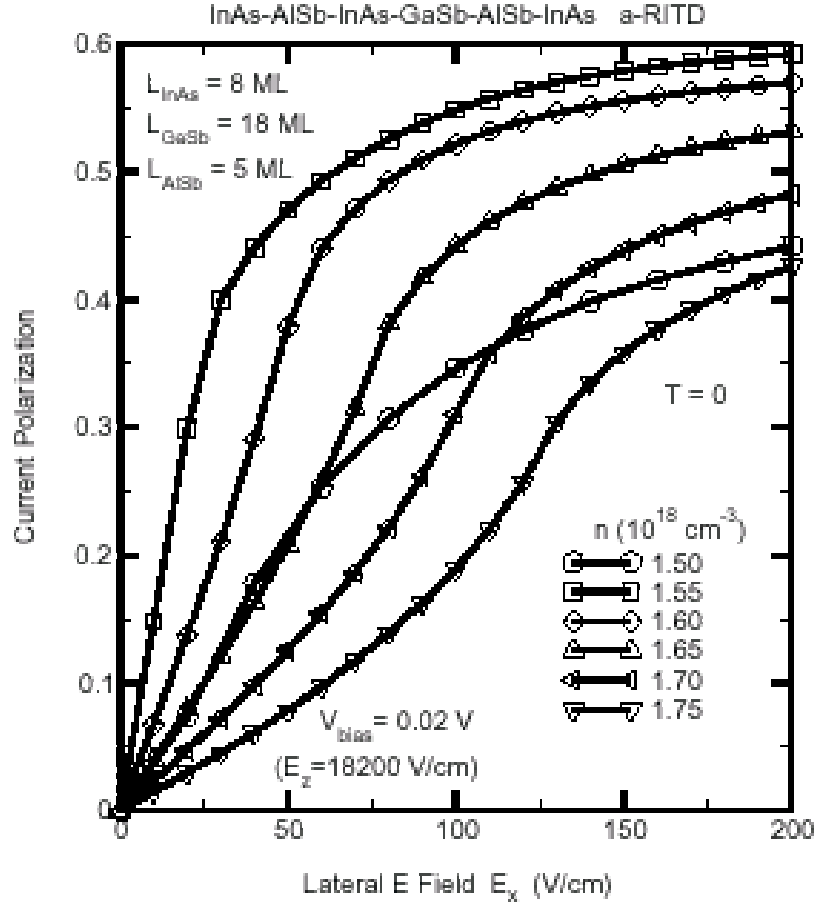


Figure 7.12: Spin polarization of the current as a function of lateral field for several emitter electron densities (reproduced from Ref. [12]).

7.6 Summary

In summary, a method for calculating spin-dependent transmission properties of tunnel structures has been presented. The multiband quantum transmitting boundary method, originally formulated in the tight binding context [13], has been adapted to the $\mathbf{k} \cdot \mathbf{p}$ formalism. This method has been employed to calculate spin-dependent transmission curves for candidate structures for a spin filter. Calculations without BIA effects show the same features as equivalent calculations using the effective bond orbital model method. Two devices, the aRTD and the aRITD, have been studied. For the aRTD, it has been shown that the inclusion of bulk inversion asymmetry (BIA) effects changes only slightly the transmission properties of the resonant structure. Finally, for the aRITD, it has been seen that BIA plays a role on the choice of

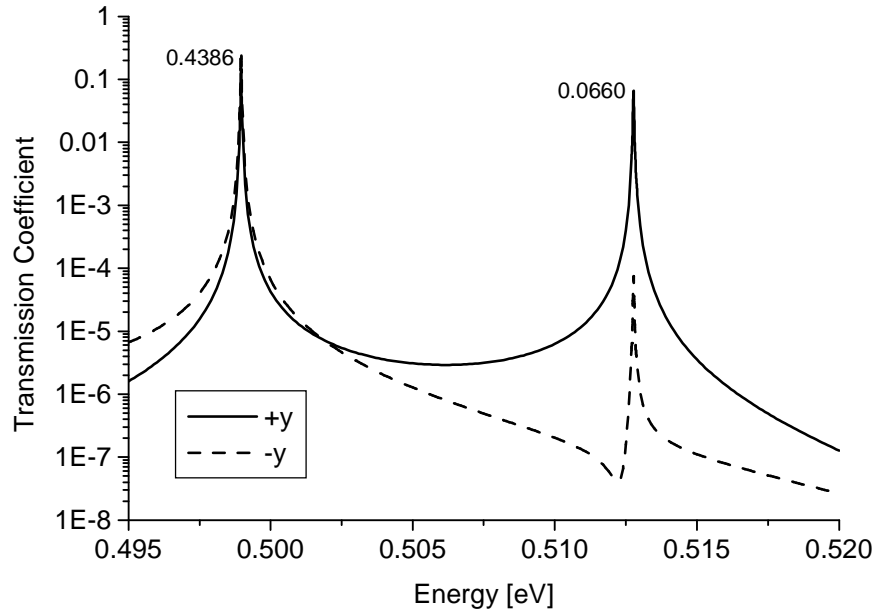


Figure 7.13: As Fig. 7.10, with BIA effects included. The numbers indicate *the sum* of the transmission coefficients for both peaks.

the transmitted spin direction, but doesn't affect appreciably the main working principle of the device, namely, the highly asymmetric peak strengths of the transmission resonances through the HH1 subbands.

Bibliography

- [1] S. A. Wolf, *J. Supercond.* **13**, 195 (2000).
- [2] R. Gawel, *Electron. Des.* **48**, 30 (2000).
- [3] S. Das Sarma, J. Fabian, X. D. Hu, and I. Zutic, *Superlattice. Microstruct.* **27**, 289 (2000).
- [4] B. Heinrich, *Can. J. Phys.* **78**, 161 (2000).
- [5] M. Johnson and R. H. Silsbee, *J. Appl. Phys.* **63**, 3934 (1988).
- [6] H. J. Zhu, M. Ramsteiner, H. Kostial, M. Wassermeier, H. P. Sch onherr, and K. H. Ploog, *Phys. Rev. Lett.* **87**, art. no. (2001).
- [7] R. Fiederling, M. Keim, G. Reuscher, W. Ossau, G. Schmidt, A. Waag, and L. W. Molenkamp, *Nature* **402**, 787 (1999).
- [8] Y. Ohno, D. K. Young, B. Beschoten, F. Matsukura, H. Ohno, and D. D. Awschalom, *Nature* **402**, 790 (1999).
- [9] E. A. D. E. Silva and G. C. LaRocca, *Phys. Rev. B* **59**, R15583 (1999).
- [10] A. Voskoboynikov, S. S. Lin, C. P. Lee, and O. Tretyak, *J. Appl. Phys.* **87**, 387 (2000).
- [11] Y. A. Bychkov and E. I. Rashba, *J. Phys. C* **17**, 6039 (1984).
- [12] D. Z.-Y. Ting, X. Cartoixà, D. H. Chow, J. S. Moon, D. L. Smith, T. C. McGill, and J. N. Schulman, *IEEE Trans. Magn.* (2002), to be published.
- [13] D. Z.-Y. Ting, E. T. Yu, and T. C. McGill, *Phys. Rev. B* **45**, 3583 (1992).
- [14] Y. X. Liu, D. Z.-Y. Ting, and T. C. McGill, *Phys. Rev. B* **54**, 5675 (1996).

- [15] W. R. Frensley, *Reviews Of Modern Physics* **62**, 745 (1990).
- [16] E. O. Kane, in *Tunneling Phenomena in Solids*, edited by E. Burstein and S. Lundqvist (Plenum Press, New York, 1969), p. 1.
- [17] D. L. Smith and C. Mailhot, *Phys. Rev. B* **33**, 8345 (1986).
- [18] D. Y. K. Ko and J. C. Inkson, *Phys. Rev. B* **38**, 9945 (1988).
- [19] G. Y. Wu, K. M. Hung, and C. J. Chen, *Phys. Rev. B* **46**, 1521 (1992).
- [20] G. Dresselhaus, *Phys. Rev.* **100**, 580 (1955).
- [21] T. Koga, J. Nitta, H. Takayanagi, and S. Datta, *Phys. Rev. Lett.* **88**, art. no. (2002).
- [22] J. M. Ziman, *Principles of the Theory of Solids*, 2nd ed. (Cambridge University Press, Cambridge, Uk, 1972), pp. 216–217.

Chapter 8 Photon generation for a Monte Carlo ray tracing LED simulator

8.1 Introduction

A requirement for the development of spintronic devices is the achievement of reliable spin injection. Once a candidate for a spin injector has been identified, there must be a means of quantifying its performance. This leads to mainly two families of experiments for measuring spin injection; namely, electrical experiments [1] and optical experiments [2–4].

In electrical experiments the spin polarized electrons inside the material of interest, which will be considered to be a semiconductor but could be a metal as well, are collected by a ferromagnetic contact. Then, depending on the relative orientation of the majority electron spins and the magnetization of the collector, a higher or lower resistance is measured. From that data, the existence of spin injection can be established. However, in recent years electrical measurement methods have fallen into disgrace due to the possibility of the presence of spurious local Hall voltages due to the ferromagnetic contact fringing fields [5]. Another inconvenience is that it has also been shown [6, 7] that one should expect only a very small effect in the standard ferromagnet-semiconductor-ferromagnet configuration.

Optical detection of spin injection is based on the polarization state of the photon emitted after a direct interband electron-hole recombination. If we consider the light coming from direct transitions, say in a III-V zincblende semiconductor, the polarization state of the emitted photons will depend on the direction of emission and the initial and final states of the electron making the transition. By analyzing the emitted light, one can obtain statistical information about the initial electron states, and from there the spin polarization of the electrons before making the transition. This

method is considered to be more direct and less subject to criticism than the electrical detection method. It has been successfully employed to detect significant amounts of electrical spin injection both from a semiconductor into another semiconductor [3, 4], and from a ferromagnet into a semiconductor [8].

However, the effects of refraction on the polarization of the emitted light have been mostly overlooked. Ichiriu *et al.* [9] have investigated these effects using a Monte Carlo ray tracing algorithm that follows the photons from their generation at the p - n junction until they hit the detector. They conclude that, for emissions that aren't parallel or perpendicular to the junction plane, the effect of refraction will be to increase the observed degree of polarization with respect to that actually emitted in the bulk of the semiconductor.

In order to perform this kind of calculations, a method that generates single photons with the adequate polarization is needed. This article describes in detail such a method. In the discussion in Sec. 8.2, it is shown how Fermi's golden rule does not specify the polarization of the emitted photon. The time-dependent perturbation theory is used instead to derive the polarization of a photon emitted in an arbitrary direction for transitions between two bands of a crystal in Sec. 8.3. In Sec. 8.4, the formalism is applied to zincblende and wurtzite bulk and quantum well semiconductors. Section 8.5 describes the use of a Monte Carlo scheme to generate single photons ready for use in a ray tracing algorithm and yielding the ensemble results derived in Sec. 8.3. Finally, Sec. 8.6 shows results from the application of the method to a bulk zincblende.

A reader not familiar with group theoretical arguments might find it useful to refer to Appendix B for a utilitarian introduction to group theory.

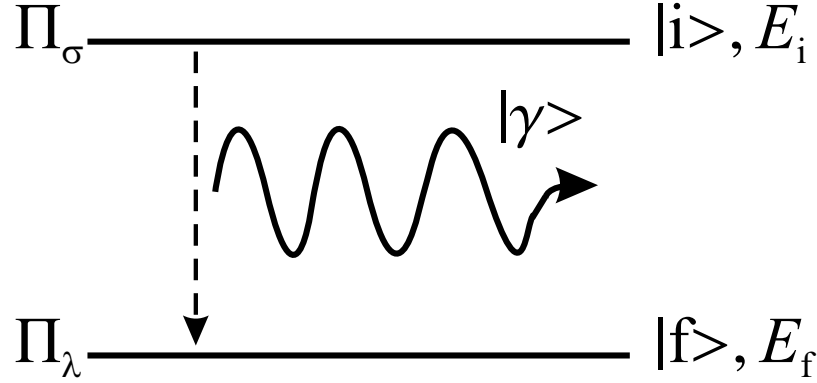


Figure 8.1: Schematic of the interband photon emission process.

8.2 The interaction Hamiltonian and Fermi's golden rule

Figure 8.1 describes schematically the photon emission process under study. Π_σ (Π_λ) is the label of the initial (final) irreducible representation. These labels indicate the starting and final bands between which the interband transition takes place. $|i\rangle$ and $|f\rangle$ denote the specific initial and final states, respectively, inside each band. Their corresponding energies are E_i and E_f . Finally, $|\gamma\rangle$ represents the state of the emitted photon.

To study this process, consider a plane wave interacting with a crystal. The plane wave can be described by just its vector potential in the radiation gauge [10]:

$$\mathbf{A} = A_0 \mathbf{a} \cos(\mathbf{q} \cdot \mathbf{r} - \omega t), \quad (8.1)$$

where \mathbf{A} is the vector potential, A_0 is the amplitude of the wave, \mathbf{a} is a unit vector in the direction of \mathbf{A} , \mathbf{q} is the wavevector of the wave and ω is its frequency. The electric and magnetic fields can be found using the usual relations:

$$\mathbf{E} = -\frac{\partial \mathbf{A}}{\partial t} \quad (8.2)$$

$$\mathbf{B} = \nabla \times \mathbf{A}, \quad (8.3)$$

where the radiation gauge condition $\nabla \cdot \mathbf{A} = 0$ has been used. From Eq. (8.2) it is seen that \mathbf{a} determines the polarization of the plane wave. \mathbf{a} can take complex values to describe an elliptical polarization state.

The Hamiltonian of a crystal coupled to an applied electromagnetic plane wave can be written, in the low-intensity limit and dipole approximation (*i.e.*, the photon wavelength much bigger than the primitive cell size), as [11]:

$$H = H_0 - \frac{e}{m_o} \mathbf{P} \cdot \mathbf{A}, \quad (8.4)$$

where the dipole magnetic term has been omitted because it is much weaker than the dipole electric term, e is the absolute value of the electron charge, m_o is the free electron mass and \mathbf{P} is the momentum operator.

Following Ridley [12], the cosine in Eq. (8.1) can be expanded into a sum of complex exponentials and introduced into Eq. (8.4) to yield, by selecting the appropriate terms, the space part of the Hamiltonian describing the photon emission process:

$$H_{\nu \text{ em}} = -\frac{e}{m_o} \left\{ \frac{\hbar (n_\nu + 1)}{2V \epsilon_\nu \omega_\nu} \right\}^{1/2} \mathbf{a} \cdot \mathbf{P}, \quad (8.5)$$

where \hbar is the reduced Planck constant, n_ν is the number of photons present corresponding to the mode ν and having a frequency ω_ν , ϵ_ν is the optical permittivity of that mode and V is the volume of the crystal. The time part of the Hamiltonian leads to the appearance of the Dirac delta factor in energy in Eq. (8.6).

On the other hand, Fermi's golden rule can be used to find $W_{i \rightarrow f}$, the probability per unit time that an initial state $|i\rangle$ will make a transition to any $|f\rangle$ belonging to a family with dS_f degenerate states due to the action of a perturbation $H_{\nu \text{ em}}$. It states [12]:

$$W_{i \rightarrow f} = \frac{2\pi}{\hbar} |\langle f | H_{\nu \text{ em}} | i \rangle|^2 \delta(E_i - E_f) dS_f. \quad (8.6)$$

Thus, the probability of spontaneous emission into a solid angle $d\Omega$ per unit time W_{em} can be obtained by taking $n_\nu = 0$ in Eq. (8.5) and plugging this equation into

Eq. (8.6):

$$W_{\text{em}} = \frac{e^2}{4\pi\epsilon_0} \frac{4}{\hbar\omega_\nu} \frac{|\mathbf{a} \cdot \mathbf{P}_{fi}|^2}{2m^2} \frac{\eta_r \omega_\nu^2}{c^3} \frac{d\Omega}{4\pi}, \quad (8.7)$$

where ϵ_0 is the vacuum permittivity, c is the speed of light, η_r is the crystal refractive index and \mathbf{P}_{fi} is the momentum matrix element between the initial and the final states.

The important point about Eq. (8.7) is that the probability of emission is proportional to the scalar product of the polarization vector of the plane wave and the matrix element of the momentum operator between the initial and final states. If only transitions between two bands are of interest, as is commonly the case in semiconductors, all the photons emitted will have the same frequency and the only thing that will change between two emission events will be the $|\mathbf{a} \cdot \mathbf{P}_{fi}|^2$ factor. Therefore, the knowledge of that factor is the only thing needed to determine the relative transition rates between some initial and final states belonging to two given bands. Mathematically, this can be written as:

$$\frac{W_{i \rightarrow f, \mathbf{a}}}{W_{i' \rightarrow f', \mathbf{a}'}} = \frac{|\mathbf{a} \cdot \mathbf{P}_{fi}|^2}{|\mathbf{a}' \cdot \mathbf{P}_{f'i'}|^2}. \quad (8.8)$$

8.2.1 The Wigner-Eckart theorem for point groups applied to momentum matrix elements

The expression in Eq. (8.8) can be further simplified by making use of symmetry considerations. The Wigner-Eckart theorem for point groups (see Ref. [13] and appendix B.3) isolates the symmetry effects from other contributions in the matrix elements of tensor operators. In particular, the momentum matrix elements can be written as follows:

$$\begin{aligned} P_{\mu fi}^m &= \langle f | P_\mu^m | i \rangle = \sum_{k \in \kappa} \sum_{l \in \lambda} \langle f | \kappa, k \rangle \langle \kappa, k | P_\mu^m | \lambda, l \rangle \langle \lambda, l | i \rangle = \\ &\langle \kappa || P_\mu || \lambda \rangle \sum_{k \in \kappa} \sum_{l \in \lambda} \langle f | \kappa, k \rangle \langle \mu, m; \lambda, l | \kappa, k \rangle \langle \lambda, l | i \rangle, \end{aligned} \quad (8.9)$$

T_d	$SO(3)$
Γ_5	$ l = 1\rangle$
Γ_6	$ l = 0\rangle \otimes s = 1/2\rangle$
Γ_7	$ l = 1\rangle \otimes s = 1/2\rangle$ such that $j = 1/2$
Γ_8	$ j = 3/2\rangle$

Table 8.1: Table of selected irreducible representations (irreps) of the zincblende point group T_d and their equivalent full rotation group $SO(3)$ irreps.

where the initial and final states have been expanded into the basis states corresponding to their irreducible representation (irrep). Greek indices label irreps and latin indices label specific basis states inside an irrep. $\langle \kappa || P_\mu || \lambda \rangle$ is the so-called reduced matrix element [14], and will not depend on $|i\rangle$ nor $|f\rangle$ as long as these are taken as linear combinations of basis states belonging to the Π_λ and Π_κ bands, respectively. The symbol $\langle \mu, m; \lambda, l | \kappa, k \rangle$ represents the complex conjugate of the Clebsch-Gordan coefficient for the point group under consideration.

8.2.2 Application to III-V zincblendes

To exemplify this abstract formalism, consider a transition between the conduction band and the valence band of a III-V zincblende at the zone center. For most of the III-Vs, the conduction band edge is described by the Γ_6 irrep of the T_d point group; while the valence band edge is described by the Γ_8 irrep, where the Koster-Dimmock-Wheeler-Statz (KDWS) [15] notation is being used. The treatment of T_d is simplified by the fact that some of their irreps can be identified with full rotation group irreps according to Table 8.1. Assume also that the electron in the conduction band has spin up in the z axis and it can go to either the heavy hole state $|3/2, +3/2\rangle$ or the light hole $|3/2, -1/2\rangle$, and the photon is being emitted along the z direction. The

relative transition rates will be given by the ratio of the momentum matrix elements:

$$\frac{W_{s\uparrow\rightarrow|3/2,+3/2\rangle}}{W_{s\uparrow\rightarrow|3/2,-1/2\rangle}} = \frac{\left| \langle 3/2 \| P_{\Gamma_5} \| s \rangle \sum_{k \in \Gamma_8} \sum_{l \in \Gamma_6} \langle 3/2, +3/2 | 3/2, k \rangle \langle 1, +1; 1/2, l | 3/2, k \rangle \langle 1/2, l | 1/2, +1/2 \rangle \right|^2}{\left| \langle 3/2 \| P_{\Gamma_5} \| s \rangle \sum_{k \in \Gamma_8} \sum_{l \in \Gamma_6} \langle 3/2, -1/2 | 3/2, k \rangle \langle 1, -1; 1/2, l | 3/2, k \rangle \langle 1/2, l | 1/2, +1/2 \rangle \right|^2}. \quad (8.10)$$

The reduced matrix elements in Eq. (8.10) cancel out and, using the orthonormality of the basis kets, one is left with the simple expression:

$$\frac{W_{s\uparrow\rightarrow|3/2,+3/2\rangle}}{W_{s\uparrow\rightarrow|3/2,-1/2\rangle}} = \frac{|\langle 1, +1; 1/2, +1/2 | 3/2, +3/2 \rangle|^2}{|\langle 1, -1; 1/2, +1/2 | 3/2, -1/2 \rangle|^2} = \frac{1}{1/3} = 3, \quad (8.11)$$

where the Clebsch-Gordan coefficients are for the full rotation group, and can be found in any standard quantum mechanics book.

8.2.3 Complications following the path of Fermi's golden rule

In the previous two subsections it has been shown how to find ratios between the probabilities that a photon be emitted from a transition into a given band using Fermi's golden rule. This might seem good enough to achieve the goal of generating single events using a random number generator. However, in the derivation of Eq. (8.11), the formalism has left discretionary choices that make it unsuitable for event generation. Some of the questions that arise are

- What set of final states must be chosen?

In Sec. 8.2.2, it was assumed that the initial state transitioned to either $|3/2, +3/2\rangle$ or $|3/2, -1/2\rangle$, where the quantization axis for the final states was chosen to point along the z axis. However, had another quantization axis been chosen, the matrix element \mathbf{P}_{fi} would have taken another value and the re-

sults for the probability of emission and photon polarization would have been different.

- What polarization of the emitted photon must be chosen?

Also in Sec. 8.2.2, it was implicitly assumed that the polarization vector \mathbf{a} was parallel to \mathbf{P}_{fi} . The polarization of the emitted photon is given by the vector \mathbf{a} [cf. Eq. (8.1)]. In principle, one might think that the polarization of the emitted photon should be independent of the choice of polarization basis vectors. But in this formalism, falling back to the example in Sec. 8.2.2 and considering emission along the z axis; the following choice of polarization modes: $\mathbf{a}_1 = \hat{x}$, $\mathbf{a}_2 = \hat{y}$ with \hat{x} (\hat{y}) a unit vector along the x (y) axis, would have generated photons with linear polarizations only. This is clearly unacceptable because it is known that when the electron spin points along the z axis and light is emitted along that axis too, a circular polarization of 50 % is expected [16].

In principle, one could overcome these difficulties by adopting the prescription that any basis set spanning the final state subspace can be chosen, and then pick a polarization that is in the same direction as \mathbf{P}_\perp , where \mathbf{P}_\perp is the component of \mathbf{P} perpendicular to the direction of emission. Alas, this is an *ad hoc* prescription, which does not shed any insight on the nature of the radiative process. But this prescription yields, indeed, the correct results. In the next section a more natural and univocal way of obtaining a prescription is shown.

8.3 Polarization of the emitted photon

Spontaneous emission is a purely quantum-field-theoretical effect. Consider, for the sake of argument, an atom in an excited state. Quantum mechanics states that if the electron is in an eigenstate of the system, it will remain there forever. The difference between classical and quantum fields manifests itself in the definition of system. In the classical viewpoint the electromagnetic bath surrounding that atom can totally vanish, therefore the system is the electron and its interaction with the nucleus, and

the electron will remain in the excited state. In the quantum field theory (QFT) viewpoint, the electromagnetic bath has a finite amplitude even at its ground state, so it must be included in the system. These zero point fluctuations will interact with the electron and cause the emission process.

In a sense, spontaneous emission is nothing more than stimulated emission caused by the ground state of the electromagnetic environment.

The Hamiltonian in Eq. (8.4) can be rewritten [10] in terms of the photon creation and annihilation operators a_s^\dagger and a_s , where the s is an index including the wavevector \mathbf{k} and the polarization mode:

$$H = H_0 + H_{DE}(t) = H_0 - \frac{e}{m} \sum_s \sqrt{\frac{2\pi}{kV}} [a_s (\mathbf{P} \cdot \mathbf{a}_s) e^{-i\omega t} + a_s^\dagger (\mathbf{P} \cdot \mathbf{a}_s^*) e^{i\omega t}], \quad (8.12)$$

where $H_{DE}(t)$ is the perturbation to the crystal Hamiltonian.

The two possible polarization modes are conveniently chosen to be the polar and azimuthal unit vectors. This way, any polarization of the photon will be described in terms of these two direction dependent linear polarization modes:

$$\mathbf{a}_{\hat{\theta}\varphi} = \hat{e}_\theta = \cos \theta \cos \varphi \hat{x} + \cos \theta \sin \varphi \hat{y} - \sin \theta \hat{z} \quad (8.13)$$

$$\mathbf{a}_{\theta\hat{\varphi}} = \hat{e}_\varphi = -\sin \varphi \hat{x} + \cos \varphi \hat{y}. \quad (8.14)$$

All this said, now the Hamiltonian (8.12) can be applied to an initial state $|i\rangle \otimes |\dots 0_{\hat{\theta}\varphi} 0_{\theta\hat{\varphi}} \dots\rangle$ to generate the time evolution of that state. The symbol $|i\rangle$ represents the initial state of solely the electron, and the symbol $|\dots 0_{\hat{\theta}\varphi} 0_{\theta\hat{\varphi}} \dots\rangle$ says that there are no photons propagating in the θ, φ direction with either \hat{e}_θ or \hat{e}_φ polarization. The formalism of first-order time-dependent perturbation theory will be applied to find the quantum state after a time t has elapsed, and the question of the probability that a photon has been emitted can be answered.

Note that this method shows the physics underlying the transition process in a much clearer way. Once the initial state and the Hamiltonian of the system are given, the state at any time, including the photon polarization, is fully determined. The only

arbitrary choice in this approach is the basis with which the states are represented; but, of course, that does not alter the physics of the problem.

Following Ref. [14], the final state can be written as follows:

$$\begin{aligned}
|f(t)\rangle_{electron} \otimes |f(t)\rangle_{photon} = & \\
\sum_{k \in \kappa} \int \frac{d\Omega}{4\pi} e^{-iE_{\kappa}t/\hbar} |\kappa, k\rangle \otimes & \left(b_{k\kappa, i, \hat{\theta}\varphi}(t) |\dots 1_{\hat{\theta}\varphi} 0_{\theta\hat{\varphi}} \dots\rangle + b_{k\kappa, i, \theta\hat{\varphi}}(t) |\dots 0_{\hat{\theta}\varphi} 1_{\theta\hat{\varphi}} \dots\rangle \right) + \\
\sum_{l \in \lambda} \int \frac{d\Omega}{4\pi} e^{-iE_{\lambda}t/\hbar} |\lambda, l\rangle \otimes & \left(1 - b_{l\lambda, i, \hat{\theta}\varphi}(t) - b_{l\lambda, i, \theta\hat{\varphi}}(t) \right) |\dots 0_{\hat{\theta}\varphi} 0_{\theta\hat{\varphi}} \dots\rangle, \quad (8.15)
\end{aligned}$$

where λ represents the initial band, κ the final band, E_{λ} and E_{κ} are their respective energies, and

$$\begin{aligned}
b_{k\kappa, i, \hat{\theta}\varphi}(t) = & \\
\frac{\langle \kappa, k | \otimes \langle 1_{\hat{\theta}\varphi} 0_{\theta\hat{\varphi}} | H_{DE}(0) | i \rangle \otimes | 0_{\hat{\theta}\varphi} 0_{\theta\hat{\varphi}} \rangle}{2i\hbar} & \left[\frac{1 - e^{i(\omega_{\kappa i} + \omega)t}}{\omega_{\kappa i} + \omega} + \frac{1 - e^{i(\omega_{\kappa i} - \omega)t}}{\omega_{\kappa i} - \omega} \right] = \\
- \frac{e}{m} \sqrt{\frac{2\pi}{kV}} \frac{\langle \kappa, k | \mathbf{P} | i \rangle \cdot \langle 1_{\hat{\theta}\varphi} 0_{\theta\hat{\varphi}} | \sum_s (a_s \mathbf{a}_s + a_s^\dagger \mathbf{a}_s^*) | 0_{\hat{\theta}\varphi} 0_{\theta\hat{\varphi}} \rangle}{2i\hbar} & \times \\
& \left[\frac{1 - e^{i(\omega_{\kappa i} + \omega)t}}{\omega_{\kappa i} + \omega} + \frac{1 - e^{i(\omega_{\kappa i} - \omega)t}}{\omega_{\kappa i} - \omega} \right]
\end{aligned}$$

$$\begin{aligned}
b_{k\kappa, i, \theta\hat{\varphi}}(t) = & \\
\frac{\langle \kappa, k | \otimes \langle 0_{\hat{\theta}\varphi} 1_{\theta\hat{\varphi}} | H_{DE}(0) | i \rangle \otimes | 0_{\hat{\theta}\varphi} 0_{\theta\hat{\varphi}} \rangle}{2i\hbar} & \left[\frac{1 - e^{i(\omega_{\kappa i} + \omega)t}}{\omega_{\kappa i} + \omega} + \frac{1 - e^{i(\omega_{\kappa i} - \omega)t}}{\omega_{\kappa i} - \omega} \right] = \\
- \frac{e}{m} \sqrt{\frac{2\pi}{kV}} \frac{\langle \kappa, k | \mathbf{P} | i \rangle \cdot \langle 0_{\hat{\theta}\varphi} 1_{\theta\hat{\varphi}} | \sum_s (a_s \mathbf{a}_s + a_s^\dagger \mathbf{a}_s^*) | 0_{\hat{\theta}\varphi} 0_{\theta\hat{\varphi}} \rangle}{2i\hbar} & \times \\
& \left[\frac{1 - e^{i(\omega_{\kappa i} + \omega)t}}{\omega_{\kappa i} + \omega} + \frac{1 - e^{i(\omega_{\kappa i} - \omega)t}}{\omega_{\kappa i} - \omega} \right] \quad (8.16)
\end{aligned}$$

are the time-dependent coefficients of the expansion in terms of the chosen basis set. These coefficients can be simplified by the proper action of the creation and

annihilation operators:

$$\begin{aligned} b_{k\kappa,i,\hat{\theta}\varphi}(t) &= -\frac{e}{m} \sqrt{\frac{2\pi}{kV}} \frac{\langle \kappa, k | \mathbf{P} | i \rangle \cdot \mathbf{a}_{\hat{\theta}\varphi}^*}{2i\hbar} g(t; \omega) \\ b_{k\kappa,i,\theta\hat{\varphi}}(t) &= -\frac{e}{m} \sqrt{\frac{2\pi}{kV}} \frac{\langle \kappa, k | \mathbf{P} | i \rangle \cdot \mathbf{a}_{\theta\hat{\varphi}}^*}{2i\hbar} g(t; \omega), \end{aligned} \quad (8.17)$$

where

$$g(t; \omega) \equiv \left[\frac{1 - e^{i(\omega_{\kappa i} + \omega)t}}{\omega_{\kappa i} + \omega} + \frac{1 - e^{i(\omega_{\kappa i} - \omega)t}}{\omega_{\kappa i} - \omega} \right] \quad (8.18)$$

has been defined.

Once the final state is known, expectation values for the polarization of a photon emitted along a given direction can be found. For this purpose, the following photon polarization operators are first defined following the Stokes parameters' notation for plane waves (see, for example, Ref. [17] for an introduction to the Stokes parameters)

$$\begin{aligned} Q|1_{\hat{\theta}\varphi}\rangle &= +1|1_{\hat{\theta}\varphi}\rangle & Q|1_{\hat{\theta}\varphi}\rangle &= +1|1_{\hat{\theta}\varphi}\rangle \\ Q|1_{\theta\hat{\varphi}}\rangle &= -1|1_{\theta\hat{\varphi}}\rangle & Q|1_{\theta\hat{\varphi}}\rangle &= -1|1_{\theta\hat{\varphi}}\rangle \end{aligned} \quad (8.19)$$

$$\begin{aligned} U \frac{1}{\sqrt{2}} (|1_{\hat{\theta}\varphi}\rangle + |1_{\theta\hat{\varphi}}\rangle) &= +1 \frac{1}{\sqrt{2}} (|1_{\hat{\theta}\varphi}\rangle + |1_{\theta\hat{\varphi}}\rangle) & U|1_{\hat{\theta}\varphi}\rangle &= +1|1_{\hat{\theta}\varphi}\rangle \\ U \frac{1}{\sqrt{2}} (|1_{\hat{\theta}\varphi}\rangle - |1_{\theta\hat{\varphi}}\rangle) &= -1 \frac{1}{\sqrt{2}} (|1_{\hat{\theta}\varphi}\rangle - |1_{\theta\hat{\varphi}}\rangle) & U|1_{\theta\hat{\varphi}}\rangle &= +1|1_{\theta\hat{\varphi}}\rangle \end{aligned} \quad (8.20)$$

$$\begin{aligned} V \frac{1}{\sqrt{2}} (|1_{\hat{\theta}\varphi}\rangle + i|1_{\theta\hat{\varphi}}\rangle) &= +1 \frac{1}{\sqrt{2}} (|1_{\hat{\theta}\varphi}\rangle + i|1_{\theta\hat{\varphi}}\rangle) & V|1_{\hat{\theta}\varphi}\rangle &= +i|1_{\theta\hat{\varphi}}\rangle \\ V \frac{1}{\sqrt{2}} (|1_{\hat{\theta}\varphi}\rangle - i|1_{\theta\hat{\varphi}}\rangle) &= -1 \frac{1}{\sqrt{2}} (|1_{\hat{\theta}\varphi}\rangle - i|1_{\theta\hat{\varphi}}\rangle) & V|1_{\theta\hat{\varphi}}\rangle &= -i|1_{\hat{\theta}\varphi}\rangle, \end{aligned} \quad (8.21)$$

and the expectation values for the measurement of polarization for a photon emitted in the θ, φ direction can be evaluated, for example, for V:

$$\begin{aligned} \langle f(t) | V | f(t) \rangle &= \langle f(t) | f(t) \rangle_{electron} \langle f(t) | V | f(t) \rangle_{photon} = \sum_{k' \in \kappa} \sum_{k \in \kappa} \langle \kappa, k' | \kappa, k \rangle \times \\ &\left(b_{k'\kappa,i,\hat{\theta}\varphi}^*(t) \langle 1_{\hat{\theta}\varphi} 0_{\theta\hat{\varphi}} | + b_{k'\kappa,i,\theta\hat{\varphi}}^*(t) \langle 0_{\hat{\theta}\varphi} 1_{\theta\hat{\varphi}} | \right) V \left(b_{k\kappa,i,\hat{\theta}\varphi}(t) | 1_{\hat{\theta}\varphi} 0_{\theta\hat{\varphi}} \rangle + b_{k\kappa,i,\theta\hat{\varphi}}(t) | 0_{\hat{\theta}\varphi} 1_{\theta\hat{\varphi}} \rangle \right) = \\ &\sum_{k \in \kappa} i b_{k\kappa,i,\hat{\theta}\varphi}(t) b_{k\kappa,i,\theta\hat{\varphi}}^*(t) - i b_{k\kappa,i,\hat{\theta}\varphi}^*(t) b_{k\kappa,i,\theta\hat{\varphi}}(t). \end{aligned} \quad (8.22)$$

Equations (8.17) can be plugged into the previous expression to obtain:

$$\langle f(t) | V | f(t) \rangle = \frac{e^2}{m^2} \frac{2\pi}{kV} \frac{|g(t; \omega)|^2}{4\hbar^2} \times i \sum_{k \in \kappa} \left(\langle \kappa, k | \mathbf{P} | i \rangle \cdot \mathbf{a}_{\hat{\theta}_\varphi}^* \langle \kappa, k | \mathbf{P} | i \rangle^* \cdot \mathbf{a}_{\theta_{\hat{\varphi}}} - \langle \kappa, k | \mathbf{P} | i \rangle^* \cdot \mathbf{a}_{\hat{\theta}_\varphi} \langle \kappa, k | \mathbf{P} | i \rangle \cdot \mathbf{a}_{\theta_{\hat{\varphi}}}^* \right). \quad (8.23)$$

At this point, a comment about this result is required. The question that the above equation is answering is: “Given an initial state $|i\rangle$, what is the probability that a photon is detected along a certain direction and has a given circular polarization after a time t ?”, rather than the more adequate question: “Given an initial state $|i\rangle$ and that a photon has been detected along a certain direction after a time t , what is the probability that it has a given circular polarization?” In order to answer this last question, Eq. (8.23) must be divided by the probability that a photon has been emitted along the required direction. That yields the expectation value of the circular polarization for a single photon or, equivalently, the measured circular polarization for an ensemble of photons V_{meas} :

$$V_{meas} = \frac{i \sum_{k \in \kappa} \left(\langle \kappa, k | \mathbf{P} | i \rangle \cdot \mathbf{a}_{\hat{\theta}_\varphi}^* \langle \kappa, k | \mathbf{P} | i \rangle^* \cdot \mathbf{a}_{\theta_{\hat{\varphi}}} - \langle \kappa, k | \mathbf{P} | i \rangle^* \cdot \mathbf{a}_{\hat{\theta}_\varphi} \langle \kappa, k | \mathbf{P} | i \rangle \cdot \mathbf{a}_{\theta_{\hat{\varphi}}}^* \right)}{\sum_{k \in \kappa} \left(\left| \langle \kappa, k | \mathbf{P} | i \rangle \cdot \mathbf{a}_{\hat{\theta}_\varphi}^* \right|^2 + \left| \langle \kappa, k | \mathbf{P} | i \rangle \cdot \mathbf{a}_{\theta_{\hat{\varphi}}} \right|^2 \right)} \quad (8.24)$$

The two other measured Stokes parameters can be found by an analogous calculation, yielding

$$Q_{meas} = \frac{\sum_{k \in \kappa} \left(\left| \langle \kappa, k | \mathbf{P} | i \rangle \cdot \mathbf{a}_{\hat{\theta}_\varphi}^* \right|^2 - \left| \langle \kappa, k | \mathbf{P} | i \rangle \cdot \mathbf{a}_{\theta_{\hat{\varphi}}} \right|^2 \right)}{\sum_{k \in \kappa} \left(\left| \langle \kappa, k | \mathbf{P} | i \rangle \cdot \mathbf{a}_{\hat{\theta}_\varphi}^* \right|^2 + \left| \langle \kappa, k | \mathbf{P} | i \rangle \cdot \mathbf{a}_{\theta_{\hat{\varphi}}} \right|^2 \right)} \quad (8.25)$$

$$U_{meas} = \frac{\sum_{k \in \kappa} \left(\langle \kappa, k | \mathbf{P} | i \rangle \cdot \mathbf{a}_{\hat{\theta}_\varphi}^* \langle \kappa, k | \mathbf{P} | i \rangle^* \cdot \mathbf{a}_{\theta_{\hat{\varphi}}} + \langle \kappa, k | \mathbf{P} | i \rangle^* \cdot \mathbf{a}_{\hat{\theta}_\varphi} \langle \kappa, k | \mathbf{P} | i \rangle \cdot \mathbf{a}_{\theta_{\hat{\varphi}}}^* \right)}{\sum_{k \in \kappa} \left(\left| \langle \kappa, k | \mathbf{P} | i \rangle \cdot \mathbf{a}_{\hat{\theta}_\varphi}^* \right|^2 + \left| \langle \kappa, k | \mathbf{P} | i \rangle \cdot \mathbf{a}_{\theta_{\hat{\varphi}}} \right|^2 \right)} \quad (8.26)$$

where the common denominator in Eqs. (8.24)-(8.26) yields the angular distribution

of light intensity. It can also be thought of as the Stokes parameter S:

$$S_{meas} = \sum_{k \in \kappa} \left(\left| \langle \kappa, k | \mathbf{P} | i \rangle \cdot \mathbf{a}_{\hat{\theta}\varphi}^* \right|^2 + \left| \langle \kappa, k | \mathbf{P} | i \rangle \cdot \mathbf{a}_{\hat{\theta}\hat{\varphi}}^* \right|^2 \right). \quad (8.27)$$

Finally, all reference to the momentum operator can be eliminated by means of the Wigner-Eckart theorem as in Eq. (8.9). Symmetry considerations will govern completely the polarization of the emitted photons as long as:

- Only two bands are involved in the light emission process.
- The direction towards which the light is being emitted is such that all the relevant momentum components belong to the same irrep of the point group of the crystal.

In that case,

$$Q_{meas} = \frac{\sum_{k \in \kappa} \sum_{l \in \lambda} \sum_{m \in \mu} \left(\left| \langle \mu, m; \lambda, l | \kappa, k \rangle \langle \lambda, l | i \rangle \hat{e}_m \cdot \mathbf{a}_{\hat{\theta}\varphi}^* \right|^2 - \left| \langle \mu, m; \lambda, l | \kappa, k \rangle \langle \lambda, l | i \rangle \hat{e}_m \cdot \mathbf{a}_{\hat{\theta}\hat{\varphi}}^* \right|^2 \right)}{\sum_{k \in \kappa} \sum_{l \in \lambda} \sum_{m \in \mu} \left(\left| \langle \mu, m; \lambda, l | \kappa, k \rangle \langle \lambda, l | i \rangle \hat{e}_m \cdot \mathbf{a}_{\hat{\theta}\varphi}^* \right|^2 + \left| \langle \mu, m; \lambda, l | \kappa, k \rangle \langle \lambda, l | i \rangle \hat{e}_m \cdot \mathbf{a}_{\hat{\theta}\hat{\varphi}}^* \right|^2 \right)} \quad (8.28)$$

$$U_{meas} = \frac{2\Re \left\{ \sum_{k \in \kappa} \sum_{l, l' \in \lambda} \sum_{m, m' \in \mu} \langle \mu, m; \lambda, l | \kappa, k \rangle \langle \kappa, k | \mu, m'; \lambda, l' \rangle \langle \lambda, l | i \rangle \langle \lambda, l' | i \rangle \hat{e}_m \cdot \mathbf{a}_{\hat{\theta}\varphi}^* \hat{e}_{m'} \cdot \mathbf{a}_{\hat{\theta}\hat{\varphi}} \right\}}{\sum_{k \in \kappa} \sum_{l \in \lambda} \sum_{m \in \mu} \left(\left| \langle \mu, m; \lambda, l | \kappa, k \rangle \langle \lambda, l | i \rangle \hat{e}_m \cdot \mathbf{a}_{\hat{\theta}\varphi}^* \right|^2 + \left| \langle \mu, m; \lambda, l | \kappa, k \rangle \langle \lambda, l | i \rangle \hat{e}_m \cdot \mathbf{a}_{\hat{\theta}\hat{\varphi}}^* \right|^2 \right)} \quad (8.29)$$

$$\begin{aligned}
V_{meas} = & \\
& -2\Im \left\{ \sum_{k \in \kappa} \sum_{l, l' \in \lambda} \sum_{m, m' \in \mu} \langle \mu, m; \lambda, l | \kappa, k \rangle \langle \kappa, k | \mu, m'; \lambda, l' \rangle \langle \lambda, l | i \rangle \langle \lambda, l' | i \rangle \hat{e}_m \cdot \mathbf{a}_{\hat{\theta}\hat{\varphi}}^* \hat{e}_{m'} \cdot \mathbf{a}_{\theta\hat{\varphi}} \right\} \\
& \frac{\sum_{k \in \kappa} \sum_{l \in \lambda} \sum_{m \in \mu} \left(\left| \langle \mu, m; \lambda, l | \kappa, k \rangle \langle \lambda, l | i \rangle \hat{e}_m \cdot \mathbf{a}_{\hat{\theta}\hat{\varphi}}^* \right|^2 + \left| \langle \mu, m; \lambda, l | \kappa, k \rangle \langle \lambda, l | i \rangle \hat{e}_m \cdot \mathbf{a}_{\theta\hat{\varphi}}^* \right|^2 \right)}{\hspace{10em}}
\end{aligned} \tag{8.30}$$

where \Re and \Im mean real and imaginary parts respectively, and \hat{e}_m is a unit vector pointing in the same direction as the basis function of the irrep μ to which it is related.

8.4 Application to semiconductor structures

The abstract formalism developed in the previous section can be employed to predict measured polarizations for several materials of interest. In particular, it can be used to design experiments for optical spin injection detection. The optimal location of the light detector with respect to the predominant spin can be found this way. Several cases of interest are explicitly worked out in the following subsections. In these examples, it is assumed that the electrons that are spread close to a symmetry point can be well approximated as being in that symmetry point.

8.4.1 Bulk zincblende luminescence

Bulk zincblendes possess a T_d point group symmetry. The character table and basis functions for T_d , adapted from Ref. [15], are shown in Table 8.2.

In a number of direct band gap zincblendes, the conduction band minimum is situated at the Brillouin zone center, and it is described by the Γ_6 irrep. The valence band maximum is also at the zone center, and it is described by the Γ_8 irrep. This irrep splits away from the zone center into the heavy and light hole bands, as seen in Fig. 8.2.

Consider, for example, an electron that has been injected into the conduction band (CB) with its spin pointing up in the z direction. The initial electron state will

T_d	E	\bar{E}	$8C_3$	$8\bar{C}_3$	$\frac{3C_2}{3\bar{C}_2}$	$6S_4$	$6\bar{S}_4$	$\frac{6\sigma_d}{6\bar{\sigma}_d}$	Basis Functions
Γ_1	1	1	1	1	1	1	1	1	R or xyz
Γ_2	1	1	1	1	1	-1	-1	-1	$S_x S_y S_z$
Γ_3	2	2	-1	-1	2	0	0	0	$(2z^2 - x^2 - y^2), \sqrt{3}(x^2 - y^2)$
Γ_4	3	3	0	0	-1	1	1	-1	S_x, S_y, S_z
Γ_5	3	3	0	0	-1	-1	-1	1	x, y, z
Γ_6	2	-2	1	-1	0	$\sqrt{2}$	$-\sqrt{2}$	0	$ s = 1/2, -1/2\rangle, s = 1/2, +1/2\rangle$
Γ_7	2	-2	1	-1	0	$-\sqrt{2}$	$\sqrt{2}$	0	$\Gamma_6 \times \Gamma_2$
Γ_8	4	-4	-1	1	0	0	0	0	$ j = 3/2, -3/2\rangle, j = 3/2, -1/2\rangle,$ $ j = 3/2, +1/2\rangle, j = 3/2, +3/2\rangle$

Table 8.2: Character and basis functions table for T_d

be $|i\rangle = |s = 1/2, -1/2\rangle$. If the luminescence due to recombination with the valence band (VB) Γ_8 is under study, the expressions in Eqs. (8.28)—(8.30) can be used to calculate the light polarization in an arbitrary direction.

We know that the initial state belongs to the Γ_6 irrep, the final state to the Γ_8 irrep and Table 8.2 shows that the momentum operator transforms according to the Γ_5 irrep. The Clebsch-Gordan coefficients for T_d (aka. coupling coefficients) can be looked up, for example, in Table 83 of Ref. [15]. In this table the notation is confusing, in the sense that the basis functions for O and T_d are reshuffled, and the table can be employed *as is* for O only. The equivalence between the O and the T_d basis functions is shown in Table 8.3. Table 8.4 shows the coefficients in a ready-to-use way for T_d .

O	T_d
$ \Gamma_8, -3/2\rangle$	$ \Gamma_8, +1/2\rangle$
$ \Gamma_8, -1/2\rangle$	$ \Gamma_8, +3/2\rangle$
$ \Gamma_8, +1/2\rangle$	$ \Gamma_8, -3/2\rangle$
$ \Gamma_8, +3/2\rangle$	$ \Gamma_8, -1/2\rangle$

Table 8.3: Equivalence table of basis functions for O and T_d .

	$ x\rangle_5 -\frac{1}{2}\rangle_6$	$ x\rangle_5 +\frac{1}{2}\rangle_6$	$ y\rangle_5 -\frac{1}{2}\rangle_6$	$ y\rangle_5 +\frac{1}{2}\rangle_6$	$ z\rangle_5 -\frac{1}{2}\rangle_6$	$ z\rangle_5 +\frac{1}{2}\rangle_6$
$7\langle-1/2 $	0	$\frac{-i}{\sqrt{3}}$	0	$\frac{-1}{\sqrt{3}}$	$\frac{i}{\sqrt{3}}$	0
$7\langle+1/2 $	$\frac{-i}{\sqrt{3}}$	0	$\frac{1}{\sqrt{3}}$	0	0	$\frac{-i}{\sqrt{3}}$
$8\langle-3/2 $	$\frac{-i}{\sqrt{2}}$	0	$\frac{-1}{\sqrt{2}}$	0	0	0
$8\langle-1/2 $	0	$\frac{i}{\sqrt{6}}$	0	$\frac{1}{\sqrt{6}}$	$i\sqrt{\frac{2}{3}}$	0
$8\langle+1/2 $	$\frac{-i}{\sqrt{6}}$	0	$\frac{1}{\sqrt{6}}$	0	0	$i\sqrt{\frac{2}{3}}$
$8\langle+3/2 $	0	$\frac{i}{\sqrt{2}}$	0	$\frac{-1}{\sqrt{2}}$	0	0

Table 8.4: The Clebsch-Gordan coefficients for $\Gamma_5 \otimes \Gamma_6$ belonging to T_d , with $|j\rangle_i$ a shorthand for $|\Gamma_i, j\rangle$.

Therefore, for the degree of circular polarization:

$$\begin{aligned}
V_{meas} = & \\
& -2\Im \left\{ \frac{\sum_{k \in \Gamma_8} \sum_{m, m' \in \Gamma_5} \langle \Gamma_5, m; \Gamma_6, +1/2 | \Gamma_8, k \rangle \langle \Gamma_8, k | \Gamma_5, m'; \Gamma_6, +1/2 \rangle \hat{e}_m \cdot \mathbf{a}_{\hat{\theta}\varphi}^* \hat{e}_{m'} \cdot \mathbf{a}_{\theta\hat{\varphi}}}{\sum_{k \in \Gamma_8} \sum_{m \in \Gamma_5} \left(\left| \langle \Gamma_5, m; \Gamma_6, +1/2 | \Gamma_8, k \rangle \hat{e}_m \cdot \mathbf{a}_{\hat{\theta}\varphi}^* \right|^2 + \left| \langle \Gamma_5, m; \Gamma_6, +1/2 | \Gamma_8, k \rangle \hat{e}_m \cdot \mathbf{a}_{\theta\hat{\varphi}} \right|^2 \right)} \right\} \\
& \tag{8.31}
\end{aligned}$$

and plugging in the numbers, one obtains

$$V_{meas} = -\frac{\frac{2}{3} \cos \theta}{4/3} = -\frac{1}{2} \cos \theta, \tag{8.32}$$

where θ is the angle between the injected electron spin and the direction of emission. The denominator in Eq. (8.31) yields the angular distribution of the emitted radiation, which is isotropic for this case.

Similarly, for the two modes of linear polarization:

$$Q_{meas} = 0 \quad U_{meas} = 0. \tag{8.33}$$

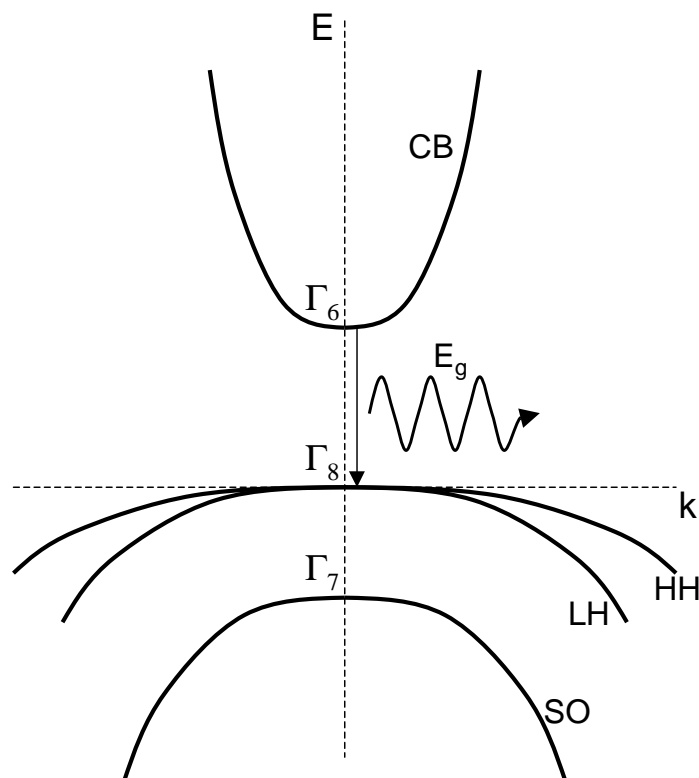


Figure 8.2: Band structure for a zincblende near the zone center. The irreps at $\mathbf{k} = 0$ are labeled, and their respective bands too. A transition between Γ_6 and Γ_7 has been depicted, yielding a photon having the gap energy E_g .

8.4.2 Quantum well luminescence

In this section, only quantum wells (QWs) constructed with zincblende semiconductors will be considered.

Most of the times, the confining and the active layers will not have the same lattice parameter. This will produce stress in the active layer which, in turn, will cause the lifting of the degeneracy between heavy holes and light holes at the zone center of zincblendes. Another source of splitting will be the reduction of symmetry due to the quantum confinement of the electrons. Stress and confinement will reduce the symmetry point group of the active layer from T_d to D_{2d} or C_{2v} [18], depending respectively on whether the $[110]$ and $[\bar{1}10]$ directions are equivalent or not. The interplay of confinement and stress effects will determine whether the heavy hole or light hole bands will remain at the top of the valence band.

D_{2d}	E	\bar{E}	$2S_4$	$2\bar{S}_4$	C_2 \bar{C}_2	$2C'_2$ $2\bar{C}'_2$	$2\sigma_d$ $2\bar{\sigma}_d$	Basis Functions
Γ_1	1	1	1	1	1	1	1	R
Γ_2	1	1	1	1	1	-1	-1	S_z
Γ_3	1	1	-1	-1	1	1	-1	$(x^2 - y^2)$
Γ_4	1	1	-1	-1	1	-1	1	xy or z
Γ_5	2	2	0	0	-2	0	0	S_x, S_y
Γ_6	2	-2	$\sqrt{2}$	$-\sqrt{2}$	0	0	0	$ s = 1/2, -1/2\rangle, s = 1/2, +1/2\rangle$
Γ_7	2	-2	$-\sqrt{2}$	$\sqrt{2}$	0	0	0	$\Gamma_6 \times \Gamma_3$

Table 8.5: Character and basis functions table for D_{2d}

QWs with D_{2d} symmetry

QWs with symmetric walls, common atom and an even number of monolayers in the active layer (eg. AlSb/GaSb/AlSb) have D_{2d} symmetry. The character table of D_{2d} is shown in Table 8.5.

By checking the Clebsch-Gordan coefficients in Ref. [15] or the compatibility relations for the basis states of C_{4v} [19], it can be deduced that the conduction band edge states and the top¹ heavy hole-like (HH1) state will transform according to Γ_6 , while the top light hole-like (LH1) and split-off-like (SO) states will transform according to Γ_7 .

The polarization of the emitted light will depend on whether the valence band edge is described by states with predominantly HH or LH character (see Fig. 8.3). The other valence states are assumed to lie deep enough in energy that no transitions are made. Table 8.6 shows the appropriate Clebsch-Gordan coefficients for the transitions depicted in Fig. 8.3. When studying case a), it can be seen from Eq. (8.30) that, for vertical emission and for a single spin injected,

$$V_{meas} = \frac{-2\Im \{ \langle \Gamma_5, x; \Gamma_6, +1/2 | \Gamma_6, -1/2 \rangle \langle \Gamma_6, -1/2 | \Gamma_5, y; \Gamma_6, +1/2 \rangle \}}{|\langle \Gamma_5, x; \Gamma_6, +1/2 | \Gamma_6, -1/2 \rangle|^2 + |\langle \Gamma_5, y; \Gamma_6, +1/2 | \Gamma_6, -1/2 \rangle|^2} = -1, \quad (8.34)$$

while no net linear polarization would be measured.

¹HH_{odd} and LH_{even} (HH_{even} and LH_{odd}) states transform according to Γ_6 (Γ_7) [18]. Even and odd also label the parity of the total wavefunction. The even-odd mixing is due to the fact that zincblendes don't possess inversion symmetry, explaining the observation of parity forbidden transitions [20].

	$ x\rangle_5 -\frac{1}{2}\rangle_6$	$ x\rangle_5 +\frac{1}{2}\rangle_6$	$ y\rangle_5 -\frac{1}{2}\rangle_6$	$ y\rangle_5 +\frac{1}{2}\rangle_6$
$6\langle-1/2 $	0	$\frac{i}{\sqrt{2}}$	0	$\frac{-1}{\sqrt{2}}$
$6\langle+1/2 $	$\frac{i}{\sqrt{2}}$	0	$\frac{1}{\sqrt{2}}$	0
$7\langle-1/2 $	0	$\frac{i}{\sqrt{2}}$	0	$\frac{1}{\sqrt{2}}$
$7\langle+1/2 $	$\frac{i}{\sqrt{2}}$	0	$\frac{-1}{\sqrt{2}}$	0

Table 8.6: The Clebsch-Gordan coefficients for $\Gamma_5 \otimes \Gamma_6$ belonging to D_{2d} , with $|j\rangle_i$ a shorthand for $|\Gamma_i, j\rangle$.

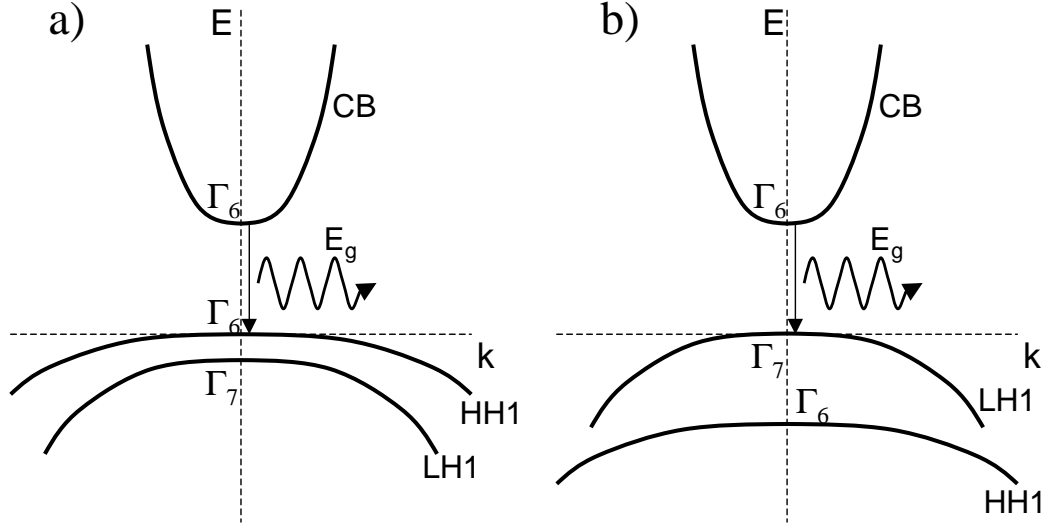


Figure 8.3: Band structure near the zone center for a QW with D_{2d} symmetry. (a) shows the case where the heavy hole band has higher energy, while (b) shows the case where the light hole band has higher energy.

When the LH band is the one having higher energy [see Fig. 8.3, (b)], a similar analysis yields

$$Q_{meas} = 0 \quad U_{meas} = 0 \quad V_{meas} = +1. \quad (8.35)$$

The fact that the z basis function—therefore P_z —belongs to a different irrep than x and y will make an exact statement about the polarization for a direction other than along z impossible. However, some good approximations can be made in the case where a few assumptions are valid.

When the symmetry of a system is reduced, levels that were previously degenerate split in energy. Another consequence of the symmetry reduction is the mixing of states. But the mixing of states can only take place between original irreps that will

transform into the same irrep of the reduced symmetry group. To exemplify this, consider the CB, HH, LH and SO bands of bulk GaSb as a starting point. Inside a symmetric quantum well, the electron in a GaSb active layer will see an environment with D_{2d} symmetry. Unless the well is very narrow, the well states will keep most of the character of the bulk states they come from [21].

So, when the HH1 band is on the VB edge, the approximation can be made that the action of P_z is negligible because these states will have only a small p_z component. In that case, and assuming that the electron in the CB is the initial state $|\Gamma_6, +1/2\rangle$, the different polarizations will be given by plugging the coefficients in Table 8.6 into Eqs. (8.28)—(8.30):

$$\begin{aligned}
 S_{meas} &\propto \frac{1 + \cos^2 \theta}{2} \\
 Q_{meas} &= \frac{1 - \cos^2 \theta}{1 + \cos^2 \theta} & U_{meas} &= 0 & V_{meas} &= -\frac{2 \cos \theta}{1 + \cos^2 \theta}. \quad (8.36)
 \end{aligned}$$

These results are plotted for both input spins in Fig. 8.4. Note that, although some linear spin polarization can be measured, reaching a maximum for emission in the plane of the QW, it will not be spin-dependent. So, only optical measurements of circular polarization can be used for electron spin detection. Clearly, the direction perpendicular to the well is favored because of its higher amount of signal for a totally spin polarized electron population.

In the case of Fig. 8.3 (b), when the approximation that the top of the VB has LH character holds, a similar analysis can be performed. The polarizations that one obtains for all initial spins in the $|\Gamma_6, +1/2\rangle$ state are

$$\begin{aligned}
 S_{meas} &\propto \frac{5 - 3 \cos^2 \theta}{6} \\
 Q_{meas} &= 1 - \frac{2}{5 - 3 \cos^2 \theta} & U_{meas} &= 0 & V_{meas} &= \frac{2 \cos \theta}{5 - 3 \cos^2 \theta}. \quad (8.37)
 \end{aligned}$$

These results are plotted for both input spins in Fig. 8.5. Again, the only means to detect spin injection is through measurements of circular polarization. The amount of polarization expected for emission perpendicular to the QW plane is the same as

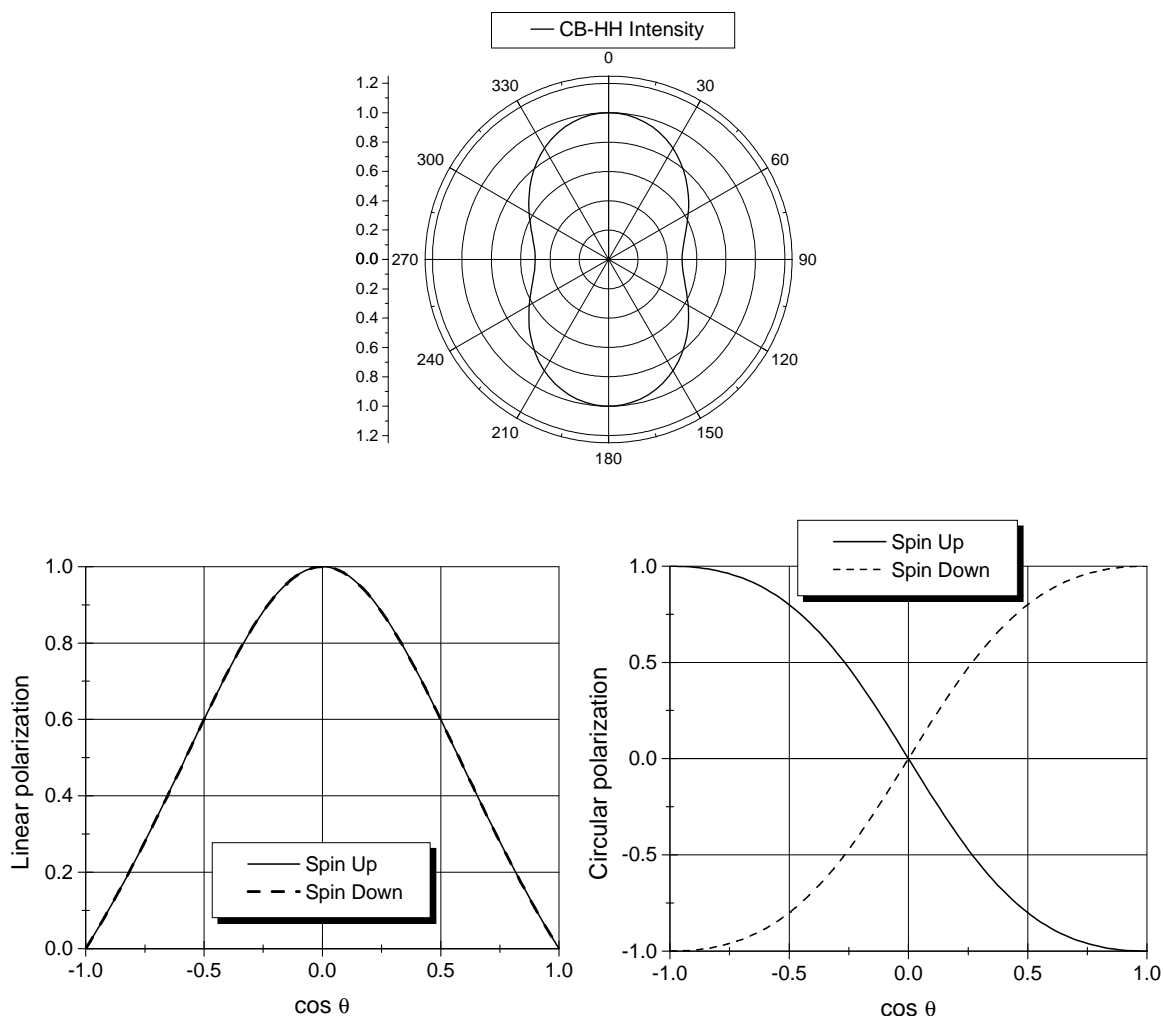


Figure 8.4: Approximate intensity pattern, linear and circular polarization for radiation coming from band-to-band recombination for a QW with D_{2d} symmetry. These results are valid only when the top of the valence band is HH-like.

in CB-HH1 transitions. However, if one is forced to perform measurements off-axis, it is clearly more convenient to resort to a CB-HH1 structure because of the greater maximum attainable signal.

QWs with C_{2v} symmetry

All of the QWs having asymmetric confinement layers (eg. an AlSb/InAs/GaSb/AlSb QW), most of the QWs having symmetric walls but noncommon atom (eg. AlSb/InAs/AlSb) and QWs with common atoms and an odd number of monolayers [18] (eg. AlSb/GaSb/AlSb) possess C_{2v} point group symmetry. In this class of

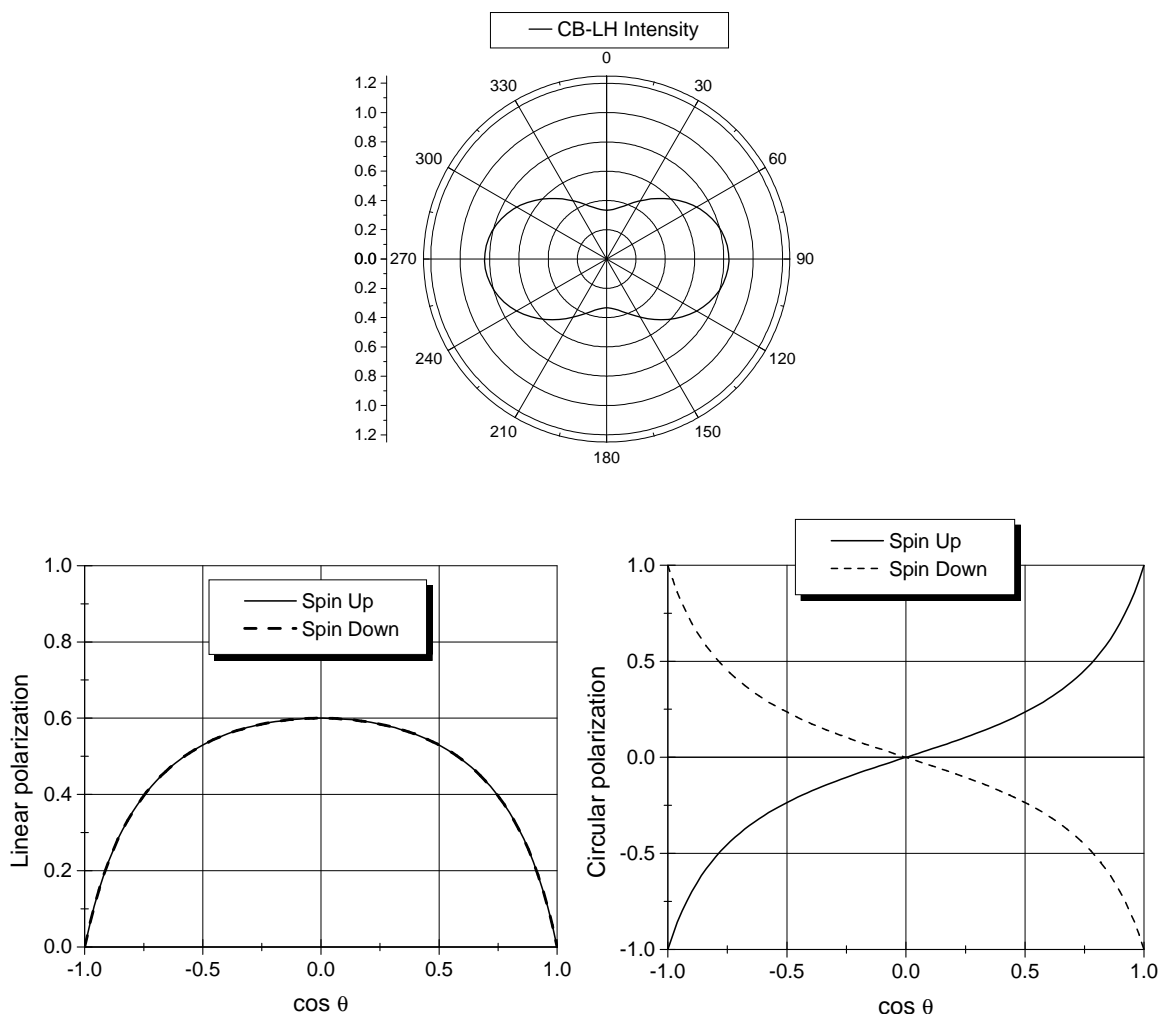


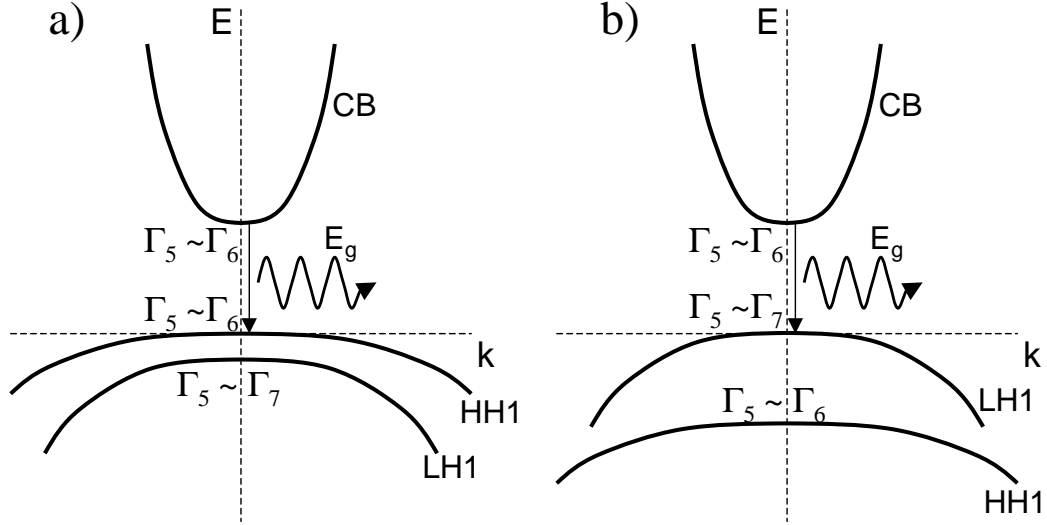
Figure 8.5: As in Fig. 8.4, but the top of the valence band is LH-like.

QWs, as opposed to the D_{2d} QW's, a rotation of 180° about the x or y axes will not result in the same structure. Its character table, adapted from Ref. [15], is shown in Table 8.7.

The x and y axis are not equivalent for this family of quantum wells. Of course, the z axis, being the direction of growth, will not be equivalent to any of those, either. Therefore, in a strict sense, symmetry arguments cannot help in determining the average polarization of the emitted photons, and Eqs. (8.24)—(8.26) should be employed.

However, in some cases the reduction of the symmetry from D_{2d} to C_{2v} is due to small effects. For example, in an AlSb/InAs/AlSb QW, the symmetry is reduced

C_{2v}	E	\bar{E}	C_2 \bar{C}_2	σ_v $\bar{\sigma}_v$	σ'_d $\bar{\sigma}'_d$	Basis Functions
Γ_1	1	1	1	1	1	z
Γ_2	1	1	-1	1	-1	S_y or x
Γ_3	1	1	1	-1	-1	S_z or xy
Γ_4	1	1	-1	-1	1	S_x or y
Γ_5	2	-2	0	0	0	$ s = 1/2, -1/2\rangle, s = 1/2, +1/2\rangle$

Table 8.7: Character and basis functions table for C_{2v} Figure 8.6: Band structure near the zone center for a QW with C_{2v} symmetry. Γ_5 is the exact irrep for any band, and their approximate counterpart irreps in D_{2d} are also shown.

because of the different nature of the interface bonds; Sb-In at one interface and As-Al at the other. This is only an interface contribution, which should cause a very small mixing between the D_{2d} Γ_6 and Γ_7 states. Following the $\mathbf{k} \cdot \mathbf{p}$ spirit, these interface effects can be neglected, and it can be assumed that all the C_{2v} states behave according to their original D_{2d} irreps (see Fig. 8.6). When these assumptions hold, the analysis performed for D_{2d} QWs will also be valid for asymmetric QWs.

8.4.3 Bulk wurtzite luminescence

Bulk wurtzites, such as the stable phase at room temperature of GaN, AlN, InN [22, 23], possess a C_{6v} point group symmetry. The character table for this point group is given in Table 8.8. In that table the notation from Koster *et al.* [15] has been

C_{6v}	E	\bar{E}	$\begin{matrix} C_2 \\ \bar{C}_2 \end{matrix}$	$2C_3$	$2\bar{C}_3$	$2C_6$	$2\bar{C}_6$	$\begin{matrix} 3\sigma_d \\ 3\bar{\sigma}_d \end{matrix}$	$\begin{matrix} 3\sigma_v \\ 3\bar{\sigma}_v \end{matrix}$	Basis Functions
Γ_1	1	1	1	1	1	1	1	1	1	R or z
Γ_2	1	1	1	1	1	1	1	-1	-1	S_z
Γ_3	1	1	-1	1	1	-1	-1	1	-1	$x^3 - 3xy^2$
Γ_4	1	1	-1	1	1	-1	-1	-1	1	$y^3 - 3yx^2$
Γ_5	2	2	-2	-1	-1	1	1	0	0	$(S_x - iS_y), -(S_x + iS_y)$
Γ_6	2	2	2	-1	-1	-1	-1	0	0	$\Gamma_3 \times \Gamma_5$
Γ_7	2	-2	0	1	-1	$\sqrt{3}$	$-\sqrt{3}$	0	0	$ 1/2, -1/2\rangle, 1/2, +1/2\rangle$
Γ_8	2	-2	0	1	-1	$-\sqrt{3}$	$\sqrt{3}$	0	0	$\Gamma_7 \times \Gamma_3$
Γ_9	2	-2	0	-2	2	0	0	0	0	$ 3/2, -3/2\rangle, 3/2, +3/2\rangle$

Table 8.8: Character and basis functions table for C_{6v} .

used. The reader must be careful because often in literature Herring's scheme [24] is used. In this scheme, the Γ_5 and Γ_6 irreps are interchanged respect to Koster's sequence [25].

Figure 8.7 (a) shows the band structure of GaN near the zone center. As opposed to zincblendes, the top of the valence band in wurtzites is split into two spin degenerate bands. The uppermost—heavy hole (HH)—transforms according to the Γ_9 irrep of C_{6v} , while the light hole (LH) and the crystal split band (CR) transform according to Γ_7 . The crystal split band receives this name because, even when the spin orbit interaction is not considered, that band is split from the others due to the crystal field being different along z than along x and y . Panel (b) shows the splittings between the different subbands. The numeric values are for GaN, but the behavior shown is also applicable to InN. That panel also shows the allowed dipole transitions and their polarization for vertical emission depending on the incoming spin (quantized along the z axis).

At low temperatures, the thermal occupancy factor will make transitions to bands other than the HH highly improbable. In that case (or, for that matter, whenever transitions to the HH can be resolved spectroscopically), the polarization of the emitted light in an arbitrary direction can be determined. The Clebsch-Gordan coefficients for transitions from the CB into the HH band are basically the same than in the case of D_{2d} QWs, except for an overall factor. This is understandable, because in D_{2d}

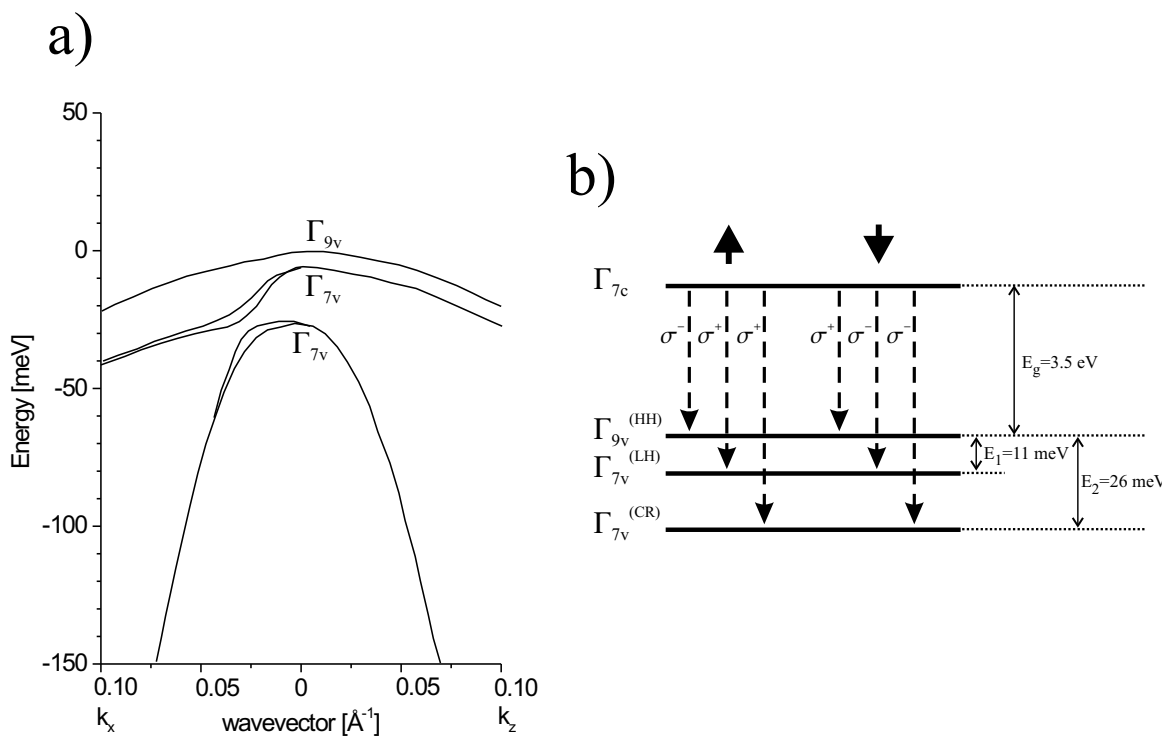


Figure 8.7: Band structure near the zone center for GaN. (a) has been adapted from Ref. [26]. The band structure for InN is the same except for the numerical values of the splittings and the band gap. (b) shows the allowed dipole transitions and their polarization for vertical emission as a function of the electron spin (taken along the z direction).

heterostructures the x and y are also equivalent, while the z axis is singled out. Therefore, the results shown in Fig. 8.4 will also be valid for transitions from the CB into the Γ_9 band in wurtzites.

8.5 Monte Carlo photon generation

At this point a single event generation scheme can be devised in order to reproduce the above results and, once the photons are generated, study phenomena that might alter their behavior depending on their polarization, such as interface refraction, magneto-optical Kerr effect, passage through polarizers...

After that, it will be shown that the time-dependent perturbation picture and the Monte Carlo scheme yield the same results when a large number of photons is

considered.

8.5.1 Single event generation scheme

Figure 8.8 displays the general steps to generate a single photon using random numbers in such a way that their electric fields have the adequate polarization to reproduce the results predicted by the time-dependent perturbation theory derivation. This paragraph will discuss the steps inside the dashed rectangle in Fig. 8.8, namely how to assign an electric field to a generated photon.

The recipe and its application to photon generation for a bulk zincblende are described in the following steps:

- I. A basis set of states $\{|\kappa, k\rangle\}$ spanning the arrival band must be chosen.
- II. A direction of propagation for the photon is generated according to the intensity distribution given by Eq. (8.27). In the cases with axial symmetry, the probability of emission towards a solid angle $d\Omega$ will depend only on the polar angle θ :

$$p(\theta, \varphi) d\Omega = \frac{f(\cos \theta)}{2\pi} d(\cos \theta) d\varphi, \quad (8.38)$$

with $f(\cos \theta)$ properly normalized to 1 and, if x is the generated random number between 0 and 1, the appropriate $\cos \theta$ can be found by solving the following equation:

$$x = \int_{-1}^{\cos \theta} f(\cos \theta') d(\cos \theta'). \quad (8.39)$$

- III. A quantization axis for the electron spin must be chosen. The direction of the electron spin is determined according to whether it is required to be random, all or predominantly pointing in one direction...
- IV. The momentum matrix element between the initial state and all the possible arrival basis states $\langle \kappa, k | \mathbf{P} | i \rangle$ is found.
- V. The transition from $|i\rangle$ to the final state is partitioned to transitions to basis

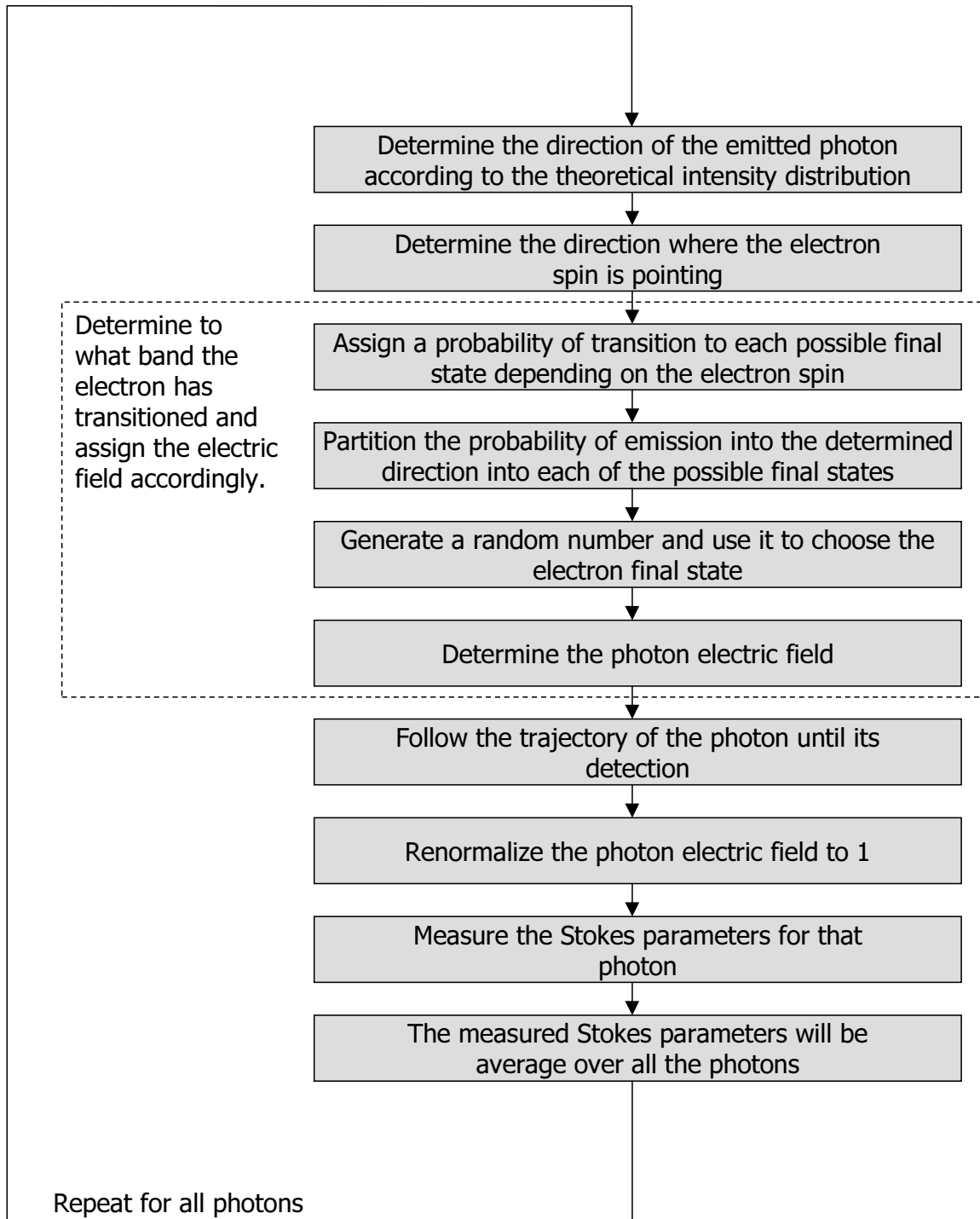


Figure 8.8: Flowchart for the Monte Carlo photon generation process.

states $|\kappa, k\rangle$, each taking place with a probability

$$p(\kappa, k) = \frac{|\langle \kappa, k | \mathbf{P} | i \rangle \cdot \mathbf{a}_{\theta\varphi}^*|^2 + |\langle \kappa, k | \mathbf{P} | i \rangle \cdot \mathbf{a}_{\theta\hat{\varphi}}^*|^2}{\sum_{k' \in \kappa} \left(|\langle \kappa, k' | \mathbf{P} | i \rangle \cdot \mathbf{a}_{\theta\varphi}^*|^2 + |\langle \kappa, k' | \mathbf{P} | i \rangle \cdot \mathbf{a}_{\theta\hat{\varphi}}^*|^2 \right)}. \quad (8.40)$$

VI. Generate a random number between 0 and 1, and choose the state to which the transition has taken place according to the probabilities calculated in the previous step.

VII. The electric field of the photon is set to

$$\mathbf{E} = \langle \kappa, k | \mathbf{P} | i \rangle \cdot \mathbf{a}_{\theta\varphi}^* \mathbf{a}_{\theta\varphi} + \langle \kappa, k | \mathbf{P} | i \rangle \cdot \mathbf{a}_{\theta\hat{\varphi}}^* \mathbf{a}_{\theta\hat{\varphi}}, \quad (8.41)$$

where the units here are of no importance because in the end the electric field will be renormalized. The components of the electric field can also be thought of as the coefficients of the photon state.

VIII. Propagate the photon through the desired structure.

IX. Normalize the electric field of the photon to one. The amplitude of the electric field given before carries information about the probability that the photon is emitted along that direction. Since, by construction, the photon has made it to the present point, the probability that it is there is one. With the normalization, all photons will have the same weight when averaging electric fields.

X. Compute the Stokes parameter for that photon.

XI. Perform the average of the Stokes parameters for all photons hitting the desired location.

8.5.2 Equivalence of the Monte Carlo and the time-dependent perturbation pictures

The fact that the prescription given in Sec. 8.5.1 yields the same results as Eqs. (8.24)—(8.26) is not obvious at first sight, and requires some thought. Here the equivalence will be shown for the light emitted in the semiconductor structure, when its polarization has not been affected by any extraneous element.

In Sec. 8.5.1 different quantum states are being generated according to a classical probability. Density matrices [27] are the ideal tool to describe this situation. In particular, the density matrix describing a generated photon will be

$$\rho = \sum_{k \in \kappa} p(\kappa, k) |\kappa, k\rangle \langle \kappa, k| \otimes \frac{\langle \kappa, k | \mathbf{P} | i \rangle \cdot \left(\mathbf{a}_{\hat{\theta}\varphi}^* |1_{\hat{\theta}\varphi}\rangle + \mathbf{a}_{\hat{\theta}\hat{\varphi}}^* |1_{\theta\hat{\varphi}}\rangle \right) \left(\mathbf{a}_{\hat{\theta}\varphi} \langle 1_{\hat{\theta}\varphi}| + \mathbf{a}_{\theta\hat{\varphi}} \langle 1_{\theta\hat{\varphi}}| \right) \cdot \langle \kappa, k | \mathbf{P} | i \rangle^*}{\left| \langle \kappa, k | \mathbf{P} | i \rangle \cdot \mathbf{a}_{\hat{\theta}\varphi}^* \right|^2 + \left| \langle \kappa, k | \mathbf{P} | i \rangle \cdot \mathbf{a}_{\theta\hat{\varphi}}^* \right|^2}, \quad (8.42)$$

where $p(\kappa, k)$ is given by Eq. 8.40 and the denominator comes from the normalization of the electric field or, in other words, the normalization of the photon state. The expectation value of an operator, say the linear polarization parameter Q , will be given by the trace over the photon and electron states of that operator times the density matrix:

$$Q_{meas} = \text{Tr}(\rho Q) = \sum_{k' \in \kappa} \sum_{s' \in \hat{\theta}, \hat{\varphi}} (\langle \kappa, k' | \otimes \langle 1_{s'} |) \rho Q (| \kappa, k' \rangle \otimes | 1_{s'} \rangle) = \sum_{k \in \kappa} \sum_{s' \in \hat{\theta}, \hat{\varphi}} p(\kappa, k) \times \frac{\langle \kappa, k | \mathbf{P} | i \rangle \cdot \langle 1_{s'} | \left(| 1_{\hat{\theta}\varphi} \rangle \mathbf{a}_{\hat{\theta}\varphi} + | 1_{\theta\hat{\varphi}} \rangle \mathbf{a}_{\theta\hat{\varphi}} \right) \left(\mathbf{a}_{\hat{\theta}\varphi} \langle 1_{\hat{\theta}\varphi}| + \mathbf{a}_{\theta\hat{\varphi}} \langle 1_{\theta\hat{\varphi}}| \right) Q | 1_{s'} \rangle \cdot \langle \kappa, k | \mathbf{P} | i \rangle^*}{\left| \langle \kappa, k | \mathbf{P} | i \rangle \cdot \mathbf{a}_{\hat{\theta}\varphi}^* \right|^2 + \left| \langle \kappa, k | \mathbf{P} | i \rangle \cdot \mathbf{a}_{\theta\hat{\varphi}}^* \right|^2}, \quad (8.43)$$

and we can use the action of operator Q as defined in Eq. (8.19) to arrive at the

previously given expression:

$$Q_{meas} = \frac{\sum_{k \in \kappa} \left(\left| \langle \kappa, k | \mathbf{P} | i \rangle \cdot \mathbf{a}_{\hat{\theta}\varphi}^* \right|^2 - \left| \langle \kappa, k | \mathbf{P} | i \rangle \cdot \mathbf{a}_{\theta\varphi}^* \right|^2 \right)}{\sum_{k \in \kappa} \left(\left| \langle \kappa, k | \mathbf{P} | i \rangle \cdot \mathbf{a}_{\hat{\theta}\varphi}^* \right|^2 + \left| \langle \kappa, k | \mathbf{P} | i \rangle \cdot \mathbf{a}_{\theta\varphi}^* \right|^2 \right)}. \quad (8.25)$$

The proof of equivalence for the other polarization operators U and V goes in a very similar manner.

8.6 Application to a bulk zincblende

The general steps outlined in Sec. 8.5.1 can be made more explicit for the case of bulk zincblendes due to the high symmetry they show. The following list is the equivalent of the one previously shown, but adapted to bulk zincblendes:

- I. The obvious choice for the basis for the arrival space are the $\{|3/2, m_j\rangle\}$ states quantized along the z axis, due to the fact that tables of Clebsch-Gordan coefficients are readily available for them.
- II. The emission process—without taking polarization into account—is isotropic. Therefore, two random numbers must be generated to obtain the polar angles θ and φ of the unit vector along the direction of propagation of the photon. A random number between -1 and 1 will yield $\cos \theta$; and a number between 0 and 2π will yield φ .
- III. The quantization axis for the electron spin is chosen to be the z axis. Again, this is because it is the convention used in the existing tables. Once the direction where the spin is pointing has been set, the initial state is set to [27]

$$|i\rangle = \cos\left(\frac{\theta}{2}\right) |\Gamma_6, +1/2\rangle + \sin\left(\frac{\theta}{2}\right) e^{i\varphi} |\Gamma_6, -1/2\rangle \equiv b_+ |\Gamma_6, +1/2\rangle + b_- |\Gamma_6, -1/2\rangle. \quad (8.44)$$

State	$p(\kappa, k)$
$ 3/2, -3/2\rangle$	$\frac{ b_- ^2}{4} (3 + \cos(2\theta))$
$ 3/2, -1/2\rangle$	$\frac{ b_+ ^2}{6} (1 + \cos^2 \theta) + \frac{2 b_- ^2}{3} \sin^2 \theta$
$ 3/2, +1/2\rangle$	$\frac{ b_- ^2}{6} (1 + \cos^2 \theta) + \frac{2 b_+ ^2}{3} \sin^2 \theta$
$ 3/2, +3/2\rangle$	$\frac{ b_+ ^2}{4} (3 + \cos(2\theta))$

Table 8.9: Transition probability for a state in the conduction band and arbitrary spin into each of the states forming a basis in the valence band edge space.

- IV. By virtue of the Wigner-Eckart theorem, the only component of the momentum matrix element between the initial state and all the possible arrival basis states $\langle 3/2, k | \mathbf{P} | i \rangle$ will be given by the Clebsch-Gordan coefficients in Table 8.4.
- V. The probability of transition to each of the states will be given by the application of Eq. (8.40), and the results are listed in Table 8.9.
- VI. Generate a random number between 0 and 1, and choose the state to which the transition has taken place according to the probabilities calculated in the previous step.
- VII. The electric field of the photon is set to

$$\mathbf{E} = \sum_{j=x,y,z} (b_+ \langle \Gamma_5, j; \Gamma_6, +1/2 | \kappa, k \rangle + b_- \langle \Gamma_5, j; \Gamma_6, -1/2 | \kappa, k \rangle) \hat{j} \cdot \mathbf{a}_{\hat{\theta}\hat{\varphi}}^* \mathbf{a}_{\hat{\theta}\hat{\varphi}} + \sum_{j=x,y,z} (b_+ \langle \Gamma_5, j; \Gamma_6, +1/2 | \kappa, k \rangle + b_- \langle \Gamma_5, j; \Gamma_6, -1/2 | \kappa, k \rangle) \hat{j} \cdot \mathbf{a}_{\hat{\theta}\hat{\varphi}} \mathbf{a}_{\theta\hat{\varphi}}, \quad (8.45)$$

where \hat{j} can be \hat{x} , \hat{y} or \hat{z} .

- VIII. Propagate the photon through the desired structure.
- IX. Normalize the electric field of the photon to one.
- X. Compute the Stokes parameter for that photon.
- XI. Perform the average of the Stokes parameters for all photons hitting the desired location.

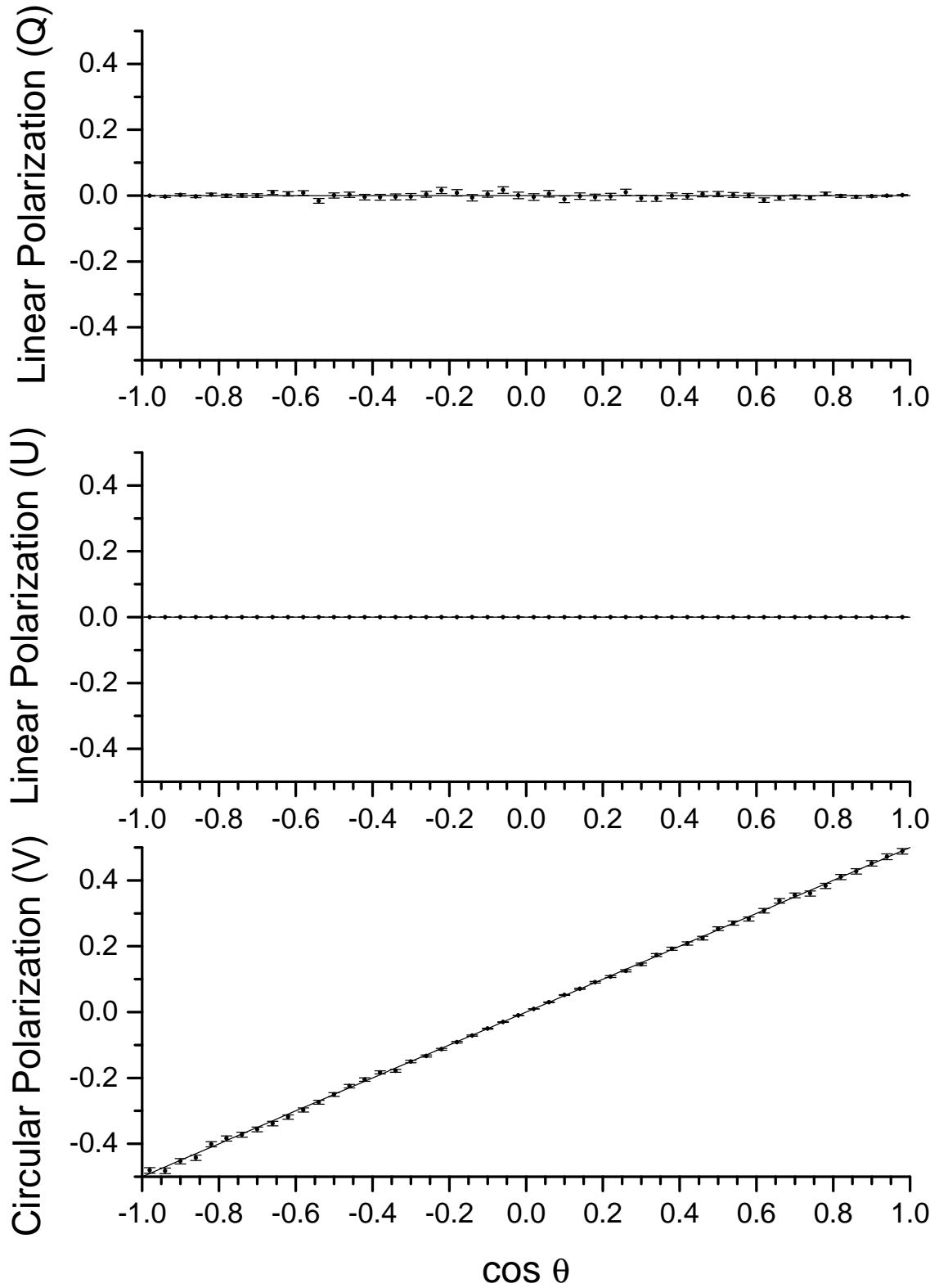


Figure 8.9: Monte Carlo calculation of photon polarization for a zincblende for spin down electrons. The data points and their standard deviation are shown. The lines correspond to the theoretical values.

Figure 8.9 shows the results for a Monte Carlo (MC) simulation of the light emitted by a GaAs substrate [9]. It shows the different Stokes parameters for the generated photons as a function of the cosine of the polar angle. The representation in terms of the cosine of the polar angle is preferable because an interval in solid angle maps into the same interval in $\cos\theta$ no matter what the θ is. The points are the values obtained following the steps just mentioned; while the error bars correspond to one standard deviation. It is clearly seen that the photons generated using the MC method follow the theoretical predictions of Eqs. (8.32)-(8.33). Of course, the MC values show the fluctuations inherent to the statistical nature of that method.

8.7 Summary

In summary, a method for determining the polarization of light emitted in arbitrary directions for an arbitrary initial electron spin population has been developed. This method allows the generation of single photons having a polarization such that, when averaged over a large number of events, reproduce the results from first-order time-dependent perturbation theory. The limitations of Fermi's golden rule for single photon generation have been shown.

Bibliography

- [1] M. Johnson and R. H. Silsbee, *J. Appl. Phys.* **63**, 3934 (1988).
- [2] S. F. Alvarado and P. Renaud, *Phys. Rev. Lett.* **68**, 1387 (1992).
- [3] R. Fiederling, M. Keim, G. Reuscher, W. Ossau, G. Schmidt, A. Waag, and L. W. Molenkamp, *Nature* **402**, 787 (1999).
- [4] B. T. Jonker, A. T. Hanbicki, Y. D. Park, G. Itskos, M. Furis, G. Kioseoglou, A. Petrou, and X. Wei, *Appl. Phys. Lett.* **79**, 3098 (2001).
- [5] F. G. Monzon and M. L. Roukes, *J. Magn. Magn. Mater.* **199**, 632 (1999).
- [6] G. Schmidt, D. Ferrand, L. W. Molenkamp, A. T. Filip, and B. J. van Wees, *Phys. Rev. B* **62**, R4790 (2000).
- [7] D. L. Smith and R. N. Silver, *Phys. Rev. B* **64**, art. no. (2001).
- [8] H. J. Zhu, M. Ramsteiner, H. Kostial, M. Wassermeier, H. P. Sch onherr, and K. H. Ploog, *Phys. Rev. Lett.* **87**, art. no. (2001).
- [9] S. R. Ichiriu, X. Cartoixà, and T. C. McGill, , in preparation.
- [10] A. Messiah, in *Quantum Mechanics*, 1st ed. (Dover, New York, 1999), pp. 1016–1017.
- [11] C. Cohen-Tannoudji, B. Diu, and F. Laloë, in *Quantum Mechanics*, 2nd ed. (Wiley, New York, 1977), pp. 1306–1307.
- [12] B. K. Ridley, in *Quantum Mechanics*, 1st ed. (Dover, New York, 1999), pp. 184–187.
- [13] W.-K. Tung, in *Group Theory in Physics*, 1st ed. (World Scientific, Singapore, 1985), pp. 60–61.

- [14] C. Cohen-Tannoudji, B. Diu, and F. Laloë, *Quantum Mechanics*, 2nd ed. (Wiley, New York, 1977).
- [15] G. F. Koster, J. O. Dimmock, R. G. Wheeler, and H. Statz, *Properties of the Thirty-Two Point Groups*, 1st ed. (M.I.T. Press, Cambridge, MA, USA, 1963).
- [16] M. Wöhlecke and G. Borstel, *Phys. Stat. Sol. B* **107**, 653 (1981).
- [17] D. Kliger, J. Lewis, and C. Randall, *Polarized Light in Optics and Spectroscopy*, 1st ed. (Academic Press, Inc., New York, NY, USA, 1990).
- [18] R. Magri and A. Zunger, *Phys. Rev. B* **62**, 10364 (2000).
- [19] Y. Onodera and M. Okazaki, *J. Phys. Soc. Jpn.* **21**, 2400 (1966).
- [20] R. C. Miller, A. C. Gossard, G. D. Sanders, Y. C. Chang, and J. N. Schulman, *Phys. Rev. B* **32**, 8452 (1985).
- [21] D. Z.-Y. Ting, E. T. Yu, and T. C. McGill, *Phys. Rev. B* **45**, 3576 (1992).
- [22] O. Lagerstedt and B. Monemar, *Phys. Rev. B* **19**, 3064 (1979).
- [23] S. Iwama, K. Hayakawa, and T. Arizumi, *Journal Of Crystal Growth* **56**, 265 (1982).
- [24] C. Herring, *J. Franklin Inst.* **233**, 525 (1942).
- [25] M. J. Lax, *Symmetry principles in solid state and molecular physics*, 1st ed. (Wiley-Interscience, New York, USA, 1974).
- [26] Y. C. Yeo, T. C. Chong, and M. F. Li, *J. Appl. Phys.* **83**, 1429 (1998).
- [27] J. J. Sakurai, *Modern Quantum Mechanics*, 1st ed. (Addison-Wesley, Redwood City, CA, USA, 1985).

Appendices

Appendix A Explicit form of the 8-band $\mathbf{k} \cdot \mathbf{p}$ Hamiltonian

The calculations in Chapters 5, 6 and 7 are based in the 8-band $\mathbf{k} \cdot \mathbf{p}$ Hamiltonian derived by Trebin *et al.* [1]. This Hamiltonian has the nice property that it has been constructed using the theory of invariants [2], and thus it correctly describes the T_d symmetry of bulk zincblendes. In particular, it includes terms breaking the spin degeneracy of the bands at a general point in the Brillouin zone, making it ideal for the study of inversion asymmetry effects. It also accounts for the effects of strain and an external magnetic field.

Although the Hamiltonian is explicitly shown in Ref. [1], it will be rewritten here to provide a higher degree of self containment to this thesis. Some typos present in the original work by Trebin *et al.* are removed and, hopefully, no new ones will be introduced.

The 8-band $\mathbf{k} \cdot \mathbf{p}$ Hamiltonian will be expressed in the basis $\{|\Gamma_6, +\frac{1}{2}\rangle, |\Gamma_6, -\frac{1}{2}\rangle, |\Gamma_8, +\frac{3}{2}\rangle, |\Gamma_8, +\frac{1}{2}\rangle, |\Gamma_8, -\frac{1}{2}\rangle, |\Gamma_8, -\frac{3}{2}\rangle, |\Gamma_7, +\frac{1}{2}\rangle, |\Gamma_7, -\frac{1}{2}\rangle\}$. It can be written in a block diagonal form

$$H = \begin{pmatrix} H^{cc} & H^{cv} & H^{cs} \\ H^{vc} & H^{vv} & H^{vs} \\ H^{sc} & H^{sv} & H^{ss} \end{pmatrix}, \quad (\text{A.1})$$

where, of course, $(H^{\alpha\beta})^\dagger = H^{\beta\alpha}$, c refers to the two conduction band (CB) states, v to the four heavy hole (HH) and light hole (LH) states and s to the two spin-orbit split off (SO) states.

The constituent blocks of the Hamiltonian are shown in Table A.1. The meaning of the different parameters is listed in Table 5.4 in the main text. The phases of the wavefunctions and the prefactors in Table A.1 are chosen in a way that all the parameters are real. The $\boldsymbol{\sigma}$ and the $\boldsymbol{\rho}$ matrices are the Pauli matrices; the T matrices

$$\begin{aligned}
H^{cc} &= E_v + E_g + \frac{\hbar^2 k^2}{2m} + A' k^2 - g_s \frac{e\hbar}{4mc} \boldsymbol{\sigma} \cdot \mathbf{H} + C_1 \text{tr}\bar{\epsilon} \\
H^{vv} &= H_k^{vv} + H_\epsilon^{vv} + H_{kl}^{vv} + H_{ek}^{vv} \\
H_k^{vv} &= -\frac{\hbar^2}{m} \left\{ \frac{1}{2} \gamma_1 k^2 - \gamma_2 \left[\left(J_x^2 - \frac{1}{3} J^2 \right) k_x^2 + cp \right] - 2\gamma_3 \left[\{J_x J_y\} \{k_x k_y\} + cp \right] \right\} - \\
&\quad \frac{e\hbar}{mc} \left\{ (\kappa J_x + q J_x^3) H_x + cp \right\} \\
H_\epsilon^{vv} &= D_d \text{tr}\bar{\epsilon} + \frac{2}{3} D_u \left[\left(J_x^2 - \frac{1}{3} J^2 \right) \epsilon_{xx} + cp \right] + \frac{2}{3} D'_u \left[2 \{J_x J_y\} \epsilon_{xy} + cp \right] \\
H_{kl}^{vv} &= \frac{2}{\sqrt{3}} C \left[\{J_x (J_y^2 - J_z^2)\} k_x + cp \right] \\
H_{ek}^{vv} &= [C_4 (\epsilon_{yy} - \epsilon_{zz}) k_x + C'_5 (\epsilon_{xy} k_y - \epsilon_{xz} k_z)] J_x + cp \\
H^{ss} &= -\Delta_{so} + \frac{\hbar^2}{2m} \gamma_1 k^2 - 2\kappa \frac{e\hbar}{2mc} \boldsymbol{\sigma} \cdot \mathbf{H} + D_d \text{tr}\bar{\epsilon} \\
H^{cv} &= \sqrt{3} [P (k_x T_x + cp) + iB (T_x \{k_y k_z\} + cp) + iC_2 (T_x \epsilon_{yz} + cp)] \\
H^{cs} &= -\frac{1}{\sqrt{3}} [P (k_x \rho_x + cp) + iB (\rho_x \{k_y k_z\} + cp) + iC_2 (\rho_x \epsilon_{yz} + cp)] \\
H^{vs} &= H_k^{vs} + H_\epsilon^{vs} + H_{ek}^{vs} \\
H_k^{vs} &= -\frac{\hbar^2}{2m} [-3\gamma_2 (U_{xx} k_x^2 + cp) - 6\gamma_3 (U_{xy} \{k_x k_y\} + cp)] - \frac{e\hbar}{mc} \frac{3}{2} (U_x H_x + cp) \\
H_\epsilon^{vs} &= 2D_u (U_{xx} \epsilon_{xx} + cp) + 2D'_u (2U_{xy} \epsilon_{xy} + cp) \\
H_{ek}^{vs} &= \frac{3}{2} [C_4 (\epsilon_{yy} - \epsilon_{zz}) k_x + C'_5 (\epsilon_{xy} k_y - \epsilon_{xz} k_z)] U_x + cp
\end{aligned}$$

cp means cyclic permutation, $\{AB\} = \frac{1}{2}(AB + BA)$, $\text{tr}\bar{\epsilon} = \epsilon_{xx} + \epsilon_{yy} + \epsilon_{zz}$

Table A.1: Matrix elements of the 8-band $\mathbf{k} \cdot \mathbf{p}$ Hamiltonian.

are given by

$$\begin{aligned}
T_x &= \frac{1}{3\sqrt{2}} \begin{pmatrix} -\sqrt{3} & 0 & 1 & 0 \\ 0 & -1 & 0 & \sqrt{3} \end{pmatrix} & T_y &= \frac{-i}{3\sqrt{2}} \begin{pmatrix} \sqrt{3} & 0 & 1 & 0 \\ 0 & 1 & 0 & \sqrt{3} \end{pmatrix} & T_z &= \frac{\sqrt{2}}{3} \begin{pmatrix} 0 & 1 & 0 & 0 \\ 0 & 0 & 1 & 0 \end{pmatrix} \\
T_{xx} &= \frac{1}{3\sqrt{2}} \begin{pmatrix} 0 & -1 & 0 & \sqrt{3} \\ -\sqrt{3} & 0 & 1 & 0 \end{pmatrix} & T_{yy} &= \frac{1}{3\sqrt{2}} \begin{pmatrix} 0 & -1 & 0 & -\sqrt{3} \\ \sqrt{3} & 0 & 1 & 0 \end{pmatrix} & T_{zz} &= \frac{\sqrt{2}}{3} \begin{pmatrix} 0 & 1 & 0 & 0 \\ 0 & 0 & -1 & 0 \end{pmatrix} \\
T_{yz} &= \frac{i}{2\sqrt{6}} \begin{pmatrix} -1 & 0 & -\sqrt{3} & 0 \\ 0 & \sqrt{3} & 0 & 1 \end{pmatrix} & T_{zx} &= \frac{1}{2\sqrt{6}} \begin{pmatrix} -1 & 0 & \sqrt{3} & 0 \\ 0 & \sqrt{3} & 0 & -1 \end{pmatrix} & T_{xy} &= \frac{i}{\sqrt{6}} \begin{pmatrix} 0 & 0 & 0 & -1 \\ -1 & 0 & 0 & 0 \end{pmatrix}.
\end{aligned} \tag{A.2}$$

The matrices U are simply given by $U_i = T_i^\dagger$.

Bibliography

- [1] H.-R. Trebin, U. Rössler, and R. Ranvaud, *Phys. Rev. B* **20**, 686 (1979).
- [2] G. L. Bir and G. E. Pikus, *Symmetry and Strain-Induced Effects in Semiconductors*, 1st ed. (Wiley, New York, USA, 1974).

Appendix B Group theory for band structures

In this thesis an extensive use of group theoretical arguments is made. The following lines are meant to be a utilitarian crash course on group theory for the reader not familiar with the group theory (GT) concepts and language applied to semiconductor band structure theory. This appendix is not by any means rigorous in the derivations, proofs or definitions, but hopefully it is with the results. What will be presented here is mainly a repetition, rephrasing or elaboration on the notes from the Ph129 course by Kerry Vahala and the textbook used there [1]. Falicov [2] wrote another excellent textbook with more emphasis on the applications of GT to solid-state physics.

B.1 Definitions

First, a group G consists of a set of elements and an operation that sends a pair of elements back into another¹ element of the set. The operation must satisfy the following three properties for the set to be a group:

- The operation must be associative: $a(bc) = (ab)c$ for all $a, b, c \in G$
- There must be an *identity* element e such that $ae = a$ for all $a \in G$.
- For each $a \in G$ there must be an *inverse* element a^{-1} such that $aa^{-1} = e$.

Then, the symmetry group of a crystal will be the set of operations that send a crystal to itself, which can be shown to form a group. This group is called the space group of the crystal, and there are 230 of them [3]. For each space group, there will be a subset of operations that leave a certain point in the crystal invariant. This subset

¹It does not need to be different from the original two.

also forms a group and is called the point group of a crystal. There are 32 of these crystallographic point groups [4] (*i.e.*, point groups compatible with the existence of a crystal). An example of a point group *not* being a crystallographic point group would be the symmetry group of a molecule with pentagonal symmetry.

Now, focusing in the electronic band structure of a solid, one must consider that the points in the Brillouin zone will have symmetry properties associated with the point group of the parent crystal. In particular, it can be shown [2] that a state in the zone center has the same symmetry properties as the underlying lattice, and that the symmetry of a general state at \mathbf{k} *inside* the Brillouin zone will be governed by the subset of operations of the point group that leave \mathbf{k} invariant. This set of operations forms the “small group of \mathbf{k} .”

At this point, a mathematical object satisfying the group multiplication table is needed. If the group is commutative (aka. Abelian), plain numbers will do the job. If the group is not, one has to resort to matrices. A set of numbers or matrices that satisfies the group multiplication table, each one associated to a group member and acting on a vector space V , constitutes a *representation*. If the elements of a representation can (cannot) be put in a block diagonal form all at the same time, the representation is called reducible (irreducible). The trace of a matrix belonging to a representation is called the character. Obviously, the character of the matrix representing the identity element will yield the dimensionality of the representation. There exist published tables of characters for irreducible representations of the most important groups.

B.2 Degeneracies, splittings and eigenstates

Finally, a point has been reached where one of the most important results of GT with regard to crystals can be enunciated [1]:

Lemma 1 (Schur’s 1st) *Let $U(G)$ be an irreducible representation of a group G on the vector space V , and H be an arbitrary operator on V . If H commutes with all*

the operators $\{U(g), g \in G\}$, then H must be a multiple of the identity operator \mathbb{I} , i.e. $H = \lambda\mathbb{I}$, where λ is a number.

On the other hand, the crystal Hamiltonian at a point \mathbf{k} will commute with all the symmetry operations S belonging to the small group of \mathbf{k} :

$$SH(\mathbf{k}) = H(\mathbf{k})S. \quad (\text{B.1})$$

Putting Eq. (B.1) together with Schur's first lemma, one obtains that the subspace upon which an irreducible representation of the small group of \mathbf{k} acts will be degenerate. From this conclusion the power of GT to predict degeneracies at points of high symmetry in the Brillouin zone is drawn.

Once this has been said, the recipe to find degeneracies at a given \mathbf{k} point inside the Brillouin zone² can be stated:

- I. Find the small group $G(\mathbf{k})$ corresponding to \mathbf{k} .
- II. Look at the character table of $G(\mathbf{k})$. Koster *et al.* [4] provide a good compilation of tables for the crystallographic point groups.
- III. The character of the identity element yields the degeneracy of the level transforming according to the selected irreducible representation. If basis functions are listed, they indicate the symmetry of the states.

An example the procedure described above can be the degeneracy of the levels at the zone center in GaN. GaN has wurtzite structure. The point group at the zone center (Γ point) is C_{6v} . From Table 65 in page 67 in Koster *et al.* [4] it is seen that (spin resolved) states at the zone center can transform according to three different irreducible representations, each one of them twofold degenerate. A single electron can transform only according to the irreducible representations that change sign under a 2π rotation³. Looking at the tables of bases, and in the cases where the

²The treatment for points on the Brillouin zone boundary is more complicated.

³The irreducible representations above the line are useful for the study of systems with an even number of electrons.

states come from s or p states (that is, an sp model), one can see that the Γ_9 states will be proportional to $|x + iy\rangle|\uparrow\rangle$ and $|x - iy\rangle|\downarrow\rangle$. Less can be said about the Γ_7 and Γ_8 . d type orbitals are needed to generate Γ_8 states, so they will not appear in an sp description, but that is not an inconvenience when describing the lower conduction band and the upper valence bands of wurtzites.

B.3 Matrix elements

The consistency of the matrix elements of an operator O with the crystal symmetry imposes certain restrictions on these matrix elements. The Wigner-Eckart theorem exploits these restrictions to show that the matrix elements between states belonging to given irreducible representations factor into a very small number of operator-dependent constants and the rest is determined only by symmetry.

Theorem 1 (Wigner-Eckart) *If $\{P_i^\alpha\}$ is a set of components of the operator P transforming according to the irreducible representation (irrep) α , then the matrix element between states $|v_j^\beta\rangle$ where β denotes the irrep and j labels the specific state inside the β irrep is given by*

$$\langle v_n^\gamma | P_i^\alpha | v_j^\beta \rangle = \sum_k c_k^{\beta,\gamma} U_{ij,n}^{\alpha,\beta,\gamma*}, \quad (\text{B.2})$$

where k runs over the number of times that the irrep Γ^γ is contained in $\Gamma^\alpha \otimes \Gamma^\beta$, $c_k^{\beta,\gamma}$ is the irreducible matrix element, and does not depend on the indices i, j or n ⁴, and $U_{ij,n}^{\alpha,\beta,\gamma}$ is the Clebsch-Gordan coefficient for the appropriate point group connecting states transforming according to the product group $\Gamma^\alpha \otimes \Gamma^\beta$ to states that transform under the irrep Γ^γ .

The importance of this theorem is that it provides with selection rules and strength ratios between matrix elements. As an example, one can evaluate the ratio of the

⁴It does, of course, also depend on the operator P .

matrix elements

$$\frac{\langle \Gamma_8, -3/2 | P_x^5 | \Gamma_6, -\frac{1}{2} \rangle}{\langle \Gamma_8, +1/2 | P_x^5 | \Gamma_6, -\frac{1}{2} \rangle} = \frac{-ic_1^{6,8}/\sqrt{2}}{-ic_1^{6,8}/\sqrt{6}} = \sqrt{3} \quad (\text{B.3})$$

just by the application of the Wigner-Eckart theorem and looking up the coefficients in Table 8.4.

Bibliography

- [1] W.-K. Tung, *Group Theory in Physics*, 1st ed. (World Scientific, Singapore, 1985).
- [2] L. M. Falicov, *Group Theory and Its Physical Applications, Chicago Lectures in Physics*, 1st ed. (The University of Chicago Press, Chicago, 1966).
- [3] G. F. Koster, in *Solid State Physics*, edited by F. Seitz and D. Turnbull (Academic Press, New York, 1957), pp. 173–256.
- [4] G. F. Koster, J. O. Dimmock, R. G. Wheeler, and H. Statz, *Properties of the Thirty-Two Point Groups*, 1st ed. (M.I.T. Press, Cambridge, MA, USA, 1963).

Appendix C Derivation of the formula for the transmission coefficients

The aim of this appendix is to prove the formula for the transmission coefficients due to tunneling

$$T(E, k_{\parallel}) = \sum_{j=1}^8 |t_j(E, k_{\parallel})|^2 \frac{|v_j(E, k_{\parallel}; R)|}{|v_I(E, k_{\parallel}; L)|}. \quad (7.13)$$

C.1 Expansion to the Hellmann-Feynman theorem

In order to prove the formula above, the following generalization to the Hellmann-Feynman theorem will be useful.

Theorem 2 *Let $A(\lambda)$ be a Hermitian operator, and let $|u(\lambda)\rangle$ and $|v(\lambda)\rangle$ be two eigenvectors of $A(\lambda)$ having the same eigenvalue $a(\lambda)$. If $\langle v(\lambda)|u(\lambda)\rangle$ does not depend on λ , then*

$$\left\langle v(\lambda) \left| \frac{\partial A(\lambda)}{\partial \lambda} \right| u(\lambda) \right\rangle = \frac{\partial a(\lambda)}{\partial \lambda} \langle v(\lambda)|u(\lambda)\rangle. \quad (C.1)$$

Proof: Following the original proof of the Hellmann-Feynman theorem (see, for example, Ref. [1]), the left hand side of Eq. (C.1) can be written as

$$\left\langle v(\lambda) \left| \frac{\partial A(\lambda)}{\partial \lambda} \right| u(\lambda) \right\rangle + a(\lambda) \left\{ \left[\frac{\partial}{\partial \lambda} \langle v(\lambda)| \right] |u(\lambda)\rangle + \langle v(\lambda)| \left[\frac{\partial}{\partial \lambda} |u(\lambda)\rangle \right] \right\}, \quad (C.2)$$

where the assumption that $\langle v(\lambda)|u(\lambda)\rangle$ does not depend on λ has been used. Now, since A is Hermitian, $a(\lambda)|u(\lambda)\rangle = A(\lambda)|u(\lambda)\rangle$ and $\langle v(\lambda)|A(\lambda) = a(\lambda)\langle v(\lambda)|$, therefore the above equation becomes

$$\left\langle v(\lambda) \left| \frac{\partial A(\lambda)}{\partial \lambda} \right| u(\lambda) \right\rangle + \left[\frac{\partial}{\partial \lambda} \langle v(\lambda)| \right] A(\lambda)|u(\lambda)\rangle + \langle v(\lambda)|A(\lambda) \left[\frac{\partial}{\partial \lambda} |u(\lambda)\rangle \right] = \frac{\partial}{\partial \lambda} \langle v(\lambda)|A(\lambda)|u(\lambda)\rangle = \frac{\partial}{\partial \lambda} [a(\lambda)\langle v(\lambda)|u(\lambda)\rangle], \quad (C.3)$$

which proves Eq. (C.1) because of the assumption that $\langle v(\lambda)|u(\lambda)\rangle$ is independent of λ .

The Hellmann-Feynman theorem is recovered taking $A \rightarrow H$ and $|u(\lambda)\rangle = |v(\lambda)\rangle$ (properly normalized) into Eq. (C.1):

$$\left\langle v(\lambda) \left| \frac{\partial H(\lambda)}{\partial \lambda} \right| v(\lambda) \right\rangle = \frac{\partial E(\lambda)}{\partial \lambda}. \quad (\text{C.4})$$

Another useful case is when $\langle v(\lambda)|u(\lambda)\rangle = 0$. Then, a straightforward application of Eq. (C.1) shows

$$\left\langle v(\lambda) \left| \frac{\partial A(\lambda)}{\partial \lambda} \right| u(\lambda) \right\rangle = 0. \quad (\text{C.5})$$

In particular, this is useful when evaluating matrix elements of operators that are a derivative of the Hamiltonian respect to some parameter. The above equation is saying that $\frac{\partial H(\lambda)}{\partial \lambda}$ is diagonal within a degenerate subspace of states.

C.2 Transmission coefficient

The transmission coefficient for the tunneling process in a heterostructure is given by the ratio of probability currents flowing across a plane perpendicular to the growth direction (chosen to be z) of the transmitted state respect to the incident state¹:

$$T(E, k_{\parallel}) = \frac{\int_R \langle t | \hat{J}_z(\mathbf{r}) | t \rangle dx dy}{\int_L \langle I | \hat{J}_z(\mathbf{r}) | I \rangle dx dy}, \quad (\text{C.6})$$

where L and R refer to the left and right electrode, respectively, and the current operator is given by [2]

$$\hat{\mathbf{J}}(\mathbf{r}_0) = \frac{1}{2m} [\mathbf{P}\delta(\mathbf{r} - \mathbf{r}_0) + \delta(\mathbf{r} - \mathbf{r}_0)\mathbf{P}]. \quad (\text{C.7})$$

¹The ratio should only include the current due to transmitting, as opposed to evanescent, components.

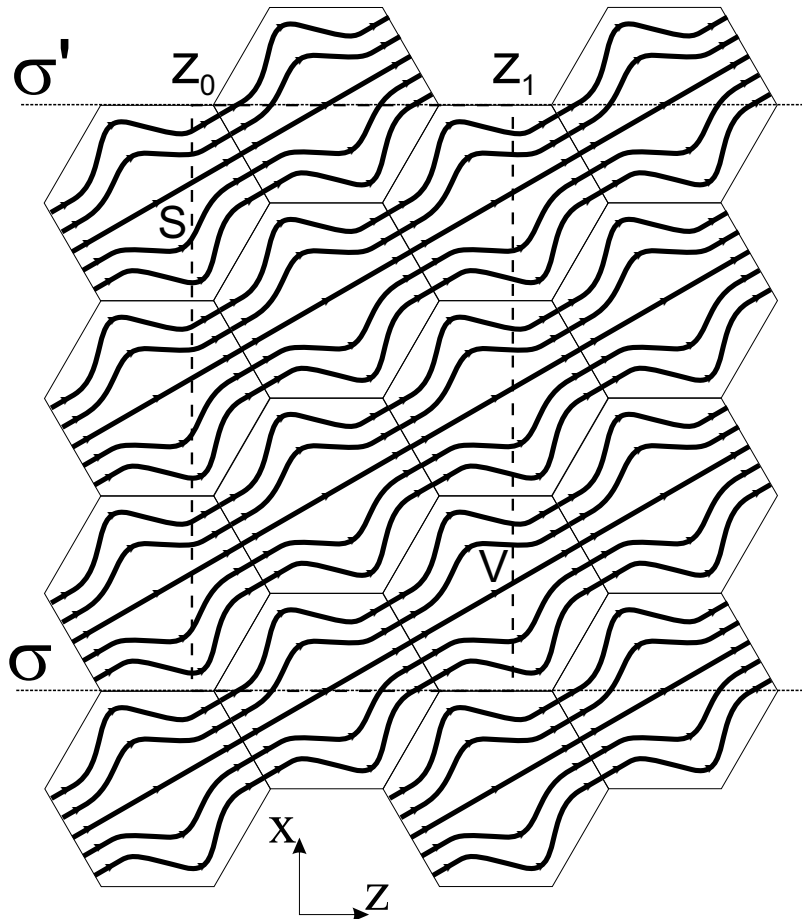


Figure C.1: Illustration of the independence of $\int J_z dx dy$ with respect to the plane of integration. σ and σ' are equivalent through the cyclic boundary conditions. The thick lines represent current lines, and the hexagons are primitive zone boundaries. The number of current lines cutting through the plane z_0 is independent its z position. Also, an appropriate control volume V for the mathematical proof and its boundary S are shown.

It is easily seen that the usual value for the probability current is recovered by taking the expectation value of $\hat{\mathbf{J}}(\mathbf{r})$:

$$\mathbf{J}(\mathbf{r}) = \langle \psi | \hat{\mathbf{J}}(\mathbf{r}) | \psi \rangle = \frac{\hbar}{2mi} [\psi^*(\mathbf{r}) (\nabla \psi(\mathbf{r})) - (\nabla \psi(\mathbf{r}))^* \psi(\mathbf{r})]. \quad (\text{C.8})$$

However, in quantum mechanics one is normally more comfortable taking volume integrals (*i.e.*, matrix elements) than integrals over a plane. To progress towards that direction, first it must be shown that the integrals over the plane in Eq. (C.6) are independent of the position z_0 of the plane. To do this, only the bulk properties of the

crystal need be considered. Cyclic boundary conditions for a bulk crystal are chosen to facilitate the argument. A control volume V is defined in such a way that encloses all the crystal along the x and y directions, but has an arbitrary thickness along the z direction. Figure C.1 shows V limited by the closed surface S .

Since the current is being sought for a stationary state, $\frac{\partial \rho}{\partial t} = 0$, therefore

$$\nabla \cdot \mathbf{J}(\mathbf{r}) = 0. \quad (\text{C.9})$$

This equation can be integrated over V to obtain

$$0 = \int_V \nabla \cdot \mathbf{J}(\mathbf{r}) dx dy dz = \int_S \mathbf{J} \cdot d\mathbf{S} = \int_{z_1} J_z dx dy - \int_{z_0} J_z dx dy, \quad (\text{C.10})$$

where in the last step the fact that the planes σ and σ' (and the set perpendicular to y) are equivalent under the cyclic boundary conditions has been used. Since z_1 and z_0 were arbitrary, the independence of $\int_z J_z dx dy$ on z has been proved.

Now, each of the integrals appearing in Eq. (C.6) can be trivially integrated respect to z , with the limits chosen as described in Fig. C.2. Therefore,

$$T(E, k_{\parallel}) = \frac{\int_{z_R}^{z_R+d_{hkl,R}} \left(\int_R J_{z,t}(\mathbf{r}) dx dy \right) dz / d_{hkl,R}}{\int_{z_L}^{z_L+d_{hkl,L}} \left(\int_L J_{z,I}(\mathbf{r}) dx dy \right) dz / d_{hkl,L}}, \quad (\text{C.11})$$

where $d_{hkl,L}$ ($d_{hkl,R}$) denotes the distance between planes with Miller indices $[hkl]$ in the left (right) electrode and $J_{z,t} = \langle t | \hat{J}_z(\mathbf{r}) | t \rangle$. Note that the indices don't need to be the same in both electrodes.

The integrals in Eq. (C.11) can be transformed into integrals over the electrode volume as follows

$$\int_{z_R}^{z_R+d_{hkl,R}} \left(\int_R J_{z,t}(\mathbf{r}) dx dy \right) dz = n_{hkl} S \int_{PC} J_{z,t}(\mathbf{r}) dV, \quad (\text{C.12})$$

where n_{hkl} is the number of lattice points per unit surface in the $[hkl]$ plane, S is the transverse area of the crystal and the PC symbol means that the integral is to be performed over a primitive cell. Following Feynman [3], the integral of the current

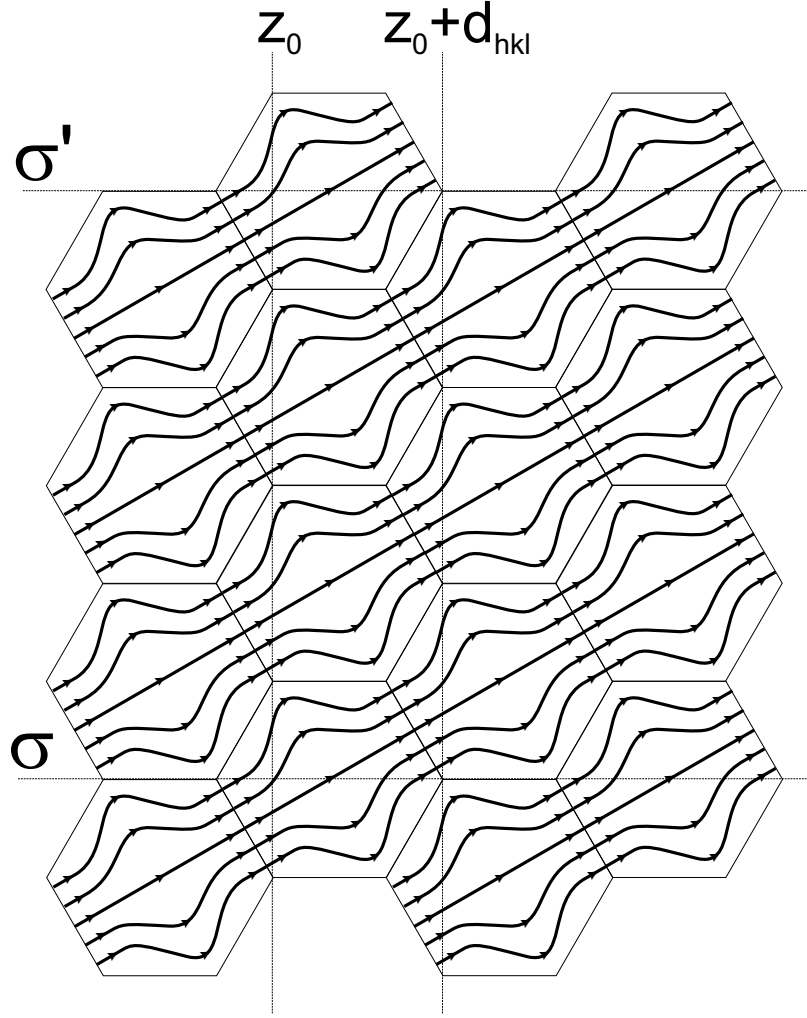


Figure C.2: Integration region for J_z . d_{hkl} is the distance between $[hkl]$ planes, perpendicular to which the heterostructure is grown.

density over the primitive cell becomes

$$\int_{PC} J_{z,t}(\mathbf{r})dV = \left\langle t \left| \frac{P_z}{m} \right| t \right\rangle, \quad (\text{C.13})$$

but P_z/m is simply v_z , the z component of the velocity operator. Therefore

$$\int_{PC} J_{z,t}(\mathbf{r})dV = \langle t | v_z | t \rangle = v_z(E, k_{\parallel}; t) \langle t | t \rangle, \quad (\text{C.14})$$

where $v_z(E, k_{\parallel}; t)$ is the group velocity of the transmitted state. An analogous expression is obtained for the current of the incoming state.

Now, using Eqs. (C.14) and (C.12), the average current through a crystal plane can be obtained

$$\frac{\int_R J_z(\mathbf{r}) dx dy}{\int_R dx dy} = \frac{\langle t|t \rangle v_z(E, k_{\parallel}; t)}{V_{PC,R}}, \quad (\text{C.15})$$

where $V_{PC,R}$ is the primitive cell volume of the right electrode and z is the direction perpendicular to the plane under study. This is the same result shown in Shockley [4], but generalized to states that are not pure Bloch states. From Eq. (C.15) and Eq. (C.6)

$$T(E, k_{\parallel}) = \frac{\langle t|t \rangle v_z(E, k_{\parallel}; t)/V_{PC,R}}{\langle I|I \rangle v_z(E, k_{\parallel}; I)/V_{PC,L}}. \quad (\text{C.16})$$

More progress can be made substituting the expression for $|t\rangle$ in terms of the Bloch states

$$|t\rangle = t_j |\mathbf{B}_{k_{\parallel}, k_{z,j}}, R\rangle, \quad (\text{C.17})$$

with $|\mathbf{B}_{k_{\parallel}, k_{z,j}}, R\rangle$ given by Eq. (7.2') and being orthogonal to each other, into Eq. (C.13):

$$\left\langle t \left| \frac{P_z}{m} \right| t \right\rangle = \frac{1}{m} t_l^* t_j \left\langle \mathbf{B}_{k_{\parallel}, k_{z,l}}, R \left| P_z \right| \mathbf{B}_{k_{\parallel}, k_{z,j}}, R \right\rangle. \quad (\text{C.18})$$

The Einstein summation convention is used. The matrix element on the right hand side will only be different from zero when $k_{z,l} = k_{z,j}$ because of the space group selection rules for a position independent operator². The matrix element between Bloch states can be further developed considering the following two cases:

- $k_{z,l} = k_{z,j}$ and $l = j$

The matrix element yields the velocity of the state $|\mathbf{B}_{k_{\parallel}, k_{z,j}}, R\rangle$

$$\frac{1}{m} \left\langle \mathbf{B}_{k_{\parallel}, k_{z,j}}, R \left| P_z \right| \mathbf{B}_{k_{\parallel}, k_{z,j}}, R \right\rangle = v_j(E, k_{\parallel}; R). \quad (\text{C.19})$$

Since

$$v_j(E, k_{\parallel}; R) = \frac{1}{\hbar} \left. \frac{\partial E(k_{\parallel}, k_z)}{\partial k_z} \right|_{k_{z,j}} = \frac{1}{\hbar} \left\langle u_{k_{\parallel}, k_{z,j}} \left| \frac{\partial H(k_{\parallel}, k_z)}{\partial k_z} \right| u_{k_{\parallel}, k_{z,j}} \right\rangle, \quad (\text{C.20})$$

²Implicitly, the assumption is made that the tunneling process does not involve states in the edge of the Brillouin zone.

where the Hellmann-Feynman theorem has been used in the last step, a velocity operator appropriate for application to the periodic part of the Bloch states can be defined [5]:

$$\hat{v} = \frac{1}{\hbar} \nabla_{\mathbf{k}} H(k_{\parallel}, k_z). \quad (\text{C.21})$$

Remember that now \mathbf{k} in $H(k_{\parallel}, k_z)$ plays the role of three parameters in the $\mathbf{k} \cdot \mathbf{p}$ Hamiltonian.

- $k_{z,l} = k_{z,j}$ and $l \neq j$

In this case, it is easily seen that

$$\frac{1}{m} \left\langle \mathbf{B}_{k_{\parallel}, k_{z,l}}, R \mid P_z \mid \mathbf{B}_{k_{\parallel}, k_{z,j}}, R \right\rangle = \frac{1}{m} \left\langle u_{k_{\parallel}, k_{z,l}} \mid P_z \mid u_{k_{\parallel}, k_{z,j}} \right\rangle, \quad (\text{C.22})$$

and, using the form (C.21) for the velocity operator,

$$\frac{1}{m} \left\langle \mathbf{B}_{k_{\parallel}, k_{z,l}}, R \mid P_z \mid \mathbf{B}_{k_{\parallel}, k_{z,j}}, R \right\rangle = \frac{1}{\hbar} \left\langle u_{k_{\parallel}, k_{z,l}} \left| \frac{\partial H(k_{\parallel}, k_z)}{\partial k_z} \right| u_{k_{\parallel}, k_{z,j}} \right\rangle = 0, \quad (\text{C.23})$$

where the result in Eq. (C.5) has been used in the last step.

Therefore, one is only left with the diagonal elements of the velocity operator. Collecting Eqs. (C.23), (C.19), (C.18) and (C.15) into Eq. (C.16) one obtains

$$T(E, k_{\parallel}) = \frac{\sum_{j=1}^8 |t_j(E, k_{\parallel})|^2 v_j(E, k_{\parallel}; R)/V_{PC,R}}{\sum_{l=1}^8 |I_l(E, k_{\parallel})|^2 v_l(E, k_{\parallel}; L)/V_{PC,L}}. \quad (\text{C.24})$$

The volume factors appear because $|I\rangle$ and $|t\rangle$ are subject to normalization over the whole structure, as can be seen if one considers a case where an electron propagates in free space and partitions one region with cells of volume $V_{PC,L}$ and another with cells of volume $V_{PC,R}$. But if one solves for coefficients of the envelope function, as usually done, then each Bloch state is normalized to one within a primitive cell and the volume factors can be dropped off, resulting in

$$T(E, k_{\parallel}) = \frac{\sum_{j=1}^8 |t_j(E, k_{\parallel})|^2 v_j(E, k_{\parallel}; R)}{\sum_{l=1}^8 |I_l(E, k_{\parallel})|^2 v_l(E, k_{\parallel}; L)}, \quad (\text{C.25})$$

which reduces to Eq. (7.13) when the incident state is supposed to be a pure Bloch state.

Bibliography

- [1] C. Cohen-Tannoudji, B. Diu, and F. Laloë, *Quantum Mechanics*, 2nd ed. (Wiley, New York, 1977).
- [2] A. Messiah, *Quantum Mechanics*, 1st ed. (Dover, New York, 1999).
- [3] R. P. Feynman, *Statistical Mechanics*, 1st ed. (Addison-Wesley, Reading, Ma, 1998).
- [4] W. Shockley, *Electrons and Holes in Semiconductors*, 1st ed. (D. Van Nostrand, New York, 1950).
- [5] E. L. Ivchenko, A. Y. Kaminski, and U. Rossler, *Phys. Rev. B* **54**, 5852 (1996).

Appendix D Velocity operator in the $\mathbf{k} \cdot \mathbf{p}$ formalism

Probably the following development or something very similar to it is already somewhere else, but since I came up with it and it helped me clarify some aspects of the $\mathbf{k} \cdot \mathbf{p}$ formalism and understand better the origin of

$$v_g = \frac{\partial E(\mathbf{k})}{\partial \mathbf{k}}, \quad (\text{D.1})$$

I decided to include it in this thesis.

The eigenstates of the Hamiltonian of a crystal can also be chosen to be eigenstates of the translation operations corresponding to that crystal. By Bloch's theorem [1], these states will have the form

$$\Psi_{\mathbf{k}} = e^{i\mathbf{k}\cdot\mathbf{r}} u_{\mathbf{k}}^n, \quad (\text{D.2})$$

where n labels the band and \mathbf{k} is the electron wavevector.

The Schrödinger equation with spin-orbit interaction states

$$H\Psi_{\mathbf{k}} = \left\{ \frac{P^2}{2m} + V(\mathbf{r}) + \frac{\hbar}{4m^2c^2} [\nabla V(\mathbf{r}) \times \mathbf{P}] \cdot \boldsymbol{\sigma} \right\} \Psi_{\mathbf{k}} = E\Psi_{\mathbf{k}}. \quad (\text{D.3})$$

Plugging Eq. (D.2) into the Schrödinger equation, and equation that the $u_{\mathbf{k}}^n$'s must satisfy is obtained [2]:

$$\mathcal{H}u_{\mathbf{k}}^n = \left\{ H + \frac{\hbar}{m} \mathbf{k} \cdot \mathbf{P} + \frac{\hbar^2 k^2}{2m} + \frac{\hbar}{4m^2c^2} [\nabla V(\mathbf{r}) \times \mathbf{k}] \cdot \boldsymbol{\sigma} \right\} u_{\mathbf{k}}^n = Eu_{\mathbf{k}}^n. \quad (\text{D.4})$$

Note that, although \mathcal{H} is commonly called the Hamiltonian of the crystal, it is really not a true Hamiltonian because of the presence of the extra terms. However, to stick with the convention, the term Hamiltonian is used throughout this thesis for \mathcal{H} or

H indistinctly. From a more mathematical point of view, \mathcal{H} is just an operator that happens to have the same spectrum as the true Hamiltonian of the system.

A velocity operator in quantum mechanics consistent with the Ehrenfest theorem can be defined by

$$\frac{d\mathbf{r}}{dt} = \frac{-i}{\hbar} [\mathbf{r}, H] \quad \Rightarrow \quad \frac{d\mathbf{r}}{dt} = \frac{\mathbf{P}}{m} + \frac{\hbar}{4m^2c^2} [\boldsymbol{\sigma} \times \nabla V(\mathbf{r})]. \quad (\text{D.5})$$

Now, keeping with the philosophy of using the $u_{\mathbf{k}}^n$'s instead of the $\Psi_{\mathbf{k}}$'s, one looks for a velocity operator \hat{v} such that

$$\left\langle \Psi_{\mathbf{k}'}^{n'} \left| \frac{d\mathbf{r}}{dt} \right| \Psi_{\mathbf{k}}^n \right\rangle = \left\langle u_{\mathbf{k}'}^{n'} | \hat{v} | u_{\mathbf{k}}^n \right\rangle. \quad (\text{D.6})$$

Plugging Eq. (D.5) into Eq. (D.6) one obtains

$$\left\langle u_{\mathbf{k}'}^{n'} | \hat{v} | u_{\mathbf{k}}^n \right\rangle = \left\langle \Psi_{\mathbf{k}'}^{n'} \left| \frac{\mathbf{P}}{m} + \frac{\hbar}{4m^2c^2} [\boldsymbol{\sigma} \times \nabla V(\mathbf{r})] \right| \Psi_{\mathbf{k}}^n \right\rangle, \quad (\text{D.7})$$

and from Eq. (D.2)

$$\begin{aligned} \left\langle u_{\mathbf{k}'}^{n'} | \hat{v} | u_{\mathbf{k}}^n \right\rangle &= \frac{\hbar \mathbf{k}}{m} \left\langle u_{\mathbf{k}'}^{n'} \left| e^{i(\mathbf{k}-\mathbf{k}')\cdot\mathbf{r}} \right| u_{\mathbf{k}}^n \right\rangle + \left\langle u_{\mathbf{k}'}^{n'} \left| e^{i(\mathbf{k}-\mathbf{k}')\cdot\mathbf{r}} \frac{\mathbf{P}}{m} \right| u_{\mathbf{k}}^n \right\rangle + \\ &\quad \left\langle u_{\mathbf{k}'}^{n'} \left| e^{i(\mathbf{k}-\mathbf{k}')\cdot\mathbf{r}} \frac{\hbar}{4m^2c^2} [\boldsymbol{\sigma} \times \nabla V(\mathbf{r})] \right| u_{\mathbf{k}}^n \right\rangle. \end{aligned} \quad (\text{D.8})$$

Comparing the equation above with Eq. (D.4), one sees that the matrix elements of the tentative velocity operator must satisfy¹

$$\left\langle u_{\mathbf{k}'}^{n'} | \hat{v} | u_{\mathbf{k}}^n \right\rangle = \left\langle u_{\mathbf{k}}^{n'} \left| \frac{1}{\hbar} \frac{\partial \mathcal{H}}{\partial \mathbf{k}} \right| u_{\mathbf{k}}^n \right\rangle \delta_{\mathbf{k}'\mathbf{k}}, \quad (\text{D.9})$$

and from here the definition of the velocity operator [3] in the $\mathbf{k} \cdot \mathbf{p}$ formalism

$$\hat{v} = \frac{1}{\hbar} \frac{\partial \mathcal{H}}{\partial \mathbf{k}} \quad (\text{D.10})$$

¹Note that, since this offers a prescription for the evaluation of matrix elements between any Bloch state, it is also valid for arbitrary states.

follows. However, it must be emphasized that, as shown in the above derivation, this definition only applies when looking at matrix elements between states with the same \mathbf{k} .

At this point, one can find the expectation value of the velocity of a Bloch state quite easily:

$$v_{\mathbf{k}}^n = \left\langle \Psi_{\mathbf{k}}^n \left| \frac{d\mathbf{r}}{dt} \right| \Psi_{\mathbf{k}}^n \right\rangle = \left\langle u_{\mathbf{k}}^n \left| \frac{1}{\hbar} \frac{\partial \mathcal{H}}{\partial \mathbf{k}} \right| u_{\mathbf{k}}^n \right\rangle = \frac{1}{\hbar} \frac{\partial E^n(\mathbf{k})}{\partial \mathbf{k}}, \quad (\text{D.11})$$

where, in the last step, the theorem proved in Sec. C.1 has been used.

Bibliography

- [1] N. W. Ashcroft and N. D. Mermin, *Solid State Physics*, 1st ed. (Saunders College, Philadelphia, PA, USA, 1976).
- [2] E. O. Kane, in *Tunneling Phenomena in Solids*, edited by E. Burstein and S. Lundqvist (Plenum Press, New York, 1969), p. 1.
- [3] E. L. Ivchenko, A. Y. Kaminski, and U. Rossler, *Phys. Rev. B* **54**, 5852 (1996).